Manoeuvring model of a high-speed craft

From empirical relations to sea trials validation

MSc Thesis

Annemiek Schwippert



TU Delft DAMEN

Manoeuvring model of a high-speed craft

From empirical relations to sea trials validation

by

Annemiek Schwippert

in collaboration with

Damen Shipyards Group

to obtain the degree of Master of Science
in Marine Technology in the specialisation Ship Hydromechanics
at the Delft University of Technology.
To be defended publicly on Thursday 3 December 2026 at 16:30.

Student number:	5127955	
Report number:	MT.26/27.013.M	
Project duration:	1 March, 2026 – 3 December, 2026	
Thesis committee:	Prof. dr. G. Weymouth,	TU Delft, supervisor
	Dr. H. Seyffert,	TU Delft
	G. Anastasopoulos,	Damen Research, Development & Innovation
	S. Terry,	Damen Research, Development & Innovation

Cover: RD&I Damen research vessel

An electronic version of this thesis is available at http://repository.tudelft.nl/.

TU Delft DAMEN

Preface

Dear reader,

This thesis was written during a nine-month research project into high-speed manoeuvring with a semi-planing vessel. It not only marks the end of these nine months of hard work. It also marks the end of my time as a student in Delft and the end of roughly 20 years in school. What a journey it has been. I arrived in Delft full of expectations, and I am leaving full of experiences and good friendships. Although COVID-19 left a big mark on the first few years, it also made the bonds with friends stronger. Together with the experiences I gained at S.G. William Froude, D.R.S.V Laga and various (student) orchestras, I would not have wanted my student days to have been any different.

Since manoeuvring was not part of our study program, I started the project without any prior knowledge. Although I had to learn manoeuvring theory on the way, I really enjoyed discovering a new part of Marine Technology. From struggling in the beginning with all the different coefficients and parameters, to really understanding the fundamental physics behind manoeuvring at the end of the project, working on this thesis involved a steep learning curve. I am proud of how I handled it, of everything I have learned along the way, and of the result that lies before you in this report.

During the thesis, I received weekly support from both my university and company supervisors. I am very grateful to George Anastasopoulos for his time and guidance, both on a professional and personal level. Our meetings were genuinely fun and inspiring and helped me stay motivated throughout the project. My thanks also go to Scott Terry for keeping the scope clear and asking critical questions when necessary. I would also like to thank Gabe Weymouth for guiding me through the entire process. Your feedback and probing questions have kept me inspired to keep looking further than the obvious. Furthermore, I would like to thank Harleigh Seyffert for taking place in my thesis committee and for the interesting discussion we had about the subject.

Finally, I want to thank my friends and family for their support, and for the welcome distractions from studying. Thanks to my parents and little brother who, despite not getting everything, keep on asking questions and trying to understand what I have been working on. Moreover, thanks to Dennis for lending me your second screen and cooking for me, so that I could finish my report on time. And to *opa Guus* for the fun stories about TU Delft back in the day, now you're no longer the only engineer in the family! Thank you all for these amazing years in Delft full of experiences, knowledge and, above all, so much fun. I am grateful to everyone with whom I have been able to share that.

Annemiek Schwippert
Delft, November 2026

Summary

Damen Shipyards Group is refitting a 12 m pilot vessel (with a maximum speed of 19kts) into an autonomous vessel, which requires a real-time high-speed manoeuvring model. Existing standards and models were developed for large displacement vessels at low Froude numbers ($Fr_L < 0.4$). High-speed craft ($Fr_L \geq 0.7$–0.8) are largely supported by hydrodynamic lift, causing speed-dependent sinkage and trim (running attitude), changing wetted geometry and strong motion coupling. This thesis addresses the question: *How can empirical formulations and dynamic running attitude corrections be combined with sea trial data to construct and validate a computationally efficient 4+2DOF manoeuvring model for high-speed craft?*

The MMG model was chosen over the Abkowitz and Nomoto models because it separates hull, propeller and rudder components, allowing new physics to be added easily. Empirical formulations were chosen over towing tank tests and CFD for their low computational cost. The 3DOF model was reconstructed, extended to 4DOF with roll, and verified with the KVLCC2, KCS and a twin-screw ferry. Steering models were added for a gear-case (General Prismatic Planing Hull, GPPH) and a twin-propeller twin-rudder system (pilot vessel). The hull forces follow Lewandowski's empirical formulations for hard-chine planing hulls, and a speed-dependent running attitude table updates the transom draft and wetted geometry at every time step (+2DOF). Reference bands were built from two CFD studies for the GPPH ($Fr_L = 1.85$) and from sea trial data for the pilot vessel, each with a 10% margin.

Correcting a double-counted surge added mass (m_x) in the sway equation removed a 7% force imbalance in the turn. Removing C_V^2 from Y'_v and correcting the sign of N'_r gave the linear derivatives the right order of magnitude, and the running attitude made them follow the captive-CFD trends. The model keeps steady turns up to $25°$, where the reference CFD spins out from $20°$. Roll coupling tightens the turn and running attitude widens it, so the diameter alone is not a sufficient check: only the 4+2DOF model brings both turning diameter and drift angle within the reference band. From $15°$, however, the inward heel is over-predicted, because the model's hull roll moment pushes inward where the CFD pushes outward. This remains with captive-CFD derivatives, pointing to a missing non-linear term; a single-term sweep identified $Y'_{vv\phi}$ and $K'_{vv\phi}$ as the most consistent candidates. The propeller torque reaction reduced the heel by $1.6°$–$2.6°$. The drift under-prediction from $15°$ is a separate error: unaffected by KG, K_ϕ or torque, and also present with the CFD derivatives.

At 800, 1400 and 2050rpm ($Fr_L \approx 0.3$–0.9) for the pilot vessel, the running attitude reduced the turning diameter deviation from up to seven to about two times the trial values, and the heel over-prediction by a factor of 2.5–5 compared to the fixed attitude model. In contrast to the GPPH, it tightened the turn, while roll had little effect. The model does not reproduce the trials' change from outward heel at low speed to inward heel at the highest speed, and predicts smaller zigzag overshoots, indicating an over-damped steering response. At lower speeds, Lewandowski's planing formulations are applied outside their domain.

The GPPH running attitude table is based on straight-ahead tests only, and the pilot vessel table has four speed points with a gap between 5 and 9 m/s. The coefficient sweep rests on three steady turns, and the trials were affected by current and wind. The work revealed that published manoeuvring models are difficult to reproduce, and that no quantitative manoeuvring criteria exist for high-speed craft. It also indicated that the propeller torque reaction is significant for small high-speed craft; however, it is neglected in the standard MMG convention. Recommended are running attitude tables covering a large range of Froude number, trim and heel (including the hump region), captive tests at fixed heel and drift angles to isolate non-linear terms, and a model that transitions from a displacement MMG model to the planing model with Froude number. In its current form, the model is suited for comparing early design options and steady-turn trends in the early design stage; its low-speed behaviour and dynamic response must be improved before it can support real-time vessel control.

Contents

Preface i

Summary ii

Nomenclature ix

1 Introduction 1
1.1 Research gap and question . . . 2

2 Literature review 4
2.1 Manoeuvring background . . . 4
2.1.1 Coordinate system . . . 6
2.2 High speed manoeuvring . . . 7
2.2.1 Heel angle in turning motion . . . 8
2.2.2 Instabilities during manoeuvres . . . 9
2.3 Model selection . . . 9
2.3.1 MMG model adaptation to high-speed craft . . . 11
2.4 Forces on a bare hull during manoeuvring . . . 12
2.4.1 Hydrodynamic coefficients . . . 15
2.4.2 Methods to obtain the coefficients . . . 16
2.4.3 Reproducibility of published manoeuvring models . . . 17
2.5 High-speed hull data . . . 18
2.5.1 General Prismatic Planing Hull . . . 18
2.5.2 Pilot vessel . . . 18

3 Methodology 20
3.1 Standard 3DOF MMG model . . . 20
3.2 Expansion to 4DOF MMG model . . . 22
3.3 Additional steering models . . . 24
3.3.1 Gear-case model - GPPH . . . 24
3.3.2 Twin-propeller twin-rudder model . . . 26
3.4 Empirical model - Pilot vessel . . . 27
3.4.1 Sway/roll/yaw hull force . . . 28
3.4.2 Surge hull force . . . 29
3.4.3 Propeller force . . . 29
3.4.4 Rudder force . . . 29
3.5 Expansion to 4+2DOF model . . . 30

4 Assessment of simulation models 31
4.1 3DOF MMG model . . . 31
4.2 4DOF MMG model . . . 33
4.3 Twin propeller twin rudder model . . . 35
4.4 Gear-case model . . . 37
4.5 Empirical hull model assessment with GPPH-model . . . 38

5 Results and discussion 40
5.1 Empirical hull model analysis with GPPH-model . . . 41
5.1.1 Corrections to the formulations . . . 46
5.1.2 Analysis of adjusted model . . . 48
5.1.3 Impact of drift and roll . . . 52
5.1.4 Assessment of the final model against free-running CFD data for the GPPH . . . 55
5.2 Sensitivity study non-linear coefficients planing model . . . 57

5.2.1 GPPH coefficient sweep results . . . 58
5.3 Sea trial data analysis - Pilot vessel . . . 61
5.4 Influence of model extensions . . . 64
5.4.1 GPPH . . . 65
5.4.2 Pilot vessel . . . 66
5.5 Discussion of results . . . 67
5.5.1 Contributions of the presented method . . . 69
5.5.2 Limitations of the presented method . . . 70

6 Conclusion **71**
6.1 Recommendations . . . 74

References **75**

A Simulations input tables **81**
A.1 3DOF MMG model . . . 81
A.2 Additional input data 4DOF MMG model . . . 82
A.3 Twin-propeller twin-rudder model . . . 83
A.4 Empirical coefficients model . . . 84
A.5 General Prismatic Planing Hull (GPPH) model . . . 85

B Final simulation model **86**

List of Figures

1.1 Pilot boat turning behind stern of container vessel [10]. 2

2.1 Different phases and numerical measures of the (starboard) turning path of a vessel [6]. 5
2.2 Various executes of the zigzag manoeuvre [23]. 5
2.3 The relationship between the yaw turning rate (r) and rudder angle (δ) following the spiral manoeuvre test for both a stable (left, Dieudonné spiral) and unstable (right, Bech spiral) vessel [6]. 6
2.4 The translations and rotations of a vessel around axes in six degrees of freedom [15]. . 7
2.5 The coordinate system commonly used in manoeuvring theory [25]. 7
2.6 Resistance/weight ratio versus volumetric Froude number for deadrise angles 12.5° and 25°, $L_p/B_{pX} = 2.0$ and $LCG = 8\%$ [26]. 7
2.7 Forces acting on the hull of a high-speed craft in a turning manoeuvre [12]. 8
2.8 Typical relationship between the surge force X and the longitudinal acceleration $\dot{u}$ ([3]). 12
2.9 A vessel in transverse acceleration to starboard [14]. 13
2.10 Typical relationship between the sway force Y and the transverse acceleration $\dot{v}$ [14]. . 13
2.11 A vessel in rotational acceleration in clockwise direction [14]. 13
2.12 Typical relationship between the yaw moment N and the rotational acceleration $\dot{r}$ ([3]).. 13
2.13 A vessel in both longitudinal and transverse velocity [14]. 14
2.14 Typical relationship between the sway force Y, the yaw moment N and the transverse velocity v [14]. 14
2.15 A vessel in both longitudinal velocity (u) and rotational velocity (r) [14]. 14
2.16 Typical relationship between the sway force Y, the yaw moment N and the rotational velocity r [14]. 14
2.17 A vessel experiencing roll velocity (p) and moment (K) [3]. 15
2.18 The typical relationship between the roll moment K and the roll velocity p [3]. 15
2.19 Typical relationship between the roll moment K and the roll angle ϕ [3]. 15
2.20 Visualisation of the oblique towing tests [3]. 17
2.21 Visualisation of circular motion tests in a rotating arm tank [3]. 17
2.22 Front and side view of the General Prismatic Planing Hull (GPPH) [43]. 18
2.23 Pilot vessel used to create sea trial dataset [76]. 19

3.1 Propeller force and moment around the z-axis in a twin-propeller configuration. . . . 26

4.1 Straight sailing run with the $KVLCC2_{L3}$ model for various propeller rps settings with an approach speed of 0.76m/s, run with the standard 3DOF MMG model. 31
4.2 Straight sailing run with the $KVLCC2$ full-scale model for various propeller rpm settings and resistance coefficients, run with the standard 3DOF MMG model. 32
4.3 Straight sailing run with the $KVLCC2_{L7}$ model for various propeller rps settings and resistance coefficient, run with the standard 3DOF MMG model. 32
4.4 Turning circle run for KVLCC2 full scale and L7-model with standard 3DOF MMG model, compared with digitised data from [22]. 32
4.5 Turning circle run for the KCS_{L4} model comparing rudder rate and instant step simulation, with digitised data from [46].. 33
4.6 Turning circle timeseries run for the KCS_{L4} model with the 4DOF MMG model, compared against digitised data from [46]. 34
4.7 Turning circle run for KCS in 4DOF MMG model, compared with digitised data from [46]. 35
4.8 Straight sailing run for the TPTR model with various resistance coefficient values. . . 36

4.9 Time-series and trajectory run with the TPTR-model in the 4DOF MMG model, compared with data digitised from [80]. . . . 36
4.10 Comparison of propeller and gearcase using trim data from the paper and simulation model forces with [19] tables. . . . 37
4.11 Turning circle run with a steering angle of 5deg of the empirical model with the GPPH gearcase steering model, compared with data from [43]. . . . 38
4.12 Turning circle run with a steering angle of 10deg of the empirical model with the GPPH gearcase steering model, compared with data from [43]. . . . 39
4.13 Turning circle run with a steering angle of 15deg of the empirical model with the GPPH gearcase steering model, compared with data from [43]. . . . 39

5.1 Linear hull derivatives for the GPPH-model at the starting condition of the simulation model, compared with captive-CFD data from [43]. . . . 41
5.2 Linear hull derivatives for the GPPH-model without Cv2 in Y_v and shifted points to be in the right reference frame (body vs horizontal), compared with captive-CFD from [43]. 42
5.3 Running attitude test for GPPH for 4 cases: A baseline = start model, B= running transom draft calculated with T_transom = L_K*sin(trim), C = Y_v without Cv2, D= Y_v with captive-CFD data from [43]. . . . 43
5.4 Linear hull derivatives for the GPPH-model with running attitude addition, compared to captive-CFD from [43]. . . . 44
5.5 Turning circle run for 5deg steering angle GPPH with addition of running attitude and excluding Cv2 for Y_v coefficient, compared to [43]. . . . 45
5.6 Turning circle run for 10deg steering angle GPPH with addition of running attitude and excluding Cv2 for Y_v coefficient, compared to [43]. . . . 45
5.7 Turning circle run for 15deg steering angle GPPH with addition of running attitude and excluding Cv2 for Y_v coefficient, compared to [43]. . . . 46
5.8 Effect of removing the factor C_V^2 from the empirical sway derivative Y'_v of Lewandowski [5], for the fixed attitude (solid) and running attitude (dashed) model, compared with the captive-CFD data points of Yasukawa et al. [43]. . . . 46
5.9 Effect of changing the sign from the empirical yaw derivative N'_r of Lewandowski [5], for the fixed attitude (solid) and running attitude (dashed) model, compared with the captive-CFD data points of Yasukawa et al. [43]. . . . 47
5.10 Effect of addition of the dynamic lift to the empirical heel derivatives Y'_ϕ and N'_ϕ of Lewandowski [5], for the fixed attitude (solid) and running attitude (dashed) model, compared with the captive-CFD data points of Yasukawa et al. [43]. . . . 48
5.11 Margin for data explained based on two papers presenting CFD data used for comparisons; [19, 43]. . . . 48
5.12 Run of the model with CFD hull force values from [43]. . . . 49
5.13 Analysis of the equations of motion, bug found: m_x counted double. . . . 49
5.14 Turning circle run with 5deg steering angle for GPPH with final model (no Cv2, running attitude, mx fix), compared with [43] CFD data. . . . 50
5.15 Turning circle run with 10deg steering angle for GPPH with final model (no Cv2, running attitude, mx fix), compared with [43] CFD data. . . . 50
5.16 Turning circle run with 15deg steering angle for GPPH with final model (no Cv2, running attitude, mx fix), compared with [43] CFD data. . . . 51
5.17 Steady-turn validation of the running attitude and fixed attitude model against the CFD reference band of [19, 43]. . . . 52
5.18 Turning circle run for the GPPH for various values of KG and roll restoring coefficient K_ϕ, and the propeller torque reaction addition compared to a baseline run for the running attitude model. . . . 53
5.19 Steady-turn validation of forces from the running attitude and fixed attitude model against the CFD reference band of [19, 43]. . . . 54
5.20 Net hull roll moment of the GPPH hull in the CFD state . . . 54
5.21 Drift angle of model with captive CFD input from [43]. . . . 55
5.22 Steady-turn validation of the trajectories from the running attitude and fixed attitude model against the CFD reference band of [30, 43]. . . . 56

5.23 Sway coefficient sweep for the GPPH hull. 58
5.24 Roll coefficient sweep for the GPPH hull. 59
5.25 Yaw coefficient sweep for the GPPH hull. 59
5.26 Overview of turning circle simulations together with the sea trial data of the pilot vessel, run with the velocity and propeller rpm as measured during the trials. 61
5.27 Overview of zigzag simulations together with the sea trial data of the pilot vessel, run with the velocity and propeller rpm as measured during the trials 61
5.28 Steady-turn validation of the running attitude and fixed attitude model against the sea trial data, results presented for various steering angles. 63
5.29 Steady-turn validation of the running attitude and fixed attitude model against the sea trial data for a 30° turning circle, results presented based on approach speed. 64
5.30 3vs4DOF comparison of the GPPH hull for turning parameters. 65
5.31 3vs4DOF comparison of the GPPH hull for turning diameter and drift angle at 10 and 15° steering angles. 66
5.32 3vs4DOF comparison of the pilot vessel for turning diameter and drift angle at a 30° steering angle for the 2050rpm run. 67

List of Tables

2.1 Comparison of Abkowitz and MMG manoeuvring model (Note: sources in table are in addition to [3, 22]). . . . 10
2.2 Various estimation methodologies for the hydrodynamic manoeuvring coefficients as presented in the literature. . . . 16

3.1 Input parameters 3DOF displacement simulations; KVLCC2 data from [22], KCS data from [46]. The parameters marked with a star* have a different origin and are elaborated further in the text below the table. . . . 21
3.2 Additional input parameters for the 4DOF displacement simulations; KCS data from [46]. The parameters marked with a star* have a different origin and are elaborated further in the text below the table. . . . 24
3.3 Empirical hydrodynamic coefficients bare hull [5]. . . . 28
3.4 Contribution of appendages [5]. . . . 28

5.1 Tested cases of the simulation models, with the vessels, comparison data and the sections where each model is described, assessed and its input data is given. . . . 40
5.2 Steady-turn validation of the fixed attitude against the CFD reference band of Wang et al. (2025) and Yasukawa et al. (2025). Inside = inside reference band, Margin = within 10% of the band edge (both sides), Outside = outside reference band. . . . 56
5.3 Steady-turn validation of the final model (running attitude) against the CFD reference band of Wang et al. (2025) and Yasukawa et al. (2025). Inside = inside reference band, Margin = within 10% of the band edge (both sides), Outside = outside reference band. . . . 56
5.4 Steady-turn results at 20° and 25° of the fixed attitude and running attitude models. . . . 57

A.1 Input data 3DOF displacement simulations; KVLCC2 data from [22], KCS data from [46]. The numbers marked with a star* have a different origin and are elaborated further in the Section 3.1 and Section 3.2. . . . 81
A.2 Additional input data 4DOF displacement simulations; KCS data from [46]. The numbers marked with a star* have a different origin and are elaborated further inSection 3.2. 82
A.3 Input data twin-propeller twin-rudder displacement simulations; model data from [80]. The numbers marked with a star* have a different origin and are elaborated further in Section 3.3.2. . . . 83
A.4 Input data GPPH simulations; model data from [19, 30, 43].. . . . 85
A.5 Running attitude GPPH model as function of speed. The Absolute Pitch is the static trim added to the measured trim and is the value used for the running attitude. Data is from [73]. . . . 85

Nomenclature

Abbreviations

Abbreviation	*Description*
CFD	Computational Fluid Dynamics
CMT	Circular Motion Test
COG	Centre of gravity
DOF	Degree(s) of freedom; e.g. 3DOF (surge, sway, yaw), 4DOF (+ roll)
4+2DOF	4DOF model with speed-dependent heave and pitch (running attitude) as input
GPPH	General Prismatic Planing Hull (benchmark hull)
IMO	International Maritime Organization
ITTC	International Towing Tank Conference
JASNAOE	Japan Society of Naval Architects and Ocean Engineers
KCS	KRISO Container Ship (benchmark hull)
KVLCC2	KRISO Very Large Crude Carrier 2 (benchmark hull)
MCR	Maximum Continuous Rating
MMG	Maneuvering Modeling Group (standard manoeuvring model)
OTT	Oblique Towing Test
PCC	Pure Car Carrier (benchmark hull)
PS	Port-side
RANS	Reynolds-Averaged Navier–Stokes
RK45	Runge–Kutta 4(5) adaptive-step integration scheme
rps	Revolutions per second
SB	Starboard
SI	System Identification
TPTR	Twin-propeller twin-rudder

Latin symbols

Symbol	*Description*	*Unit*
a	Empirical linear roll damping factor	–
a_H	Rudder force increase factor	–
A_e	Effective rudder aspect ratio	–
A_R	Rudder area	m^2
b	Empirical quadratic roll damping factor	–
B	Width of the vessel	m
B_{ac}	Average wetted chine beam	m
c	Fitted coefficient of a tested term (coefficient sweep)	–
c_i	Single-angle fitted coefficient, d_i^*/t_i	–
c_R	Rudder chord length	m
C_1, C_2	Coefficients for the change of propeller wake fraction during manoeuvring	–

C_B, C_b	Block coefficient	–
CL	Rudder lift coefficient	–
CL_{lin}	Linear rudder lift coefficient	–
CL_{max}	Maximum (stall) rudder lift coefficient	–
C_V	Speed coefficient, $U/\sqrt{gB}$	–
d	Draft	m
d_{inst}	Instantaneous draft	m
d^*	Missing hull force: CFD minus simulation model (coefficient sweep)	–
D	Turning diameter	m
D_P	Propeller diameter	m
D_R	Rudder drag force	N
f_α	Rudder lift gradient coefficient	–
f_{sw}	Side wetting correction factor	–
F_x^*, F_y^*, F_z^*	Empirical gear-case and propeller force components	N
F_N	Rudder normal force	N
F_ϕ	Roll-induced change in dynamic normal force (per side)	$\mathrm{N\,rad^{-1}}$
Fn, Fr_L	Froude number based on length, $U/\sqrt{gL}$	–
Fr_B	Froude number based on beam, $U/\sqrt{gB}$	–
Fr_∇	Volumetric Froude number, $U/\sqrt{g\nabla^{1/3}}$	–
g	Gravitational acceleration	$\mathrm{m\,s^{-2}}$
$\overline{\mathrm{GM}}$	Metacentric height	m
h_1, h_2, h_3	Lever arms in Lewandowski's formulae	m
h_R	Lever arm of the rudder roll moment	m
H_R	Rudder span	m
I_{xx}	Moment of inertia in roll	$\mathrm{kg\,m^2}$
I_{xz}	Product of inertia in the xz-plane	$\mathrm{kg\,m^2}$
I_{yy}	Moment of inertia in pitch	$\mathrm{kg\,m^2}$
I_{zG}, I_{zz}	Moment of inertia in yaw	$\mathrm{kg\,m^2}$
J	Propeller advance ratio	–
J_{xx}	Added moment of inertia in roll	$\mathrm{kg\,m^2}$
J_z, J_{zz}	Added moment of inertia in yaw	$\mathrm{kg\,m^2}$
k	Exponent of the stall-limit function	–
k_0, k_1, k_2	Coefficients of the K_T polynomial in J	–
$k(\beta)$	Added-mass coefficient as a function of deadrise angle	–
k'_{xx}	Non-dimensional roll radius of gyration (including added inertia)	–
K	Roll moment	$\mathrm{N\,m}$
KB	Height of the centre of buoyancy above the keel	m
$K_{D\phi}$	Roll restoring derivative due to dynamic lift	$\mathrm{N\,m\,rad^{-1}}$
K_{dm}	Roll damping moment	$\mathrm{N\,m}$
KG	Height of the centre of gravity above the keel	m
$\overline{\mathrm{KM}}$	Height of the metacentre above the keel	m
K_Q	Propeller torque coefficient	–
K_{rm}	Roll restoring moment	$\mathrm{N\,m}$
K_T	Propeller thrust coefficient (open water)	–
l_R	Effective longitudinal coordinate of the rudder	m
L	Length overall	m
L_{PP}	Length between perpendiculars	m

L_C	Wetted chine length	m
LCG	Longitudinal centre of gravity	m
LCP	Longitudinal centre of pressure	m
L_D	Dynamic lift force	N
L_K	Wetted keel length	m
L_{keel}	Keel length	m
L_R	Rudder lift force	N
$L_{towpoint}$	Longitudinal distance between COG and tow point in GPPH towing tank tests	m
m	Ship mass	kg
m_F	Added mass of the appendage (fin)	kg
m_x	Added mass in surge	kg
m_y	Added mass in sway	kg
M	Pitch moment	$\mathrm{N\,m}$
n, n_p, n_P	Propeller revolutions	s^{-1}
N	Yaw moment	$\mathrm{N\,m}$
N_m	Yaw moment about midship	$\mathrm{N\,m}$
$o_0 - x_0y_0z_0$	Earth-fixed coordinate system	
$o - xyz$	Ship-fixed coordinate system (x forward, y to starboard, z downward)	
p	Roll rate	$\mathrm{rad\,s}^{-1}$
q	Pitch rate	$\mathrm{rad\,s}^{-1}$
r	Yaw rate	$\mathrm{rad\,s}^{-1}$
R'_0	Non-dimensional straight-ahead resistance coefficient	–
Rr	Rudder rate	$^\circ\,\mathrm{s}^{-1}$
$R(u)$	Bare-hull resistance as a function of surge velocity	N
t	Value of the tested term at the CFD state (coefficient sweep)	–
t_P	Thrust deduction factor	–
t_R	Steering resistance deduction factor	–
T	Propeller thrust	N
T'	Non-dimensional transom draft in Lewandowski's formulae	–
T_{static}	Static transom draft	m
$T_{transom}$	Running transom draft	m
u	Surge velocity	$\mathrm{m\,s}^{-1}$
u_P	Longitudinal inflow velocity at the propeller	$\mathrm{m\,s}^{-1}$
u_R, v_R	Longitudinal and lateral inflow velocity at the rudder	$\mathrm{m\,s}^{-1}$
U	Resultant ship speed	$\mathrm{m\,s}^{-1}$
U_R	Resultant inflow velocity at the rudder	$\mathrm{m\,s}^{-1}$
U_0	Approach speed	$\mathrm{m\,s}^{-1}$
v	Sway velocity	$\mathrm{m\,s}^{-1}$
v_m	Sway velocity at midship	$\mathrm{m\,s}^{-1}$
$v_{R,loc}$	Local lateral flow velocity at the rudder	$\mathrm{m\,s}^{-1}$
V_A	Axial inflow velocity at the propeller	$\mathrm{m\,s}^{-1}$
w	Heave velocity	$\mathrm{m\,s}^{-1}$
w_P	Effective wake fraction at the propeller	–
w_R	Effective wake fraction at the rudder	–
w_{P0}	Wake fraction at the propeller in straight motion	–
W	Vessel weight, mg	N
x_F, y_F, z_F	Coordinates of the appendage (fin)	m

x_G, y_G, z_G	Coordinates of the centre of gravity	m
x_H	Longitudinal acting point of the additional lateral force induced by steering	m
x_P, y_P, z_P	Coordinates of the propeller	m
x_R, y_R, z_R	Coordinates of the rudder	m
X	Surge force	N
Y	Sway force	N
Y_{aH}	Lateral force induced on the hull by the rudder	N
Y_N	Rudder force normal to the blade	N
z_H	Vertical acting point of the hull lateral force	m
Z	Heave force	N

Greek symbols

Symbol	*Description*	*Unit*
α_R	Effective angle of attack of the rudder	rad
α_{trim}	Geometric inflow angle at the rudder due to trim and heel	rad
α_z	Vertical acting point of the lateral added mass m_y	m
β	Drift angle; deadrise angle in Lewandowski's formulae	$\mathrm{rad}, ^\circ$
β_P	Effective inflow angle at the propeller	rad
β_R	Effective inflow angle at the rudder	rad
γ_R	Flow straightening coefficient	–
δ	Rudder (steering) angle	$\mathrm{rad}, ^\circ$
δ_R	Effective inflow angle at the rudder (twin-rudder model)	rad
ε	Ratio of wake fraction at the rudder to that at the propeller	–
ϵ	Tilt angle of the gear-case	rad
η	Ratio of propeller diameter to rudder span, D_P/H_R	–
Δ	Displacement	kg, N
θ	Pitch (trim) angle	$\mathrm{rad}, ^\circ$
$\Delta\theta$	Change in trim angle relative to the static trim	$\mathrm{rad}, ^\circ$
κ	Experimental constant for the rudder inflow velocity	–
λ	Scale factor; mean wetted length–beam ratio $(L_K + L_C)/2B$ in Lewandowski's formulae	–
Λ	Rudder aspect ratio H_R^2/A_R; rudder lift-curve slope in Section 3.4.4; appendage lift parameter in Table 3.4	–
τ	Trim angle in Lewandowski's formulae; tilt angle of the rudder in Section 3.4.4	$\mathrm{rad}, ^\circ$
ρ	Water density	$\mathrm{kg\,m^{-3}}$
ϕ	Roll (heel) angle	$\mathrm{rad}, ^\circ$
φ_R	Cant angle of the rudder	rad
ψ	Heading (yaw) angle	$\mathrm{rad}, ^\circ$
∇	Displaced volume	$\mathrm{m^3}$

Hydrodynamic derivatives

Symbol	*Description*	*Unit*
$Y_v, K_{\dot{p}}, \ldots$	Dimensional hydrodynamic derivative: force or moment (X, Y, K, N) with respect to the motion variable in the subscript, e.g. $Y_v = \partial Y / \partial v$	varies
X'_H, Y'_H, N'_H	Non-dimensional hull force and moment polynomials (also written X^*_H, Y^*_H, N^*_H)	–
$X'_{vv}, Y'_{vvr}, \ldots$	Non-dimensional (non-linear) hull derivatives; the subscript lists the variables of the term, e.g. Y'_{vvr} multiplies $v'^2_m r'$	–
$X_{\dot{u}}$	Surge force due to surge acceleration (surge added mass)	kg
$Y_{\dot{v}}$	Sway force due to sway acceleration (sway added mass)	kg
Y_v	Sway force due to sway velocity	$\mathrm{N\,s\,m^{-1}}$
$Y_{\dot{r}}$	Sway force due to yaw acceleration	$\mathrm{kg\,m}$
Y_r	Sway force due to yaw rate	$\mathrm{N\,s\,rad^{-1}}$
Y_ϕ	Sway force due to roll angle	$\mathrm{N\,rad^{-1}}$
K_p	Roll moment due to roll rate (roll damping)	$\mathrm{N\,m\,s\,rad^{-1}}$
K_ϕ	Roll moment due to roll angle (roll restoring)	$\mathrm{N\,m\,rad^{-1}}$
$K_{\dot{\phi}}$	Linear roll damping coefficient (equivalent to K_p)	$\mathrm{N\,m\,s\,rad^{-1}}$
$K_{\dot{\phi}\dot{\phi}}$	Quadratic roll damping coefficient	$\mathrm{N\,m\,s^2\,rad^{-2}}$
K_v	Roll moment due to sway velocity	$\mathrm{N\,s}$
$K_{\dot{p}}$	Roll moment due to roll acceleration (added moment of inertia)	$\mathrm{kg\,m^2}$
$N_{\dot{r}}$	Yaw moment due to yaw acceleration (added moment of inertia)	$\mathrm{kg\,m^2}$
N_v	Yaw moment due to sway velocity	$\mathrm{N\,s}$
$N_{\dot{v}}$	Yaw moment due to sway acceleration	$\mathrm{kg\,m}$
N_r	Yaw moment due to yaw rate	$\mathrm{N\,m\,s\,rad^{-1}}$
N_ϕ	Yaw moment due to roll angle	$\mathrm{N\,m\,rad^{-1}}$

Subscripts and superscripts

Symbol	*Description*
$(\cdot)'$	Non-dimensional quantity (MMG convention, see Section 3.1)
$\dot{(\cdot)}$	Time derivative
$(\cdot)_0$, $(\cdot)_{initial}$	Straight-ahead or initial condition (e.g. w_{P0}, $U_{initial}$)
$(\cdot)_{ap}$, $(\cdot)_{app}$	Appendage
$(\cdot)_b$	Body-fixed (heeled and trimmed) frame
$(\cdot)_{full}$	Full scale
$(\cdot)_{GC}$	Gear-case
$(\cdot)_H$	Hull
$(\cdot)_{L3}, (\cdot)_{L4}, (\cdot)_{L7}$	Model-scale vessel, identified by its length in metres
$(\cdot)_m$	Midship (e.g. v_m, N_m); model scale (e.g. U_m)
$(\cdot)_P$	Propeller
$(\cdot)_R$	Rudder
$(\cdot)_{(\mathrm{s})}$	Starboard propeller or rudder
$(\cdot)_{(\mathrm{p})}$	Port-side propeller or rudder
$(\cdot)_{(\mathrm{s,p})}$	Starboard or port-side propeller or rudder
$(\cdot)_{total}$	Sum of both propellers or rudders

1. Introduction

Maritime automation and autonomous vessel operations have attracted significant attention in recent years, driven by the operational need to increase safety, optimise fuel efficiency, lower environmental emissions, and address growing crew shortages. Although automated systems such as autopilots and dynamic positioning are already used daily onboard vessels, these technologies still rely on continuous human control to program routes or define position coordinates. Driven by intensifying personnel shortages and demanding operational profiles, a critical need has emerged to develop fully autonomous sailing vessels. This will not only reduce onboard crew requirements but also enable safer and more efficient route planning, decrease fuel consumption, minimise human error, and mitigate overall environmental impact.

Damen Shipyards Group recognises that developments in the maritime technology sector are moving towards remote control and autonomous vessels. Increased levels of automation in the future are explored at the Research, Development and Innovation department by investigating the integration of navigation automation on board vessels. As part of this research, a 12m pilot vessel with a maximum speed of 19kts is being refitted to be an autonomous sailing research vessel. In order to create a fully autonomous sailing vessel, a manoeuvring model capable of simulating (high-speed) vessel motions needs to be developed.

Vessel controllability is divided into course keeping, speed changing, and manoeuvring, with this work focusing specifically on manoeuvring, defined as the controlled change in direction of motion and responsiveness to environmental forces [1]. Scientific research in this field began with Euler's 1749 work *Scientia Navalis* and advanced significantly with Abkowitz's 1964 publications on motion stability, manoeuvring, and control [2, 3]. Regulatory frameworks subsequently evolved through the International Maritime Organization (IMO), starting with onboard information requirements in 1971, interim standards in 1993, and formal requirements adopted in 2002 under Resolution MSC.137(76) [4].

Under these regulations, a vessel's manoeuvrability is evaluated across specific performance metrics including directional stability, initial turning ability, turning capability, yaw-checking, and stopping ability [4, 5]. Although standard manoeuvres are established by the International Towing Tank Conference (ITTC) to test these guidelines, both were designed exclusively for displacement ships exceeding 100 meters in length operating at low Froude numbers [4, 6]. Consequently, these standards fail to address high-speed craft, where dynamic lift alters wetted geometry, running attitude, and directional stability characteristics.

As well as being more manoeuvrable (as depicted in Figure 1.1), there are several other aspects differentiating the physical behaviour of high-speed (semi-planing/planing) craft from regular displacement vessels. High speed is defined as the speed at which dynamic lift becomes significant. [5] proposed this to occur above $Fn \geq 0.7 - 0.8$ as the (maximum speed) operating range of the vessel. Where displacement vessels rely on hydrostatic buoyancy force, the weight of a vessel at high speed is mainly supported by hydrodynamic lift force [7, 8]. This force is generated by a pressure build-up caused by the flow along the hull [8, 9].

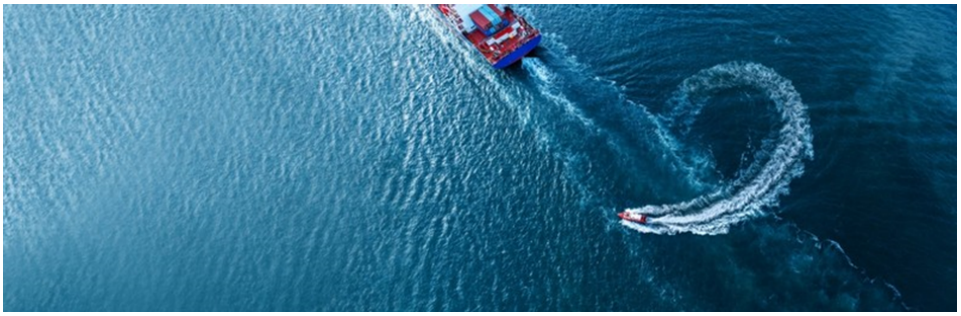

Figure 1.1: Pilot boat turning behind stern of container vessel [10].

The pilot vessel's maximum operating speed falls within the high-speed regime. This report will therefore focus on the manoeuvrability of a high-speed craft. The pilot vessel is equipped with two shaft lines, both with a 4-blade propeller and a conventional rudder. Its cruising speed is between $0 - 12\mathrm{kn}$ and its maximum speed is about $19\mathrm{kn}$. The vessel is 12 meters long and 4 meters wide. Sea trials across various speed regimes have been performed with the pilot vessel to create a dataset on which the research in this thesis is based. At its maximum speed of $19\mathrm{kn}$ (9.7 m/s), the pilot vessel operates at a Froude number of about $Fr_L = 0.9$.

Manoeuvring at high speed introduces several complexities which do not occur for vessels operating at low speed. The hydrodynamic manoeuvring coefficients governing hull forces do not remain constant across varying forward speeds. As speed increases, not only does the wave system change, but the generation of dynamic lift causes the vessel to start planing too [8, 11]. As a result, the wetted hull geometry changes, making the coefficients speed-dependent [5, 12, 13].

Additionally, while conventional manoeuvring models restrict motion to the horizontal plane, research highlights that high-speed craft experience strong motion coupling across both horizontal and vertical degrees of freedom [14–18]. Additionally, operating at high speed introduces unique instabilities in both longitudinal and transversal directions. The coupling of these instabilities can result in a loss of control of the vessel [5, 8, 19–21].

1.1. Research gap and question

As the standards for manoeuvring focus on conventional displacement vessels, the existing models were developed for relatively slow, heavy vessels. As a result, the manoeuvring characteristics of high-speed craft have been less covered, with the models not being appropriately tuned to high-speed craft. This thesis contributes by investigating several models and methods and how to adapt them to simulate the manoeuvring behaviour of a high-speed semi-planing vessel. The use of a full-scale sea trial dataset to calibrate and validate the model contributes to understanding the manoeuvring behaviour of a high-speed semi-planing craft based on hydrodynamic theory.

The introduction of Computational Fluid Dynamics (CFD) has improved simulation accuracy. However, these simulations are very computationally expensive. This makes them impractical for situations where fast computation is necessary, such as the manoeuvring system of an autonomous sailing vessel, where control inputs must be predicted in real time. Creating an efficient manoeuvring model that captures the essential physics required to simulate a high-speed craft would be very useful for these real-time applications. Furthermore, the model can be used during the design process; by performing rapid simulations, the need for CFD is reduced, which can shorten the overall process.

Based on the above declared gap in the literature, the following research question is established:

How can empirical formulations and dynamic running attitude corrections be combined with sea trial data to construct and validate a computationally efficient 4+2DOF manoeuvring model for high-speed craft?

To answer this question, several sub-questions have been identified. The goal of the research is to create an effective model with low computational cost which can be used in early design estimations. Full-scale sea trials have been performed across various speed regimes with the pilot vessel to create a dataset which can be used to calibrate and/or validate the model. In line with this goal, the following sub-questions will be investigated:

- What are unique elements distinguishing high-speed craft from conventional displacement vessels?
- What is the state-of-the-art in adapting models for displacement vessels to capture the manoeuvring characteristics of high-speed craft?
- What methods exist to capture the hydrodynamic coefficients of manoeuvring?
- How can empirical hydrodynamic formulations and speed-dependent running attitude lookup tables be integrated into an MMG framework to determine the forces acting on a high-speed hull?
- How accurately does the 4+2DOF empirical manoeuvring model replicate benchmark CFD data and full-scale sea trial behaviour across operational speed regimes?

The first three sub-questions are answered in the literature review, which is presented in Chapter 2 of this report, where it is shown how manoeuvring theory and the unique elements of high-speed craft combined led to the choice of a manoeuvring model. Also, the forces during manoeuvring are analysed alongside the hydrodynamic coefficients that describe them. The methodology is presented in Chapter 3. This chapter introduces the simulation models developed in this thesis. In Chapter 4 the performance of the developed models is assessed. The Results are presented in Chapter 5 together with the discussion of the results, the contributions of the thesis and limitations of the method. The findings of the thesis, together with the answer to the research questions, are presented in Chapter 6. In this chapter the recommendations for further research are also presented. In Chapter A, tables with the input values of the various ship types used in this thesis can be found. In Chapter B, the Python code blocks can be found of the final hull, propulsion and steering models.

2. Literature review

This chapter presents the findings of the literature research performed for this thesis. First, a short manoeuvring theory background is given. Followed by an overview of the specific aspects of manoeuvring at high speed in Section 2.2. The mathematical models used to describe manoeuvring behaviour are presented in Section 2.3, together with a study on how the selected model has been adapted for high-speed craft. In Section 2.4 the forces working on a vessel during manoeuvring are analysed, as well as methods to obtain the coefficients describing these forces. The chapter concludes with Section 2.5 giving an overview of two high-speed hulls used in this thesis.

2.1. Manoeuvring background

In addition to the geometric design requirements, a vessel must also meet several manoeuvring requirements. The first one is *directional stability*, being the ability of the vessel to sail in a straight line with the rudder set at midship in the absence of external influences. During sea trials, this characteristic is tested by comparing the rate of turn with the rudder direction during spiral tests. The second requirement is its response to a change in steering angle within a certain specified time with minimal overshoot in heading. During sea trials, this characteristic is tested by performing zigzag manoeuvres [1].

The interaction between rudder and ship can be modelled considering the hydrodynamic interaction of a wing with a flap [22]. When the helmsman, or autopilot system controlling the rudder, decides on a (corrective) course change, the helm is changed in the direction of the new path. This prompts the steering gear to change the steering angle. In response to a change in steering angle, a lift force is induced on the rudder (flap) itself. This induces an additional force component on the hull (wing). An angle of attack relative to the original forward motion is induced on the hull by this force, eventually leading to angular velocity and other motions. These motions will lead to hydrodynamic forces and moments, which in turn will affect the path and change in heading of the vessel [14]. The vessel starts turning in response to the hydrodynamics of the flow around the ship [1].

Next to directional stability (i.e. course-keeping ability), the IMO has defined manoeuvring standards that specify the required manoeuvrability of a vessel [4, Res. MSC137(76)]. Which is assessed by the following criteria [4, 14]:

Initial turning ability	The response of the ship to deflection of the rudder. For the initial turning ability, a maximum of 2.5 ship lengths is defined in which the vessel's heading must have turned 10° from the original path (both for a starboard and port turn).
Turning ability	The response of the ship to a hard-over rudder deflection. For the distance travelled during the turn in the x- and y-direction, the max distance is 4.5 ship lengths and 5 ship lengths respectively.
Yaw checking ability	The response of the ship to a counter-rudder applied during a turning manoeuvre. This is measured in terms of the overshoot angles during the zigzag test, which is the delay in heading compared to the steering angle.
Stopping ability	The response of the ship to a full astern order. The length which the ship travels along its track should not exceed 15 ship lengths (with an exception of 20 ship lengths for vessels with very large displacement).

The International Towing Tank Conference (ITTC) has established several manoeuvres with which the manoeuvrability can be determined [6], which a vessel should be able to perform within certain established limits. Each manoeuvre has the goal of assessing a manoeuvring characteristic; the *turning ability* is tested by performing turning circles, the *initial turning ability* and the *yaw checking ability* are tested by performing a zigzag manoeuvre, and the degree of *directional stability* is tested by performing a spiral manoeuvre.

The turning motion of a vessel can be divided into three phases. Different numerical measures characterise each phase. Figure 2.1 presents the turning phases and measures of a starboard turn. The advance is the distance from the vessel's position at the moment the rudder is turned to its location when the vessel is turned 90° in the original x-axis direction; the distance at that point in the turn to the original y-axis is called the transfer. After the vessel has turned 180°, the distance from the original x-axis to the new x-axis is labelled as the tactical diameter [14].

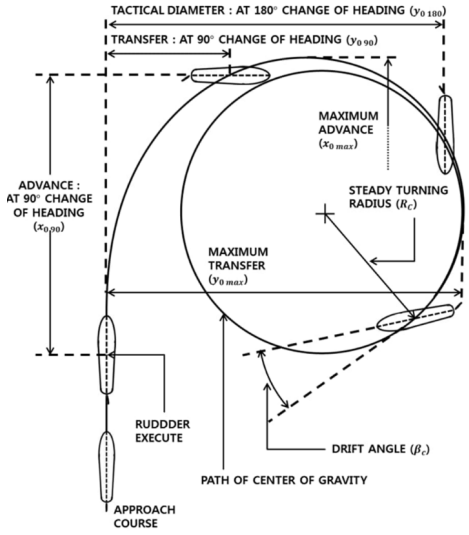

Figure 2.1: Different phases and numerical measures of the (starboard) turning path of a vessel [6].

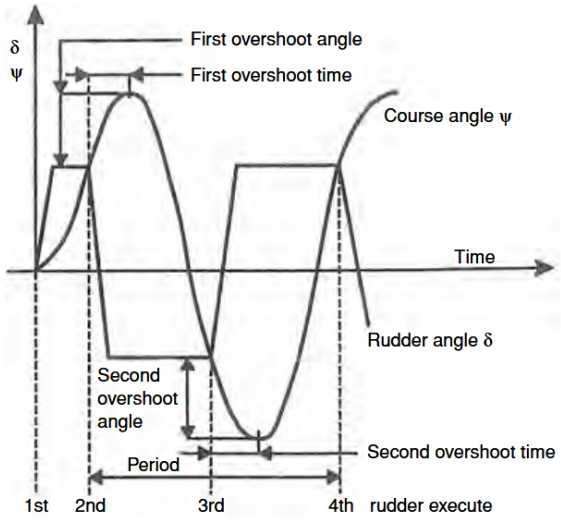

Figure 2.2: Various executes of the zigzag manoeuvre [23].

At the beginning of the zigzag manoeuvre, the *initial turning ability* can be determined. For this, the distances travelled (ahead and sideways) after a change in rudder deflection, along with the change in the vessel's heading angle per unit change in steering angle, are needed. To determine the *yaw checking ability*, the first overshoot angle is used [14]. The manoeuvre must be performed on both the starboard and port-sides, with steering angles ranging between 10/10 and 20/20 degrees. While the vessel has a steady approach speed, the rudder (δ) is deflected to a certain angle (first execute). When the heading (ψ) of the vessel has changed to the same angle, the rudder is reversed to the opposite side with the same steering angle (second execute) . This is repeated several times on both sides, as illustrated in Figure 2.2 above.

Directional stability is evaluated using the (Dieudonné) spiral manoeuvre. As the vessel is sailing on a straight course, the rudder is set to a certain angle and held fixed until a steady yaw rate is achieved. A steady-state yaw rate is measured across the full steering range by changing the rudder in steps of usually $5°$. The slope of the resulting yaw rate curve at zero steering angle indicates the degree of directional stability (see the left plot in Figure 2.3). Where a stable vessel finds a unique steady yaw rate for each steering angle, an unstable vessel will have multiple turning rates for a given deflection. This creates a region around zero steering angle in which the vessel can spontaneously transition to the opposite heading. To fully map this non-linear stability characteristic, the Bech reverse spiral test is performed. By steering the craft to constant rates of turn, the mean steering angle required for each rate is measured. The height and width of the resulting "dead rudder region" directly quantify the magnitude of the vessel's instability (see the right plot in Figure 2.3).

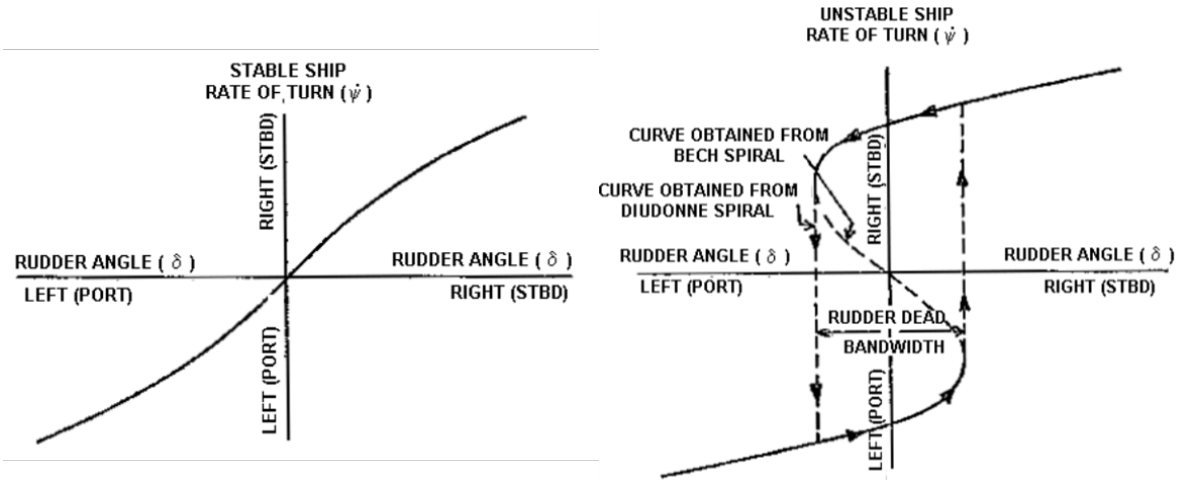

Figure 2.3: The relationship between the yaw turning rate (r) and rudder angle (δ) following the spiral manoeuvre test for both a stable (left, Dieudonné spiral) and unstable (right, Bech spiral) vessel [6].

It should be noted that the manoeuvres described above originate from the IMO Standards for Ship Manoeuvrability [4], which were developed for large displacement ships (100 m and longer) and explicitly exclude high-speed craft. Their applicability to small high-speed craft is therefore limited, as will be explained in further detail in Section 2.2 below. Firstly, the acceptance criteria are expressed in ship lengths, which become physically meaningless for a vessel of only a few metres travelling at high speed. Secondly, the hydrodynamic behaviour of planing and semi-planing hulls changes considerably with speed, as trim, sinkage and wetted surface vary. Therefore, a single test speed cannot represent the full operating range.

In addition, high-speed craft show strong coupling between the vertical and horizontal planes. During turns, the vessel heels, which in turn alters the manoeuvring forces, and hard-over manoeuvres at full speed may even lead to instabilities. High-speed craft can experience dynamic instabilities such as porpoising and chine walking, which the quasi-steady spiral tests cannot capture. Also, many small craft steer with waterjets or outboard engines; the steering force also depends on thrust, which weakens the assumed relationship between steering angle and heading. For these reasons, small high-speed craft manoeuvrability is usually assessed by speed-dependent trials that also consider heel angle, lateral accelerations and dynamic stability, rather than by the conventional IMO criteria alone [8, 24].

2.1.1. Coordinate system

The motions of a vessel can be distinguished into translations (surge, sway, heave) and rotations (roll, pitch, yaw), each consisting of motions in the direction of or around an axis. In Figure 2.4, the motions are illustrated. It should be noted that, contrary to the commonly used coordinate system in the maritime sector, for manoeuvring the y-axis is positive to starboard and the z-axis is positively defined downwards.

In ship manoeuvring, two different coordinate systems are used to locate the vessel and simulate its motions. The first is the earth-fixed system $o_0 - x_0 y_0 z_0$, where the origin is fixed to the still water surface in the $x_0 - y_0$ plane. The second is the ship-fixed coordinate system $o - xyz$, where the origin is either chosen at midship or the centre of gravity. In Figure 2.5 the coordinate system used in manoeuvring is presented, here ψ is the heading of the vessel, δ is the rudder angle, β is the drift angle, U the resultant velocity of the vessel, and X, Y and N the forces and moment acting on the hull.

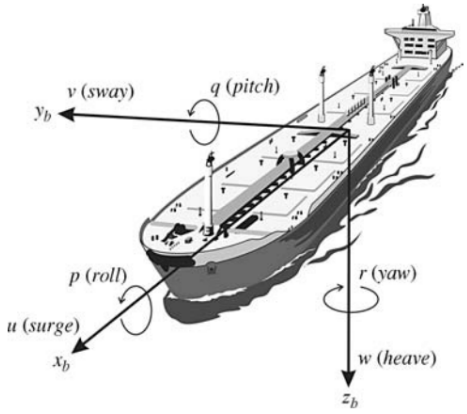

Figure 2.4: The translations and rotations of a vessel around axes in six degrees of freedom [15].

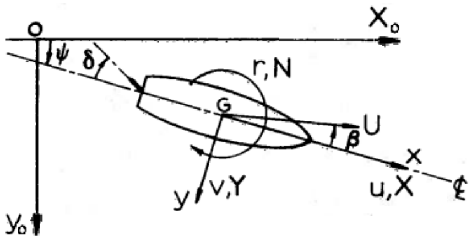

Figure 2.5: The coordinate system commonly used in manoeuvring theory [25].

2.2. High speed manoeuvring

The most significant difference between traditional displacement vessels and high-speed craft lies in the forces supporting the vessel's weight. A distinction is made between two categories: hydrostatic buoyancy forces, which follow Archimedes' principle, and hydrodynamic forces, which depend on the flow around the hull [7]. Organising vessels from a hydrodynamic perspective is based on their operating speed, categorised by the Froude number ($Fn = {}^{U}/\sqrt{gL}$), which is the ratio of the inertia of the water to the gravity force [15]. For traditional displacement vessels, operating at a Froude number below 0.4, buoyancy is the dominant force [8].

As the speed increases, dynamic lift is produced on the submerged flat surfaces of the hull. In addition to the hydrodynamic displacement of water, which causes the lift force to develop at low speeds, the lift force at high speeds is also due to the change in the water's momentum, resulting from it breaking away along the hull. As speed increases, these forces lift the vessel out of the water, reducing its buoyancy and thus the hydrostatic force. As a result, at high speeds (Fn => 1.0-1.2), the weight of the vessel is mainly supported by the dominant hydrodynamic lift force [8, 16]. Semi-displacement vessels operate with their maximum speed in the region between displacement and planing vessels. Although the buoyancy force for these vessels is not dominant at maximum speed, they are not (fully) planing either [15].

In the transient phase from displacement to planing, the 'hump' has to be exceeded. This region in the resistance curve is clearly visible in Figure 2.6. Next, due to uneven pressure build-up from more water breaking away at the front, bow waves shift the centre of pressure forward, lifting the bow upward and increasing the backward tilt. At this speed, the vessel is severely trimmed, creating large waves and experiencing significant resistance. As the hydrodynamic lift acting on the hull overcomes the static buoyancy forces, the hull begins to lift out of the water. The bottom pressure has pushed the vessel upwards, decreasing the trim; the vessel is now planing. As a result, there is less volume in the water, reducing the wave-making resistance. The wetted surface of the vessel dramatically shrinks as the hull is pushed more out of the water, causing the friction resistance to decrease [8, 9, 15]. This is also clearly visible in Figure 2.6.

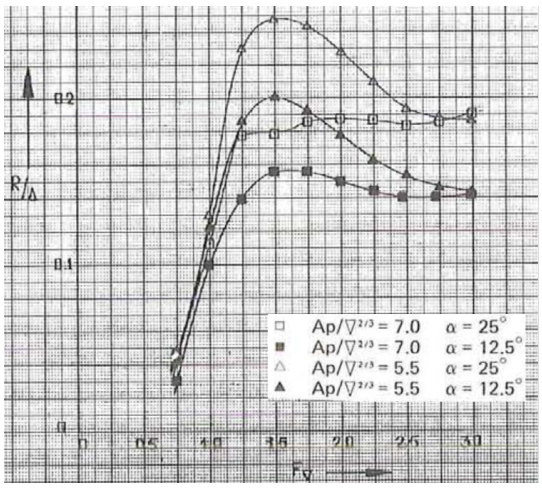

Figure 2.6: Resistance/weight ratio versus volumetric Froude number for deadrise angles 12.5° and 25°, $L_p/B_{pX} = 2.0$ and $LCG = 8\%$ [26].

To maximise this pressure build-up, high-speed craft utilise hard-chine hull forms, which provide the large, flat submerged areas necessary for lift generation; in contrast, round-bilge hulls lack these surfaces and often fail to generate sufficient pressure to overcome static buoyancy. If the water does not separate from the hull, it will climb up on the sides, pulling the hull downwards. This decreases the lift, increases the trim, and, as a result, increases the resistance [5, 8, 9]. While the underwater shape of a conventional displacement vessel stays relatively constant during motions and speed changes, the underwater geometry of a high-speed craft becomes dynamically dependent on the speed, altering the hydrodynamic forces along the hull [5, 12, 16, 21]. In the literature, this dynamical change in trim and sinkage is referred to as *running attitude*. Research has demonstrated that the manoeuvring hydrodynamic coefficients when operating at high speeds vary a lot from those for operating at moderate speeds, showing a clear Froude dependency [8, 11, 13, 27].

Due to changes in wetted geometry at high-speed operations, it is common to use the Froude number based on volume ($Fr_\nabla = {}^{U}/\sqrt{g\nabla^{1/3}}$) for high-/speed craft. As the vessel starts to plane, there is less submerged surface area to generate lift. However, the vessel's weight still has to be supported, which means a higher speed is needed to generate enough lift. The lift force scales with the square of the velocity times the area. Therefore, the volumetric Froude number better represents the vessel's mass relative to the speed needed, relating speed directly to the load the craft must support.

2.2.1. Heel angle in turning motion

When comparing displacement vessels and high-speed craft in a turn, both experience a loss of speed and develop a drift angle. At low speed, a high-speed craft operating in displacement mode behaves like a conventional displacement vessel, as the yaw motion generates insufficient force to induce a significant heel angle and dynamic effects remain small [12]. At high speed, however, the turning behaviour changes. Due to cross-coupling, a rudder deflection intended to change only the yaw motion also induces pitch and roll motions.

At the start of the turn, the centrifugal force at the centre of gravity builds up quickly. In contrast, the slowly developing dynamic restoring side forces cause the craft to roll inward and alter its underwater geometry [8]. In Figure 2.7 this interaction of forces is visualised. This initial inward heel is relatively small; in the steady turn the heel angle is much larger and directed outward [14]. This outward roll results from the large vertical distance between the points of application of the centrifugal force and the hydrodynamic side force, which is typical for craft with a high centre of gravity above the waterline. Since large heel angles can lead to roll instability and even capsizing, high-speed craft are often forced to roll into the turn to keep the resultant force perpendicular to the deck [14]. Once the roll is introduced, the steering force must be decomposed into a horizontal and a vertical component [12]. A steady turn is only reached when, together with the yaw rate and restoring forces, also the trim and roll angle have become constant [5].

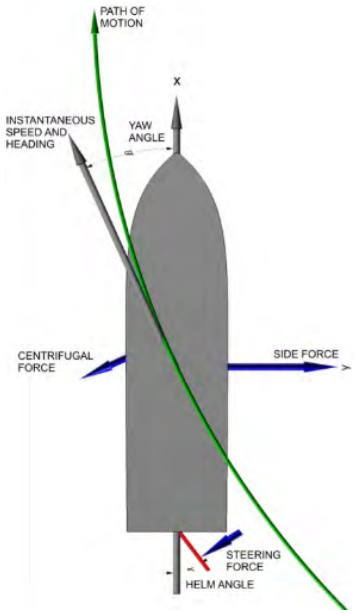

Figure 2.7: Forces acting on the hull of a high-speed craft in a turning manoeuvre [12].

In the high-speed operating regime, the heave and pitch motions, i.e., sinkage and trim, significantly influence the drag, wetted area, and submerged volume of the craft, which, in turn, contribute substantially to the restoring force and moment coefficients. As mentioned earlier, increased drag will cause the craft to lose speed. This decrease in speed is generally more pronounced for high-speed craft, compared to displacement vessels with the same ratio of waterline length to turning radius (Martin, 1976 as cited in [12]).

Any misalignment between the longitudinal axis and the resultant velocity vector increases drag, causing speed loss during a turn; the magnitude of this effect primarily depends on the turning diameter [14]. Davidson [28] showed that reducing the tactical diameter to two ship lengths or less significantly increases the speed loss and the time required to regain the original speed. When a craft enters a turn just above its planing speed, the speed loss can abruptly remove the restoring roll moment, causing the craft to return upright or even heel outward while the turn tightens [8].

2.2.2. Instabilities during manoeuvres

The operating regime of high-speed craft introduces instabilities that are rarely encountered by conventional displacement vessels [21, 24, 29, 30]. In the longitudinal direction, *porpoising* is a coupled heave–pitch oscillation that occurs at large trim angles and increases with speed. It causes variations in thrust and speed and can be reduced by lowering the trim angle, for example by shifting the centre of gravity forward [5, 8, 27]. At low trim angles, *bow drop* can occur, where, in the case of an immersed bow, a low-pressure zone is created that pulls the vessel further down. This is prevented by placing the centre of gravity sufficiently backwards [5].

In the transverse direction, *chine-walking* is a roll oscillation in which the craft repeatedly shifts between opposite heel angles. It can be mitigated by increasing the roll-restoring moment, for example, with spray rails. The roll resonance with the pitch or wave frequency is reduced by increasing roll damping and the metacentric height [8, 20]. Coupled instabilities can also occur. With *corkscrewing*, the asymmetric wetted surface during a high-speed turn creates a roll moment. The resulting changes in trim and sinkage introduce pitch and yaw motions that can lead to a loss of steering control [5, 20, 24, 31]. In following or stern-quartering waves at a speed close to the wave speed, the craft can surf and start *broaching*. As a result, it can lose its directional stability, where giving a counter-rudder could increase the roll moment and cause capsizing [9].

Finally, *spin-out* can occur when sudden deceleration or a large heel angle shifts the centre of the hull forces forward of the centre of gravity. This would rapidly increase the drift angle and yaw rate [30–32]. Since the IMO standards do not account for these phenomena, Wang et al. [24] proposed alternative performance criteria for high-speed craft.

2.3. Model selection

In this Section, the methods used to model manoeuvring behaviour are presented, bringing together the manoeuvring background given in Section 2.1 and the specific manoeuvring behaviour of high-speed craft explored in Section 2.2. This chapter reviews existing conventional manoeuvring models, demonstrates how researchers have adapted them to capture the characteristics of high-speed craft, and justifies the selection of the most suitable model for this research.

In maritime manoeuvring research, the Nomoto, Abkowitz, and Maneuvering Modeling Group (MMG) model are widely used to model the forces and moments in the equations of motion [16, 33–37]. In 1957 Nomoto et al. introduced a simplified model describing the turning response of a vessel in the horizontal xy-plane. Nomoto et al. [38] was the first to demonstrate that the linear equations of motion can be rewritten by reducing the complex interaction between the vessel's motions in the other planes to a single differential equation, focussing on the yaw rate (r).

A constant K is introduced as a measure of manoeuvrability, called the *Ship Gain*. It represents the steady-state yaw rate at a constant steering angle, with a high value indicating a smaller turning circle. To assess the steering response and directional stability, a constant T is introduced, referred to as the *time delay*. It represents the time required to start the turning motion after a steering angle deflection, where a low value indicates quick response and higher course stability [14, 38]. The constants are both dependent on speed; [39] showed that by including non-linear terms in an extended Nomoto model, a dynamically updated method can be obtained.

The model, named after Nomoto et al. [38], is based on a vessel's response to a control action. It is very simply formulated, which makes it easy to see the connection between the manoeuvre and the coefficients describing it. However, due to these simplifications, it focuses only on the yaw rate; the influence of other motions in the horizontal and vertical planes is not considered. Therefore, it cannot accurately predict the ship's actual path in space [39, 40]. As a result, the Nomoto model is not

deemed suitable for predicting the manoeuvring behaviour of a high-speed craft to the level required for this research.

Unlike the Nomoto model, both the Abkowitz and MMG models treat the vessel's forces and moments as an integrated system: Abkowitz as a single body, and MMG as separate components. Both describe the effect of the forces and moments acting on the vessel. In 1964 Abkowitz published the full text of his lectures on motion stability, manoeuvring and control [3]. The MMG model as presented by Yasukawa and Yoshimura [22] is based on the MMG standard model proposed by the research committee on "standardisation of mathematical model for ship manoeuvring predictions" organised by the Japan Society of Naval Architects and Ocean Engineers (JASNAOE). In Table 2.1 below, various aspects of both models are presented.

	Abkowitz	**MMG**
Degree of freedom	3DOF: surge, sway, yaw	3DOF: surge, sway, yaw
Origin taken	At COG (on centreline)	At vessel's midship
Forces/moments	Taylor series expansion as function of kinematic parameters [13]	Decompose forces into hull, propeller, rudder contributions
System	Single rigid body [41]	Component-based including their influence on each other [41]
Coefficients	One set of coefficients for entire vessel [35]	For each component and force contribution own set of coefficients
Flexibility	Difficult to modify a single part	Easy to swap or add new physics
Physical interpretability	No clear link between coefficients and physics	Clear insight in physical meaning of different components [13]
Rudder/Propeller	Included in derivative system [35]	Explicit force equations including interactions [41]
Extension to higher DOF	Re-evaluate Taylor-expansion equation set	Add equation of motion to existing system
Cross-coupling	Included in derivative system	Included in interaction of components

Table 2.1: Comparison of Abkowitz and MMG manoeuvring model (Note: sources in table are in addition to [3, 22]).

The Abkowitz model uses a Taylor series expansion to express forces and moments as functions of kinematic parameters within a single rigid-body system. Forces and moments are defined as functions of motion properties, orientation parameters, and steering inputs. The derivatives in the Taylor series are called the hydrodynamic coefficients. Each represents the slope of a force or moment curve relative to a specific motion parameter. Derivatives with respect to position, velocity, and acceleration represent the restoring, damping, and added-mass force/moment coefficients, respectively. Heave, roll and pitch are assumed to be zero for both standard models.

Liu et al. [35] argued that the Abkowitz model is preferred, especially since the hull-rudder-propeller interactions are automatically included. Because of the single-body approach, there is no need to determine the hull–rudder–propeller interaction coefficients. The Abkowitz model is a general, comprehensive mathematical model. However, the Abkowitz model's representation of the vessel as a single body can cause difficulties. Yang and El Moctar [42] mentioned this as a limitation when changing water depth, where the hydrodynamic coefficients had to be estimated for each specific water depth.

To adapt the hydrodynamic force and moment data, the JASNAOE proposed the MMG standard method, which was published by Yasukawa and Yoshimura [22]. The model divides the hydrodynamic forces into contributions of the hull, propeller and rudder, and accounts for the interactions between them with feedback loops. The coordinate system is fixed at midship, so the origin requires no adjustment if the centre of gravity shifts due to a change in load condition. The total external forces (X, Y) and moment (N_m), which form the right-hand side of the equations of motion, are calculated as the sum of the hull ($_H$), propeller ($_P$) and rudder ($_R$) contributions:

$$\text{Surge: } X = X_H + X_P + X_R, \qquad \text{Sway: } Y = Y_H + Y_R, \qquad \text{Yaw: } N_m = N_H + N_R \tag{2.1}$$

For a single-screw displacement vessel, the lateral propeller force and its yaw moment are small compared to the other contributions and are therefore neglected. Therefore, the propeller contributes only to the surge force.

The hull forces are those acting on the bare hull. The surge force (X_H) includes the straight-line resistance and higher-order terms that account for the change in resistance during drift and turning. The sway force (Y_H) and yaw moment (N_H) are the lateral force and moment generated by drift and rotation of the hull. The hull forces are expressed as polynomial functions of the non-dimensional lateral velocity at midship (v'_m) and yaw rate (r'), with the hydrodynamic derivatives as coefficients (these are further elaborated in Section 2.4.1). The propeller force (X_P) follows from the thrust, reduced by the thrust deduction factor. The interaction with the hull enters through the effective wake fraction at the propeller. The rudder forces (X_R, Y_R, N_R) follow from the rudder normal force. The interaction with the propeller and hull is included through the increased inflow speed in the propeller slipstream, the flow-straightening effect of the hull, and the additional hull forces induced by the rudder. The derivation of the constants in the thrust and steering formulae is detailed in [22].

Following from Section 2.2, it is understood that high-speed craft hydrodynamics requires isolating the individual contributions of various interacting components, a capability the Abkowitz model does not meet by treating the vessel as a single body. Although mathematically comprehensive, this approach complicates the analysis of component interactions. The MMG model addresses this by breaking down the total forces and moments into distinct components, enabling independent analysis of each element's hydrodynamic characteristics. Consequently, this research examines the modularity of the MMG model in greater detail, as this component separation provides the framework needed to understand how individual elements interact in high-speed craft manoeuvring. The MMG model is therefore selected, not because its standard form suits high-speed craft, but because its modular structure allows the components that do not hold to be replaced.

2.3.1. MMG model adaptation to high-speed craft

The standard MMG method is built on several assumptions: heave, roll, and pitch are zero during manoeuvring, the forces are quasi-steady, and the manoeuvring coefficients are constant with speed. For high-speed craft, none of these assumptions holds: the craft heels significantly in turns, its running attitude and wetted surface change continuously with speed and during the manoeuvre itself, and as a result its hull coefficients vary strongly with Froude number [5, 13, 43]. Since the hull force polynomials of the standard model are derived under these assumptions, the standard MMG model is not simply inaccurate for high-speed craft, but conceptually unsuitable for them. What remains usable is the modular structure of the framework, in which the hull, propeller and rudder contributions are separated. The question is therefore not whether the standard model must be modified, but which of its components must be replaced. The modifications researchers have introduced to extend its applicability and replace these components are discussed below.

High-speed craft experience significant heel angles during a turn, which affect the hydrodynamic forces and moments in all directions. To account for this, researchers have extended the standard MMG model to be 4DOF by adding the roll equation of motion and including roll-related coefficients in the whole system of equations [44–46]. Yasukawa, Sakuno, and Yoshimura [44] estimated the roll moments by multiplying the lateral force by the distance to its vertical acting point, presenting a practical approach sufficiently accurate for practical engineering uses. Fukui et al. [45] captured roll effects by performing CMT tests with fixed heel angles. Based on these tests, they extracted the effects of the roll angle and eliminated the less contributing parts. Okuda, Yasukawa, and Matsuda [46] validated an earlier established 4DOF MMG model across various speeds, showing that the simulations are consistent with the free-running tests performed. In the studies presented, the standard equations remained unchanged; only the roll equation and roll-related coefficients were added. This directly demonstrates the strength of the MMG model by layering new physics onto the existing framework without altering its core.

The continuous changes in wetted surface and trim, resulting from the lift force that lifts the hull out of the water generated by high speed, cause the hydrodynamic coefficients to change. To account for the running-attitude- and speed-dependent coefficients, researchers have implemented various adaptations. Either by measuring trim/sinkage at different speeds and incorporating them with look-up tables [47] , by using 2D+T theory to compute forces along the hull in sections [17, 48] or by introducing the

heave and pitch as functions of only the forward speed [49]. External disturbances can also influence the wetted surface; Wang et al. [50] adapted the standard model to account for the effects of water banks, shallow water, wind, and waves. All implementations are added to the force equations of the standard model. Only the input of the coefficients are changed or made dependent on speed-dependent tables. If the Abkowitz model was used, the entire coefficient set must be re-determined [42]. At the same time, these adaptations clearly show how easily different components within the MMG model can be adapted to the situation.

The studies presented above clearly show the modularity of the MMG model; however, it should be assessed whether the adapted models can predict manoeuvring of a high-speed craft with sufficient accuracy. Yasukawa et al. [43] presented a method to predict the manoeuvring of the General Prismatic Planing Hull (GPPH) using a 4DOF MMG model. The hydrodynamic coefficients are calculated using captive Computational Fluid Dynamics (CFD) at various speeds. The simulation predictions and the CFD results showed good correspondence, although both diverge at large steering angles. Diez et al. [51] integrated the MMG model with multi-fidelity CFD input data, showing that flexible integration with computational models is possible. Yasukawa, Hirata, and Nakayama [18] studied the effect of attitude change and the presence of appendages on the manoeuvring coefficients, and Yasukawa, Ishikawa, and Yoshimura [52] investigated the steering angle limitations for the MMG model, both showing the sensitivity of components in the MMG model to design changes. Wang et al. [19] presented a method to analyse the steady turning circle, using different coordinate systems. The proposed method is applied to both a displacement hull and a high-speed planing hull, showing differences in how the model captures each.

These studies show that the MMG framework can take input from different sources without structural changes. Its modular structure allows the roll equation to be added and the running attitude to be integrated in several ways. However, the adapted models remain reliable only in a limited operating range. Predictions diverge at large steering angles, where spin-out occurs, and the steering-angle limitations of the model are reached. The running attitude is generally taken from straight-ahead runs, so the effect of heel on the wetted geometry during a turn is not captured. Moreover, the hull coefficients of the adapted models are obtained from captive model tests or CFD, which are costly and must be repeated for every speed and hull. The models are mostly validated against model tests or CFD rather than full-scale measurements. The transition region between displacement and planing, where most semi-planing craft operate, is hardly covered. The modularity of the MMG framework thus makes it a suitable basis for high-speed manoeuvring. However, a computationally efficient model that does not rely on captive tests and is validated against full-scale data across the operating range of a semi-planing craft is still lacking.

2.4. Forces on a bare hull during manoeuvring

To better understand the physics of manoeuvring, the forces acting on the vessel during motion will be analysed. The forces fall into three categories: reactions to acceleration (added mass: $X_{\dot{u}}$, $Y_{\dot{v}}$, $N_{\dot{r}}$, $K_{\dot{p}}$), to velocity (damping and lift: Y_v, N_v, Y_r, N_r, K_p), and to position (restoring: K_φ).

First, a vessel accelerating in the forward direction is considered. When the vessel changes its forward speed u, the water surrounding the hull must be accelerated as well. The hull therefore experiences an inertial reaction force from this water, proportional to the acceleration: $X_{\dot{u}}\dot{u}$. This force acts as an additional mass, known as the added mass in surge ($m_x = -X_{\dot{u}}$), and opposes any change in speed. At a constant forward speed ($\dot{u} = 0$), this force is zero. The speed loss of an unpropelled vessel is caused by its resistance, which depends on the velocity rather than the acceleration. The relationship between the surge force and the forward acceleration is presented in Figure 2.8, showing a negative slope.

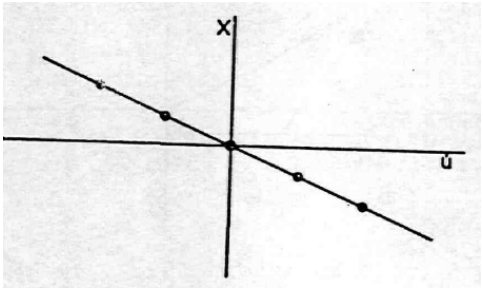

Figure 2.8: Typical relationship between the surge force X and the longitudinal acceleration $\dot{u}$ ([3]).

Secondly, a vessel in transverse acceleration ($\dot{v}$) will be evaluated, considering an acceleration to starboard. The motion is visualised in Figure 2.9, where u is the forward speed in the positive x-direction and Y is the sway force in the positive y-direction, with the origin at midship length. With positive acceleration to starboard, the reaction force due to the inertia of the accelerated water will always oppose the direction of the acceleration. This force is denoted as the derivative $Y_{\dot{v}}$, being the slope of the sway force Y with respect to the transverse acceleration $\dot{v}$. The relationship between the sway force and the acceleration in the y-direction is portrayed in Figure 2.10, showing a negative slope.

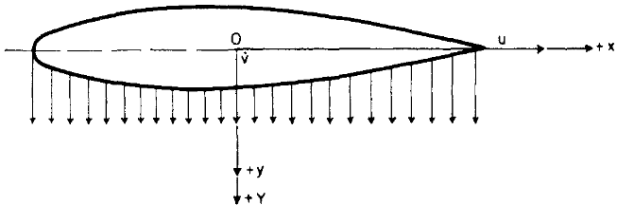

Figure 2.9: A vessel in transverse acceleration to starboard [14].

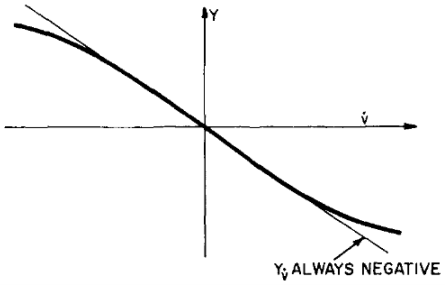

Figure 2.10: Typical relationship between the sway force Y and the transverse acceleration $\dot{v}$ [14].

Thirdly, a vessel undergoing rotational acceleration ($\dot{r}$) will be evaluated, assuming clockwise acceleration. The motion is visualised in Figure 2.11. With the positive acceleration of the bow to starboard (clockwise rotation), the reaction moment due to the inertial reaction of the water will always oppose the angular acceleration. This moment is denoted as the derivative $N_{\dot{r}}$. The relationship between the yaw moment and acceleration will follow the same relationship as shown in figure 2.12, showing a negative slope.

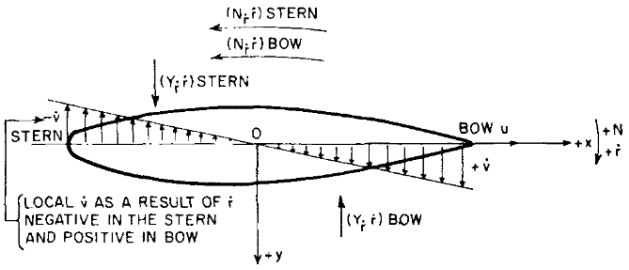

Figure 2.11: A vessel in rotational acceleration in clockwise direction [14].

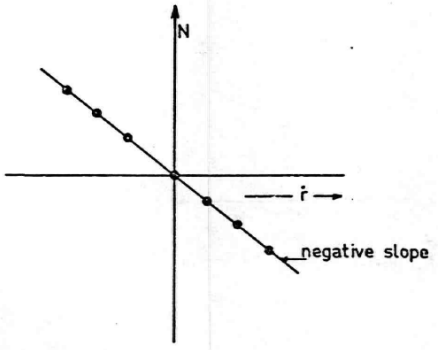

Figure 2.12: Typical relationship between the yaw moment N and the rotational acceleration $\dot{r}$ ([3]).

Next, a vessel with both longitudinal and transverse velocities, u and v, respectively, is analysed. The motion is visualised in Figure 2.13, where $Y_v v$ is the lift force countering the transverse motion v. As a result, the derivative Y_v will always be negative, as can be seen on the left graph in Figure 2.14. If a bare hull is considered, the contribution of the lift force on the stern is usually smaller than on the bow, creating a net negative moment $N_v v$ in the counter-clockwise direction. However, the addition of a rudder at the stern increases the force contribution of the stern, reducing the negative impact of $N_v v$. The relationships between the yaw moment and the transverse velocity are illustrated in the right graph in Figure 2.14.

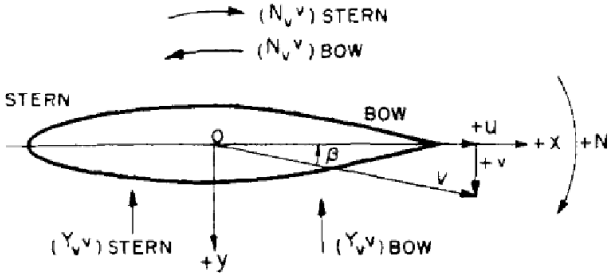

Figure 2.13: A vessel in both longitudinal and transverse velocity [14].

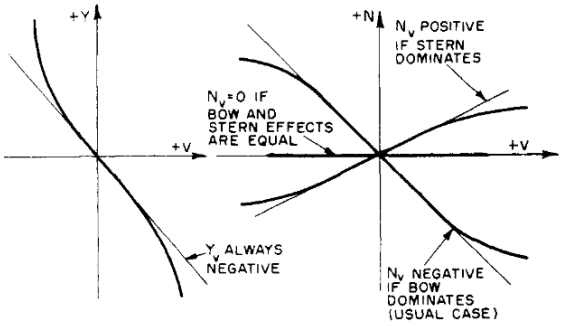

Figure 2.14: Typical relationship between the sway force Y, the yaw moment N and the transverse velocity v [14].

Additionally, a vessel in both longitudinal velocity (u) and rotational velocity (r) is considered. The motion is visualised in Figure 2.15, where B and S visualise a point near the bow and stern, respectively, on which the sway force acts. Point B has an angle of attack from the starboard side, resulting in a negative force ($Y_r r$) and moment ($N_r r$); for point S, the force is in the opposite direction, but the moment has the same sign. As a result, the contributions of both the bow and stern to the total yaw moment (N) are large negative for a positive rotational velocity (r). In contrast, a small or even negative contribution is made to the total sway force (assuming a dominating bow). The relationship between the sway force, yaw moment and the rotational velocity is illustrated in Figure 2.16.

In the equations of motion, these derivatives appear as added mass: the sway added mass is $m_y = -Y_{\dot{v}}$ and the added moment of inertia in yaw is $J_z = -N_{\dot{r}}$. Both are added to the vessel's mass and moment of inertia. The coupled inertia coefficients $Y_{\dot{r}}$ and $N_{\dot{v}}$ would be zero if the vessel were symmetrical fore and aft (about the yz-plane) [14].

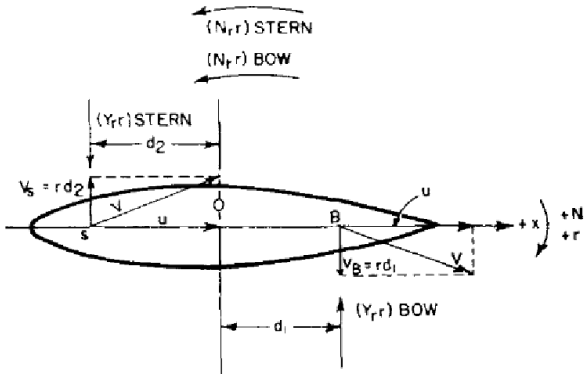

Figure 2.15: A vessel in both longitudinal velocity (u) and rotational velocity (r) [14].

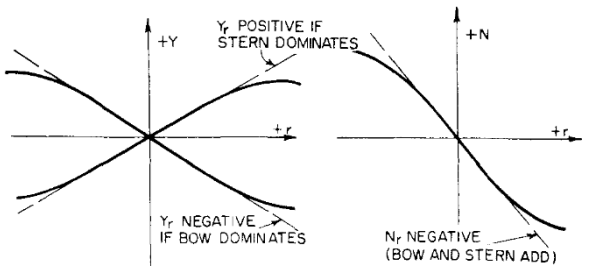

Figure 2.16: Typical relationship between the sway force Y, the yaw moment N and the rotational velocity r [14].

To conclude, the roll moment is analysed. When the vessel rolls with a positive angular velocity p (rotation over starboard), the hull sides move through the water with a local velocity (pd in Figure 2.17). The water opposes this motion through wave radiation and, at forward speed, lift on the hull and appendages. Because these forces act on the hull and not through the centre of gravity, they create a roll moment opposing the roll velocity. This damping effect is described by the derivative K_p, which is therefore negative, as illustrated in Figure 2.18. The reaction to a roll acceleration, the added moment of inertia in roll, is described separately by $K_{\dot{p}}$.

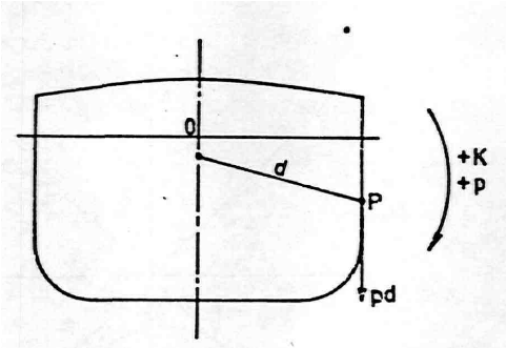

Figure 2.17: A vessel experiencing roll velocity (p) and moment (K) [3].

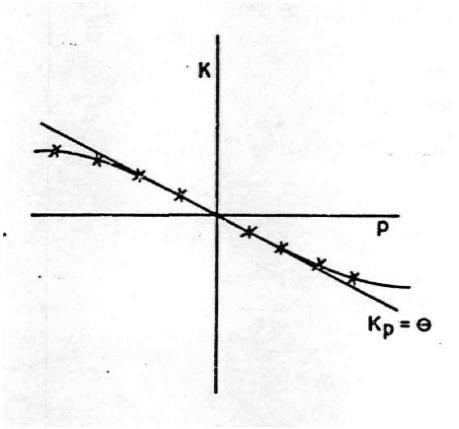

Figure 2.18: The typical relationship between the roll moment K and the roll velocity p [3].

Next to damping, a heeled vessel experiences a restoring moment. For a positive roll angle (ϕ), the righting moment acts in the opposite direction of the heel. Since the righting moment opposes the heel, the roll moment due to the roll angle (K_ϕ) is negative for a stable vessel, i.e. a vessel with a positive metacentric height. At high speed, the hydrodynamic pressure on the hull adds to this restoring moment. The relationship between the roll angle and the roll moment is shown in Figure 2.19, which shows a negative slope.

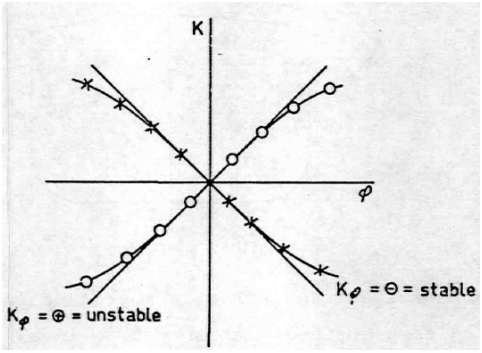

Figure 2.19: Typical relationship between the roll moment K and the roll angle ϕ [3].

2.4.1. Hydrodynamic coefficients

Above, the forces working on a hull during manoeuvring are explored. In Section 2.3, several manoeuvring models have been introduced. Considering the abilities and attributes of each model, the MMG model was chosen to suit this thesis's approach best. To better understand the physical meaning of the parameters used in the standard MMG model and how to modify it to better model the manoeuvring behaviour of a high-speed craft, a study is conducted to determine the hydrodynamic coefficients.

In the standard MMG model, as presented by Yasukawa and Yoshimura (2015), the forces acting on the vessel are divided into contributions from the hull, propeller, and rudder. The hull forces are expressed as a function of density (ρ), length (L_{pp}), draft (d), velocity (U) and polynomial functions of v'_m and r', the non-dimensional lateral velocity and yaw rate, respectively:

$$X_H = {}^1\!/_2\rho L_{PP} d U^2 X^*_{\mathsf{H}}(v'_m, r'), \quad Y_H = {}^1\!/_2\rho L_{PP} d U^2 Y^*_{\mathsf{H}}(v'_m, r'), \quad N_H = {}^1\!/_2\rho L^2_{PP} d U^2 N^*_{\mathsf{H}}(v'_m, r') \tag{2.2}$$

Where $X^*_{\mathsf{H}}(v'_m, r'), Y^*_{\mathsf{H}}(v'_m, r'), N^*_{\mathsf{H}}(v'_m, r')$ are the polynomials functions being defined as follows:

$$X^*_{\mathsf{H}}(v'_m, r') = -R'_0 + X'_{vv} v'^2_m + X'_{vr} v'_m r' + X'_{rr} r'^2 + X'_{vvvv} v'^4_m \tag{2.3}$$

$$Y^*_{\mathsf{H}}(v'_m, r') = Y'_v v'_m + Y'_r r' + Y'_{vvv} v'^3_m + Y'_{vvr} v'^2_m r' + Y'_{vrr} v'_m r'^2 + Y'_{rrr} r'^3 \tag{2.4}$$

$$N^*_{\mathsf{H}}(v'_m, r') = N'_v v'_m + N'_r r' + N'_{vvv} v'^3_m + N'_{vvr} v'^2_m r' + N'_{vrr} v'_m r'^2 + N'_{rrr} r'^3 \tag{2.5}$$

The parameters placed before each v'_m and r' combination are called the hydrodynamic derivatives. The $'$ means the parameters are made non-dimensional, which is done as follows: velocity by U, length by L_{pp}, forces by ${}^1\!/_2\rho L_{pp} d U^2$, moments by ${}^1\!/_2\rho L^2_{pp} d U^2$, mass by ${}^1\!/_2\rho L^2_{pp} d$ and moment of inertia by ${}^1\!/_2\rho L^4_{pp} d$. The physical meaning of each part of the polynomials is further elaborated on the next page (explanations based on interpretations of [17, 22, 49, 53, 54]).

Term	*Physical meaning*
R'_0	Ship resistance coefficient in straight moving
$X'_{vv}v'^2_m$	Force due to linear sway motion in surge direction
$X'_{vr}v'_m r'$	The altered asymmetric pressure distribution along the hull due to sway-yaw coupling
$X'_{rr}r'^2$	Force due to angular yaw motion in surge direction
$X'_{vvvv}v'^4_m$	Higher order non-linear surge resistance due to drift
$Y'_v v'_m$	Damping force due to linear sway motion in sway direction
$Y'_R r'$	Damping force due to angular yaw motion in sway direction
$Y'_{vvv}v'^3_m$	Third order sway force change due to sway speed change
$Y'_{vvr}v'^2_m r'$	The altered flow effects due to a yaw motion at drift angle
$Y'_{vrr}v'_m r'^2$	The altered effective lift response to a drifting angle while experiencing yaw motion
$Y'_{rrr}r'^3$	Third order sway force change due to yaw rate change
$N'_v v'_m$	Damping moment due to linear sway motion in yaw direction
$N'_R r'$	Damping moment due to angular yaw motion in yaw direction
$N'_{vvv}v'^3_m$	Third order yaw moment change due to sway speed change
$N'_{vvr}v'^2_m r'$	Drift dominated cross coupling yaw moment
$N'_{vrr}v'_m r'^2$	Yaw rate dominated cross coupling yaw moment
$N'_{rrr}r'^3$	Third-order yaw moment change due to yaw rate change

2.4.2. Methods to obtain the coefficients

Hydrodynamic manoeuvring coefficients are derived using three principal methodologies: experimental towing-tank testing, numerical simulations, and empirical formulae. Recent literature reflects a shift from static experiment-driven approaches toward physics-informed, dynamic force descriptions [55].

Experimental: towing tank	Numerical: CFD, potential flow	Empirical formulations
Straight ahead resistance - surge	RANS CFD virtual OTT, CMT	Fast baseline tests
Oblique Towing Tests (OTT) - sway	Free-running (RANS) CFD	Displacement-base
Circular Motion Tests (CMT) - yaw	Slender body theorem	High-speed semi-empirical
Heel-fixed OTT, CMT - roll	System Identification	Hybrid correction models

Table 2.2: Various estimation methodologies for the hydrodynamic manoeuvring coefficients as presented in the literature.

Experimental towing tank approaches

Physical model testing isolates force derivatives through specialised motion procedures [1, 3, 56]. Oblique Towing Tests (OTT) determine sway velocity derivatives, whereas Circular Motion Tests (CMT) in a rotating arm tank isolate yaw rate derivatives (Y_r, N_r). Executing CMT across varying drift angles (β) identifies non-linear cross-coupling terms (vvr, vrr), capturing flow asymmetries and velocity distributions caused by simultaneous turning and drifting [17, 22, 49, 53, 54].

For high-speed craft, hydrodynamic coefficients become strongly speed-dependent due to pressure distribution variations and dynamic lift changing the running attitude and thus the wetted geometry. Towing tank tests require a dense matrix of speed measurements, particularly around the transient (hump) region. During towing tank tests, the model is commonly fixed to the trim and sinkage values measured during straight-ahead runs [34, 47, 57–60]. As a result of the fixed position, the effect of heel and drift during a turn is lost. To incorporate roll dynamics, the roll period and damping are derived from free roll decay tests. The added moment of inertia can be derived from the roll period. These tests are often performed at zero speed, while the damping of a high-speed craft depends on its speed. The roll-coupling derivatives (Y_ϕ, K_ϕ, N_ϕ) can be extracted by performing OTT and CMT with the model fixed across a range of heel angles (ϕ) [37, 44, 45].

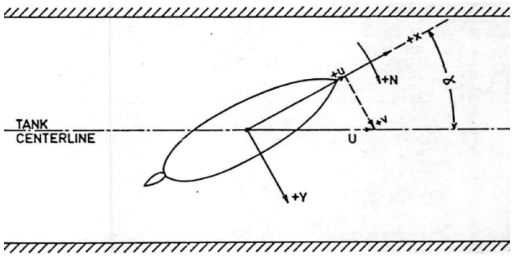

Figure 2.20: Visualisation of the oblique towing tests [3].

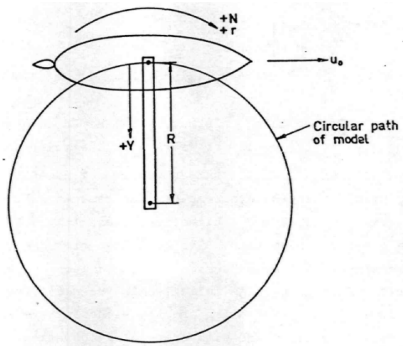

Figure 2.21: Visualisation of circular motion tests in a rotating arm tank [3].

Numerical and theory-based approaches

Numerical solvers avoid the high costs of physical towing tank campaigns. Reynolds-Averaged Navier–Stokes (RANS) CFD models perform virtual OTT and CMT to evaluate force derivatives [13, 35, 61–65], or run free-running self-propelled simulations to calculate manoeuvre trajectories directly without intermediate coefficient estimation [30, 31, 56, 66]. To mitigate the substantial computational cost of RANS simulations, potential-flow solvers utilising slender-body theory evaluate hydrodynamic forces by integrating the rate of change of fluid momentum along the hull length [17, 58]. Additionally, System Identification (SI) techniques are used to estimate sets of coefficients directly from measured vessel trajectories [33, 37, 60, 67, 68].

Empirical approaches

Empirical methods provide fast, low-cost baseline evaluations suitable for early design phases and real-time control. While extensive empirical formulations exist for conventional displacement vessels [14, 36, 41, 69–71], high-speed hard-chine craft primarily utilise the semi-empirical relations compiled by Lewandowski, which cover sway, roll, and yaw added mass, restoring forces, and damping coefficients [5]. Hybrid approaches combine empirical relations with numerical methods, such as applying empirical heel-induced load corrections or converting velocity derivatives into drift angle formulations, to enhance simulation accuracy without heavy computational loads [16, 17, 64, 72].

2.4.3. Reproducibility of published manoeuvring models

Although the MMG framework is well documented, it was found during this thesis that published models are often not reproducible from the information given in the papers alone. Reconstructing the benchmark cases used in this thesis (Chapter 4) revealed recurring gaps. Input parameters are frequently not reported, such as the propeller open-water coefficients [44], the rudder span and the propeller and rudder positions [46]. The values had to be estimated, measured from public geometry models, or taken from other sources.

In addition, the reported approach speed, propeller revolutions and resistance coefficient were not always consistent. With the published values, the simulated vessels lost between 1.3% and 3.8% of their speed in straight sailing, so that either the propeller revolutions or the resistance coefficient had to be retuned before a turn could be simulated. Simulation settings such as the rudder rate were often not stated, while they visibly affect the trajectory.

The component positions of the GPPH gear-case had to be derived from published force data [19, 30], the empirical formulations of Lewandowski [5] contain terms whose form or sign does not match captive-CFD data, and two CFD studies of the same hull at the same speed report different turning results [19, 43]. As a consequence, the published models could not be used as a ready-made references. Each reconstruction requires calibration choices that themselves influence the result. This underlines the need for complete reporting of input data and for validation against independent reference data, and is the reason the benchmark reconstructions in this thesis are treated as a verification step rather than an exact replication.

2.5. High-speed hull data

The empirical planing hull model will be tested on two high-speed hulls. The General Prismatic Planing Hull (GPPH) is a model hull generally used in research about planing vessels. The studies presented in Section 2.5.1 are used to validate the empirical hull model. As mentioned in the introduction, sea trials have been performed across various speed regimes with a 12m pilot vessel. The manoeuvres performed are presented in Section 2.5.1 below.

2.5.1. General Prismatic Planing Hull

The GPPH model is a planing hull used in various high-speed studies. A 3D Rhinoceros model was presented at the Multi-Agency Craft Conference 2018 website (`https://www.navalengineers.org/symposia/MACC-2018`). This model has been used for the geometric input parameters. The model used has a length of 2.414m, a chine width of 0.627m and a static waterline reference draft of 0.148m. The model has a deadrise angle of 17.2deg at midship, a static trim of 0.127deg (bow up) and a static reference transom draft of 0.148m [73]. For propulsion, the vessel uses a Mercury 4.6 L V8 rated at 300 HP gear-case[30]. The hull is illustrated in Figure 2.22 below.

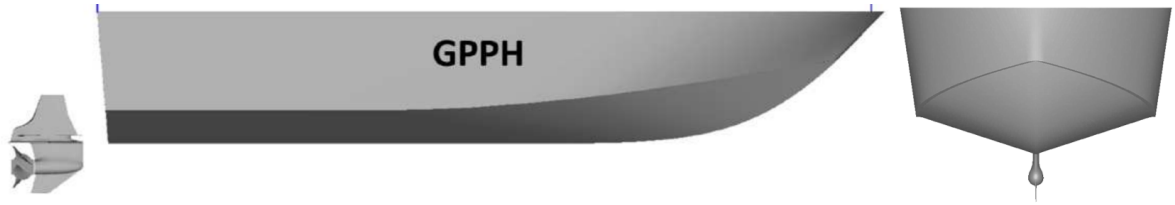

Figure 2.22: Front and side view of the General Prismatic Planing Hull (GPPH) [43].

Towing tank tests have been performed by Lee et al. (2017) [73, 74] for a range of volumetric Froude numbers of $Fr_\nabla = 2.6-5.72$, which translates to $Fr_L = 1.14-2.52$ for the model with $L_{PP} = 2.414m$. In recent studies, the GPPH model is used in high-speed CFD tests. For example, Park (2022) presented in his PhD a 6DOF free-running CFD study for a high-speed craft [75]. The findings were published together with sea trial data of a full-scale deep V fishing boat in [30].

The GPPH hull is outfitted with a gear-case for propulsion and steering; see Figure 2.22 for a visualisation of this. In [30], the propeller open-water diagram for various speeds is presented, along with propeller and gear case force formulas. The same configurations were used in [19, 24] to study planing-hull turning circles and dynamic instabilities, respectively. In [43], the MMG model is used to predict the turning circles of a GPPH hull, which diverge at large steering angles.

2.5.2. Pilot vessel

As mentioned previously, sea trials have been conducted to generate an extensive real-life dataset of a semi-planing high-speed craft. During the sea trials, the following manoeuvres have been performed:

Manoeuvre performed	**MCR** [%]	**Side of rotation**
Speed trials ahead	100, 75, 60, 40	
Turning circle, δ=30deg	100, 40	PS, SB
Turning circle, δ=30, 20, 10deg	75	PS, SB
Spiral (Dieudonné) test sailing ahead	75, 40	PS, SB
Zigzag, δ=20-20deg	75, 40	PS, SB
Zigzag, δ=10-10deg	75, 40	PS, SB

Manoeuvre performed	**Engine** [%MCR]	**Steps** [%MCR]	δ **steps**	**Rotation**
Accelerate + crash stop, reverse rpm	max-idle, idle-max	full stop+ astern		
Accelerate + coasting stop, coasting	idle-max, max-idle	5		
Spiral (Bech)	idle-60	5	5deg	PS
Spiral (Bech)	idle-85	5	5deg	SB
Spiral (Bech)	idle-max	5	10deg	SB
Sidestep max drift				SB

By comparing the model tests analysed above with the manoeuvres performed during the full-scale sea trials, a method is established for obtaining the hydrodynamic manoeuvring coefficients from the database. The surge force coefficients due to surge motion ($X_u, X_{\dot{u}}$, and higher-order terms) can be obtained from straight-ahead speed tests. The sway force and yaw moment due to yaw motion (Y_r, N_r and higher-order terms) can be obtained from the steady-state part of the turning and spiral manoeuvres. The steady yaw rate versus steering angle curve (N_r/Y_r) can be obtained with the Dieudonné spiral tests. The overshoot dynamics can be obtained from the zigzag tests, yielding values of the sway force and yaw moment with respect to the sway velocity and acceleration (i.e., $Y_v, N_v, Y_{\dot{v}}$, and $N_{\dot{r}}$). The drift tests can be used to obtain the higher-order sway force and yaw moment resulting from sway velocity. Multicollinearity can be resolved using the drift and spiral tests. Since the manoeuvres have been performed at several speeds, a look-up table can be made for the coefficients in each speed regime.

The pilot vessel used to create the sea trial dataset is the Damen Crew tender (see Figure 2.23 on the right), measuring 12m in length and 4.20m in width. It is powered by two engines, each delivering 401 Hp / 295 kW, with a maximum speed of 19kn. The operating range of the pilot vessel varies from displacement mode to semi-planing. The sea trial tests are performed in a Froude range of $Fr_L = 0.3-0.9$, looking at the approach speeds for the turning circles and zigzags. Here, 40%MCR corresponds to 800rpm which is around $Fr_L = 0.3$, 75%MCR corresponds to 1400rpm which is around $Fr_L = 0.6$ and 100%MCR corresponds to 2050rpm which is around $Fr_L = 0.9$.



Figure 2.23: Pilot vessel used to create sea trial dataset [76].

The pilot vessel is outfitted with a twin-propeller twin-rudder steering configuration. Several researchers have used this configuration in manoeuvring simulations; however, the mathematical models and vessel types they applied it to varied. For example, [77] simulated a high-speed surface combatant outfitted with a twin-propeller, twin-rudder system and [78] simulated a large container vessel. Also, [79, 80] applied a twin-propeller, twin-rudder model to an MMG simulation model for 3DOF and 4DOF, respectively. In [41], empirical formulae are presented for, amongst others, various steering parameters used in the MMG model.

3. Methodology

This chapter describes the methods used to build the various manoeuvring models during this thesis. The chapter begins by reconstructing the standard MMG model as presented by Yasukawa and Yoshimura (2015) [22]. The addition of a fourth degree of freedom is presented in Section 3.2. Next, in Sections 3.3.1 and 3.3.2, the methods for building the gear-case used for the General Prismatic Planing Hull simulations and the twin-propeller twin-rudder model used for the pilot vessel simulations are presented, respectively. Section 3.4 presents the empirical model used for the pilot vessel. This chapter ends with the method used to implement the running attitude in Section 3.5.

3.1. Standard 3DOF MMG model

The recreation of the 3DOF MMG model is based on Yasukawa and Yoshimura [22], which presents the standard MMG model. As a starting point, two established codes are available on GitHub: `https://github.com/ShipMMG/shipmmg` and `https://github.com/nikpau/pymaneuvering`. As the first one is MIT-licensed, it is taken as the leading repository.

The following equations of motion have been used, as presented in the paper:

$$\begin{aligned}
(m+m_x)\dot{u} - (m+m_y)v_m r - x_G m r^2 &= X, & X &= X_H + X_R + X_P \\
(m+m_y)\dot{v}_m + (m+m_x)ur + x_G m\dot{r} &= Y, & Y &= Y_H + Y_R \\
\left(I_{zG} + x_G^2 m + J_z\right)\dot{r} + x_G m\left(\dot{v}_m + ur\right) &= N_m, & N_m &= N_H + N_R
\end{aligned} \tag{3.1}$$

Here the hull forces are described with polynomials which are defined as follows:

$$\begin{aligned}
X'_{\mathsf{H}}(v'_m, r') &= -R'_0 + X'_{vv}v'^2_m + X'_{vr}v'_m r' + X'_{rr}r'^2 + X'_{vvvv}v'^4_m \\
Y'_{\mathsf{H}}(v'_m, r') &= Y'_v v'_m + Y'_r r' + Y'_{vvv}v'^3_m + Y'_{vvr}v'^2_m r' + Y'_{vrr}v'_m r'^2 + Y'_{rrr}r'^3 \\
N'_{\mathsf{H}}(v'_m, r') &= N'_v v'_m + N'_r r' + N'_{vvv}v'^3_m + N'_{vvr}v'^2_m r' + N'_{vrr}v'_m r'^2 + N'_{rrr}r'^3
\end{aligned} \tag{3.2}$$

The mass matrix matrix, consisting of the mass, added masses and added inertia, has no term coupling surge to sway or yaw. The surge added-mass coupling terms ($X_{\dot{v}}$, $X_{\dot{r}}$, $Y_{\dot{u}}$ and $N_{\dot{u}}$ are zero due to the port-starboard symmetry of the hull. Since the reference point is placed at midship ($y_G = 0$), the rigid-body surge–yaw term ($-my_G$) is also zero. Sway and yaw are coupled through the term $x_G m$, which is a result of the centre of gravity not being at midship. The sway–yaw added-mass coupling terms $Y_{\dot{r}}$ and $N_{\dot{v}}$ are neglected, as in [22].

As a result, the system if solved in two parts at each integration step. The surge velocity is solved separately as follows:

$$\dot{u} = \frac{(X_H + X_R + X_P) + (m+m_y)v_m r + m x_G r^2}{(m+m_x)} \tag{3.3}$$

The sway and yaw accelerations follow from the remaining 2x2 matrix system:

$$\underline{M}\mathbf{v} = \mathbf{b} \tag{3.4}$$

$$\begin{bmatrix} m+m_y & m x_G \\ m x_G & I_{zG} + J_z + m x_G^2 \end{bmatrix} \begin{pmatrix} \dot{v_m} \\ \dot{r} \end{pmatrix} = \begin{pmatrix} (Y_H + Y_R) - (m+m_x)ur \\ (N_H + N_R) - m x_G ur \end{pmatrix} \tag{3.5}$$

For which Cramer's rule is used to solve the system, resulting in the following sway and yaw acceleration at midship:

$$\begin{aligned} \dot{v}_m &= (b1 \cdot M22 - b2 \cdot M12)/det(\underline{M}) \\ \dot{r} &= (M11 \cdot b2 - M21 \cdot b1)/det(\underline{M}) \end{aligned} \tag{3.6}$$

This gives the same result as inverting the full 3x3 mass matrix system, but with lower computational costs. Solving the surge acceleration ($\dot{u}$) separately does not make it independent of sway and yaw. All three are evaluated separately at the same state, all depending on the three velocities u, v, r. The motions are therefore coupled through the forces rather than through inertia.

The integration is performed using an adaptive-step RK45 solver, with predetermined inputs of the rudder angle, initial velocity and propeller rps. All simulations have been performed with $\rho = 1000$ & $1025 kg/m^3$ for scaled and full-scale simulations, respectively.

The input parameters are presented in Table 3.1 and the exact input values for each simulated vessel are presented in Appendix A.1. The KVLCC2 data are from [22], and the KCS data are from [46]. For several parameters, estimates were needed because the values were not stated in the article; these are marked with a star* and are explained in more detail below the table.

All parameters marked with a prime' are non-dimensional. Following the standard MMG model they are made dimensionless as follows: velocity by U, length by L_{pp}, force by $1/2 \rho L_{pp} d U^2$, moment by $1/2 \rho L_{pp}^2 d U^2$, mass by $1/2 \rho L_{pp}^2 d$, inertia by $1/2 \rho L_{pp}^4 d$, turning rate by U/L_{pp}, time by L_{pp}/U. If necessary, the model vessels are identified by their length: $KVLCC_{L7}$ and KCS_{L4}.

Table 3.1: Input parameters 3DOF displacement simulations; KVLCC2 data from [22], KCS data from [46]. The parameters marked with a star* have a different origin and are elaborated further in the text below the table.

Geometry	L_{pp}, B, d, ∇, C_b, x_G, m'_x, m'_y, J'_z
Propeller	D_P, x_P*, w_{P0}, t_P, k_0, k_1, k_2, C_1, $C_2(\beta > 0)$, $C_2(\beta < 0)$
Rudder	H_R*, A_R, x_R, f_α*, ε, κ, t_R, a_H, x'_H, l_R, $\gamma_R(\beta_R > 0)$, $\gamma_R(\beta_R < 0)$
Simulation	$U_{initial}$*, n_p*, $Duration$, $Rudder\ rate$*
Surge	R'_0*, X'_{vv}, X'_{vr}, X'_{rr}, X'_{vvvv}
Sway	Y'_v, Y'_r, Y'_{vvv}, Y'_{vvr}, Y'_{vrr}, Y'_{rrr}
Yaw	N'_v, N'_r, N'_{vvv}, N'_{vvr}, N'_{vrr}, N'_{rrr}

Propeller

x_P The value for the full-scale longitudinal position of the propeller of the $KVLCC2$ and the KCS were measured in the Rhino models as presented by `https://simman2020.kr/contents/Ship_data_summary.php`; the distances were scaled using the scaling factor for the model vessels.

w_P In the propeller force model, the following formula is used to calculate the effective wake fraction at the propeller position during manoeuvring [22] for the KVLCC2 hull:

$$\frac{1 - w_P}{1 - w_{P0}} = 1 + \left(1 - e^{-C_1 |\beta_P|}\right)(C_2 - 1) \tag{3.7}$$

For the KCS hull the values of C_1 and C_2 were not available, here the following formula is used [44]:

$$\frac{1 - w_P}{1 - w_{P0}} = 1 + (1 - cos^2(\beta_P))(1 - |\beta_P|) \tag{3.8}$$

Rudder

H_R The rudder span length of the KCS vessel was not mentioned specifically in the paper. The span length was measured at full scale as presented at `https://simman2020.kr/contents/KCS.php`, and was scaled for the model.

f_α The rudder normal force gradient coefficient of the KCS is calculated using the following formula [22]:

$$f_\alpha = \frac{6.13\Lambda}{\Lambda + 2.25} \tag{3.9}$$

Where Λ is the rudder aspect ratio and is calculated by $\Lambda = H_R^2/A_R$. This resulted in the following aspect ratios: 1.795 for KCS_{L4} and 1.801 for KCS_{full}.

Simulation input

$U_{initial}, n_p$ The turning circles start from a straight-ahead equilibrium; however, for some vessels the initial speed or propeller rpm was not given specifically for each scale. The initial velocity was scaled as follows: $U_m = U_{full}/\sqrt{\lambda}$, and the propeller rpm as follows: $n_m = n_{full} \cdot \sqrt{\lambda}$.

For the $KVLCC2$ the $U_{initial}$ and $n_{p,initial}$ were given for the model with scale of $\lambda = 110$. Additionally, the resistance coefficient was available only for this scale; however, with the exact input values from the paper, the surge acceleration was nonzero, resulting in an 18% decrease in the surge velocity. Therefore, an optimisation was performed to find the $n_{p,initial}$ for which the surge acceleration was zero. This $n_{p,initial}$ was then used to calculate the values for the L7 and full-scale simulations.

For the KCS, only the $n_{p,initial}$ of the full-scale was missing, which was scaled from the model value.

$Rudder\ rate$ If the rudder steering rate was given, it was assumed that the rudder would increase linearly from 0 to 35deg at the given rate; if no rate was presented, the rudder is turned to 35deg instantly.

The KVLCC2 rudder rate was given for full scale and was scaled to model scale as follows: $Rr_m = Rr_{full} \cdot \sqrt{\lambda}$.

The KCS rudder rate was given for both the model and full scale vessel.

Surge

R'_0 The resistance coefficient was optimised during a straight sailing simulation. Since all input data, starting velocity, and propeller rpm were known or otherwise reasonably estimated, the resistance coefficient could be obtained by tuning its value until the surge acceleration stayed zero during a straight sailing manoeuvre. However, the papers were not always clear about which starting velocity and/or propeller rpm were used for each scale (see *Simulation input*), so it remains an estimate.

3.2. Expansion to 4DOF MMG model

The extension of the manoeuvring simulation to 4DOF by integrating the roll equation of motion into the model is carried out following the method presented by Yasukawa, Sakuno, and Yoshimura [44] and validated by Okuda, Yasukawa, and Matsuda [46]. Both papers use different ship models from those in the original MMG paper (PCC in [44] and KCS in [46] respectively). However, essential geometry data of the PCC vessel was missing, which led to the decision to only include the KCS vessel. The input data is presented in Table A.1 as well. The input values have been used to validate both the 3DOF and 4DOF models with different ship types.

The following equation of motion have been used in the 4DOF model (reference point at midship), as presented in [44, 46]:

$$\begin{aligned}
(m+m_x)\dot{u} - (m+m_y)v_m r - mx_G r^2 + mz_G r\dot{\phi} &= X, \qquad X = X_H + X_R + X_P \\
(m+m_y)\dot{v}_m + (m+m_x)ur + x_G m\dot{r} - (m_y\alpha_z + mz_G)\ddot{\phi} &= Y, \qquad Y = Y_H + Y_R \\
\left(I_{zz} + J_{zz} + mx_G^2\right)\dot{r} + mx_G\left(\dot{v}_m - z_G\ddot{\phi} + ur\right) &= N, \qquad N = N_H + N_R \\
\left(I_{xx} + J_{xx} + mz_G^2\right)\ddot{\phi} - (m_y\alpha_z + mz_G)\dot{v}_m - mz_G\left(x_G\dot{r} + ur\right) &= K, \qquad K = -Y_H z_H - Y_R z_R - K_{rm} + K_{dm}
\end{aligned} \tag{3.10}$$

The surge/sway/yaw hull forces are expanded to include the roll-coupling coefficients. As a result, they become dependent on the roll angle (ϕ). The extended hull force polynomials are defined as follows:

$$\begin{aligned}
X'_H(v'_m, r', \phi) = &- R'_0 + X'_{vv}v'^2_m + X'_{vr}v'_m r' + X'_{rr}r'^2 + X'_{vvvv}v'^4_m + X'_{v\phi}v'_m\phi \\
&+ X'_{r\phi}r'\phi + X'_{\phi\phi}\phi^2
\end{aligned} \tag{3.11}$$

$$\begin{aligned}
Y'_H(v'_m, r', \phi) = &\, Y'_v v'_m + Y'_r r' + Y'_{vvv}v'^3_m + Y'_{vvr}v'^2_m r' + Y'_{vrr}v'_m r'^2 + Y'_{rrr}r'^3 \\
&+ Y'_\phi\phi + Y'_{vv\phi}v'^2_m\phi + Y'_{v\phi\phi}v'_m\phi^2 + Y'_{rr\phi}r'^2\phi + Y'_{r\phi\phi}r'\phi^2
\end{aligned} \tag{3.12}$$

$$\begin{aligned}
N'_H(v'_m, r', \phi) = &\, N'_v v'_m + N'_r r' + N'_{vvv}v'^3_m + N'_{vvr}v'^2_m r' \\
&+ N'_{vrr}v'_m r'^2 + N'_{rrr}r'^3 + N'_\phi\phi + N'_{vv\phi}v'^2_m\phi \\
&+ N'_{v\phi\phi}v'_m\phi^2 + N'_{rr\phi}r'^2\phi + N'_{r\phi\phi}r'\phi^2
\end{aligned} \tag{3.13}$$

In the 4DOF system, the axis have their origin also at midship and move with surge, sway and yaw, but do not heel. The y- and z-coordinates of the centre of gravity are therefore assumed to be dependent on the roll angle and are calculated as follows:

$$y_G = -(\overline{\mathrm{GM}} - \overline{\mathrm{KM}} + d)sin(\phi), \quad z_G = (\overline{\mathrm{GM}} - \overline{\mathrm{KM}} + d)cos(\phi) \tag{3.14}$$

With the midship sway velocity defined as $v_m = v - x_G r + z_G p$, the mass matrix is constructed as follows:

$$\begin{bmatrix}
m+m_x & 0 & 0 & 0 \\
0 & m+m_y & -(mz_G + m_y\alpha_z) & mx_G \\
0 & -(mz_G + m_y\alpha_z) & I_{xx} + J_{xx} + mz_G^2 & -mx_G z_G \\
0 & mx_G & -mx_G z_G & I_{zz} + J_{zz} + mx_G^2
\end{bmatrix} \tag{3.15}$$

where m_x is the surge added mass, m_y the sway added mass, J_x and J_z the added moments of inertia in roll and yaw about the origin. The centre of the sway added mass lies at midship ($x_\alpha = 0$), at depth $z_\alpha = \alpha_z$, and there is no added product of inertia ($J_{xz} = 0$).

The matrix system clearly shows that there are no inertia coupling terms between surge and the other motions here either. The system is again solved in two parts. First, the surge acceleration directly using only the first row of the mass matrix. The sway, roll, yaw accelerations followed from the remaining 3x3 matrix system, which is solved as a linear system. Again, this does not make $\dot{u}$ independent of the other motions. All four are evaluated at the same state and depend on u, v, r, ϕ, p for each integration step. The coupling is therefore in the forces and not in the inertia.

The first term on the right-hand side of the roll moment equation (K in Equation (3.10)) is the roll moment acting on the hull ($Y_H z_H$) and the second is due to steering ($Y_R z_R$). The z_H and z_R are the lateral acting points, which are assumed to be constant during manoeuvring. The roll-restoring and roll-damping moments, K_{rm} and K_{dm} respectively, are defined as follows:

$$K_{rm} = mg\overline{\mathrm{GM}}\phi, \quad K_{dm} = K_{\dot{\phi}}\dot{\phi} + K_{\dot{\phi}\dot{\phi}}\dot{\phi}|\dot{\phi}| \tag{3.16}$$

The roll-damping coefficients are calculated as follows:

$$K_{\dot{\phi}} = -\frac{2}{\pi}a\sqrt{mg\overline{\mathrm{GM}}\left(I_{xx} + J_{xx}\right)}, \quad K_{\dot{\phi}\dot{\phi}} = -0.75b\left(\frac{180}{\pi}\right)\left(I_{xx} + J_{xx}\right) \tag{3.17}$$

The effective inflow angles at the propeller and rudder are calculated using the following formulae:

$$\beta_P = \beta - x'_P \cdot r' + z'_P \cdot \dot{\phi}', \quad \beta_R = \beta - x'_R \cdot r' + z'_R \cdot \dot{\phi}' \tag{3.18}$$

The additional input parameters necessary for the 4DOF simulations (on top of the parameters presented in Table 3.1) are given in Table 3.2 below. The exact input values can be found in Appendix A.2. The parameters marked with a star (*) are elaborated below the table.

Table 3.2: Additional input parameters for the 4DOF displacement simulations; KCS data from [46]. The parameters marked with a star* have a different origin and are elaborated further in the text below the table.

Geometry	k'_{xx}, J'_{xx}*, GM, KM, z_H, α_z*
Propeller	z_P*
Rudder	z_R*
Simulation	-
Surge	$X'_{v\phi}$, $X'_{r\phi}$, $X'_{\phi\phi}$
Sway	Y'_{ϕ}, $Y'_{vv\phi}$, $Y'_{v\phi\phi}$, $Y'_{rr\phi}$, $Y'_{r\phi\phi}$
Yaw	N'_{ϕ}, $N'_{vv\phi}$, $N'_{v\phi\phi}$, $N'_{rr\phi}$, $N'_{r\phi\phi}$
Roll	a, b

Geometry

J'_{xx} The non-dimensional radius of roll gyration (k'_{xx}) value includes the added moment of inertia component of the roll motion for each ship type. The J'_{xx} is included for completeness, but it is given a value of zero so as not to double-count it.

α_z The vertical acting point of the lateral added mass component m_y for the KCS was not mentioned specifically. For the PCC, the paper states that $\alpha_z = z_H$; therefore, the same assumption is made for the KCS.

Propeller

z_P For the KCS, this distance was measured in the Rhino model as presented on the SIMMAN 2020 workshop website (`https://simman2020.kr/contents/Ship_data_summary.php`), which was then scaled to model scale.

Rudder

z_R The value for the lateral acting point of the roll moment due to steering was assumed to be $z_R = d + H_R/2$ for each ship type.

3.3. Additional steering models

Since both the GPPH model and the pilot vessel are outfitted with different steering configurations, two additional steering models had to be created for the propeller and rudder. First, the gear-case model is presented in Section 3.3.1 for the GPPH model. The twin-propeller, twin-rudder model used for the pilot vessel simulation is described in Section 3.3.2. The hull force model stayed unchanged.

3.3.1. Gear-case model - GPPH

To check whether the empirical hard-chine planing model was working properly, tests were performed with the General Prismatic Planing Hull (GPPH). As the GPPH is equipped with a gear-case for propulsion and steering, a new steering and propeller model was developed based on [19, 30, 43]. The resistance curve of the bare hull was taken from towing tank data presented in [73]. The input data used for the GPPH simulations is presented in Appendix A.5.

Gear-case propeller forces

The KT-curve was taken from [30] and is a function of advance ratio and Froude number. For each instantaneous speed (U), the advance ratio (J) and Froude number (based on length) are calculated, and these are then used to find the appropriate KT-curve and read the value corresponding to J. The thrust is then calculated the same as before, using $w_P = w_{P0} \cdot \exp(-4\beta_P^2)$.

The model created for this thesis assumes the horizontal plane remains constant in the still-water plane; however, the papers used as references for the gear-case tilts the xy-plane following the roll angle of the vessel. Therefore, the velocity and force equations had to be translated into the correct reference plane. The model used in this thesis does not include the Z_P and M_P; however, they were needed for this rotation and are therefore calculated as presented in the papers in the body frame.

To calculate the forces using the velocities available in the model, the velocities had to be rotated from the horizontal frame to the body frame. This was done as follows:

$$u_b = u\cos(\theta), \quad v_b = v\cos(\phi) + u\sin(\theta)\sin(\phi) \rightarrow U_b = \sqrt{u_b^2 + v_b^2}, \quad \beta_b = \tan^{-1}(-v_b/u_b) \tag{3.19}$$

The forces were then calculated as follows in the body frame ($_b$):

$$\begin{aligned} X_{P,b} &= T\cos(\delta) + F_y^*\sin(\beta_b) - F_z^*\sin(\theta) & K_{P,b} &= -Y_{P,b}\cdot z_{P,b} \\ Y_{P,b} &= -T\sin(\delta) + F_y^*\cos(\beta_b) + F_z^*\cos(\theta)\sin(\phi) & M_{P,b} &= X_{P,b}\cdot z_{P,b} - Z_{P,b}\cdot x_{P,b} \\ Z_{P,b} &= F_z^*\cos(\theta)\cos(\phi) & N_{P,b} &= Y_{P,b}\cdot x_{P,b} \end{aligned} \tag{3.20}$$

Where F_y^* and F_z^* are empirical force formulae presented by [30] as:

$$F_y^* = -0.5\rho U_b^2(\delta - \beta_b)\cdot 0.6, \quad F_z^* = -0.5\rho U_b^2(\epsilon + \theta)\cdot 1.4 \tag{3.21}$$

The units of both are inches squared per degree (in^2/deg), so both had to be converted to meters squared per radian (m^2/rad) to use them in the current model. The location of the propeller was derived from the force data presented in [19] and the force equations of $K_{P,b}$ and $N_{P,b}$. This resulted in the following:$x_{P,b} = -0.4L_{pp}$ and $z_{P,b} = 0.078L_{pp}$. The tilt angle of the gear-case (ϵ) was assumed to be zero.

The forces were translated back to the horizontal frame as follows:

$$\begin{aligned} X_P &= X_{P,b}\cos(\theta) + Y_{P,b}\sin(\phi)\sin(\theta) \\ Y_P &= Y_{P,b}\cos(\phi) \\ Z_P &= -X_{P,b}\sin(\theta) + Y_{P,b}\sin(\phi)\cos(\theta) \\ K_P &= K_{P,b}\cos(\theta) + M_{P,b}\sin(\phi)\sin(\theta) + y_G Z_P - z_G Y_P \\ N_P &= -K_{P,b}\sin(\theta) + M_{P,b}sin(\phi)\cos(\theta) + x_G Y_P - y_G X_P \end{aligned} \tag{3.22}$$

Gear-case steering forces

The same rotation of the velocities and forces had to be done for the steering forces. In the body frame, the forces were calculated as follows:

$$\begin{aligned} X_{GC,b} &= F_x^*\cos(\beta_b) + F_y^*\sin(\beta_b) - F_z^*\sin(\theta) & K_{GC,b} &= -Y_{GC,b}\cdot z_{GC,b} \\ Y_{GC,b} &= F_x^*\sin(\beta_b) + F_y^*\cos(\beta_b) + F_z^*\cos(\theta)\sin(\phi) & M_{GC,b} &= X_{GC,b}\cdot z_{GC,b} - Z_{GC,b}\cdot x_{GC,b} \\ Z_{GC,b} &= F_z^*\cos(\theta)\cos(\phi) & N_{GC,b} &= Y_{GC,b}\cdot x_{GC,b} \end{aligned} \tag{3.23}$$

Where F_x^*, F_y^* and F_z^* are empirical force formulae presented by [30] as:

$$F_x^* = -0.5\rho U_b^2\cdot 3.5, \quad F_y^* = -0.5\rho U_b^2(\delta - \beta_b)\cdot 6.8, \quad F_z^* = -0.5\rho U_b^2(\epsilon + \theta)\cdot 1 \tag{3.24}$$

The unit of F_x^* is inch squared (in^2) and of F_y^*, F_z^* is inch squared per degree (in^2/deg), thus both had to be converted to meters squared per radian (m^2/rad) to be able to use them in the current model. The location of the propeller was derived from the force data presented in [19] and the force equations of $K_{GC,b}$ and $N_{GC,b}$. This resulted in the following: $x_{GC,b} = -0.406L_{pp}$ and $z_{GC,b} = 0.085L_{pp}$. The tilt angle of the gear-case (ϵ) was assumed to be zero.

The forces were translated back to the horizontal frame as follows:

$$\begin{aligned} X_{GC} &= X_{GC,b}\cos(\theta) + Y_{GC,b}\sin(\phi)\sin(\theta) \\ Y_{GC} &= Y_{GC,b}\cos(\phi) \\ Z_{GC} &= -X_{GC,b}\sin(\theta) + Y_{GC,b}\sin(\phi)\cos(\theta) \\ K_{GC} &= K_{GC,b}\cos(\theta) + M_{GC,b}\sin(\phi)\sin(\theta) + y_G Z_{GC} - z_G Y_{GC} \\ N_{GC} &= -K_{GC,b}\sin(\theta) + M_{GC,b}\sin(\phi)\cos(\theta) + x_G Y_{GC} - y_G X_{GC} \end{aligned} \tag{3.25}$$

3.3.2. Twin-propeller twin-rudder model

To make the next step towards the pilot vessel, a second rudder and propeller have to be added to the model since the pilot vessel is outfitted with a twin-rudder twin-propeller (TPTR). Below, first the twin propeller model is presented followed by the twin rudder model, both are a combination of [41, 77–80]. Both the 3DOF and 4DOF models have been outfitted with the TPTR model. In the equations below, (s) denotes the starboard propeller/rudder and (p) the port-side propeller/rudder.

Twin propeller model

The total propeller force in the x-direction is the sum of the X_P forces of both propellers. This is calculated as follows:

$$\begin{aligned} X_{P(\mathrm{s,p})} &= (1.0 - t_P)\cdot T_{(\mathrm{s,p})}, \qquad T_{(\mathrm{s,p})} = \rho \cdot K_{T(\mathrm{s,p})} \cdot n^2 \cdot {D_p}^4 \\ X_{P,total} &= X_{P(\mathrm{p})} + X_{P(\mathrm{s})} \end{aligned} \tag{3.26}$$

For both propellers, the rpm and diameter are assumed to be the same. The open-water thrust coefficient (K_T), however, is different. The K_T is a function of the advance ratio (J), which in turn is a function of the axial flow at the propeller (V_A). The V_A is calculated using the offset in the y-direction and the wake fraction (w_P), which is different for both propellers due to a difference in effective inflow angle during manoeuvring motions ($\beta_{P(\mathrm{s,p})}$):

$$\begin{aligned} V_A &= (u - y_{P(\mathrm{s,p})} r)\cdot(1 - w_{P(\mathrm{s,p})}) \\ \text{where} \quad & w_{P(\mathrm{s,p})} = w_{P0}\cdot e^{-8(\beta_{P(\mathrm{s,p})}+0.35)^2} \\ \text{with} \quad & \beta_{P(\mathrm{s,p})} = \beta - x'_{P(\mathrm{s,p})} r' + z'_{P(\mathrm{s,p})}\dot{\phi}' \\ \text{and} \quad & x_{P(\mathrm{p})} = x_{P(\mathrm{s})}, \quad y_{P(\mathrm{p})} = -y_{P(\mathrm{s})}, \quad z_{P(\mathrm{p})} = z_{P(\mathrm{s})} \end{aligned} \tag{3.27}$$

In the 3DOF model, the $z'_{P(\mathrm{s,p})}\dot{\phi}'$ part of the propeller effective inflow angle is zero. Since both propellers have the same x- & z-position and the same wake coefficient at the propeller position in straight motion (w_{P0}), the wake fraction will be the same for both. The difference in the propeller X-force is therefore due to the off-centre addition ($y_{P(\mathrm{s,p})} r$) in the axial flow calculation (V_A).

With the addition of a second propeller, a moment is introduced around the z-axis: the propeller yaw moment N_P. Due to the off-centre placement of the propellers, a lever arm is created in the y-direction. Figure 3.1 shows this lever arm schematically for the port-side propeller.

The propeller yaw moment is calculated by multiplying the propeller X-force by its lever arm, which results in the following:

$$\begin{aligned} N_{P(\mathrm{s,p})} &= -X_{P(\mathrm{s,p})} \cdot y_{P(\mathrm{s,p})} \\ N_{P,total} &= N_{P(\mathrm{p})} + N_{P(\mathrm{s})} \end{aligned} \tag{3.28}$$



Figure 3.1: Propeller force and moment around the z-axis in a twin-propeller configuration.

The standard MMG model assumes that the transverse propeller force (Y_P) is negligible relative to the longitudinal force. Since both propellers rotate in a different direction, it is assumed that the total Y_P is zero. The roll moment due to the propeller follows from the Y-force and its lever arm, namely $K_P = Y_P \cdot z_P$. As there is no force in the y-direction, the rotational moment in roll due to the propeller is also not included in this model.

Twin rudder model

The rudders produce a force in both surge (X_R) & sway (Y_R), and a moment in yaw (N_R); the total of these is the sum of both rudders. Due to the off-centre placement of the rudders, they also produce a moment: a roll moment (K_R) due to the force in the y-direction and an additional moment in yaw (N_R) due to the force in the x-direction. This resulted in the following force equations for the rudder model:

$$\begin{aligned} X_{R,total} &= -(1-t_R)\left([F_N sin(\delta)]_{(\mathrm{p})} + [F_N sin(\delta)]_{(\mathrm{s})}\right) \cdot cos(\phi) \\ Y_{R,total} &= -(1+a_H)\left([F_N cos(\delta)]_{(\mathrm{p})} + [F_N cos(\delta)]_{(\mathrm{s})}\right) \cdot cos(\phi) \\ K_{R,total} &= \left([-z_R Y_R]_{(\mathrm{p})} + [-z_R Y_R]_{(\mathrm{s})}\right) \cdot cos(\phi) \\ N_{R,total} &= \left(-(x_R + a_H x_H)\left([F_N cos(\delta)]_{(\mathrm{p})} + [F_N cos(\delta)]_{(\mathrm{s})}\right) - [y_R X_R]_{(\mathrm{p})} - [y_R X_R]_{(\mathrm{s})}\right) \cdot cos(\phi) \end{aligned} \tag{3.29}$$

In the 3DOF model, the roll angle is zero, resulting in $cos(\phi) = 1$, and no roll moment due to steering is taken into account ($K_R = 0$). The rudder normal force has been calculated using the same formula as for a single rudder. However, both the effective total inflow velocity (U_R) and the angle of attack (α_R) are different for each rudder. The U_R is calculated as the square root of the sum of the squares of the longitudinal and transverse velocities; $U_R = \sqrt{u_R^2 + v_R^2}$. The longitudinal velocity component at the port-side rudder is calculated as follows:

$$u_{\mathrm{R(s,p)}} = \varepsilon\, u_{\mathrm{P(s,p)}} \sqrt{\eta \left[1 + \kappa\left(\sqrt{1 + \frac{8K_{\mathrm{T(s,p)}}}{\pi J^2_{\mathrm{P(s,p)}}}} - 1\right)\right]^2 + (1-\eta)} \tag{3.30}$$
$$\text{where} \quad u_{P(\mathrm{s,p})} = (u - y_{P(\mathrm{s,p})} r) \cdot (1 - w_{P(\mathrm{s,p})})$$

The transverse velocity component at the rudder is calculated using the resultant ship speed (U) and the effective rudder angle ($\delta_{R(\mathrm{s,p})}$) as follows:

$$\begin{aligned} v_{R(\mathrm{s,p})} &= U \cdot \delta_{R(\mathrm{s,p})} \\ \text{where} \quad \delta_{R(\mathrm{s,p})} &= \gamma_{R(\mathrm{s,p})} \cdot \beta_{R(\mathrm{s,p})} + tan\left(\frac{y_{R(\mathrm{s,p})}}{|x_{R(\mathrm{s,p})}|}\right) \\ \text{with} \quad \beta_{R(\mathrm{s,p})} &= \beta - l_{R(\mathrm{s,p})} \cdot r' + z'_{R(\mathrm{s,p})} \cdot p' \end{aligned} \tag{3.31}$$

In the 3DOF model, the $z'_{R(\mathrm{s,p})} \cdot p'$ part of the rudder effective inflow angle is zero. The rudder effective angle of attack is the residual of the rudder angle minus the effective angle and is calculated as follows:

$$\alpha_{R(\mathrm{s,p})} = \delta - \delta_{R(\mathrm{s,p})} \tag{3.32}$$

In Appendix table A.3, the input data is presented for the twin-propeller twin-rudder simulations. The TPTR model has been added to both the 3DOF and 4DOF models, as presented in sections 3.1 and 3.2, respectively.

It is assumed that both rudders have the same geometry and rotate in the same direction and at the same angle. Also, the x- and z-coordinates are assumed to be the same, and for the y-coordinates the following holds: $y_{P(\mathrm{s,p})} = y_{R(\mathrm{s,p})}$ and $y_{P,R(\mathrm{p})} = -y_{P,R(\mathrm{s})}$.

3.4. Empirical model - Pilot vessel

The goal of this thesis is to create a computationally efficient model which can be used for early design stage estimations. Therefore, empirical methods were used to obtain the hydrodynamic coefficients for the pilot vessel. The approach for the sway/roll/yaw coefficients is presented in Section 3.4.1, and Section 3.4.2 shows how the surge coefficients are obtained from a fitted resistance curve constructed from the pilot vessel's sea trial dataset. Next, the adapted propeller and rudder models are presented in 3.4.3 and 3.4.4 respectively. The simulations for the pilot vessel have been performed with $\rho = 1000 kg/m^3$ since the sea trials were performed on a river.

3.4.1. Sway/roll/yaw hull force

The sway/roll/yaw hull forces are modelled following the empirical equations for hard-chine planing hulls as presented by Lewandowski [5]. For the sway/roll/yaw-system of equations, the following force equations of motion have been used:

$$\begin{aligned} Y &= Y_{\dot{v}}\dot{v} + Y_v v + Y_{\dot{p}}\dot{p} + Y_p p + Y_\phi \phi + Y_{\dot{r}}\dot{r} + Y_r r \\ K &= K_{\dot{v}}\dot{v} + K_v v + K_{\dot{p}}\dot{p} + K_p p + K_\phi \phi + K_{\dot{r}}\dot{r} + K_r r \\ N &= N_{\dot{v}}\dot{v} + N_v v + N_{\dot{p}}\dot{p} + N_p p + N_\phi \phi + N_{\dot{r}}\dot{r} + N_r r \end{aligned} \tag{3.33}$$

The hydrodynamic coefficients are calculated following the equations as presented in Table 3.3 below. Some coefficients require preliminary calculations for which the equations are presented in Appendix A.4; note that in $k(\beta)$ the deadrise angle (β) is in degrees and in $K_{D\phi}$ the trim (τ) is in radians.

Table 3.3: Empirical hydrodynamic coefficients bare hull [5].

$Y_{\dot{v}}$	$= -B^2\rho \tan\beta\, k(\beta)\left[L_K + 2L_C\right]/12$
Y_v	$= -0.5\rho U B^2\left[0.6494\,\beta^{0.6}\,T'^2 C_V^2\right]$
$Y_{\dot{p}}$	$= 0$
Y_p	≈ 0
Y_ϕ	$= 2F_\phi \sin\beta$
$Y_{\dot{r}}$	$= N_{\dot{v}}$
Y_r	$= 0.5\rho U B^2 L\left[55.439\,\beta^{0.6}\,T'^3\right]\left[0.02754 - 0.5949\,T'/(\tau + 5.28)\right]$
$K_{\dot{v}}$	≈ 0
K_v	$= Y_v\left[-KG + 1.5145\,B/\beta^{0.342}\right]$
$K_{\dot{p}}$	$= -0.010237\rho B^5\lambda\,(1 - \sin\beta) + h_1 Y_{\dot{v}}$
K_p	$= -\,(1 - \sin\beta)\,(0.029 C_V + 0.02\lambda)\,\rho g B^4\sqrt{B/g} + h_1 Y_v$
K_ϕ	$= K_{D\phi} + 0.624\,f_{sw}\left[-\rho g B^3(L_K + 3L_C)/48 + (KG - KB)\Delta\right]$
$K_{\dot{r}}$	$= 0$
K_r	≈ 0
$N_{\dot{v}}$	$= -B^2\rho \tan\beta\, k(\beta)\left[L_K^2 + 2L_K L_C + 3L_C^2\right]/48$
N_v	$= Y_v\left[-LCG + 12.384\,B\,T'^{0.45}/(\tau + 5.28)\right]$
$N_{\dot{p}}$	≈ 0
N_p	≈ 0
N_ϕ	$= Y_\phi\,(LCP - LCG)$
$N_{\dot{r}}$	$= -B^2\rho \tan\beta\, k(\beta)\left[L_K^3 + 2L_K^2 L_C + 3L_C^2 L_K + 4L_C^3\right]/120$
N_r	$= 0.5\rho U B^3 L\left[73.918\,\beta^{0.6}\,T'^3\right]\left[0.00638 + 6.714\,T'^2/(\tau + 5.28)^2\right]$

Table 3.4: Contribution of appendages [5].

$Y_{\dot{v}}$	$= -m_F \cos^2\varphi_R$
Y_v	$= -\Lambda \cos^2\varphi_R/U$
$Y_{\dot{p}}$	$= m_F\,(z_F\cos\varphi_R - y_F\sin\varphi_R)\cos\varphi_R$
Y_p	$= \Lambda\cos\varphi_R\,(z_F\cos\varphi_R - y_F\sin\varphi_R)/U$
Y_ϕ	$= -\Lambda\tau\cos^2\varphi_R$
$Y_{\dot{r}}$	$= -m_F x_F\cos^2\varphi_R$
Y_r	$= -\Lambda x_F\cos^2\varphi_R/U$
$K_{\dot{v}}$	$= m_F h_3\cos\varphi_R$
K_v	$= \Lambda h_3\cos\varphi_R/U$
$K_{\dot{p}}$	$= -m_F h_3\,(z_F\cos\varphi_R - y_F\sin\varphi_R)$
K_p	$= -\Lambda h_3\,(z_F\cos\varphi_R - y_F\sin\varphi_R)/U$
K_ϕ	$= \Lambda\tau h_3\cos\varphi_R$
$K_{\dot{r}}$	$= m_F h_3 x_F\cos\varphi_R$
K_r	$= \Lambda h_3 x_F\cos\varphi_R/U$
$N_{\dot{v}}$	$= -m_F x_F\cos^2\varphi_R$
N_v	$= -\Lambda x_F\cos^2\varphi_R/U$
$N_{\dot{p}}$	$= m_F x_F\,(z_F\cos\varphi_R - y_F\sin\varphi_R)\cos\varphi_R$
N_p	$= \Lambda x_F\cos\varphi_R(z_F\cos\varphi_R - y_F\sin\varphi_R)/U$
N_ϕ	$= -\Lambda\tau x_F\cos^2\varphi_R$
$N_{\dot{r}}$	$= -m_F x_F^2\cos^2\varphi_R$
N_r	$= -\Lambda x_F^2\cos^2\varphi_R/U$

To use these formulae to calculate the hydrodynamic coefficients, values are needed for the trim (τ) and the wetted lengths of the keel and chine (L_K, L_C). At this point in the simulation, a fixed value is used as input for these parameters. In the next section, the trim and sinkage are added to the model as speed-varying parameters. The mean wetted length over beam ratio was calculated as follows [5]:

$$L_K - L_C = \frac{B\tan\beta}{\pi\tan\tau} \quad \text{and} \quad L_K + L_C = 2\lambda B \quad \text{resulted in} \quad \lambda = \frac{L_K}{B} - \frac{tan(\beta)}{2\pi tan(\tau)} \tag{3.34}$$

Lewandowski has also defined appendage coefficients as a passive contribution to the total force. In this role, the rudder acts like a fixed vertical fin that contributes to the craft's overall directional stability and damping, with the rudder's deflection set to zero. The appendage coefficients are calculated following the equations presented in Table 3.4

The decision was made to keep midship as the reference point to make switching between models easy. However, Lewandowski designed his formulae to be centred on the centre of gravity. Shifting the reference point, the sway, roll and yaw rates were obtained by solving the following system:

$$\begin{bmatrix} m - Y_{\dot{v}} & -mz_G - Y_{\dot{p}} & mx_G - Y_{\dot{r}} \\ -mz_G - K_{\dot{v}} & I_{xx} - K_{\dot{p}} + mz_G^2 & -mx_G z_G - K_{\dot{r}} \\ mx_G - N_{\dot{v}} & -mx_G z_G - N_{\dot{p}} & I_{zz} - N_{\dot{r}} + mx_G^2 \end{bmatrix} \begin{pmatrix} \dot{v_m} \\ \dot{p} \\ \dot{r} \end{pmatrix} = \begin{pmatrix} Y_H + Y_R + Y_{ap} - (m + m_x)ur \\ K_H + K_R + K_{ap} + mz_G ur \\ N_H + N_R + N_P + N_{ap} - mx_G ur \end{pmatrix} \tag{3.35}$$

$$\text{where:} \quad \begin{aligned} m_y &= -Y_{\dot{v}}, \quad & m_y x_\alpha &= -Y_{\dot{r}} = -N_{\dot{v}}, \quad & m_y z_\alpha &= Y_{\dot{p}} = K_{\dot{v}}, \\ J_x &= -K_{\dot{p}}, & J_z &= -N_{\dot{r}}, & J_{xz} &= K_{\dot{r}} = N_{\dot{p}} \end{aligned} \tag{3.36}$$

As a result the hull ($_H$) and appendage (app) forces were defined to be as follows:

$$\begin{aligned} Y_{H,app} &= Y_v v + Y_r r + Y_p p + Y_\phi \phi \\ K_{H,app} &= K_v v + K_r r + K_p p + K_\phi \phi \\ N_{H,app} &= N_v v + N_r r + N_p p + N_\phi \phi \end{aligned} \tag{3.37}$$

Both are added to the total forces as their own contribution, e.g. $Y_{total} = Y_H + Y_{app} + Y_R + Y_P$. The sway, roll, yaw accelerations are calculated by solving the 3x3 matrix system.

3.4.2. Surge hull force

From the force equations in Equation (3.33), it can be deduced that, in this model too, the surge motion is decoupled from the other motions. Since this thesis has access to full-scale sea trial data, it was decided to obtain the surge coefficients from the resistance curve generated from this dataset.

The Surge equation is assumed to be as follows:

$$X_H = -R(u) \tag{3.38}$$

Where $R(u)$ is the resistance curve, and matches the resistance for each instantaneous speed throughout the manoeuvre. The surge added mass is assumed to be 7.5% of the total mass, i.e. $m_x = 0.075 \cdot \Delta$.

3.4.3. Propeller force

The propeller model is the same as presented in Section 3.3.2, except for the wake fraction (w_P) and the calculation of the open-water thrust coefficient (K_T). The wake fraction is calculated as follows:

$$\begin{aligned} w_P &= w_{P0} \cdot e^{-4\beta^2_{P(\mathrm{s,p})}} \\ \text{where} \quad \beta_{P(\mathrm{s,p})} &= \beta - x'_{P(\mathrm{s,p})} r' + z'_{P(\mathrm{s,p})} p' \end{aligned} \tag{3.39}$$

The wake fraction is used to calculate the inflow speed, which in turn is used to calculate the advance ratio. From the open-water curve, a look-up table is constructed in which the calculated J is used to find the value of K_T. Next, this value is used to calculate the thrust and propeller force and moment components X_P and N_P.

3.4.4. Rudder force

In addition to the static contributions of the rudder as an appendage to the bare hull, the effect of a rudder deflection is modelled by calculating the lift and drag forces. Lift ($L_{R(\mathrm{s,p})}$) acts perpendicular to the flow and drag ($D_{R(\mathrm{s,p})}$) act along it. Therefore, there are two contributions to the inflow angle:

- The oblique horizontal flow from drift, yaw and roll: $\beta_R = -\gamma_R \tan^{-1}(v_{R,loc}/u_R)$. Where γ_R is the flow straightening coefficient, and u_R, v_{Rloc} are the (local) flow velocities around the rudder. This flow arrives at an angle; the lift and drag follow this rotation.
- The geometric trim-heel angle: $\alpha_{trim} = \sin(\theta)\sin(\tau)$. Here θ is the (running) trim angle of the vessel (at the current speed) and τ is the tilt angle of the rudder relative to the vertical axis (heel angle - rudder cant angle). This flow runs along the x-axis with a tilted blade. Here, lift has no x-contribution and drag acts along the negative x-direction.

This results in the following forces in the blade plane, Y_N being the force normal to the blade:

$$\begin{aligned} X_{R(\mathrm{s,p})} &= -D_{R(\mathrm{s,p})}\cos(\beta_R) - L_{R(\mathrm{s,p})}\sin(\beta_R) \\ Y_{N(\mathrm{s,p})} &= -L_{R(\mathrm{s,p})}\cos(\beta_R) + D_{R(\mathrm{s,p})}\sin(\beta_R) \end{aligned} \tag{3.40}$$

The forces were then rotated back to the boat's axis, as used in Lewandowski's empirical model, in which the xy-plane remains horizontal while the hull trims and heels. This resulted in the following force and moment equations:

$$\begin{aligned} X_{R(\mathrm{s,p})} &= -D_{R(\mathrm{s,p})}\cos(\beta_{R,lat}) - L_{R(\mathrm{s,p})}\sin(\beta_{R,lat}) \\ Y_{R(\mathrm{s,p})} &= Y_N \cdot \cos(\tau) \\ K_{R(\mathrm{s,p})} &= -h_{R(\mathrm{s,p})} \cdot (Y_N + Y_{aH}) \\ N_{R(\mathrm{s,p})} &= Y_N \cdot x_{R(\mathrm{s,p})} - X_{R(\mathrm{s,p})} \cdot y_{R(\mathrm{s,p}),b} \end{aligned} \tag{3.41}$$

The lever arm resulting in the roll moment is defined as $h_{R(\mathrm{s,p})} = y_{R(\mathrm{s,p})} \sin(\varphi_R) + z_{R(\mathrm{s,p})} \cos(\varphi_R)$, where φ_R is the cant angle of the rudder (zero in the case of the pilot vessel). Both the normal force and its line of action rotate with the hull; as a result, the lever arm does not depend on the heel angle. The lever arm resulting in the longitudinal rudder force contribution of the yaw moment is defined as $y_{R(\mathrm{s,p}),b} = y_{R(\mathrm{s,p})} \cos(\phi) - z_{R(\mathrm{s,p})} \sin(\phi)$, which is the lateral position of the rudder in boat axis corrected for heeling. The x-position of the rudder does not need to be corrected because heeling about the x-axis leaves the x-position unchanged. In the running attitude model, the $z_{R(\mathrm{s,p})}$ moves with the transom draft.

The forces and moments are calculated for each rudder and then added together. Using the axial velocity at the rudder (u_R), the rudder area (A_R), the lift coefficient (CL) and the rudder aspect ratio (A_e), the lift and drag forces were calculated as follows:

$$L_R = 0.5\rho u_R^2 A_R \cdot CL, \quad D_R = \frac{0.5\rho u_R^2 A_R \cdot CL^2}{A_e \pi} \tag{3.42}$$

For the rudder aspect ratio, Lewandowski gives two possible formulas, depending on whether there is a gap between the rudder and the hull. If no gap is visible, it is calculated as follows: $A_e = {}^{2H_R}/_{c_R}$; this is the case for the pilot vessel. The lift coefficients include a stall limit and are calculated as follows:

$$CL = \frac{CL_{lin}}{\left(1 + |\frac{CL_{lin}}{CL_{max}}|^k\right)^{1/k}} \quad \text{with} \quad CL_{lin} = \alpha_R \Lambda, \quad CL_{max} = 1.3, \quad k = 4 \tag{3.43}$$

The linear lift coefficient (CL_{lin}) is calculated using the lift curve slope $\Lambda = \frac{1.8\pi}{1+2.8/A_e}$ and the geometric inflow angle $\alpha_R = \delta - \beta_R - \alpha_{trim}$. The values for the maximum lift coefficient (CL_{max}) and the k are estimated based on planing hull data presented in [5].

The flow straightening coefficient is calculated using the block coefficient (C_B), which is in turn calculated using the changing wetted geometry of the vessel, as follows:

$$\gamma_R = \frac{1}{1 + C_B} \quad \text{with} \quad C_B = \frac{\nabla}{L_K B_{ac} d_{inst}} \tag{3.44}$$

The axial flow velocity at the rudder is calculated using the same formula as for the twin-rudder model presented above in the previous section. The local lateral velocity is corrected for the heel angle of the vessel and is calculated as follows:

$$v_{R,\mathrm{loc}} = (v + x_R r)\cos(\phi - \varphi_R) - h_3\, p \tag{3.45}$$

3.5. Expansion to 4+2DOF model

As mentioned in the previous section, the last model will include speed-varying sinkage and trim, also known as the running attitude. This is done by using a look-up table. In this table, the following items are stored for each speed (kn): volumetric Froude number, heave (m), trim (deg), wetted keel length (m), and wetted chine length (m). The GPPH running attitude table values were based on [73], the pilot vessel values were taken from the sea trial measurements.

Based on the measured trim and sinkage during the sea trials, the 3D model in Rhinoceros has been used to create the table for the pilot vessel. Using the parameters in the running attitude table, the transom draft is calculated in two ways, for the pilot vessel and GPPH hull respectively:

$$T_{transom} = L_{keel} \cdot \sin(\theta) \quad \text{and} \quad T_{transom} = T_{static} - z_{sinkage} + L_{towpoint} \cdot \sin(\Delta\theta) \tag{3.46}$$

The running transom draft is implemented in the hull coefficients from Lewandowski. Also, the $z_{R(\mathrm{s,p})}$ follows the transom draft, making the rudder model follow the running attitude. The running attitude table of the GPPH model is presented in Table A.5 in Appendix A.

4. Assessment of simulation models

In this Chapter the models presented above are assessed to produce the correct results and verified against published data. The 3DOF, 4DOF and TPTR models are assessed with displacement hulls, the gear-case and empirical hull are assessed with the GPPH hull. First, in Section 4.1, the standard 3DOF model is validated with digitised data from [22]. In Section 4.2, the assessment of the 4DOF MMG model is presented using digitised data from [46]. The force data presented in [19] is used to assess the gear-case and propeller models made for the GPPH hull in Section 4.4. The twin-rudder, twin-propeller (TPTR) model assessment was performed using digitised data from [80], and is presented in 4.3. In the last part of this section, the planing hull model is validated with digitised data from [19, 30, 43, 75].

4.1. 3DOF MMG model

In [22], the standard MMG 3DOF model was presented, along with test cases for the KVLCC2 vessel. In the paper, three scaled models were used for different tests. For the $KVLCC2_{L3}$, the resistance and model-point propeller rpm ($n_p = 17.95$rps) were given, along with the service speed for the full-scale vessel. Using the scaled-down service speed for the L3 model, straight-sailing tests were performed to check if the simulation starts from an equilibrium position. A straight-sailing test is a manoeuvre where the vessel holds a steady course and speed in calm water, with its steering fixed straight, to measure its speed, power, and resistance under undisturbed conditions. The goal is to achieve zero deflections in trajectory, speed loss, sway speed, yaw rate and rudder side force. The results of these straight sailing tests are presented in Figure 4.1. Looking at the straight-sailing test with the model-point rps, it becomes clear that the simulation was not in equilibrium, as a clear speed loss of 1.34% of the starting speed is visible (blue line). Two new rps settings were tested; both show a change in speed of 0.03% of the starting speed. The new equilibrium rps was chosen as the propeller setting, with $n_p = 18.19$rps.

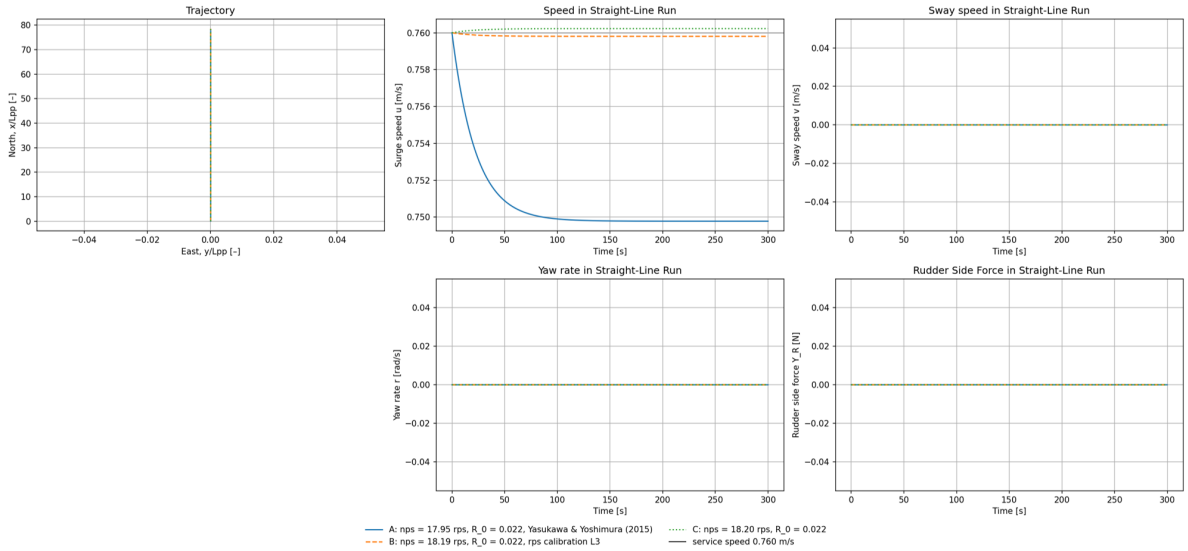

Figure 4.1: Straight sailing run with the $KVLCC2_{L3}$ model for various propeller rps settings with an approach speed of 0.76m/s, run with the standard 3DOF MMG model.

For the full-scale $KVLCC2$ vessel, both propeller rpm conditions were tested, using the resistance coefficient from the L3 Model. The result of this is presented in Figure 4.2, where $n_P = 1.734rps$ matches the new n_p of the L3-model, showing a speed loss of 3.79% of the starting speed. A new equilibrium had to be found by tuning the resistance coefficient for the full-scale vessel, resulting in a new value of $R_0 = 0.0206$. The result of this is the green dotted line in the plot. With the new propeller and resistance coefficient, the speed gain in the straight sailing run was +0.05% of the starting speed.

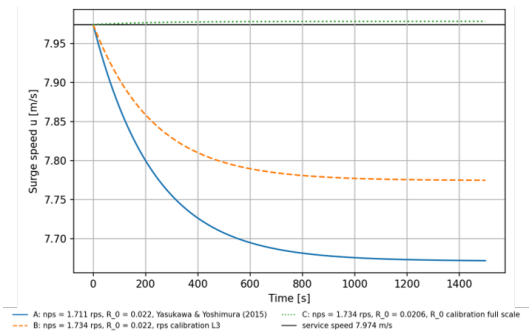

Figure 4.2: Straight sailing run with the $KVLCC2$ full-scale model for various propeller rpm settings and resistance coefficients, run with the standard 3DOF MMG model.

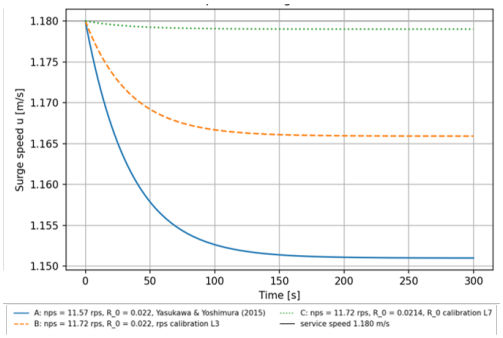

Figure 4.3: Straight sailing run with the $KVLCC2_{L7}$ model for various propeller rps settings and resistance coefficient, run with the standard 3DOF MMG model.

Since the simulation results for both the full-scale vessel and the L7-model were presented in the paper, the equilibrium check was also performed for the L7-model. The first case shows a 2.46% loss in speed relative to the starting velocity. For this model, the service speed and propeller rps were scaled to determine the resistance coefficient for this vessel. The results of this can be found in Figure 4.3, where $n_P = 11.72$rps matches the new n_p of the L3-model. With the new propeller and resistance coefficient, the speed loss in the straight sailing run was -0.08% of the starting speed.

The final check in the assessment of this model was a turning circle simulation run for both the L7 and full-scale models of the KVLCC2 vessel. The results of this are presented in Figure 4.4; here, the blue solid lines are the simulation turning circles, and the orange dotted lines are the digitised plots from [22]. As can be seen, both the simulation and the paper results are close. The standard MMG model was therefore deemed sufficiently validated.

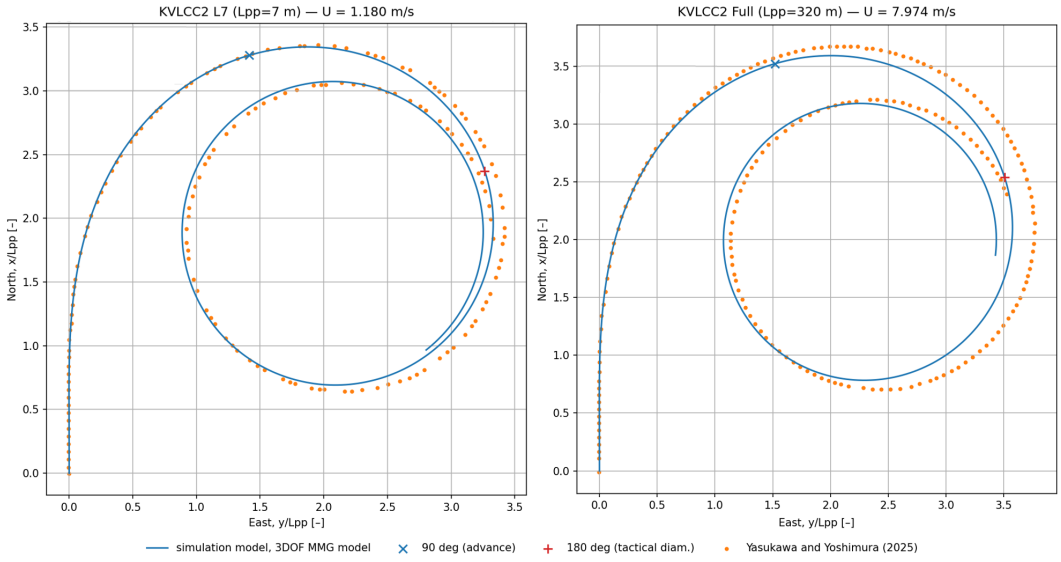

Figure 4.4: Turning circle run for KVLCC2 full scale and L7-model with standard 3DOF MMG model, compared with digitised data from [22].

4.2. 4DOF MMG model

In [46], a 4DOF MMG model presented by [44] was validated for the KCS vessel. For the KCS_{L4}, both the service speed and propeller rpm were known, of which the latter was scaled for the full-scale vessel. A straight-sailing simulation was run to determine the resistance coefficient for both models. After the straight-sailing run, a turning circle test was conducted to determine the rudder's turning rate, the results of which are shown in Figure 4.5. In the figure, the dotted line shows the digitised turning circle result for the L4 Model from [46]. The solid blue line is the simulation with an instant rudder step, meaning the rudder changed from $0°$ to $35°$ instantly. The orange solid line shows the chosen rudder rate of $19°/s$.

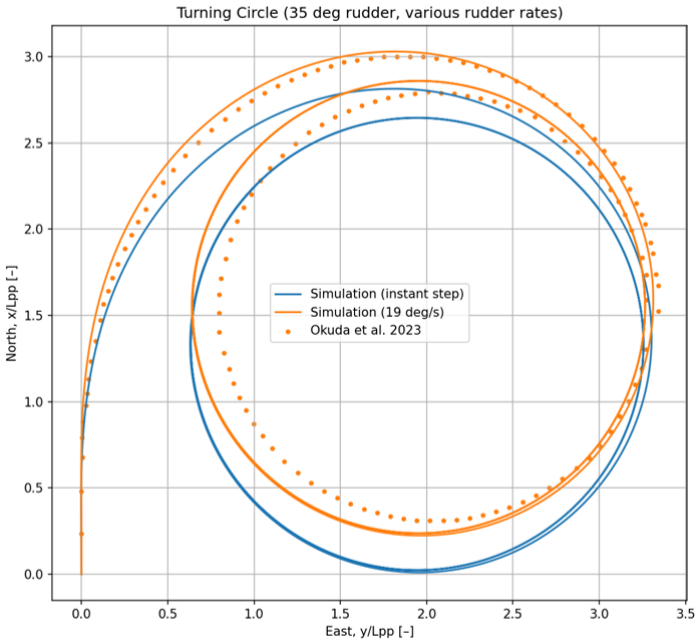

Figure 4.5: Turning circle run for the KCS_{L4} model comparing rudder rate and instant step simulation, with digitised data from [46].

To validate the model, the results for the speed loss, drift angle, yaw rate, roll angle, propeller thrust and rudder normal force were compared with the digitised data from [46] for the KCS_{L4} model. In Figure 4.6 on the next page the results of this assessment step are presented for various turning parameters. In the figure, the orange dotted lines represent the digitised data, and the solid lines show the results for two different propeller settings.

The reason for these two settings is that the paper mentions a propeller setting of $n_p = 11$rps. However, in the propeller thrust plot (third row, left plot), the blue line represents the simulation for this propeller condition. The simulation was tuned to match the propeller thrust results presented in the paper; a value of $n_P = 10.7$rps was found with the same resistance coefficient (the green line).

However, this change has little effect on the turning motion, as can be seen in the other panels. The speed loss, yaw rate and rudder normal force change by about 3–5%, while the drift and roll angle remain unchanged. With the reported 11.0rps, the yaw rate and rudder normal force even agree slightly better with the reference data. A recalibration of the model was therefore not considered necessary, and the reported propeller speed of 11.0rps was used for the remaining simulations. The thrust difference most likely originates from the propeller input data, such as the open-water curve or the wake fraction, which could not be verified with the information given in the paper.

Also, the model appears more unstable in roll, although it tracks the fluctuations in the Okuda et al.'s reference model tests and calculations. It was found that the coefficient "a" in the $K_{\dot{\phi}}$ formula was the most sensitive coefficient influencing this result, compared to the "b" coefficient in the $K_{\dot{\phi}\dot{\phi}}$ formula.

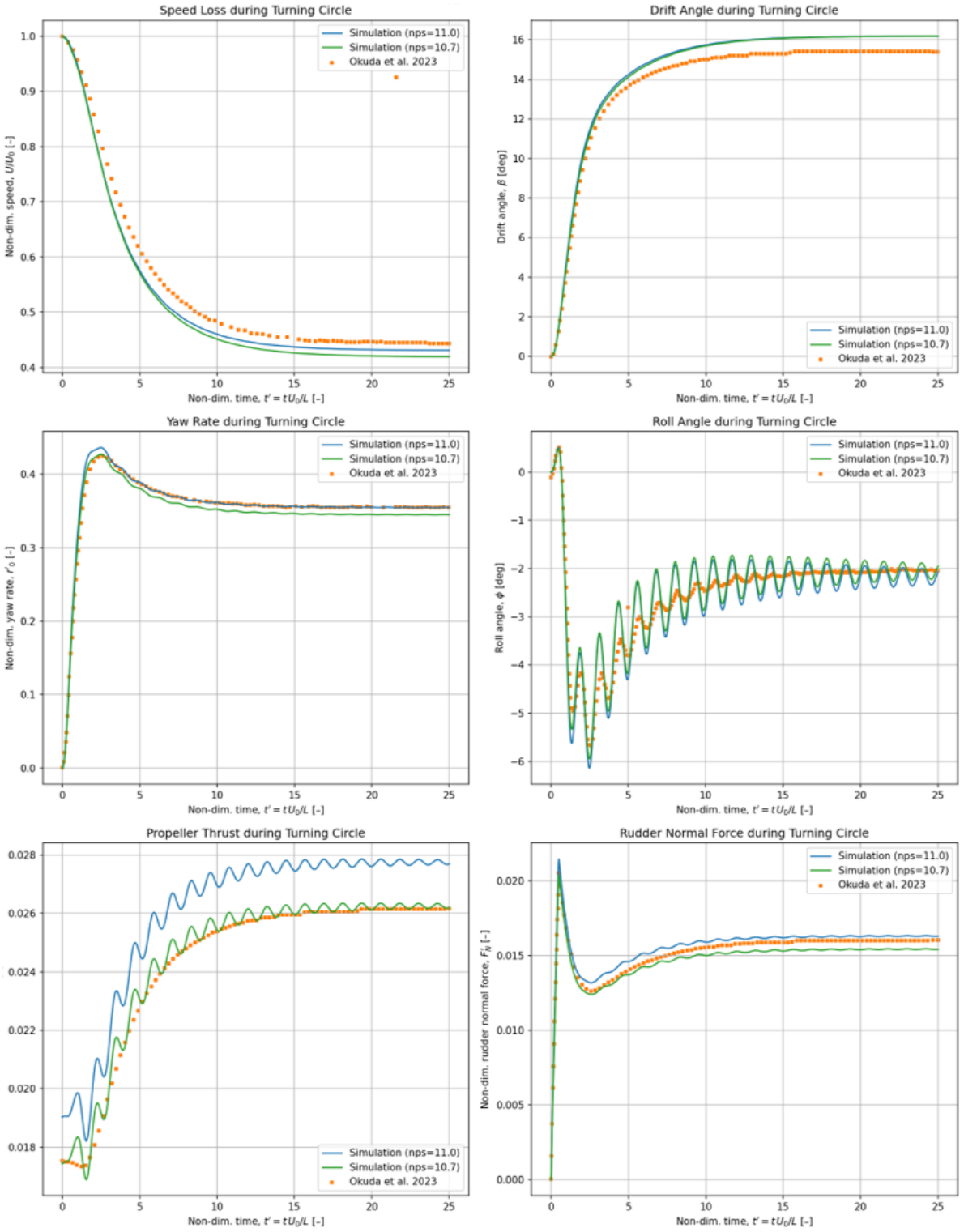

Figure 4.6: Turning circle timeseries run for the KCS_{L4} model with the 4DOF MMG model, compared against digitised data from [46].

The final step in the assessment of the 4DOF MMG model was the comparison of the turning circles for various approach speeds. The results of these simulations are presented in Figure 4.7, where the dotted orange and green lines are the digitised data from [46]. The orange dotted line (Cal.) is the result of their MMG simulation, and the green stripe-dotted line (Exp.) is the result of their free-running towing test experiments. The blue solid line represents the simulated turning circles. As can be

seen, the simulation and paper results overlap closely. The 4DOF MMG model was therefore deemed sufficiently validated.

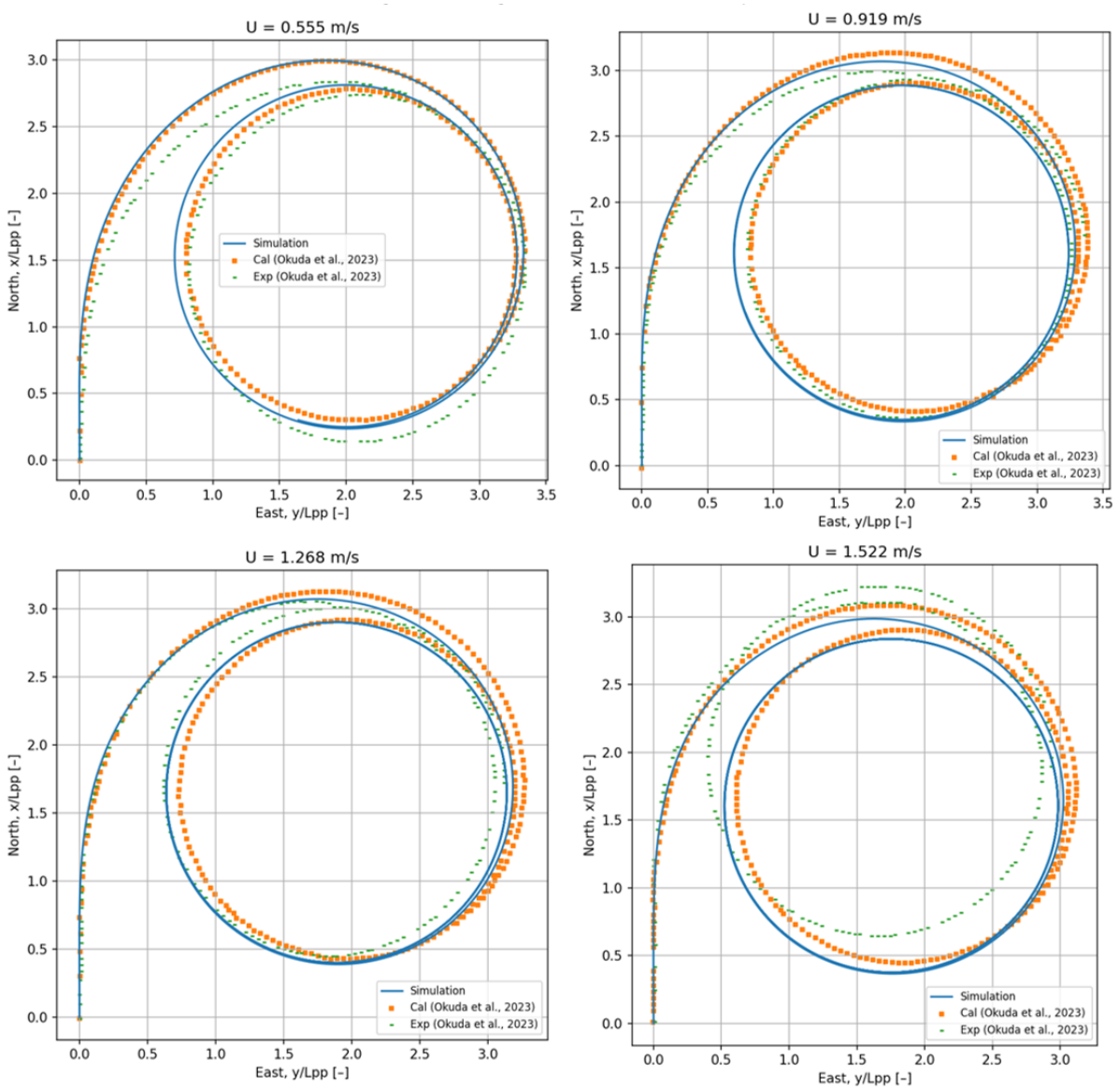

Figure 4.7: Turning circle run for KCS in 4DOF MMG model, compared with digitised data from [46].

4.3. Twin propeller twin rudder model

The vessel used for the assessment of this model 100m ferry (tested on model scale with a length of 3m) presented in [80]. For the twin-propeller, twin-rudder model, a straight-sailing simulation was run to obtain the resistance coefficient for the simulated TPTR vessel. In Figure 4.8 various values for the resistance coefficient were tested to find the (near-)equilibrium. As a starting point, the KCS value was chosen from the L4 model (orange dotted line), showing a speed loss of 2.01% compared to the starting velocity. The green dotted line and the blue solid line show two tested resistance coefficient values. The first shows a 0.05% speed gain. The chosen value of $R'_0 = 0.0177$ showed a speed loss of 0.06%.

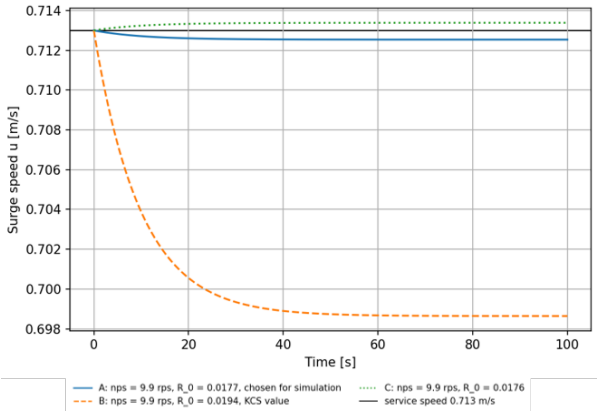

Figure 4.8: Straight sailing run for the TPTR model with various resistance coefficient values.

For assessing the TPTR model, the turning circle results from [80] were used. The comparison for the speed loss, drift angle, yaw rate, roll angle and rudder normal force is presented in Figure 4.9. As can be seen, both the simulation and the paper results overlap closely. The TPTR addition to the 4DOF MMG model was therefore deemed sufficiently validated.

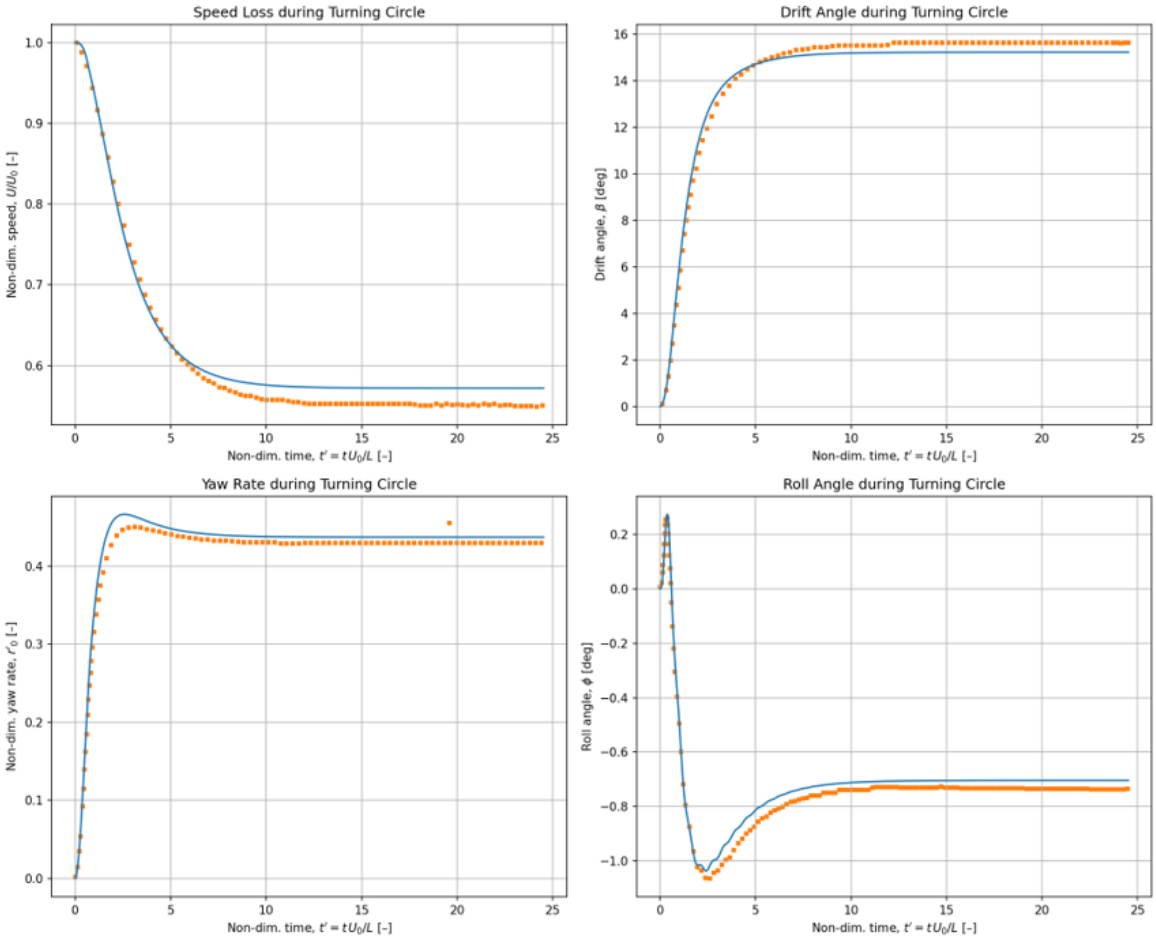

(a) Speed loss, drift angle, yaw rate and roll angle.

Figure 4.9: Time-series and trajectory run with the TPTR-model in the 4DOF MMG model, compared with data digitised from [80].

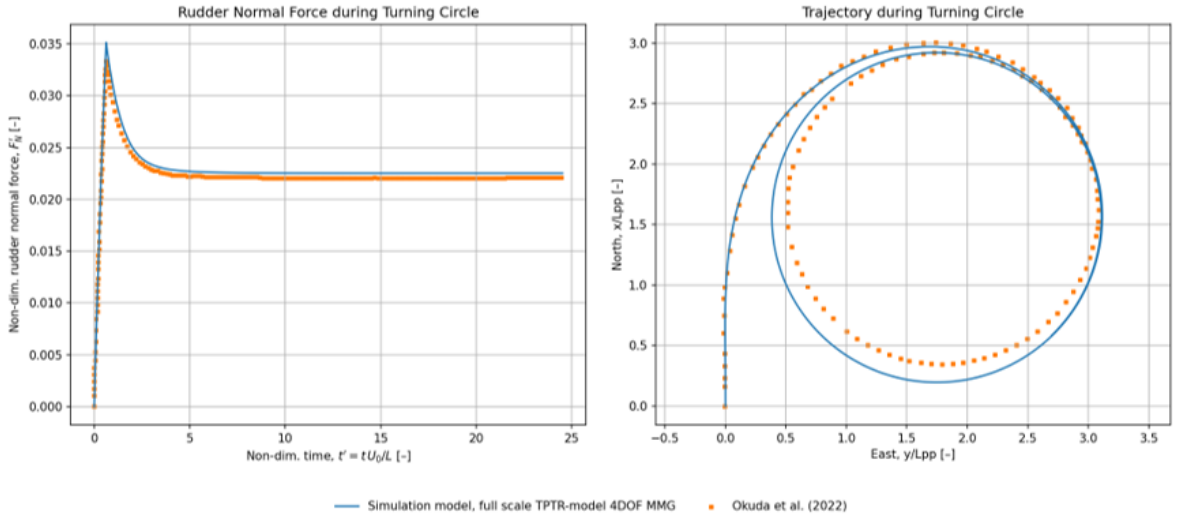

(b) Rudder normal force and trajectory.

Figure 4.9: Time-series and trajectory run with the TPTR-model in the 4DOF MMG model, compared with data digitised from [80] (continued).

4.4. Gear-case model

The gear-case and propeller models were compared against force data presented by [19]. In Figure 4.10, this comparison is presented, where the black columns on the left are the force components as presented in the paper and the red columns on the right are the results from the simulation model. The forces are made non-dimensional using the vessel's weight $W(= mg)$, and the moments are made non-dimensional using weight times length (WL_{PP}). To make a fair comparison, the simulation was run with the trim variations as presented in the paper.

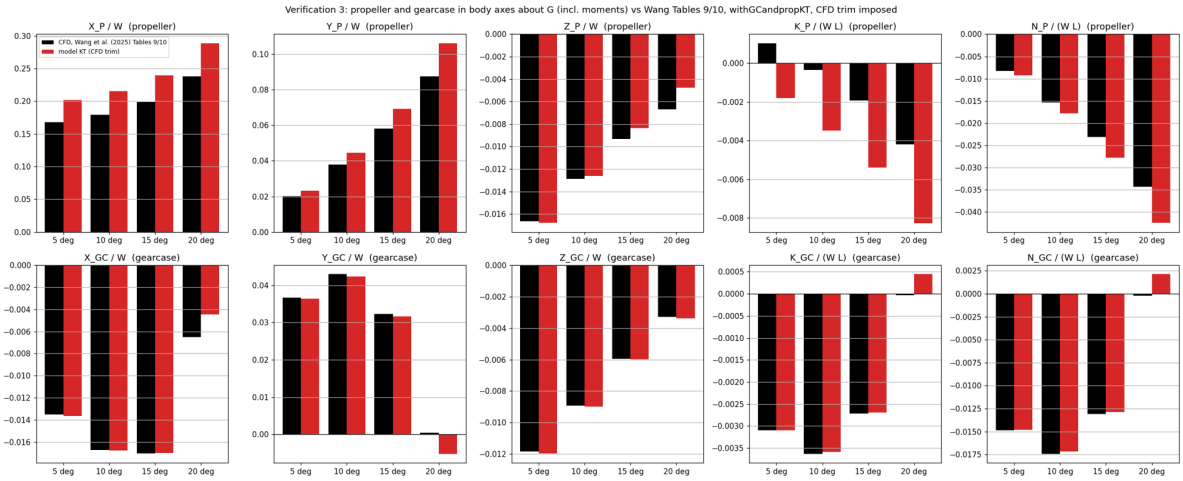

Figure 4.10: Comparison of propeller and gearcase using trim data from the paper and simulation model forces with [19] tables.

From the figure, it can be seen that the gear-case and propeller models follow the trends in the force data reported in the paper and are of the same order of magnitude. However, it does show a difference in the propeller roll moment (K_P). This was traced back to a nearly constant contribution of 0.0026WL in the CFD results, which is the propeller torque reaction. The body forces in the CFD model include this force from the propeller; however, the simulation model does not (following the standard MMG convention, in which the propeller is represented by thrust only). The K_Q curves from [30] show a torque reaction of about 0.0032WL at the approach speed; compared to their CFD data, this is about

25% and lies in the same order of magnitude as the difference in the propeller force. In section 5.2, the effect of heel is quantified.

The standard MMG framework does not include the torque reaction force in the propeller model. Excluding the thrust level and torque reaction, the gear-case and propeller models follow the trends of the CFD forces. However, leaving out the torque reaction disregards a moment that visibly changes the roll and leaves the forces about 20% off. So applying the MMG model in its standard convention neglects a contribution essential for high-speed craft. High-speed craft have a small displacement and a large power-to-weight ratio, making the torque reaction large relative to the roll restoring moment. For large displacement vessels, it is negligible compared to the large weight of the vessel, which is why the standard MMG model ignores it. Although it should be noted that for twin-propeller configurations with counter-rotating propellers, the torque is largely cancelled; thus, the neglect of the torque reaction mainly affects the single-propeller / gear-case configuration.

4.5. Empirical hull model assessment with GPPH-model

The last addition in the model, the empirical planing hull model, was validated for the GPPH hull. As mentioned in Section 2.5 the GPPH is outfitted with a gear-case. For the GPPH model, the approach speed and resistance curve were known, so a straight sailing run was performed to find the equilibrium propeller condition. Here, an equilibrium condition was found at $n_p = 53.80$rps.

An assessment run was performed, comparing it with digitised data from [43]. The simulations were run for steering angles of $5°, 10°, 15°$ and can be found in Figure 4.11, Figure 4.12, and Figure 4.13, respectively. In the trajectory plots (first row, left plot), the blue dotted line is the result of their MMG simulation, and the black dotted line is the result of free-running CFD tests they performed. The MMG result is added for comparison to show the difference and to provide a full-circle comparison in the 5deg turning circle, since the CFD result is not published in their paper.

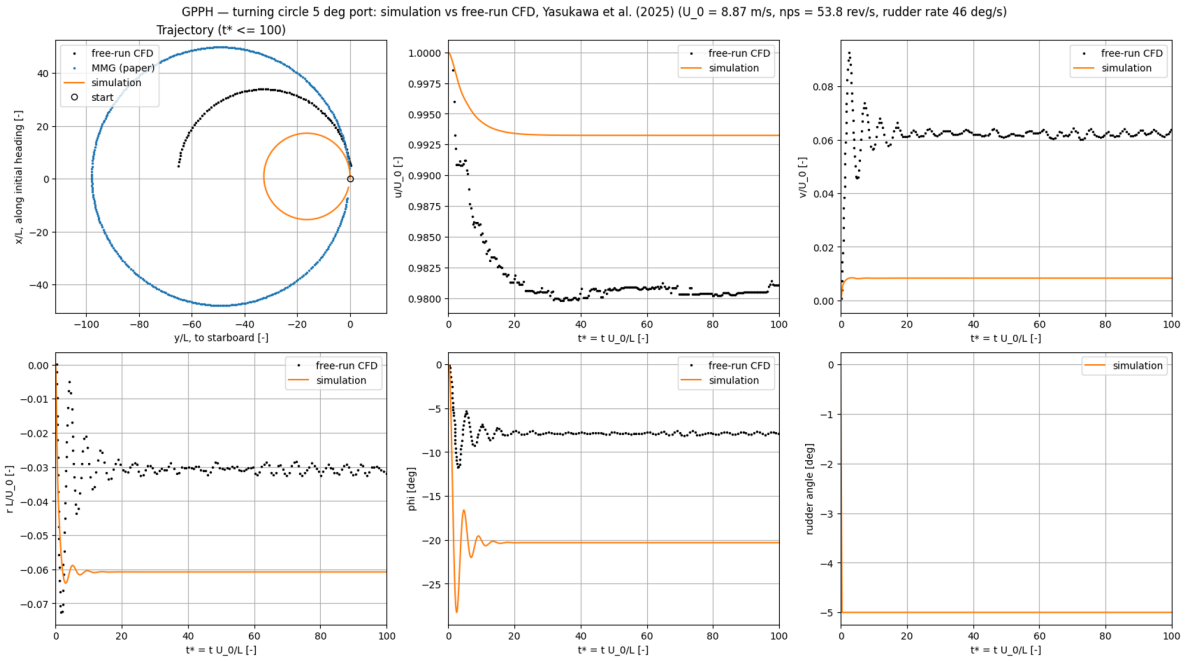

Figure 4.11: Turning circle run with a steering angle of 5deg of the empirical model with the GPPH gearcase steering model, compared with data from [43].

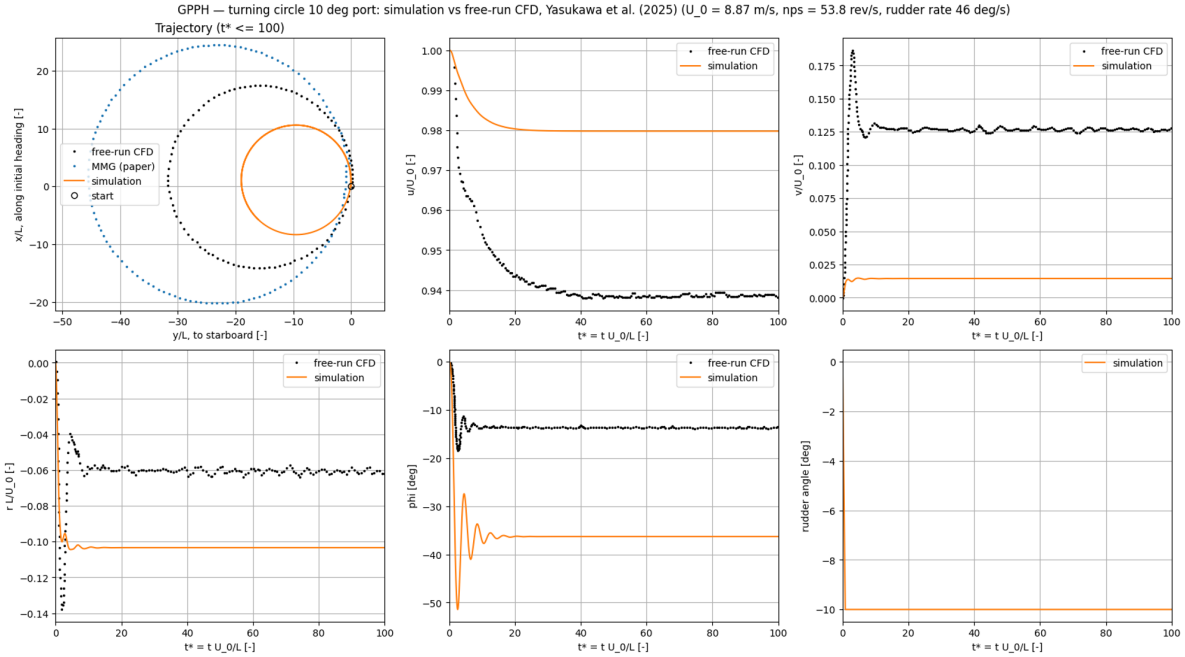

Figure 4.12: Turning circle run with a steering angle of 10deg of the empirical model with the GPPH gearcase steering model, compared with data from [43].

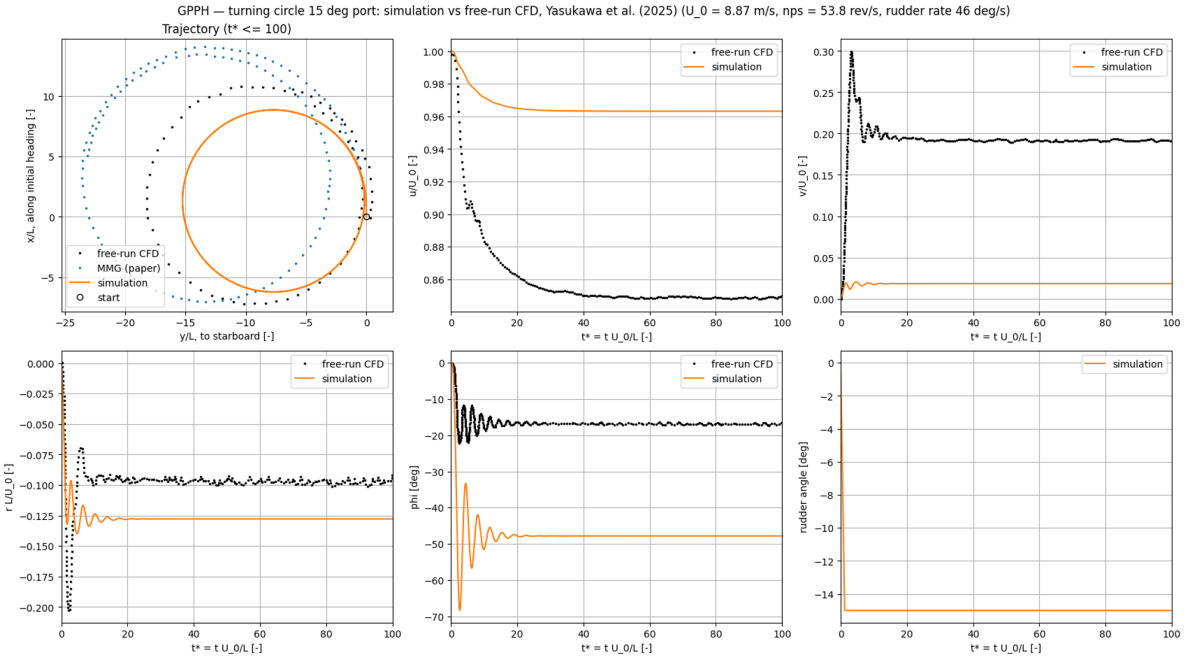

Figure 4.13: Turning circle run with a steering angle of 15deg of the empirical model with the GPPH gearcase steering model, compared with data from [43].

Looking at the three comparison plots above, it is clear that the current model does not perform well, and its results are not close to the free-running CFD results presented in the paper [43]. Therefore, an analysis was conducted to determine the source of the deviations and to test whether the differences are due to mistakes in the model or to deliberate modelling choices.

5. Results and discussion

In this chapter, the results of this thesis are presented. A standard conventional displacement manoeuvring model was used as a starting point and adapted step by step to meet the unique requirements of high-speed manoeuvring. The models presented in the previous chapter were used to improve understanding and to check at each step that it had been implemented correctly: the 3DOF recreation, the addition of roll in the 4DOF model, the twin-propeller twin-rudder addition in order to be able to model the pilot vessel and the check with the GPPH vessel to verify the simulation model in the fully planing regime. In Table 5.1 below, an overview is given of the tested cases, the sources for the comparison material and the sections giving information about the created models.

Table 5.1: Tested cases of the simulation models, with the vessels, comparison data and the sections where each model is described, assessed and its input data is given.

Model	Additions	Tested vessels	Source	Method	Assess.	Data
3DOF MMG	Recreation of the standard model	KVLCC2	[22]	3.1	4.1	A.1
4DOF MMG	+ Roll equation of motion, roll damping and restoring + Heel correction of the inflow velocities	KCS	[46]	3.2	4.2	A.2
Gear-case	+ Propulsion force and moment + Steering force and moment	GPPH	[19]	3.3.1	4.4	A.5
TPTR	+ Port and starboard propeller and rudder contributions	TPTR hull, pilot vessel	[80]	3.3.2	4.3	A.3
Empirical hull (4DOF)	+ Linear empirical sway, roll and yaw formulations + Surge from resistance curve	GPPH, pilot vessel	[5, 19, 30, 43, 75]	3.4	4.5	A.4
Running attitude (+2DOF)	+Speed-dependent heave, trim and wetted lengths + Transom draft and wetted geometry updated per time step	GPPH, pilot vessel	[73]	3.5	5.1	A.5

This chapter starts (with Section 5.1) with an analysis using the GPPH hull with the empirical hull model to assess where the deviations shown in the last plots of the previous chapter originate from. This analysis led to a sensitivity study of non-linear coefficients, with results presented in Section 5.2 using the GPPH model. In Section 5.3, the pilot vessel is simulated with the adjusted empirical hull model and compared to the sea trial dataset results. An overview of the impact of adding roll and running attitude to the standard MMG model can be found in Section 5.4, presented for both the GPPH model and the pilot vessel. This chapter ends with Section 5.5 presenting a discussion about the results together with the contributions and limitations of the method presented.

In Appendix A, tables with the input data for the simulations are presented for all tested models.
In Appendix B, the Python code blocks of the final simulation model for the hull, propulsion and steering calculations and the equations of motion are presented for both the GPPH and the pilot vessel.

5.1. Empirical hull model analysis with GPPH-model

In [43], the results of their linear hull derivatives were presented for various Froude numbers, giving the opportunity to validate the outcome of the empirical hull coefficient model. The results of this are presented in Figure 5.1. First, looking at the captive-CFD data, it is clear that the derivatives change with Froude number (and thus with speed). This provides a clear argument that, for high-speed manoeuvring, the coefficients must be obtained across various speed regimes and cannot be assumed constant throughout the manoeuvre.

Furthermore, comparing the simulation results (orange solid line) with the CFD points shows that the Y'_v of the simulation follows a different trend. This feeds into the N'_v and K'_v coefficients. Also, in the K'_r plot, the difference seems very big; however, the K'_r is assumed to be zero in the Lewandowski model, and the captive-CFD values are also very small.

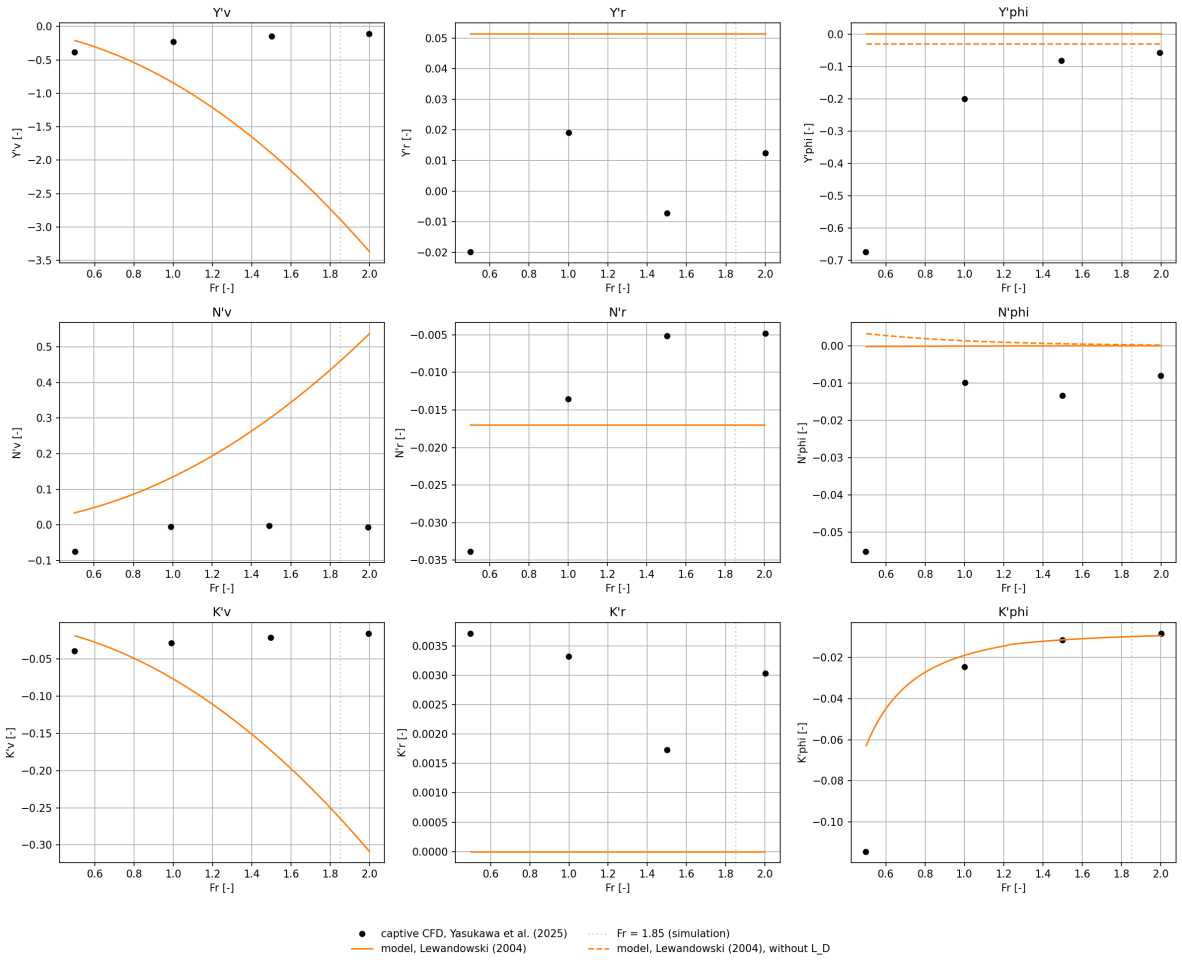

Figure 5.1: Linear hull derivatives for the GPPH-model at the starting condition of the simulation model, compared with captive-CFD data from [43].

Two deliberate changes were made to the Y'_v and Y'_ϕ coefficients based on the plots presented above. The deviation of Y'_v compared to the captive-CFD data points seemed to be exactly a factor of Fr_B^2. As a reminder, the coefficient was defined as follows: $Y_v = -0.5\rho U B^2 \left[0.6494\,\beta^{0.6}\,T'^2 C_V^2\right]$, where $C_V = U/\sqrt{gB}$ is the speed coefficient defined the same as the Froude beam number (Fr_B). Therefore, a test was done to see the effect of not including this factor in the calculation of Y'_v. In addition, the dynamic lift is included in the Y'_ϕ coefficient. Here the dynamic lift is calculated using the empirical formula as presented by [5]:

$$L_D = \frac{1}{2}\rho U^2 B^2 \left(\frac{\sin 2\tau}{2\cos\beta}\left[\frac{\pi}{4}\left(1-\sin\beta\right)\cos\tau\,\frac{\lambda}{1+\lambda} + \frac{1.33}{4}\,\lambda\cos\tau\sin 2\tau\cos\beta\right]\right) \tag{5.1}$$

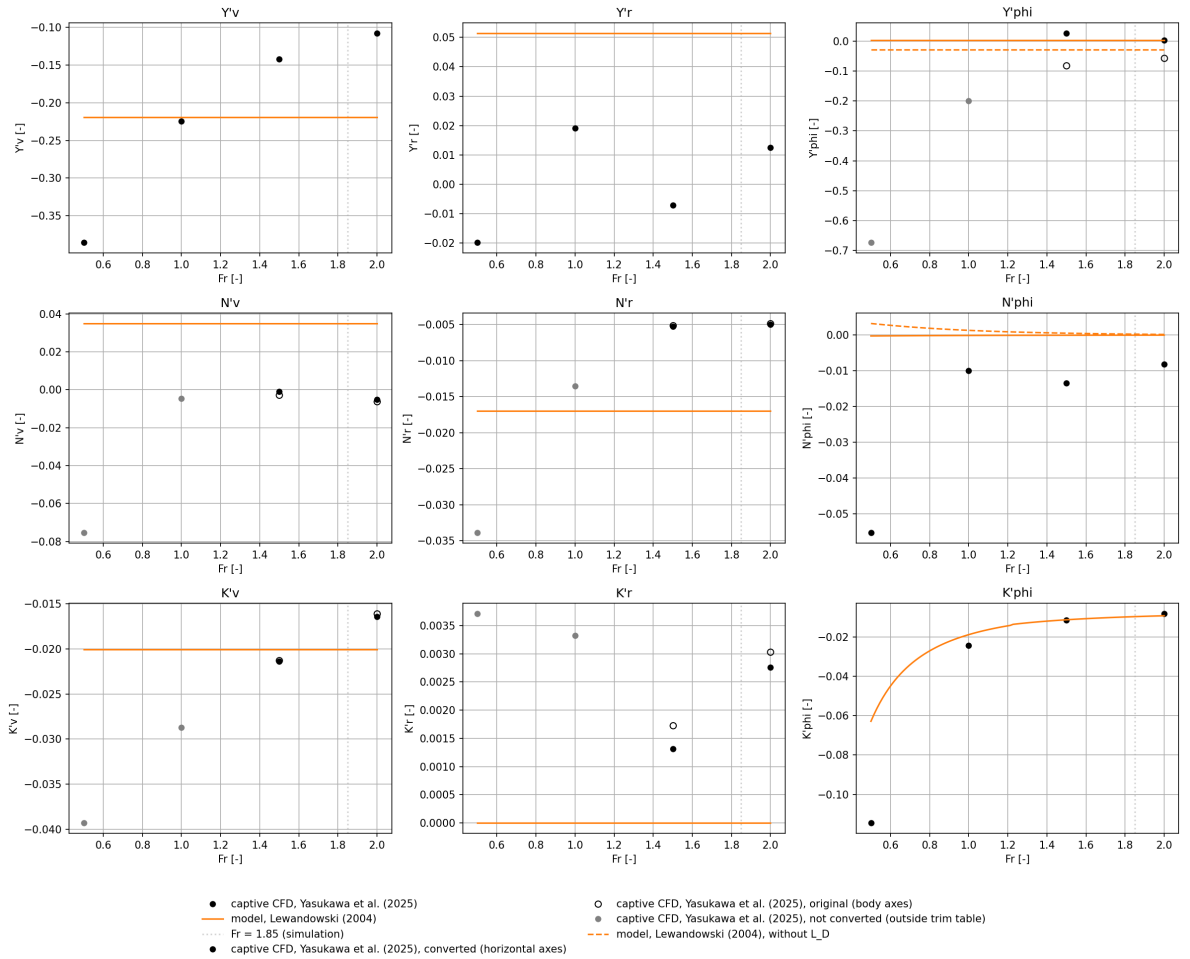

Figure 5.2: Linear hull derivatives for the GPPH-model without Cv2 in Y_v and shifted points to be in the right reference frame (body vs horizontal), compared with captive-CFD from [43].

As shown in the figure above, the changes to the model influenced the envelope and order of magnitude of the coefficients involved. However, due to the exclusion of the speed coefficient in the Y'_v coefficient (and thus N'_v, K'_v), the coefficients now stay constant for the simulation. As this is clearly not the case for the captive-CFD data points, and given that the coefficients are a function of the vessel's wetted geometry, the idea came to mind to test the coefficients using a speed-dependent wetted geometry.

To test the effect of the changing wetted geometry, a comparison was made for four different cases:

- A: The baseline simulation where the wetted geometry stayed fixed. These are the same as the simulation presented above.
- B: A running transom draft calculated based on the changing wetted geometry data from straight-line towing tank tests as presented in [73] for heave, trim, wetted keel and wetted chine length.
- C: Y_v without the C_V^2 factor
- D: The simulation but with the fixed value of $Y'_v = -0.1$ following the captive-CFD linear coefficients from [43].

The result of this comparison is presented in Figure 5.3 on the next page, where the dotted black line is the digitised CFD data from [43], the orange line is case A, the green line is case B, the purple line is case C, and the red line is case D.

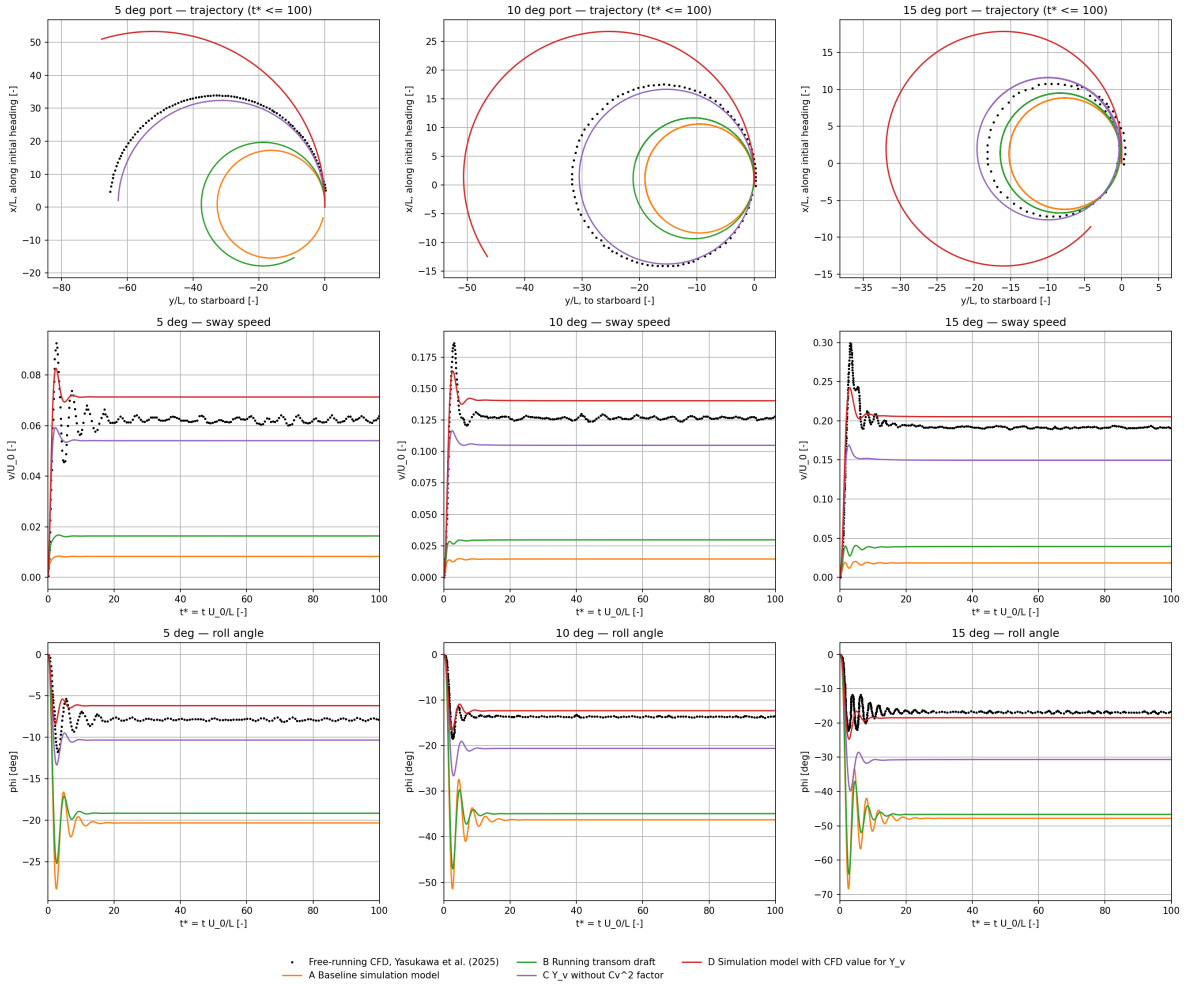

Figure 5.3: Running attitude test for GPPH for 4 cases: A baseline = start model, B= running transom draft calculated with T_transom = L_K*sin(trim), C = Y_v without Cv2, D= Y_v with captive-CFD data from [43].

Looking at the results for various steering angles, it can be seen that Y'_v controls the vessel's drift and heel. With the CFD order of magnitude for this coefficient (case D), both come close to the digitised captive-CFD data. However, a large deviation remains visible in the trajectory plot. By incorporating the running attitude (case B), the heel over-prediction is significantly reduced, thereby stabilising the trajectory plots. This plot demonstrates that incorporating dynamic sinkage and trim (i.e., running attitude) is critical to the manoeuvring simulation of planing-hull hydrodynamic models. The running attitude addition was also tested for the coefficients, the results of which are presented in Figure 5.4 on the next page.

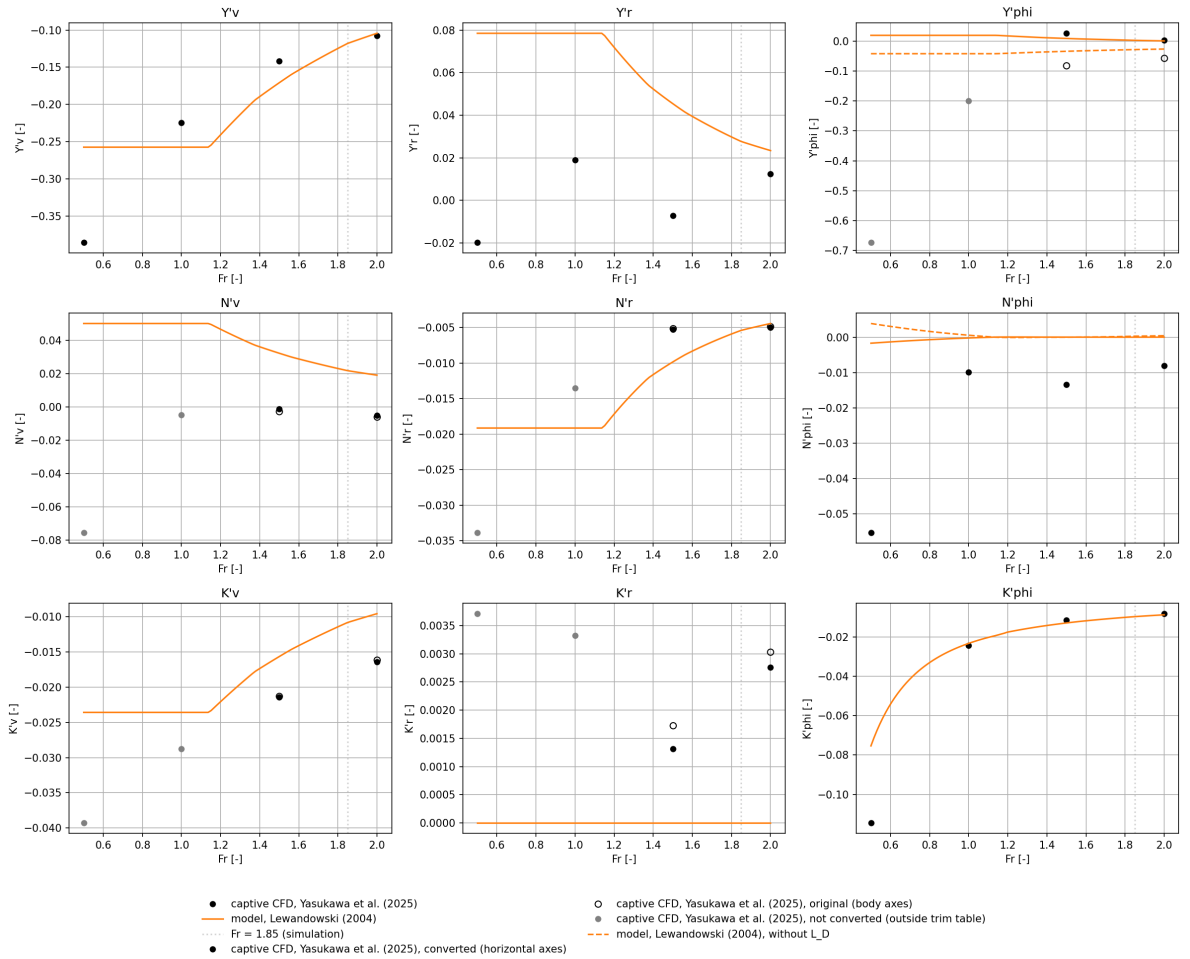

Figure 5.4: Linear hull derivatives for the GPPH-model with running attitude addition, compared to captive-CFD from [43].

Before looking at the results in the plots, an assumption has to be made clear about what these plots are based on. The captive-CFD data points from [43] were presented for the Froude numbers (based on length) of 0.5, 1, 1.5 and 2. However, the running attitude data for the GPPH hull based on towing tank test data presented in [73] was presented for the volumetric Froude numbers of 2.6, 3.13, 3.56, 4.21, 4.69, 5.19, 5.72 (this translates to Froude number based on length between 1.14-2.52 for the model with $L_{PP} = 2.414$m). Therefore, no running attitude data were available below $Fr_L = 1.14$. The assumption was made that, for cases outside the table, the lowest (or highest) values would remain constant. The decision was made to keep the values constant and not extrapolate trends for the wetted geometries, since no data were available on how the wetted geometry changes in the transient region between displacement and planing for this hull.

Comparing Figure 5.4 (where the attitude is fixed at the Fr=1.85 wetted geometry) with Figure 5.2, the influence of the running attitude becomes clearly visible. It shifts the two derivatives that dominate the turning circle, Y_v, K'_v and N_r, onto the captive-CFD and follows the correct speed trend. However, it does not fix the structural differences (N_v sign error and a nearly missing N_ϕ). With the fixed attitude, the coefficients do not depend on speed; with the running attitude, the speed dependence arises from changes in the transom draft and wetted geometry (wetted chine and keel lengths).

It should be noted that there are a few limitations in how the running attitude is implemented in the simulation model. First, the running attitude table describes the straight-ahead run and does not capture the change due to heel during the turn. Second, as mentioned above, below a Froude number of about $Fr_L = 1.14$, the model curves are constant because the running attitude table did not give values for this region.

With the exclusion of the speed coefficient in Y'_v, the addition of the dynamic lift in Y'_ϕ and the addition of the running attitude, a visible improvement can also be seen in the trajectory plots. In Figure 5.5, Figure 5.6 and Figure 5.7 below, the trajectories are presented for the GPPH hull with the gear-case steering model, for a steering angle of $5°, 10°, 15°$ respectively.

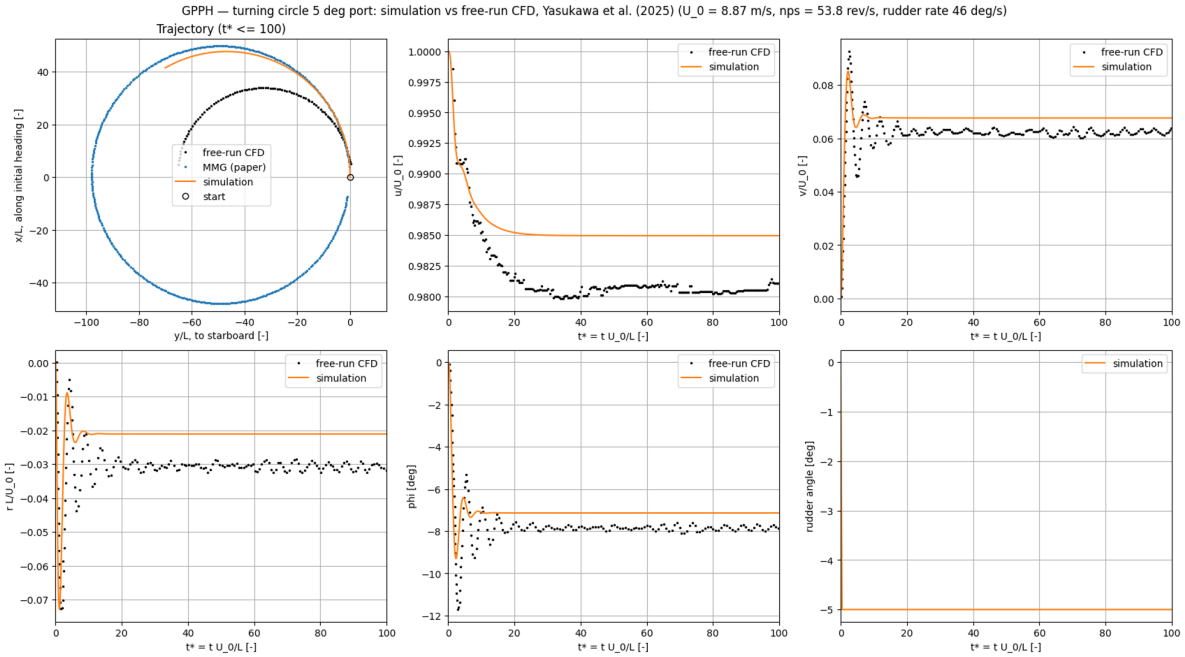

Figure 5.5: Turning circle run for 5deg steering angle GPPH with addition of running attitude and excluding Cv2 for Y_v coefficient, compared to [43].

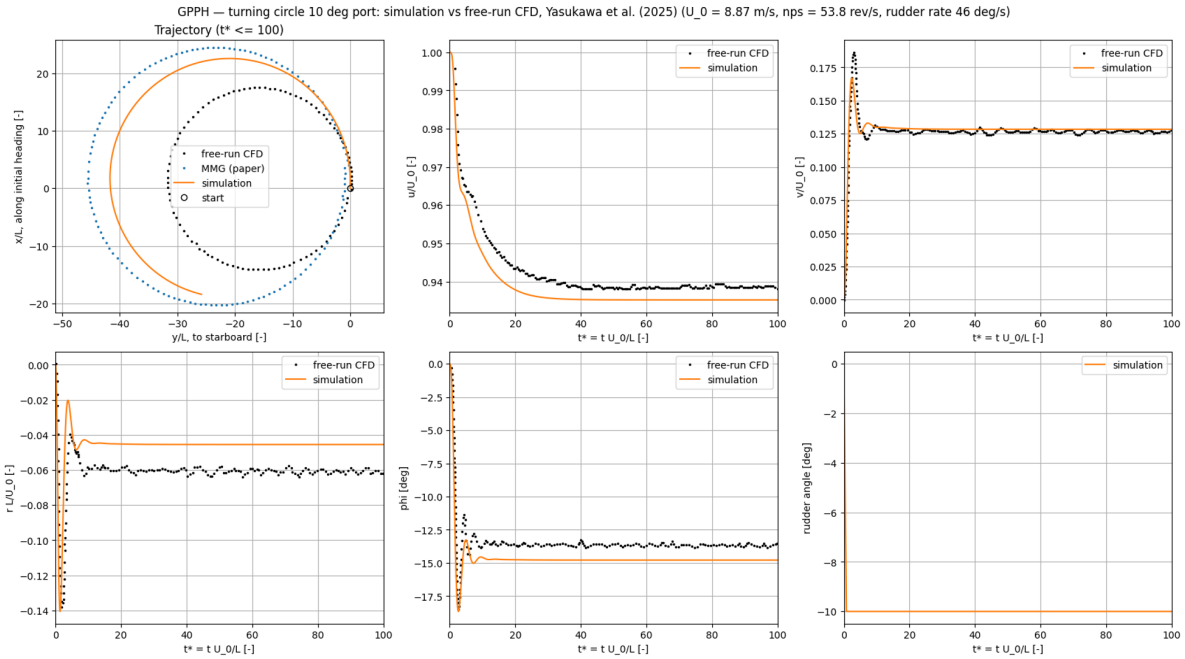

Figure 5.6: Turning circle run for 10deg steering angle GPPH with addition of running attitude and excluding Cv2 for Y_v coefficient, compared to [43].

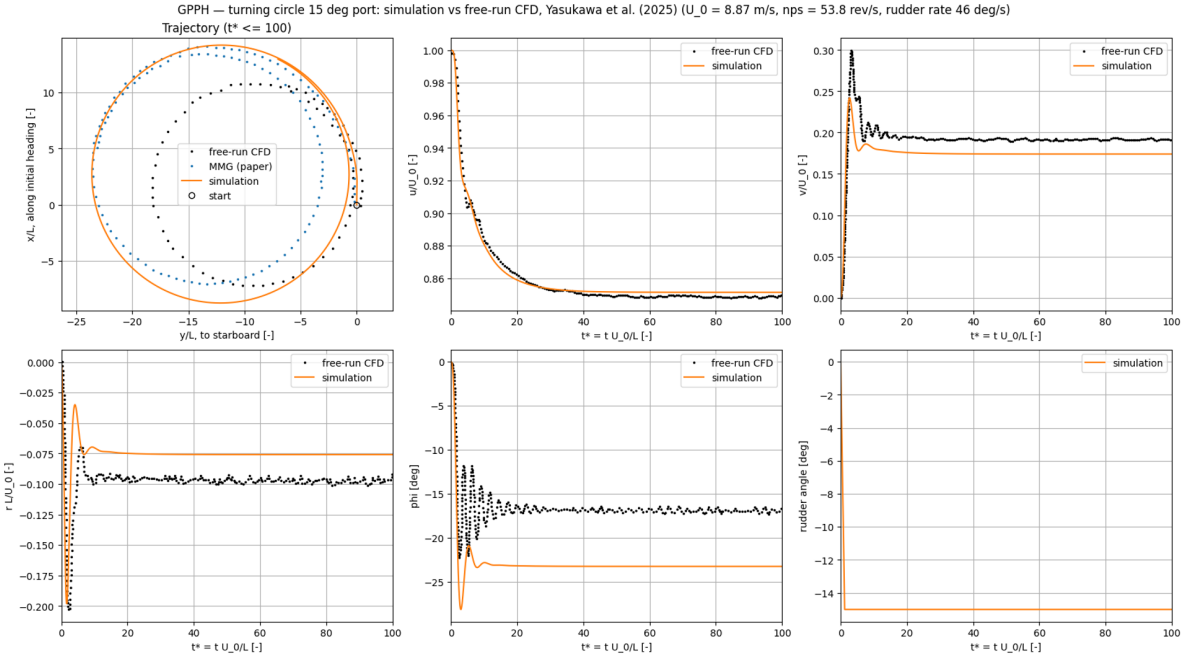

Figure 5.7: Turning circle run for 15deg steering angle GPPH with addition of running attitude and excluding Cv2 for Y_v coefficient, compared to [43].

The turning circle comparison above clearly shows a significant improvement over the trajectories presented at the beginning of this section. However, clear discrepancies remain between the simulation results (orange solid line) and the digitised free-running CFD data (blue and black dotted lines). Below is an analysis to determine the origin of these deviations.

5.1.1. Corrections to the formulations

As the first step in checking the hull force model, a hand calculation was performed for the Lewandowski coefficients. The comparison was done for the various coefficients for which a change was proposed. In the figures below, the results are presented for $Y'_v, N'_r.Y'_\phi$ and N'_ϕ. In the plots, the blue lines are the coefficients calculated as proposed by [5], and the red lines are the changes proposed in this thesis. The solid lines are the fixed running attitude results, and the dotted lines are the running-attitude results. The target values are the CFD data points from [43]. First, in Figure 5.8 below the effect of the proposed change to Y'_v is presented.

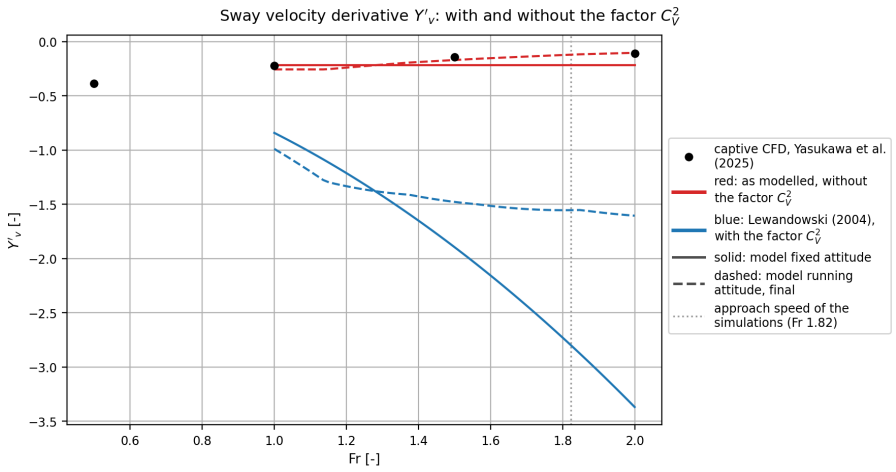

Figure 5.8: Effect of removing the factor C_V^2 from the empirical sway derivative Y'_v of Lewandowski [5], for the fixed attitude (solid) and running attitude (dashed) model, compared with the captive-CFD data points of Yasukawa et al. [43].

As mentioned before in the introduction to this section, it was found that the difference between the Y_v calculated by Lewandowski's empirical hull model and the captive CFD reference points was a factor of Fr_B^2. Remember, the empirical formulation for the sway force due to sway velocity was defined by Lewandowski as: $Y_v = -0.5\rho U B^2 \left[0.6494\,\beta^{0.6}\,T'^2 C_V^2\right]$, where $C_V = U/\sqrt{gB} = Fr_B$. Leaving the factor of C_V^2 out of the formula for the Y_v force shifted it to the right order of magnitude. The addition of the running attitude made it follow the same trend as the CFD points.

Examining the underlying physics showed that the empirical formula is inconsistent with the expected scaling. The sway force due to drift is described as $Y_v v$, and for a given drift angle, the sway velocity v is proportional to U. With the factor C_V^2 included, the empirical formula therefore makes this force scale with U^4. However, the hydrodynamic lift force scales with U^2. Disregarding the speed coefficient C_V restores the expected U^2 scaling and brings the derivative in line with the captive-CFD data.

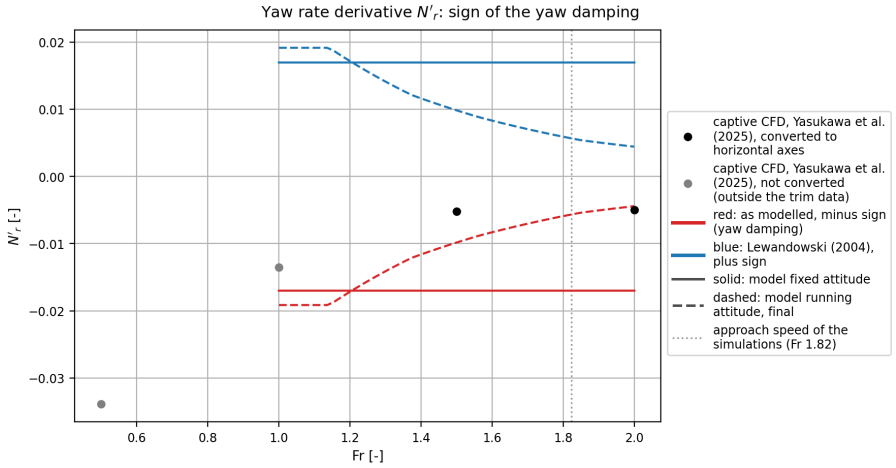

Figure 5.9: Effect of changing the sign from the empirical yaw derivative N'_r of Lewandowski [5], for the fixed attitude (solid) and running attitude (dashed) model, compared with the captive-CFD data points of Yasukawa et al. [43].

A comparison of the hand-calculated N_r from the formulation of Lewandowski [5] with the captive-CFD reference data shows a difference in sign. The empirical formulation of the yaw moment due to yaw rate is given as:$N_r = 0.5\rho U B^3 L \left[73.918\,\beta^{0.6}\,T'^3\right] \left[0.00638 + 6.714\,T'^2/(\tau + 5.28)^2\right]$. All factors in this expression are positive for any physical combination of speed, deadrise angle, draft and trim. The formulation therefore always produces a positive N_r, which means that the yaw moment acts in the same direction as the yaw rate and amplifies the rotation. Physically, however, this moment must oppose the rotation.

As discussed in Section 2.4, for a positive yaw rate the bow moves to starboard and experiences a lateral force to port, while the stern moves to port and experiences a lateral force to starboard; both contributions result in a negative yaw moment. The yaw moment due to yaw rate is therefore a damping moment, and N_r must be negative. A positive value would make the vessel directionally unstable, as the hull would amplify any small yaw rate.

A difference in coordinate system does not explain the difference in sign; the damping derivatives describe a force or moment to the velocity in that same degree of freedom. Therefore, the sign should be the same in any right-handed coordinate system. Neither can it be explained by a sign applied in the equations of motion: in the force equations of Lewandowski [5] (Equation (3.33)), all terms are added together, so the sign of each derivative must be included in the derivative itself. The term $N_r r$ can therefore only oppose the rotation if N_r is negative. Moreover, the other damping and added-mass derivatives in the same formulation, such as Y_v, K_p, $Y_{\dot{v}}$ and $N_{\dot{r}}$, are all given with an explicit minus sign. With the sign corrected, N_r is of the same order of magnitude as the captive-CFD data, and with the addition of the running attitude, it also follows the speed trend of the CFD points.

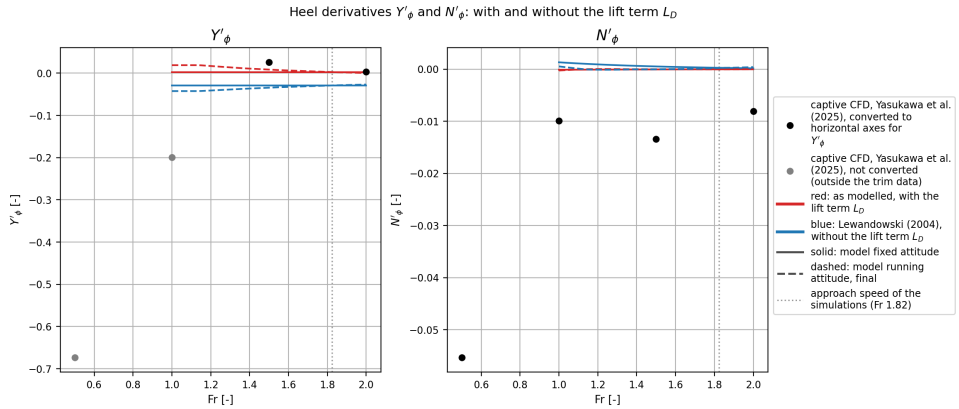

Figure 5.10: Effect of addition of the dynamic lift to the empirical heel derivatives Y'_ϕ and N'_ϕ of Lewandowski [5], for the fixed attitude (solid) and running attitude (dashed) model, compared with the captive-CFD data points of Yasukawa et al. [43].

The addition of the dynamic lift to the Y'_ϕ, N'_ϕ coefficients did not seem to make the coefficients closer to the CFD data points. The plots verify the accuracy of the mathematical implementations and confirm the formulas were implemented as intended. By including the running attitude, the exact shifts in the linear derivatives due to speed-dependent changes in sinkage and trim across Froude numbers become visible. This illustrates the influence of the running attitude on these manoeuvring coefficients.

5.1.2. Analysis of adjusted model

To assess the results of the simulations, a validation criterion was developed based on CFD data presented in [19, 43]. This band is presented in Figure 5.11 below. In the figure, it can be seen that although both papers tested the GPPH hull at the same speeds, the results for different steering angles did not agree. Therefore, both are included to create a reference band for the simulation, with a 10% margin on both ends. The CFD results from [43] diverged at a steering angle of $20°$ and are therefore not included in the reference band. So, Yasukawa et al. only go to $15°$ and only give motions, not forces. Thus, at $20°$ and in the force panels, the band shows only Wang et al.'s value.

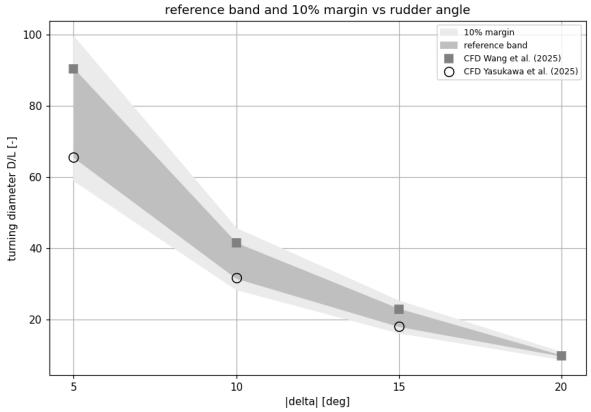

Figure 5.11: Margin for data explained based on two papers presenting CFD data used for comparisons; [19, 43].

Using this reference band, a comparison was made between the simulation using the adjusted empirical hull model and the CFD hull data presented in [43]. The result of this comparison can be found in Figure 5.12. The goal of the comparison was to determine whether the simulation results for the turning circle fall within the reference band when CFD data are used for the hull model, with everything else unchanged. The black line shows the Lewandowski hull model results, and the red line shows the implemented CFD results. The solid lines show the fixed-attitude model, and the dashed lines show the running-attitude model.

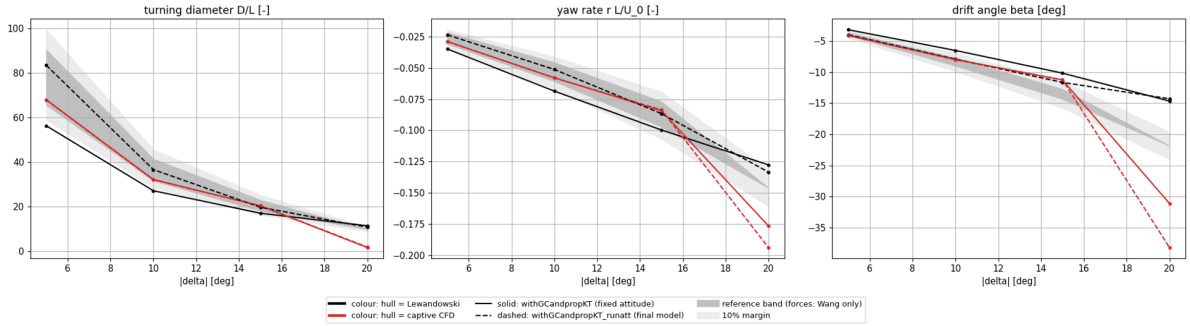

Figure 5.12: Run of the model with CFD hull force values from [43].

The turning diameters for the CFD hull derivatives from [43] fall on the lower side of the reference band, which is consistent with the Yasukawa et al. captive CFD results. The rest of the simulation model therefore produces turning circles of the correct order of magnitude, and most of the differences between the simulation model and the CFD references arise from the empirical hull model. Looking at the plots, the simulation results for the forces seemed to be about 7% off. This triggered an investigation into the formulation of the equations of motion in the simulation model. Lewandowski defined the linear equations of motion as follows [5]:

$$\begin{aligned} X &= m\dot{u} & K &= I_{xx,b}\dot{p} - I_{xz,b}\dot{r} \\ Y &= m(\dot{v} + U_0 r) & M &= I_{yy,b}\dot{q} \\ Z &= m\dot{w} & N &= I_{zz,b}\dot{r} - I_{xz,b}\dot{p} \end{aligned} \tag{5.2}$$

The Y-equation of motion used in the simulation model: $Y = (m_x + m)ur$. Where m_x was assumed to be 7.5% of the total mass m; this led to the conclusion that the hull formulas in the Lewandowski model already contain the added-mass part of the sideways force. By adding it to the Y-equation in the simulation model, it was accounted for twice. The effect is made visible in Figure 5.13 below, where the grey line is the model before, and the blue line is the model after the fix. A clear shift is visible, with the result after the fix falling within the CFD error band.

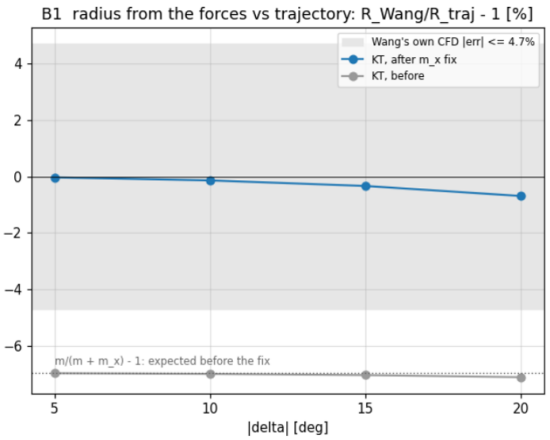

Figure 5.13: Analysis of the equations of motion, bug found: m_x counted double.

A final turning circle validation simulation was run, and the results are presented in Figure 5.14, Figure 5.15 and Figure 5.16 for a $5°, 10°, 15°$ turning circle run, respectively. In the turning-circle plots, the simulation followed the CFD data length. For this final run, the trajectories are plotted for a full circle, shown as dotted lines where the simulation goes outside the recorded CFD data.

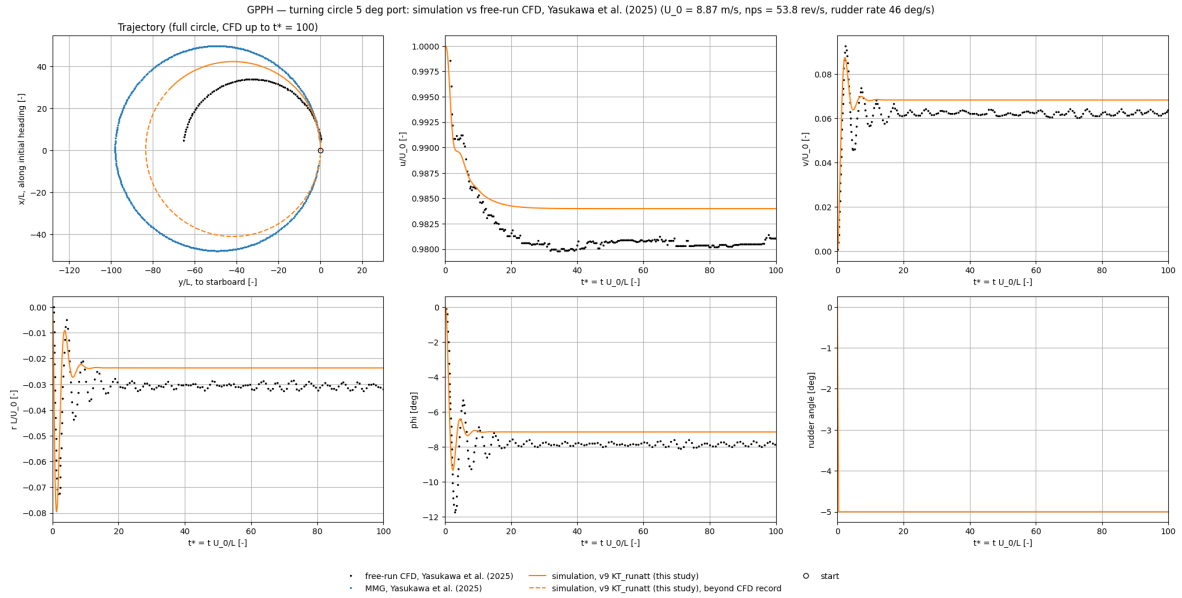

Figure 5.14: Turning circle run with 5deg steering angle for GPPH with final model (no Cv2, running attitude, mx fix), compared with [43] CFD data.

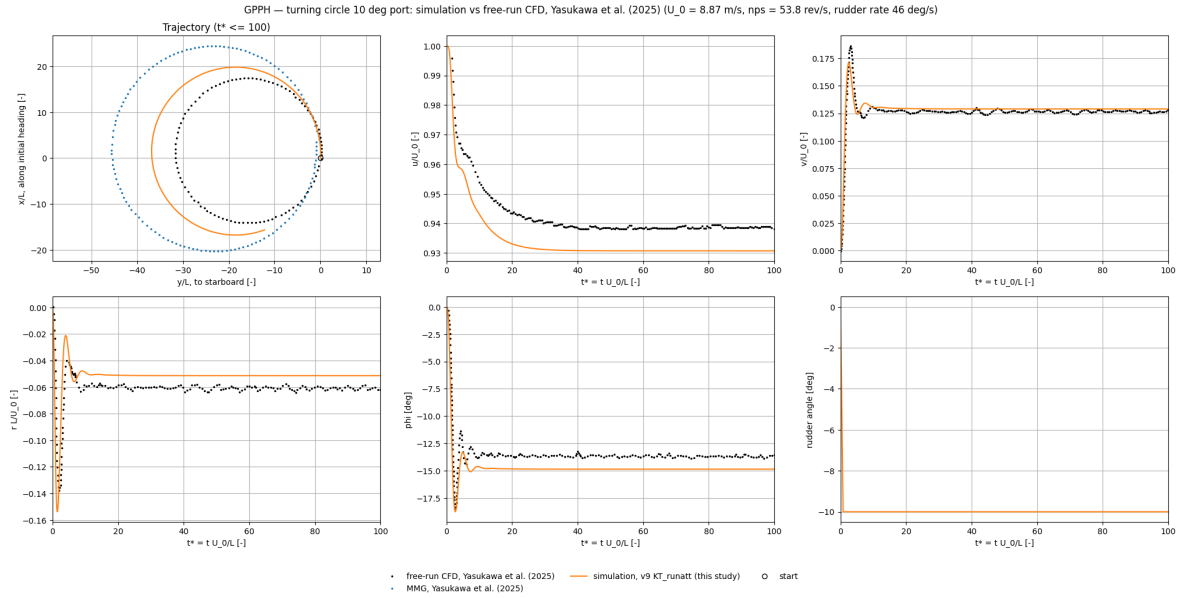

Figure 5.15: Turning circle run with 10deg steering angle for GPPH with final model (no Cv2, running attitude, mx fix), compared with [43] CFD data.

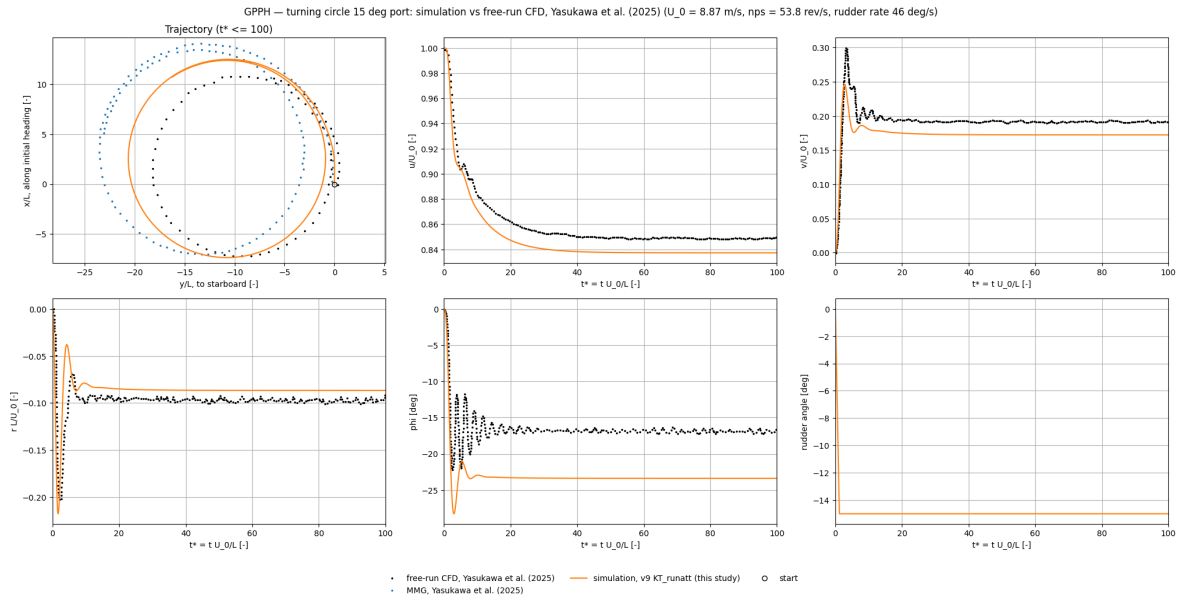

Figure 5.16: Turning circle run with 15deg steering angle for GPPH with final model (no Cv2, running attitude, mx fix), compared with [43] CFD data.

This last turning-circle run for the GPPH hull completes the time-domain validation of the corrected empirical planing hull model. The improvement of the results is visible. Below, the results for the final model are presented, along with the reference band, for the various steering angles.

For this assessment, the reference band remains unchanged; however, additional CFD data points have been added for comparison. The green diamond shapes and the grey cross are CFD data points from [75]. Park presented two different CFD runs; his body-force runs are the same as those used in [19] for comparison. This would add no information and leave the band unchanged. Park's high-fidelity CFD runs use a different gear-case model, which includes two-phase flow and ventilation.

A consequence of this improved gear-case model is that, for higher steering angles, the model turns steadily. In contrast to [19, 43], both experienced spin-out at larger steering angles (indicated with the grey cross in the turning diameter, yaw rate and speed loss panels). Also, the grey vertical line in the turning diameter and yaw rate plot is a spread showing how the result moved with the radius definition. Park writes that for the 20° run, the drift kept oscillating around the steering angle, so the turning circle could not settle. Because of this, the radius depended on how he measured it. Since the current simulation model runs steadily for larger turning circles, the high-fidelity points are added to the comparison to show a trend line.

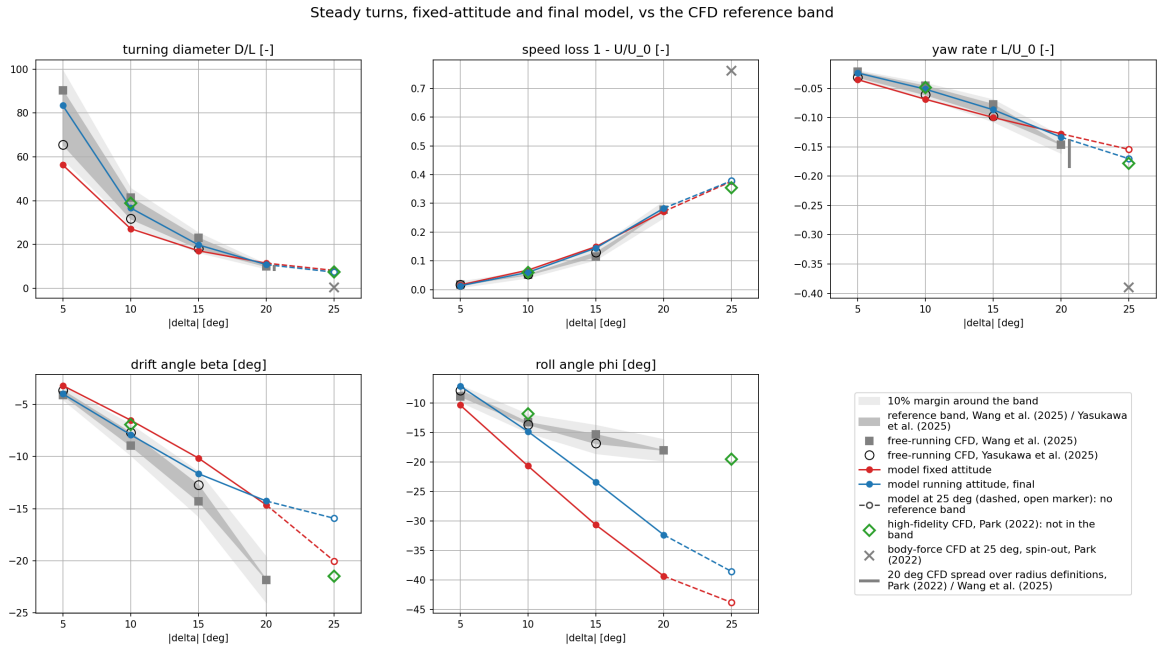

Figure 5.17: Steady-turn validation of the running attitude and fixed attitude model against the CFD reference band of [19, 43].

In Figure 5.17 above, the turning diameter, yaw rate, drift angle, roll angle and speed loss are presented for steering angles between $5° - 25°$. Here, the red lines represent the fixed attitude model, and the blue lines represent the running attitude model, marked with a dotted line outside the reference band region for larger steering angles.

Looking at the turning diameter, the running attitude model falls within the reference band and follows the trend line at higher steering angles. However, the fixed attitude model turns too tight at the $5°, 10°$ steering angles. In the speed-loss plot, both models closely follow the CFD reference band. At $15°$, both are slightly outside the reference band, but compared to the spin-out results, they follow the trend for higher steering angles very closely. The yaw rate is the speed divided by the turning radius, so it follows both and gets the same verdict.

5.1.3. Impact of drift and roll

The plots for the drift and roll angle show different results: both simulation models underpredict the drift and overpredict the heel angle. Looking at the drift angle, the running attitude model falls within the reference band for $5°, 10°$ steering angles, but is underpredicted for larger steering angles. The fixed-attitude model drifts too little at every rudder angle. Although the fixed-attitude model appears to follow the trend of the high-fidelity point better than the running attitude model, this is not a sign of a better model choice. The high-fidelity model uses the improved gear-case model, and the fixed-attitude model reaches this drift angle at a twice-as-high heel angle. Together with the turning diameter being too high at a steering angle of $25°$ (within 8% of the high-fidelity CFD point), this is more a coincidence than proof that the model works better.

The largest deviations are visible in the roll angle plots. Here the running attitude model is within the margin for $5°, 10°$ steering angles, but largely overpredicts at higher steering angles. The fixed attitude model heels too much for every steering angle. Both models keep increasing the roll almost linearly with steering angle, while the CFD data points seem to level off. The running attitude seems to reduce the heel angle but not the plot envelope. Note that the yaw rate and diameter panels look good partly because of the excess heel.

To check whether the drift and heel error is not an input error, the KG and hull restoring coefficient K_ϕ were varied during a simulation run. The results can be found in Figure 5.18, where only the results for the running attitude model are presented. Here, the black line is the baseline run; this is the same result as the plots presented in the previous section. The blue lines show the effect of changing the KG, and the red and orange lines show the effect of changing the roll coefficient.

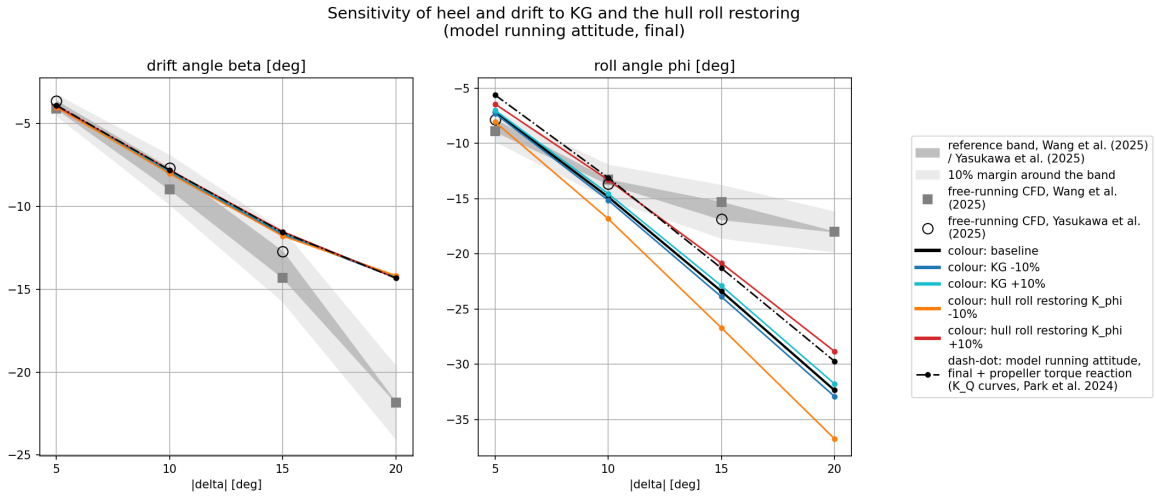

Figure 5.18: Turning circle run for the GPPH for various values of KG and roll restoring coefficient K_ϕ, and the propeller torque reaction addition compared to a baseline run for the running attitude model.

The figure shows that the change in the values of the KG and K_ϕ do not affect the drift. The drift error is thus a separate hull model error. The change in value of the KG influences the results by a very small amount. However, the K_ϕ shifts the results by about $3°$ for the $15°$ steering angle. However, even with this shift, the lines remain straight and leave the reference band after the $10°$ steering angle. A larger restoring coefficient makes the $10°$ result fall inside the reference band, but makes the $5°$ result worse.

The missing propeller torque reaction identified in Figure 4.10 was tested in the same way, shown as the black dash-dot line in the figure above. Adding it to the simulation model, the heel is reduced by $1.6° - 2.6°$ for the tested steering angles, but leaves the drift unchanged. The $5°$ result moves outside the margin, leaving only the $10°$ result close to the reference band. In the same way as the KG and K_ϕ, the torque addition shifts the heel, but does not change the envelope with steering angle. The error in the heel term is therefore structural; a roll term that grows with the turn is missing.

Due to this deviation in roll and drift, the gear-case and propeller forces seem to fall far outside the reference band, as can be seen in Figure 5.19. The forces are presented as a fraction of the vessel's weight. Although the plots below seem to show a large deviation in the propeller and gear-case side force, this is a direct consequence of the heel and drift deviations. The excess in propeller thrust has been explained in section 4.4. All three are calculated with the instantaneous inflow speed to the propeller or rudder, which is a function of the heel and drift angle of the vessel.

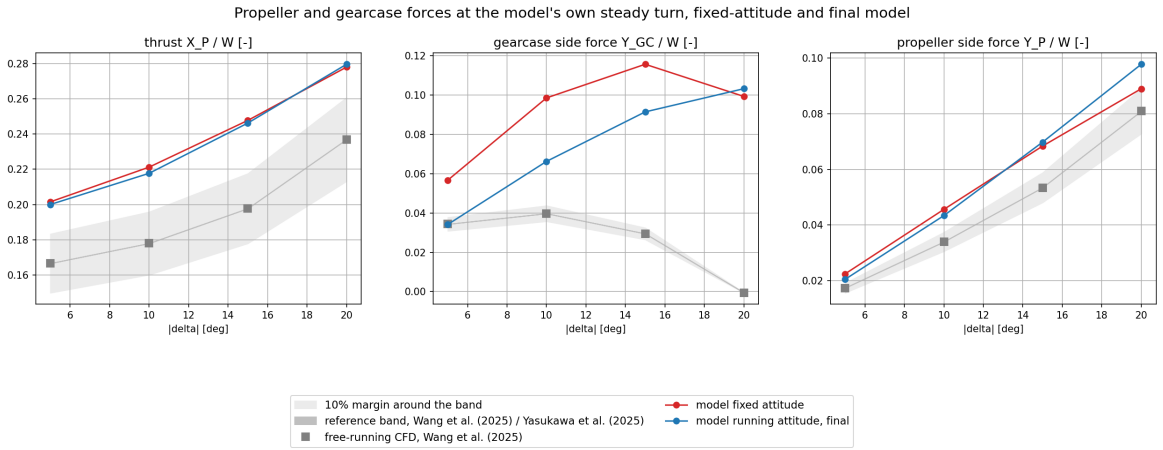

Figure 5.19: Steady-turn validation of forces from the running attitude and fixed attitude model against the CFD reference band of [19, 43].

With the gear-case and propeller analysis presented in Figure 4.10, it was shown that both models do produce the expected values and follow the trend line from the CFD data. In the current figure, the simulation was run with the model's own forces, so the gear-force and propeller models inherit every deviation in the simulation.

The observations for the over-prediction of the heel angle led to a comparison of the net hull roll moment for various cases. In Figure 5.20 the results of this analysis are presented. Here, the black column is the free-running CFD forces as presented by [19], the red column is the fixed attitude model, the blue column is the running attitude model, and the orange column is the fixed & running attitude model with the captive CFD derivatives from [43]. The results in the last case (orange columns) are the same for the fixed and running attitude, as the hull derivatives are replaced by the CFD data. Every bar is the hull roll moment computed at the CFD steady turn: i.e. speed, drift, yaw rate and heel at each steering angle come from [19]. All models are put in the same state, so the differences between columns come only from the hull formulas.

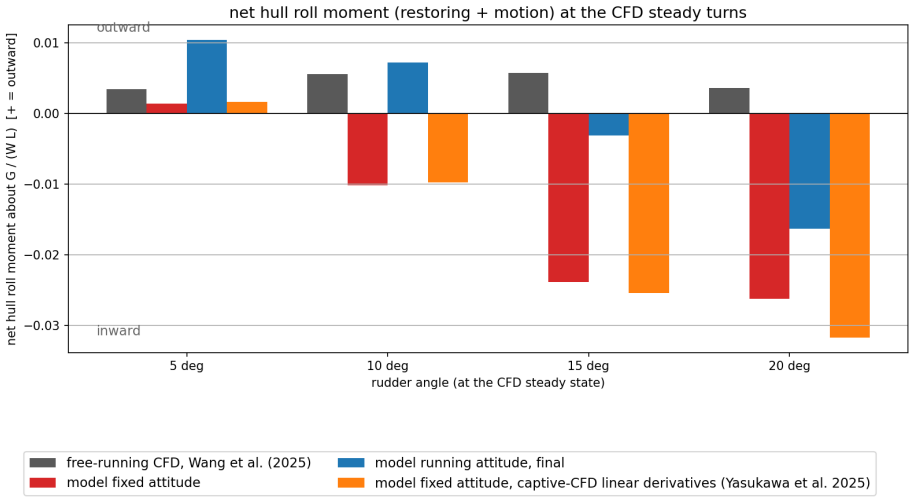

Figure 5.20: Net hull roll moment of the GPPH hull in the CFD state

When comparing the CFD columns (black) with the simulation model results, a clear difference becomes visible; in the CFD run, the hull pushes the vessel outward and balances the steering forces, while in the fixed attitude model it pushes inward from 10 to 15 degrees in the same direction as the steering forces. The running attitude model pushes more outward than the CFD for steering angles of $5° - 10°$

and inward for $15°$ and larger steering angles. The linear simulation model predicts an inward net roll moment, whereas the free-running CFD shows a net outward moment. This explains the physical moment imbalance which caused the roll angle discrepancies at larger steering angles.

The orange and red columns show almost the same result. With the CFD linear coefficients (orange), the hull still pushes inward from $10°$, following the same trend as the Lewandowski hull (red). So the outward roll moment of the CFD hull is not captured by the linear derivatives. Also, looking at the simulation results, a linear trend is visible, compared to the free-running CFD results (black), which show a non-linear trend. This gives a strong indication that a non-linear coefficient is missing.

A similar comparison analysis was performed for the drift angle; Figure 5.21 presents the results. Here, the orange line is the run of the simulation model with the captive-CFD linear derivatives from [43], the fixed attitude, and running attitude overlap for the same reason as above. The orange crosses show the spin-out behaviour the CFD hull exhibits; by substituting these values into the simulation model, the spin-out happens as well.

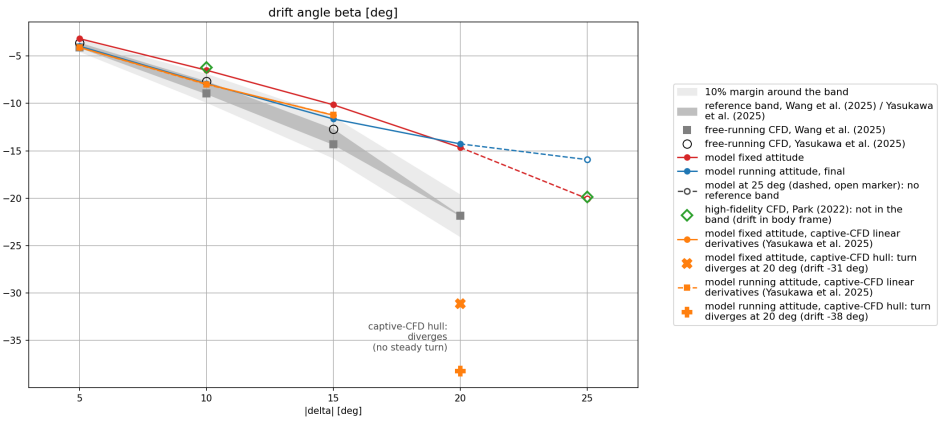

Figure 5.21: Drift angle of model with captive CFD input from [43].

The addition of the orange line to this plot shows that with the CFD hull, the vessel in the simulation model experiences the same drift as the running attitude model (blue line). At $15°$, the drift is under-predicted by the same order of magnitude as the attitude model. This shows that the drift deficit for $15°$ steering angle and above is not specific to the Lewandowski hull model; the linear CFD derivatives show a similar result.

In the simulation leading to the results presented with the orange line, only the hull formulas were changed while keeping everything else the same. This separates the effect of the hull formulas from the rest of the model. With the captive-CFD derivatives, the drift under prediction remains at a $15°$ steering angle. This indicates that it is not a specific deficit of the Lewandowski hull model, as it does not disappear with a different hull configuration. This points to a non-linear effect at large drift angles, which is not taken into account in both linear hull models. Based on these observations, a non-linear coefficient sweep has been performed, and the results are presented in the following section.

5.1.4. Assessment of the final model against free-running CFD data for the GPPH

As a last step in the validation of the GPPH model, the trajectories are also plotted. The results of the turning circle run can be found in Figure 5.22 on the next page. Here, the dotted black and grey lines are the free-running CFD trajectory results of [30, 43], respectively. The red line shows the result of the fixed attitude model and the blue line the results of the running attitude model. The simulations were run for a full turning circle, showing the trajectories with a dotted line outside the digitised recorded CFD data.

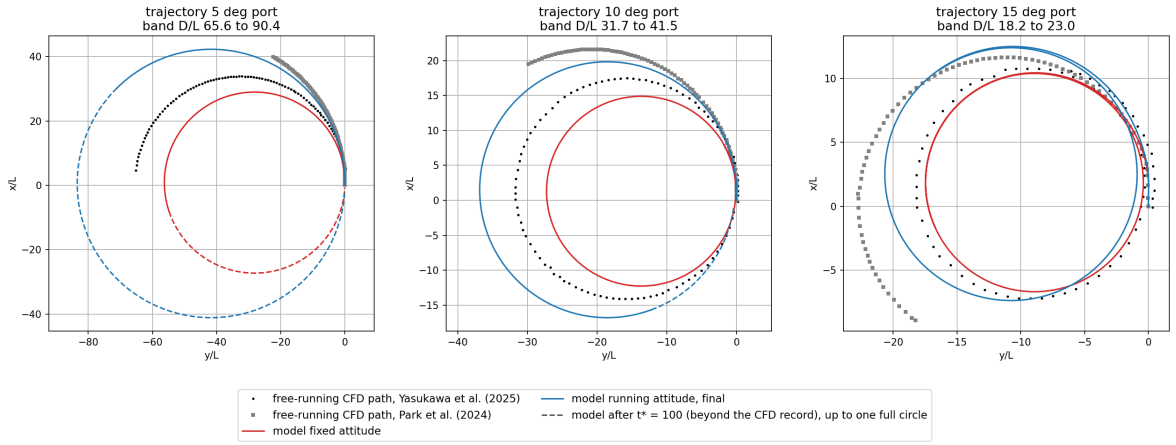

Figure 5.22: Steady-turn validation of the trajectories from the running attitude and fixed attitude model against the CFD reference band of [30, 43].

Before looking at the simulation results, it should be noted that the two CFD trajectories do not agree with each other. This creates a reference band as well for the trajectory simulations. Comparing the three figures, it becomes clear that the running attitude model falls within the reference band for all turning circles, while the fixed attitude model turns visibly tighter. From both reference papers, there are no usable reference data for larger steering angles, as both experience a spin-out. It should be noted that the current model does work for larger steering angles and keeps a stable turning circle, as is shown in Table 5.4.

In the tables below, the results in figures from the final simulation run are presented. For all parameters presented, it is indicated whether the result fell inside or outside the reference band or in the margin. The results are presented for both the fixed attitude model (Table 5.2) and running attitude model (Table 5.3). Since a comparison is made using the reference band, only the results for the $5°, 10°$ and $15°$ steering angles are presented with the verdict on their result compared to the reference band. In Table 5.4 the results for the $20°$ and $25°$ are presented with metrics only.

Table 5.2: Steady-turn validation of the fixed attitude against the CFD reference band of Wang et al. (2025) and Yasukawa et al. (2025). Inside = inside reference band, Margin = within 10% of the band edge (both sides), Outside = outside reference band.

		5°		10°		15°	
Quantity		value	verdict	value	verdict	value	verdict
Turning diameter	D/L	56.3	Outside	27.2	Outside	17.1	Margin
Yaw rate	rL/U_0	-0.0350	Outside	-0.0686	Outside	-0.0997	Margin
Drift angle	β [deg]	-3.2	Outside	-6.5	Outside	-10.1	Outside
Heel angle	ϕ [deg]	-10.4	Outside	-20.7	Outside	-30.7	Outside
Speed loss	$1 - U/U_0$	0.016	Margin	0.068	Outside	0.149	Outside

Table 5.3: Steady-turn validation of the final model (running attitude) against the CFD reference band of Wang et al. (2025) and Yasukawa et al. (2025). Inside = inside reference band, Margin = within 10% of the band edge (both sides), Outside = outside reference band.

		5°		10°		15°	
Quantity		value	verdict	value	verdict	value	verdict
Turning diameter	D/L	83.4	Inside	36.6	Inside	19.8	Inside
Yaw rate	rL/U_0	-0.0236	Inside	-0.0513	Inside	-0.0866	Inside
Drift angle	β [deg]	-4.0	Inside	-7.9	Inside	-11.6	Margin
Heel angle	ϕ [deg]	-7.2	Margin	-14.8	Margin	-23.4	Outside
Speed loss	$1 - U/U_0$	0.013	Margin	0.060	Margin	0.145	Outside

Table 5.4: Steady-turn results at 20° and 25° of the fixed attitude and running attitude models.

Quantity		Fixed attitude model		Running attitude model	
		20°	25°	20°	25°
Turning diameter	D/L	11.4	8.1	10.8	7.3
Yaw rate	rL/U_0	−0.1275	−0.1542	−0.1333	−0.1701
Drift angle	β [deg]	−14.6	−20.0	−14.3	−15.9
Heel angle	ϕ [deg]	−39.3	−43.8	−32.3	−38.6
Speed loss	$1 - U/U_0$	0.272	0.377	0.283	0.379
Thrust	X_P/W	0.2779	0.2936	0.2795	0.2897
Gear-case side force	Y_{GC}/W	0.0993	0.0756	0.1033	0.1066
Propeller side force	Y_P/W	0.0890	0.1086	0.0978	0.1200

5.2. Sensitivity study non-linear coefficients planing model

The analysis of the roll and drift deviations between the simulation results and the free-running CFD hull force data, presented in Figure 5.20 and Figure 5.21, indicated that a non-linear term is missing in the hull model. A sensitivity study was performed to find which single non-linear hull term supplies the missing force compared with the CFD results from [19, 75].

In this study, the hydrodynamic manoeuvring coefficients from the MMG polynomial force functions have been used as the test objects (Equation 3.11 - 3.13). For this, the hull force data presented in [19, 75] were used, minus the hull force from the simulation model. The sweep was performed for steering angles of $5°, 10°, 15°$, for which the CFD data showed steady turns. The $20°$ term is added to the plots for comparison, but is left out for the fit. The check was performed for one term at a time, as there are only three fit points per direction ($5°, 10°, 15°$); it cannot be determined reliably for more than one coefficient. The criterion for a term to fit was: if the coefficient can consistently fill the gap, it has the same value at every angle, so the spread (largest over smallest per-angle coefficient) should be close to 1. The linear coefficients are added as well to see whether the error is possibly in these coefficients. If a wrong linear coefficient causes the gap between the CFD data and the simulation results, it would grow proportionally to v', r' or ϕ. The per-angle coefficient would be equal for that linear term.

Below, the results are presented for the GPPH hull. The sweep was performed for the sway, roll and yaw motion, presented in this order as well. The plots should be interpreted in the following way: points close to the line at 1 mean consistent results for all steering angles tested. In the column on the right, the bold text marks the term with the lowest spread in that panel. The comment 'sign change' means no single term can fit, because the angles need coefficients of opposite sign. This becomes visible in the plots with markers on both sides of the vertical zero line.

Here, the c is the fitted (non-dimensional) value of the coefficient in that row (for all steering angles combined), showing the value that term needs in the polynomial to supply the missing hull force. It is computed using the missing hull force (CFD hull force minus simulation model hull force) for three angles (d^*) and the tested term in that row at the same time states (t), to find the single value that makes $c \cdot t$ fit d^* best at all three angles: $c = \frac{\Sigma(td^*)}{\Sigma(t^2)}$. Adding the c to the model would therefore make the hull force of the simulation model match the CFD hull force at that state as closely as one coefficient allows. Each marker is the single-fit coefficient ($c_i = d_i^*/t_i$) divided by the value of c. A best fit can be found for every term, so c on its own cannot say whether a term is the right fit. The spread (largest c_i over smallest c_i) shows whether one c can fit all angles, making the spread the real criterion. In the linear coefficient rows, the c is a correction on the model's own linear coefficient, not the whole coefficient. The values can only be compared within one row since the terms have different sizes. Thus, a large value for c does not mean a term is more important.

The points show the one-angle coefficient at $5°, 10°, 15°$, divided by the fitted coefficient; thus, a perfect term has three points on the vertical line at 1. The first panel presents the fixed attitude model, the second the running attitude, and the third the simulation model with the captive-CFD linear hull derivatives from [43]. With the captive-CFD derivatives, the hull forces at the CFD states do not depend on the attitude setting, so this panel applies to both the fixed and running attitude model. The last panel is the control case and tests whether the result depends on Lewandowski's hull model.

5.2.1. GPPH coefficient sweep results

In the three figures below, the results of the sensitivity study for the GPPH hull are presented for the sway, roll and yaw motion analysis, respectively. Surge was not included in the sweep. The surge hull force in straight sailing is always drag and thus stays negative. However, the extra part caused by the turn, the CFD hull force minus the straight-ahead resistance at the same speed, changes sign. Every candidate term in the analysis has to keep one sign. Therefore, a single term cannot be fitted for the surge motion with the current uncertainty in the data.

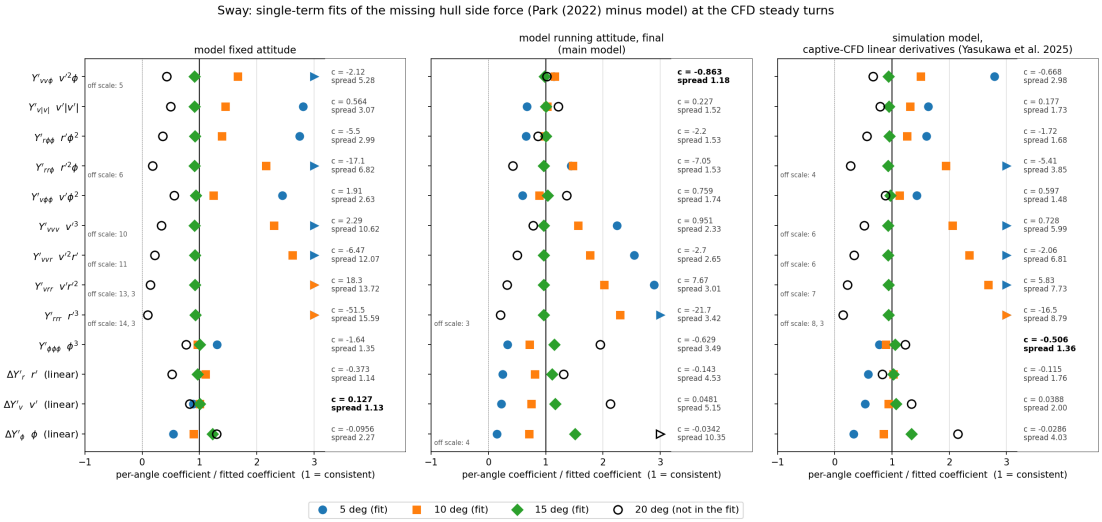

Figure 5.23: Sway coefficient sweep for the GPPH hull.

The fixed attitude and running attitude models differ in the type of sway deviation between the simulation results and the captive-CFD forces. The hull side force in the fixed attitude model (left panel) is about twice the value of the CFD force for every angle. The linear terms $Y'_v v'$ and $Y'_r r'$ fit best, with a spread of 1.13 and 1.14, respectively. Therefore, the error lies in the linear derivative itself, evaluated at one transom draft for all speeds.

In the running attitude model, the transom draft follows the running attitude, creating a side force close to the captive-CFD force at a $5°$ steering angle. Looking at the linear coefficients, it becomes clear that these terms do not describe the growing 'gap' at larger steering angles. Looking at the non-linear terms, $Y'_{vv\phi} v'^2 \phi$ is clearly the most consistent with 1.18 being the spread. Outside the fit, it predicts 0.98 times the gap at $20°$ and 1.01 times the gap at $25°$ compared to [75].

In the captive-CFD panel, the $Y'_{\phi\phi\phi} \phi^3$ and $Y'_{v\phi\phi} v' \phi^2$ fit best, with a spread of 1.36 and 1.48, respectively. The gap tried to be filled with the fitted terms is the CFD results minus the simulation results; it therefore contains both errors in the linear empirical hull model and the missing additional non-linear part. The $v'^2 \phi$ term is the most consistent term for the running attitude model; however, with the linear derivatives, it is not. Part of it could be a correction to the linear empirical Lewandowski hull model rather than a physical effect. With the three steady turns, where drift, yaw and heel grow at the same time, the two cannot be separated.

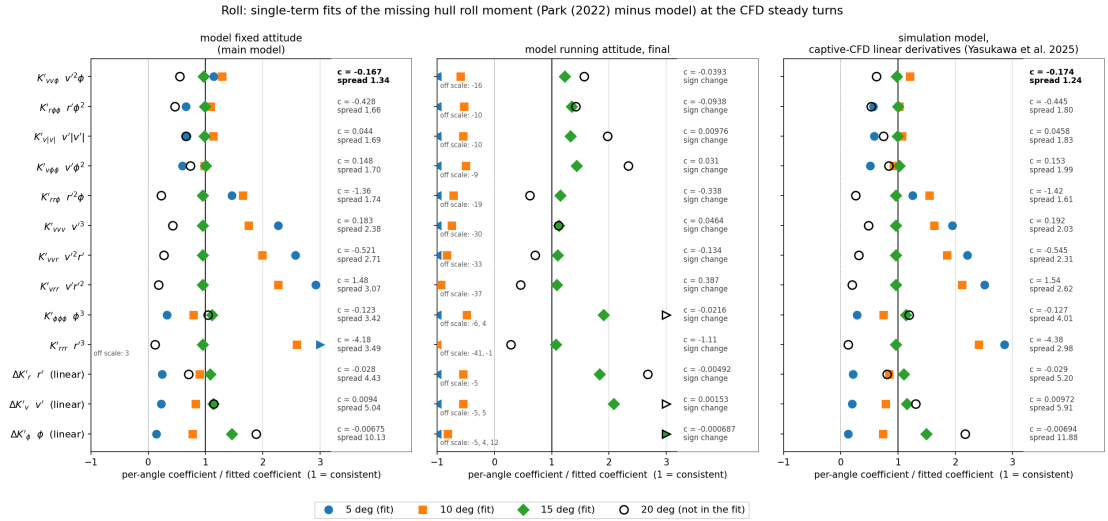

Figure 5.24: Roll coefficient sweep for the GPPH hull.

In the fixed attitude model, the roll moment gap between the simulation model and the captive-CFD data grows with the turn. None of the linear terms follows this trend, so the error is not in a linear roll coefficient. The most consistent term for this model is $K'_{vv\phi}v'^2\phi$, for which 1.34 was the spread. At a steering angle of $20°$, the simulation model predicts the value to be 1.82 times the gap, where the captive-CFD data run is not fully steady [75]. In the captive-CFD panel, the same coefficient is the most consistent (with a spread of 1.24); thus, this result does not depend on Lewandowski's empirical hull model.

In the running attitude model, the gap changes sign for different steering angles; the model hull roll moment is too far outward at $5° - 10°$ and too far inward at $15° - 20°$. Therefore, every coefficient fit has a sign change between the different tested steering angles, leaving no single fit coefficient for this model. The running attitude changes the shape of the roll gap, but does not remove it (see Figure 5.20).

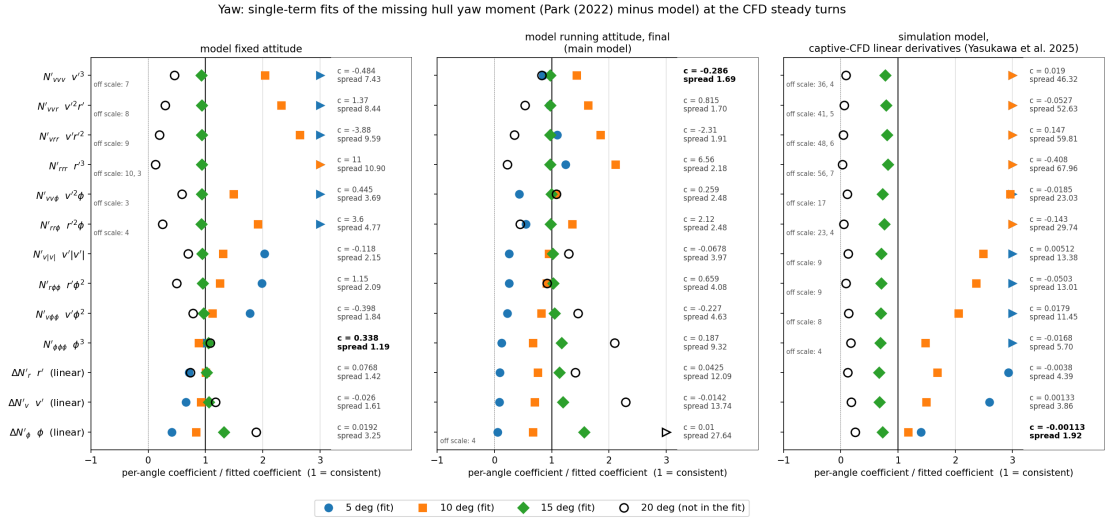

Figure 5.25: Yaw coefficient sweep for the GPPH hull.

The yaw sweep does not identify a missing term. For the running attitude model, the yaw moment gap is almost zero at $5°$ and grows only slightly for larger steering angles. The lowest spread for this model was found at the $N'_{vvv}v'^3$ and $N'_{vvr}v'^2r'$ terms with spreads of 1.69 and 1.70, respectively. The $N'_{vv\phi}v'^2\phi$

term fits the three angles with a small error and predicts even 20° well, but has a large spread (2.48) because the gap of the 5° angle is computed from a gap close to zero.

The fixed attitude model has a larger gap at all angles and points to the $N'_{\phi\phi\phi}\phi^3$ term. This term was not included in the model presented in [43]. The linear CFD derivatives describe the yaw moment with a small gap of about 10% of the hull forces. The large spreads in the panel show that almost no gap is left to fit, and that the linear derivatives already represent the yaw moment without any non-linear additions.

Summarising, the surge and yaw runs for the running attitude model were inconclusive for a single-term fit. The sway motion run showed that for the running attitude model the $Y_{vv\phi}v^2\phi$ term was the most consistent. In the fixed attitude model, the sway-fit pointed towards an error in the $Y'_v v'$ term, which was largely removed with the addition of the running attitude. In the roll motion run, the running attitude changes the sign between 5° and 15° steering angle, so no single term-fit was found as well. However, the fixed attitude model pointed towards the $K'_{vv\phi}v'^2\phi$ term. This addition to the running-attitude model reduced the heel at $15^\circ - 20^\circ$, but made it worse for a 5° steering angle. When using the larger fitted coefficient from the fixed attitude model in the running attitude model, the heel at $15^\circ - 20^\circ$ shifts within the margin, but at $5^\circ - 10^\circ$ the heel becomes too small, and drift gets worse.

As mentioned before, the so-called gap is the difference between the captive-CFD hull forces and the empirical forces. Thus containing both a possible error in Lewandowski's linear derivatives and the missing non-linear part. The sweep is not able to tell these two contributions apart; it finds the coefficient best representing the gap. The third panel is added to remove the possible error in the empirical hull formulae as much as possible. For roll, the $K'_{vv\phi}v'^2\phi$ is also the best term in the third panel.

It should be noted that adding all fitted terms to the final model will not make the simulation match the CFD data more closely. For one, the coefficients are fitted to fill the same gap. In a steady turn, the sway speed, yaw rate and roll grow together; thus, the coefficients coupling these motions will look almost the same over the tested steering angles. Each coefficient alone already accounts for the gap; adding them together would multiply this. Next, with three data points and a multiple-coefficient fit, it would create a near-exact construction of the data. This proves nothing physically, as it will also compensate for possible mistakes in the model. The coefficients can become very large with opposite signs. Therefore, a larger database would be necessary to create a multiple-coefficient fit that works.

To check the impact of the addition of these non-linear coefficients, the simulation model was run including the fitted terms. The sway motion with the fitted term for the $5^\circ - 15^\circ$ steering angle predicts the missing side force of the steady high-fidelity turn for a 25° steering angle [75]. With the addition of the $K'_{vv\phi}v'^2\phi$ term to the roll motion, the heel of the fixed-attitude model shifts close to the reference band, removing the excess heel while drift is not affected. The heel remains about 2° outside the reference band because the term only closes the gap in the hull part of the roll moment. Therefore, the remaining heel deviation is not caused only by the hull. At the CFD steady turns, the propeller roll moment of the model is more inward (0.003-0.0058WL) than the free-running CFD from [19].

The difference was mainly attributed to the propeller torque reaction, which was not included in the propeller model. Adding the propeller torque (0.0033-0.0043WL) to the propeller model closes the gap almost completely for steering angles of $5^\circ - 10^\circ$ and for about 75% at $15^\circ - 20^\circ$ steering angles. Adding both the propeller torque and the newly fitted non-linear roll term (with a value of $K'_{vv\phi} = -0.179$), the heel of the fixed attitude shifts close to the reference band at 5°, within the margin at $15^\circ, 20^\circ$ and outside for 10° steering angle. The 20° result lies within 1° of the high-fidelity CFD results. The heel deviation of the fixed attitude model can therefore be traced back to both a non-linear hull term and the propeller torque reaction.

For the running attitude model, no single term can close the gap, because it changes sign. Adding the $K'_{vv\phi}v'^2\phi$ term improves the heel at $10^\circ - 20^\circ$, but makes it worse at 5° and degrades the turning diameter. The drift is shifted inside the reference band for $5^\circ - 10^\circ$ steering angles with the additional yaw-term; however, the vessel spins out with a larger steering angle. This additional term puts the model at the CFD state, but does not affect the drift slope and thus its stability.

5.3. Sea trial data analysis - Pilot vessel

With the adjusted Lewandowski hull model, the pilot vessel could be simulated. For these simulations, the sea trial dataset was used as comparison data. In Section 2.5 the performed sea trial manoeuvres are presented. Below, in Figure 5.26 and 5.27, an overview of the turning circle trajectories and zigzag headings is presented, comparing the sea trial data (black dotted lines) with the simulation results (orange solid lines). The manoeuvres were performed for three engine settings (800, 1400, 2050rpm). The turning circles are presented for steering angles of $10, 20, 30°$ and the zigzags for $10 - 10°$ and $20 - 20°$ steering angles. To make a fair comparison, the simulation results plotted in the graphs are run with the speed and propeller settings as measured during the sea trials.

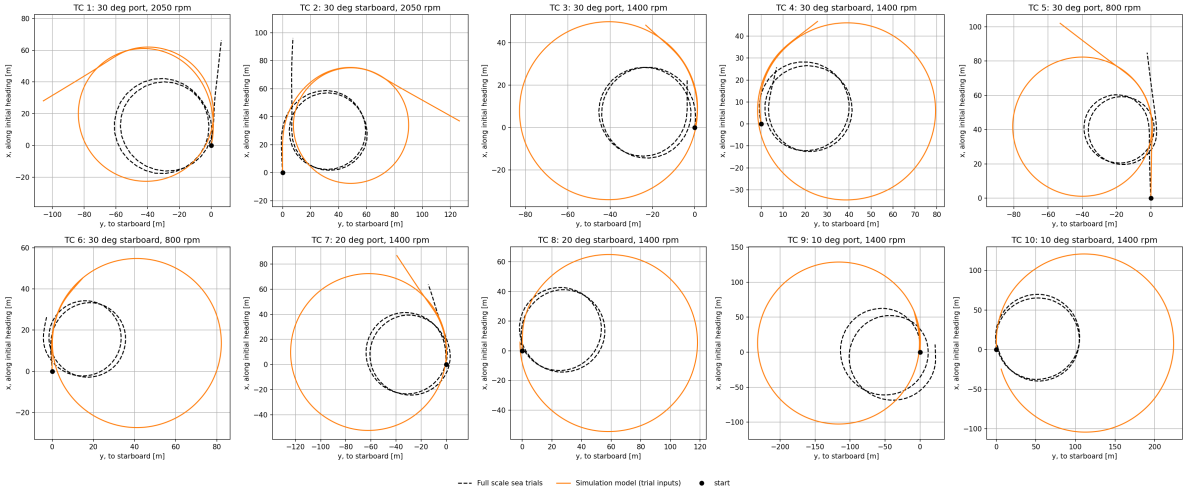

Figure 5.26: Overview of turning circle simulations together with the sea trial data of the pilot vessel, run with the velocity and propeller rpm as measured during the trials.

As can be seen in the turning circle comparison (and in the zigzag as well), not every measurement during the sea trial started at the same time. The simulation was set to start at the same turning instant. In the zigzag plots below, the black striped lines are the sea trial results, and the solid orange lines are the simulation results. The grey dotted lines are the steering angles performed by the rudders.

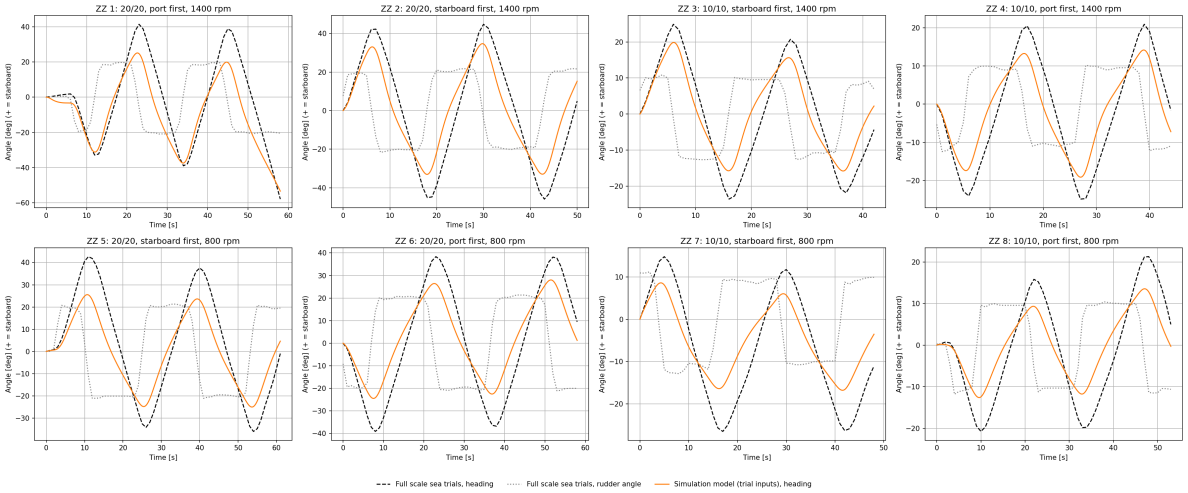

Figure 5.27: Overview of zigzag simulations together with the sea trial data of the pilot vessel, run with the velocity and propeller rpm as measured during the trials

The results of the sea trial manoeuvres vary between different measurements; even a starboard and port-side turn with the same steering and engine setting differ. This offered the opportunity to create a reference band for the pilot vessel as well. For the reference band, 10 turning circles and 4 spiral tests are used, corrected for current. From both, only the steady part is used. All turns are mirrored to starboard, each value matched to a steering angle and engine setting. This results in 20 contributions at 800rpm, 29 at 1400 rpm, and 2 at 2050rpm, again with a margin of 10% on each side.

The spread per engine setting of the comparison data is also clearly visible in Figure 5.28 on the next page. It should be noted that the reference band does not show measurement uncertainty; it is created per rudder angle using the min-max spread between all contributions available for that engine setting. This approach is sensitive to outliers (e.g. 1400rpm with 35° steering angle), so it should be used as an indication rather than a specific target.

The results for the turning diameter, speed loss, yaw rate, drift angle and roll angle are presented in Figure 5.28 on the next page. Both the fixed attitude (red lines) and the running attitude (blue lines) results are presented. It can be seen that neither model produces the sea trial data exactly. However, the running attitude model nears the sea trial data much more closely for all cases presented. Looking at the turning diameter, the fixed attitude model differs by a maximum of about seven times the trial results.

In contrast, the running attitude model differs by a maximum of about two times. The speed loss is underpredicted by both models, but stays within 3% of the trial straight-line speeds. Therefore, the large differences above do not come from a wrong starting speed. The yaw rate follows the trends of the turning diameter and speed loss.

The drift angle clearly separates both models. The fixed attitude model predicts a drift angle of about $1 - 4^\circ$, whereas the running attitude model follows the sea trial results for the 800rpm and 1400rpm. Both models heel too much into the turn compared to the roll angles measured during sea trials. This behaviour is visible with all three engine settings, and the difference grows with speed. In the trials, the heel is small and its sign changes with speed. Comparing steering angles of 30°, for the lower speeds where the vessel operates in the displacement region, an outward heel angle is visible.

In contrast, for the higher engine setting, an inward heel angle is measured. Both simulation models heel inward and grow steadily with both rudder angle and speed. The running attitude model reduces the heel by about 2.5-5 times the fixed attitude model, but the heel is still too large.

With the 800 and 1400rpm engine settings, the vessel behaves comparably; the turning diameter relative to ship length is about the same size. With an engine setting of 2050rpm, the diameter is about 1.4times wider, the yaw rate is about 30% lower and heel changes sign. The speed loss does not seem to follow a steady trend; the lowest loss is at 1400rpm. However, for the 2050rpm there is not enough data to make a fair comparison.

Looking at steering angles of 30°, it seems that the 2050rpm engine setting comes closest to the sea trial data. With this engine setting, the vessel has an approach speed of $17.7\mathrm{kn}$ ($= 9.10\mathrm{m\,s^{-1}}$) and is (at the start of the turn) operating at a Froude number of about $Fr_L = 0.9, Fr_\nabla = 1.9$. Compare this value to the planing threshold as defined in the literature study based on [8, 15] of a Froude number of $Fr \geq 1.0 - 1.2$. Therefore, in the high-speed sea trial run, the pilot vessel is not operating in the fully planing region, but just slightly below it in the semi-planing region.

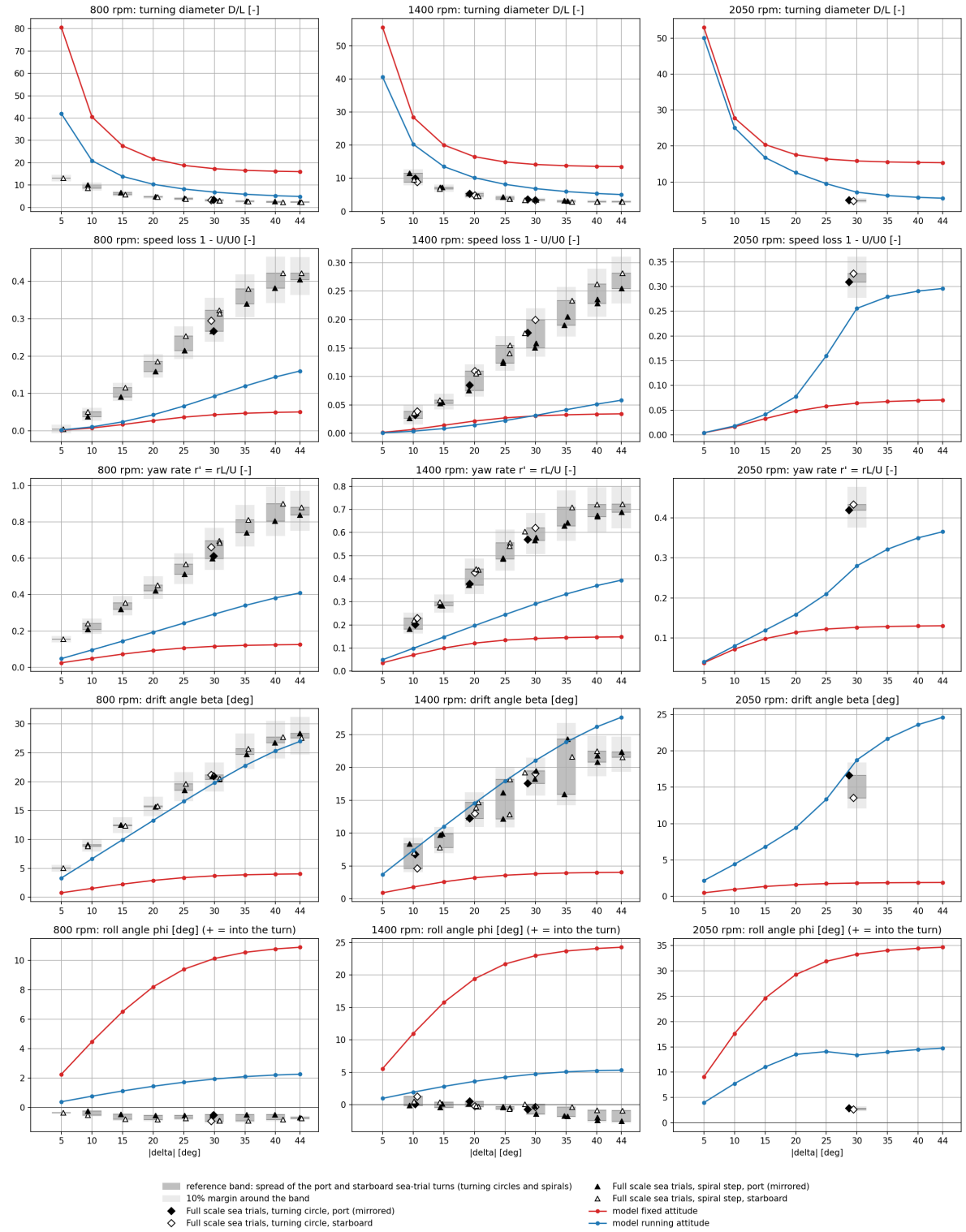

Figure 5.28: Steady-turn validation of the running attitude and fixed attitude model against the sea trial data, results presented for various steering angles.

This observation led to Figure 5.29, where the same five parameters are presented, only this time compared with speed. Only the $30°$ steering angle turning circle was performed for all three engine settings. For each approach speed from the trials, the simulation is run for both the fixed (red columns) and running attitude (blue columns) models. With a higher rpm, the vessel rotates faster while sailing faster. Going from 1400-2050rpm the speed rises about 50%, while the yaw rate only rises about 10%. This results in a drop in r' and an increase in D/L. Between 800-1400rpm the r' and D/L stay about the same, while the turning rate rises with the speed.

For the turning diameter and the yaw rate, both models are clearly off; however, the running attitude model does follow the trend with speed. In the speed loss graph, a clear dip becomes visible in both the trials and the running attitude model. The drift angle in the trials declines with more speed, but in the simulation model this trend is not followed. In the roll panel, the sign flip during trials is clearly visible.

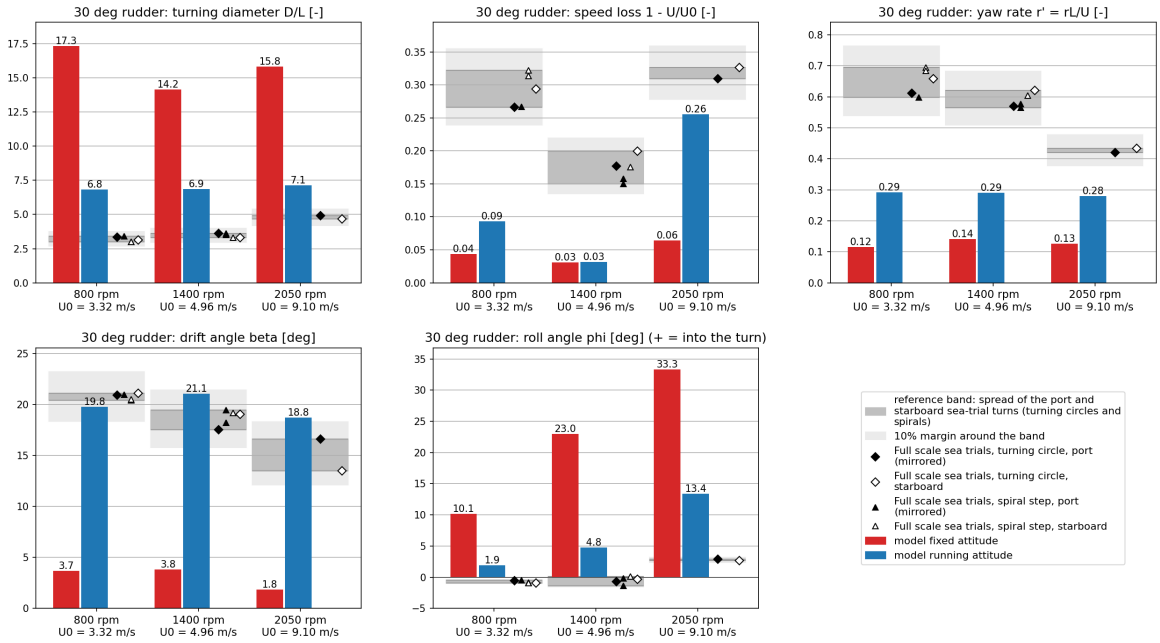

Figure 5.29: Steady-turn validation of the running attitude and fixed attitude model against the sea trial data for a $30°$ turning circle, results presented based on approach speed.

5.4. Influence of model extensions

This section presents a final analysis for both the GPPH and pilot vessel, where the additions made to a standard 3DOF MMG model are compared. For the comparison, the empirical hull model is used, presenting four different simulations:

- The fixed attitude model with all roll-related terms zero (dashed red) - 3DOF
- The running attitude model with all roll-related terms zero (dashed blue) - 3+2DOF
- The fixed attitude model with roll (solid red) - 4DOF
- The running attitude model with roll (solid blue) - 4+2DOF

The results are presented for the GPPH hull in Section 5.4.1 and in Section 5.4.2 for the pilot vessel. The GPPH is run with the gear-case steering model and the pilot vessel with the TPTR-models.

5.4.1. GPPH

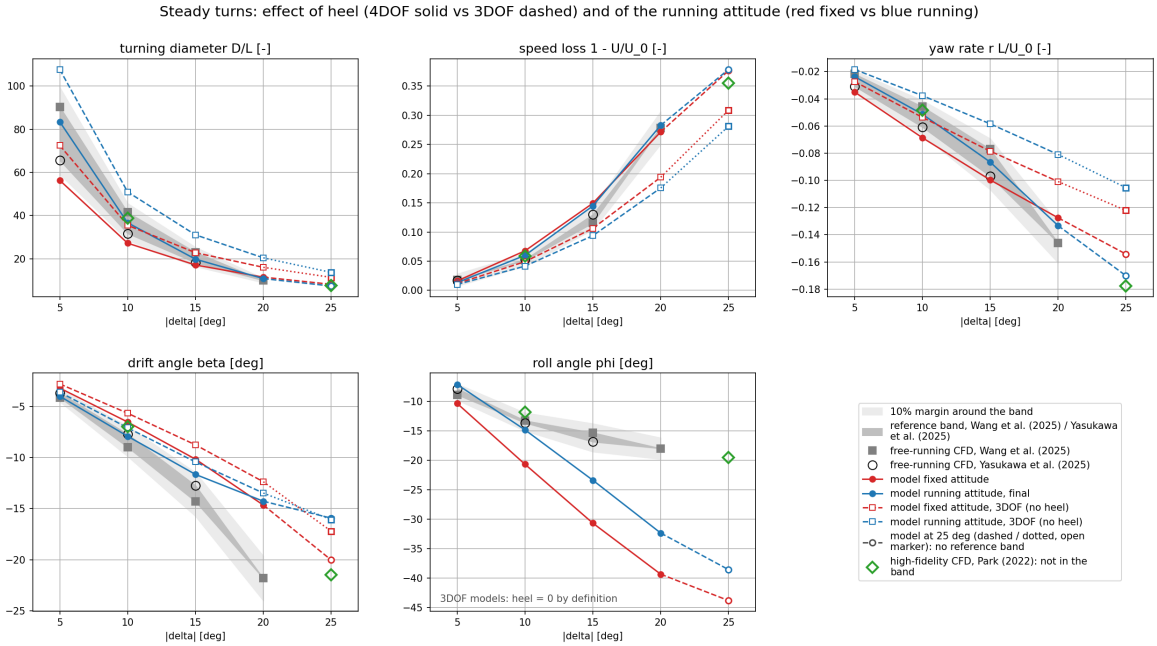

Figure 5.30: 3vs4DOF comparison of the GPPH hull for turning parameters.

The figure shows a comparison of the turning diameter, speed loss, yaw rate, drift angle and roll angle for all four cases against the CFD reference band.

The addition of heel (3DOF $\rightarrow$ 4DOF) makes the vessel turn tighter and increases the drift a little. The running attitude addition ($\rightarrow$ +2DOF) increases the turning diameter and drift. Heel and running attitude change the diameter in opposite directions; thus, by diameter alone, the models cannot be distinguished. With each addition, the simulation model gets closer to the CFD reference band for the drift angle. The 4DOF running attitude model (4+2DOF) is the only model that gets the drift angle and turning diameter together in the reference band.

In Figure 5.30 it is also shown that all four models reach a steady turn at steering angles varying from $5° - 25°$. At $25°$, the heel matters more; both 3DOF models turn wider than the high-fidelity CFD point, while the 4DOF models stay within 10% of the high-fidelity CFD data point. The yaw rate with the addition of the running attitude has a lower value than the fixed attitude models for a steering angle of $5° - 15°$. However, it becomes larger than the 4DOF fixed attitude model for a steering angle of $25°$, drawing near to the high-fidelity CFD point. In the drift panel, the fixed attitude 4DOF model is closer to the high-fidelity CFD data than the running attitude 4+2DOF model. The latter barely grows between steering angles of $20°$ and $25°$. The roll angle keeps the largest deviations, as the earlier analysis showed.

The results for a steering angle of $10°$ and $15°$ make the cleanest comparison; both CFD studies used for the reference band demonstrate a steady turn for these angles. For the $5°$ steering angle, the differences are small for all except the turning diameter, making the effects hard to see. Figure 5.31 presents a closer look into the turning diameter and drift angles for a $10°$ and $15°$ steering angle.

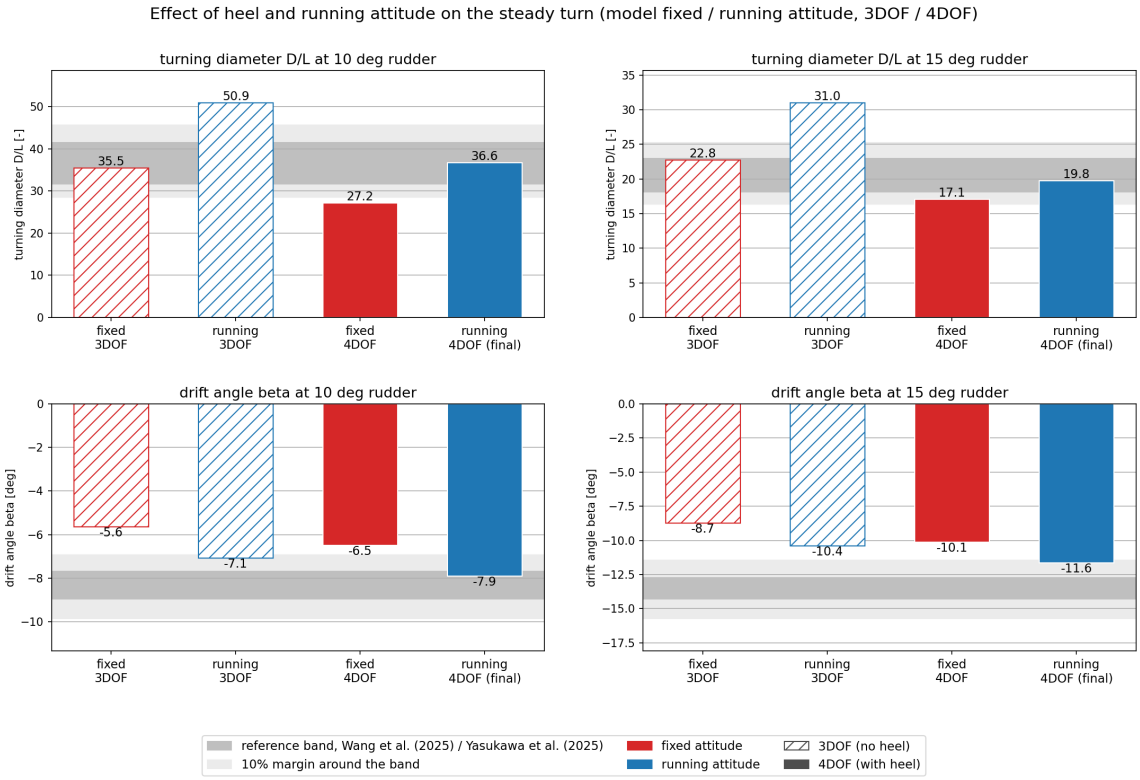

Figure 5.31: 3vs4DOF comparison of the GPPH hull for turning diameter and drift angle at 10 and 15° steering angles.

The figure shows a bar chart comparing the turning diameter and drift angle at $10°, 15°$ steering angles for all four cases relative to the CFD reference band, quantifying the impact of roll coupling. The addition of roll-coupling ($\rightarrow$ 4DOF) makes the vessel turn tighter, and the drift grows larger. For a heeled vessel, the hull lift is tilted; part of that force thus pushes the vessel into the turn. The addition of the running attitude ($\rightarrow$ +2DOF) makes the turn wider and the drift larger.

The two effects work against each other when only comparing the turning diameter. The fixed attitude 3DOF model also falls within the reference band in the turning diameter plot for both steering angles. In the drift panels, it becomes clear that each addition brings the model closer to the reference band. Here, the model with both additions (4+2DOF) comes closest to the reference band for both steering angles. Therefore, the diameter alone is not enough to validate the impact of each addition; drift and heel are also needed. Which, in turn, is a strong argument why roll coupling and running attitude are valuable additions to the manoeuvring model of a high-speed vessel.

5.4.2. Pilot vessel

The results of the comparison between the different additions for the pilot vessel is presented in Figure 5.32 on the next page. For this vessel, the running attitude has the largest effect; in the 4DOF model, it tightens the turn by about 60% for the 2050rpm engine setting (for 800 and 1400rpm, the result is a 30% and 50% reduction). It also increases the drift near the reference band. This is an opposite effect compared to the GPPH, where the running attitude widens the turning diameter. The addition of the roll motion has little influence once running attitude is implemented; for 800 and 1400rpm, the effect was at most 2% on D/L. At the 2050rpm engine setting, the impact is a bit bigger, but still not significant. In the fixed-attitude model, the heel has a larger impact; for the 2050rpm setting, a reduction of 44% is visible, but only a few per cent at large rudder angles for the 800 and 1400rpm.

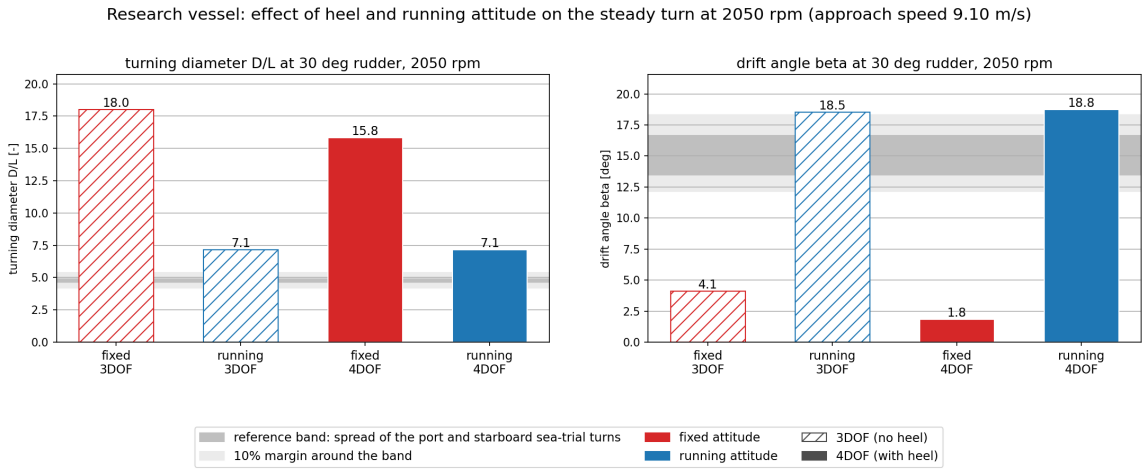

Figure 5.32: 3vs4DOF comparison of the pilot vessel for turning diameter and drift angle at a 30° steering angle for the 2050rpm run.

So for this vessel, adding the heel does not close the gap between the simulation model and the trials. Neither do the other additions bring all parameters into the reference band. The running-attitude brings the turning diameter and drift angle closer, but the circle is still too wide, and drift is too high. The running-attitude D/L at 30° for the 2050rpm setting is the closest the simulation model gets to the reference band.

5.5. Discussion of results

To establish a reliable foundation for the high-speed manoeuvring simulations, initial baseline model calibration and validation had to be performed with the 3DOF and 4DOF MMG models. Using conventional benchmark vessels, the 3DOF MMG model was evaluated with the KVLCC2 model and the 4DOF MMG model with the KCS model. The use of propeller and resistance data of different model sizes resulted in pronounced speed loss during straight sailing simulations. Therefore, re-tuning the baseline resistance coefficient (R_0) or initial propeller speed (n_P) is important to ensure steady-state straight-line equilibrium before initiating a turning motion. The steering rate analysis with the KCS vessel (Figure 4.5) showed the necessity of modelling physically correct steering dynamics. The validation of these models with conventional benchmark vessels confirmed that the MMG framework can accurately capture hydrodynamic steering forces and roll-coupling and endorsed its modularity.

In the GPPH simulations, the addition of the heel and running attitude changes the diameter in the opposite direction; the heel decreases the turning diameter, while the running attitude increases it. The fixed attitude 3DOF model falls within the reference band for the $5^\circ - 15^\circ$ turning diameter, while its drift angle is the furthest from the band. Therefore, the diameter alone is not enough to validate a planing model; drift and heel should also be included. Another clear insight from the GPPH CFD data is that the linear manoeuvring coefficients vary across Froude numbers. The addition of the running attitude had a clear improvement on the envelope of the linear hull coefficients in the Lewandowski model. This proves that high-speed manoeuvring coefficients cannot be treated as speed-constant coefficients, as is done for displacement vessels.

The deviations found for the GPPH hull fall into three categories: an implementation error, deliberate modelling choices and remaining physical effects. The implementation error, the surge added mass m_x being counted twice in the sway equation, was corrected. This removed a deviation of about 7% in the force balance of the turn (Figure 5.13). The deliberate changes to the empirical hull model are the removal of C_V^2 from Y'_v, the sign change of N'_r and the dynamic lift addition in Y'_ϕ and N'_ϕ. The hand calculation checks in Section 5.1.1 shows that these changes were implemented as intended and makes their effect on the coefficients visible. At a component level, separating the force components confirmed that the gear-case and propeller forces follow the captive-CFD reference trends. The inclusion of the propeller torque reaction (Figure 5.18) further refined the roll estimations by reducing the inward heel angle by about $1.6 - 2.6^\circ$. However, it left the envelope of the drift and roll angle unchanged. The

deviations that remain after these corrections are therefore not attributed to implementation errors, but mainly to contributions not taken into account in the linear hull model.

The largest deviation in the adjusted model is still the heel. When the simulation model is put at the CFD steady turn, the model pushes the vessel inward from a steering angle of 10° (fixed attitude) or 15° (running attitude). In contrast, the CFD roll moment pushes it outward (Figure 5.20). Varying KG and K_ϕ shifts the heel but does not change its envelope (Figure 5.18); therefore, an input error is unlikely to be the cause. The missing propeller torque reaction explains part of the difference. In the same figure, it is shown that the heel is reduced by $1.6^\circ - 2.6^\circ$, but it does not change the trend either. It was left out of the model in line with the MMG convention of representing the propeller by only the thrust. With captive-CFD linear derivatives, the hull still pushes inward; this indicates that a non-linear roll term is missing rather than that a linear coefficient is wrong. The sensitivity sweep presented in Section 5.2 supports this hypothesis for the fixed attitude model. For this model, the $K'_{vv\phi}v'^2\phi$ is the most consistent term, also compared with the captive-CFD derivatives. However, this does not prove that this is the physical term.

The drift deviation is a separate error. In Figure 5.18, it is shown that KG, K_ϕ and the torque reaction leave the drift unchanged. With captive-CFD linear derivatives, the simulation keeps following the same envelope (Figure 5.21). Therefore, it is not specific to the Lewandowski hull model and points to a missing non-linear contribution at large drift angles.

The sensitivity sweep is based on only three data points, one for each steering angle. The CFD results used as a target result only have steady turns at steering angles of $5^\circ, 10^\circ, 15^\circ$; the 20° point is added for comparison but is not a proper steady turn. These three pairs are used to calculate one coefficient c, where the spread shows how well that single coefficient fits all three rudder angles. Since there were only three points to fit, a low spread shows a term is consistent with the gap between simulation and CFD results, not necessarily that it is physically correct. Where the gap is not only the missing physics, but also contains any errors made in the linear Lewandowski model. Three points leave little room to expose a wrong term in the data. Also, the sweep was performed with the goal of finding one coefficient which could describe the missing non-linear contribution. For fixed attitude configurations, a consistent term was found; however, for the running attitude, this was not conclusive for all motions. This decision was made based on the scarcity of fitting data; only one data point would be left if a combination of two coefficients was the goal. The drift, yaw rate and heel grow together in the CFD target data, and all three turns are at the same speed. To separate them, turning model tests where parameters are decoupled should be performed. For example, the same steering angle at different speeds or model tests where the heel and drift are set. Therefore, the outcome of the sweep should be interpreted as an indication of where to look for the non-linear contribution and not as an identified term with the found value to adjust the model.

The addition of the running attitude improved the results visibly. However, the running attitude table for the GPPH was created with straight sailing data. As a result, the effect of heel on the wetted geometry was not captured. For the pilot vessel, there was running attitude data for both straight sailing and turning motion. However, for this vessel only four speed points were available for the running attitude data. Also, the speed data was not equally divided over the operating range of the vessel, leaving an opening between $5 - 9\,\mathrm{m\,s^{-1}}$.

The running attitude had an opposite effect on the turning diameter for the GPPH and the pilot vessel. For the GPPH, it widened the turn, but it tightened the pilot vessel's turn. The GPPH model is largely inside or close to the reference band, while the pilot vessel is about right for the drift angle, with a too-large diameter and too little speed loss. For the pilot vessel, the introduction of running attitude reduced the under-prediction by about 5 times compared to the fixed attitude model. Also, the heel over-prediction was reduced by about 2.5-5 times across all tested speeds. However, a speed-dependent sign flip visible in the trial results was not apparent in the simulation results. The GPPH simulation is performed at $Fr_L = 1.85$ compared to $Fr_L = 0.3 - 0.9$ for the pilot vessel. At lower velocities, the pilot vessel is operating in the displacement region, and at the highest recorded speeds, it operates around the shift between semi-planing and planing. This indicates that the Lewandowski model is operating outside its intended physical domain at lower velocities, where the vessel operates in the displacement region.

Both vessels have similar geometries, but different steering configurations. For both vessels, the heel is over-predicted. The zigzag simulations in Figure 5.27 show smaller overshoot angles for the simulation model compared to the sea trial measurements. This is consistent with a turning response that is too weak. These explanations have not been tested separately. The opportunity to make a comparison with real-size vessel data from different operating regimes confirms that, for accuracy across low- to moderate-speeds, the planing assumptions do not hold. A low-speed force correction is needed and a running-attitude table across various speeds covering the full shift from displacement to planing regime (combining trim and heel influences).

For both the GPPH and the pilot vessel, the reference band is based on limited data. The CFD studies used are based on the same method; therefore, the spread is between setups, not an independent configuration. The body-force runs do not reach a steady turn at 20° and spin out at 25°, so the band there is made with only one point. The high-fidelity points use a different gear-case model and are therefore shown separately outside the reference band. The sea trials performed with the pilot vessel were performed in one day on a river with current and wind. One fitted current vector was used per manoeuvre. However, the current can vary within a manoeuvre, especially during a spiral of about 14 minutes. Wind was not corrected for. It should be noted that the developed simulation model does maintain steady turning circles up to steering angles of 25°, closely tracking the high-fidelity CFD trend.

The current model, an adjusted linear manoeuvring model based on the empirical method presented by Lewandowski [5], can be used for trends of data and relative comparisons covering steady turns only. To improve it, a larger dataset for fitting the non-linear terms would be necessary, together with captive or force data for both hulls or the non-linear hull force coefficients of the GPPH hull. Also, a running attitude table covering multiple speeds together with heel angles would improve the implementation of speed-dependent changes of the wetted geometry.

5.5.1. Contributions of the presented method

The goal of this thesis was to construct a computationally efficient manoeuvring model for a (semi-)planing vessel and to test it against CFD and full-scale sea trial data and gain physical insights into the manoeuvring behaviour. A model that is accurate across all Froude numbers was not achieved: the model reproduces the steady-turn trends of a fully planing hull within or close to the CFD reference band, but at the lower speeds of the pilot vessel the deviations from the sea trials remain significant, and the heel angle is over-predicted for both vessels. Since the model needs only the hull geometry, a running attitude table, a resistance curve and the propeller and rudder data, it is suited for comparing design options and trends in the early design stage. Before it can be used in real-time vessel control, the dynamic response and the low-speed behaviour must be improved. The main contributions are:

- A 3DOF and 4DOF MMG model is developed and verified, which handles multiple propeller and rudder configurations as well as a gear-case unit.
- The empirical formulae developed by Lewandowski are implemented with a speed-dependent look-up table representing the running attitude of a planing hull.
- Corrections are proposed and validated to the empirical formulae using CFD results; the exclusion of the C_V^2 factor in Y_v and the sign change of N_r.
- It is shown that the addition of roll and running attitude has opposing effects on the turning diameter and drift angle of a high-speed craft, so that evaluating its manoeuvring performance requires all three items.
- A process is established for identifying the dominant non-linear coefficients which can be used to improve the performance of the linear model.
- The validation of the simulation model against full-scale trial data shows the impact of the adjustments to the empirical model.
- The limitations of the model are identified in the semi-planing regime.
- The inclusion of the torque reaction force in the propeller model was found to be essential for (small) high-speed craft.

5.5.2. Limitations of the presented method

The developed 4+2DOF model provides a computationally efficient tool to predict the manoeuvring of a high-speed craft. However, several limitations set its current operational boundaries. These limitations are presented below, grouped by physical, methodological and experimental explanations.

Physical regime validity at lower Froude numbers

- Lewandowski's empirical formulae were derived specifically for hard-chine planing hulls operating in the high-speed regime. When applied to the full operational profile of the pilot vessel, the equations operate outside their target domain. The empirical hull model assumes an inward roll across all operating conditions. As a consequence, it could not replicate the heel sign change visible in the sea trial measurements. Also, the zigzag formulations show smaller overshoot angles than the trial data, indicating that the steering response is overly damped.

Running attitude Table

- The running attitude table for the GPPH hull was established with only straight-sailing towing tank data. Because of this, the heel influence on the wetted geometry was not taken into account. Although for the pilot vessel the wetted geometry data was available during a turn, its table was only constructed with four points.

Methodological constraint of coefficient sweep

- The non-linear coefficient sweep was performed on a dataset of three points (steering angles of $5°, 10°, 15°$), derived from steady-turn CFD data found in the literature. Because the sway, yaw, and roll all grow simultaneously during the turn, a single-term fit is unable to isolate cross-coupling effects. Therefore, the identified terms serve as a diagnostic tool rather than a direct solution. Surge was excluded from the sweep because the force gap between the simulation model and the CFD data changed sign across steering angles.

Reference data scatter

- The sea trial reference band for the pilot vessel was constructed with data subjected to wind and current variations. The virtual CFD reference band was constructed from two CFD studies using models that experienced spin-out at steering angles of $\geq 20°$. As a consequence of this, the validation of the GPPH simulation runs beyond a steering angle of $15°$ relied on single high-fidelity CFD trend points.

6. Conclusion

Manoeuvring of displacement vessels has been widely studied, and various models have been established to simulate their manoeuvrability. High-speed craft, however, have not received as much attention. Several studies have been made into tuning and adapting standard models, but the manoeuvrability simulation of high-speed craft remains partly uncovered. Research has mainly stayed in the theoretical understanding; the link to real-life data has not been made frequently. This thesis addressed the following research question:

How can empirical formulations and dynamic running attitude corrections be combined with sea trial data to construct and validate a computationally efficient 4+2DOF manoeuvring model for high-speed craft?

In order to answer this question, the Maneuvering Modeling Group (MMG) framework was adapted and extended to account for high-speed semi-planing and planing vessels. Conventional manoeuvring models assume constant wetted geometries, speed-independent hydrodynamic coefficients and negligible motions in the vertical plane. However, high-speed craft generate significant hydrodynamic lift, resulting in speed-dependent changes in sinkage and trim (running attitude), varying wetted geometry and strong motion coupling across vertical and horizontal degrees of freedom. Below, the sub-research questions are answered.

What are unique elements distinguishing high-speed craft from conventional displacement vessels?

In the literature, it was found that high-speed operations ($Fr_L \geq 0.7 - 0.8$) are governed by hydrodynamic lift, rather than static buoyancy forces (as is the case for conventional displacement vessels). This introduces Froude-dependent alterations of the wetted geometry (referred to as running attitude). It also introduces unique instabilities occurring only at high speed as a result of cross-coupling between horizontal and vertical motions (e.g. chine-walking, corkscrewing, spin-out).

What is the state-of-the-art in adapting models for displacement vessels to capture the manoeuvring characteristics of high-speed craft?

Three manoeuvring models are commonly used: Nomoto, Abkowitz and MMG. The MMG model was selected for its modular structure, in which the hull, propeller and rudder contributions are modelled separately. In the literature, three adaptations of the standard 3DOF model for high-speed craft were found: the roll equation was added, the hydrodynamic derivatives were determined at multiple Froude numbers through captive tests, and the running attitude was included through look-up tables of sinkage and trim. These can be added to the core equations without re-formulating the framework. However, the adapted models remain reliable only in a limited operating range: coefficients require extensive captive tests or CFD, predictions diverge at larger steering angles, and full-scale validation is scarce.

What methods exist to capture the hydrodynamic coefficients of manoeuvring?

The hydrodynamic coefficients used to describe the forces acting on a hull during manoeuvring can be derived via experimental towing tank tests (e.g. OTT, CMT), numerical Computational Fluid Dynamics (CFD, e.g. virtual-captive or free-running simulations), system identification or (semi-)empirical formulations. While captive-CFD provides high accuracy, its computational costs are high. In environments where instant decisions have to be made, a computationally efficient model may be preferred. For this thesis, the choice was made to use empirical formulations.

How can empirical hydrodynamic formulations and speed-dependent running attitude look-up tables be integrated into an MMG framework to determine the forces acting on a high-speed hull?

Lewandowski's empirical formulations were implemented in a 4DOF MMG framework, expanded with appendage models (gear-case and twin-propeller twin-rudder) and a speed-dependent look-up table for the running attitude implementation. The integration of the running attitude, where the transom draft dynamically follows the trim angle of the vessel, stabilised the system. The uncorrected fixed-attitude simulations experienced too high heel angles and large trajectory deviations. The running-attitude simulations, where the wetted geometry was updated per time step, shifted the linear manoeuvring coefficients onto captive-CFD trend lines across various Froude numbers.

It was deemed necessary to establish a baseline resistance coefficient (R_0) or propeller rotations (n_P) to achieve steady-state straight-line equilibrium before introducing a turning manoeuvre. Furthermore, the addition of deflection rates (compared to an instant rudder shift) was found necessary to capture the trajectory accurately. The structural assessment of the model revealed an error in the sway equation, where the surge added mass (m_x) was accounted for already in the empirical formulae.

Evaluating the turning diameters alone can give a distorted picture. The implementation of a fourth degree of freedom (roll) tightened the turn, but increased the drift angle. Conversely, implementing the running attitude widened the turning diameter while also increasing the drift angle. Only the combined 4DOF simulation model with running attitude (4+2DOF) simultaneously brought the turning diameter and the drift angle into the Computational Fluid Dynamics (CFD) reference band for the GPPH and closer to the experimental sea trial reference band for the pilot vessel.

How accurately does the 4+2DOF empirical manoeuvring model replicate benchmark CFD data and full-scale sea trial behaviour across operational speed regimes?

The General Prismatic Planing Hull (GPPH) was tested against CFD data found in the literature at a Froude number of $Fr_L = 1.85$. For this vessel, the 4+2DOF model achieved steady turns across steering angles of $5°, 10°, 15°$, falling within or nearing the CFD reference band. While the published CFD models experienced spin-out or trajectory divergence for a steering angle of $\geq 20°$, the developed simulation model maintained steady turning circles. Tested up to $25°$, the simulation results neared high-fidelity CFD trends. At steering angles $\geq 15°$, the empirical model over-predicts heel, where the simulation model pushes the vessel into the turn, the free-running CFD data pushed the vessel outward. By substituting the linear captive-CFD coefficients, the simulation model still produced an inward moment, leading to the hypothesis that a non-linear contribution was missing rather than it being an error in the empirical hull model.

A single-term coefficient sweep against captive-CFD hull force coefficients was performed. This identified the $Y'_{vv\phi}v'^2\phi$ and $K'_{vv\phi}v'^2\phi$ terms (with a spread of 1.18 and 1.24, respectively) as the most consistent missing non-linear sway and roll terms. This supports the hypothesis that the under-prediction of the drift angle and the over-prediction of the heel angle originate from non-linear cross-coupling contributions, which the linear hull model does not account for, rather than from errors in the linear derivatives. However, the sway, yaw and roll motions grow simultaneously during steady turns; therefore, the sweep serves more as a diagnostic tool than as a direct solution.

The pilot vessel was tested against sea trial data performed across various operational engine speeds (800, 1400, 2050rpm). The comparison simulation showed accuracy improvements following the addition of the fourth degree of freedom and the running attitude. Implementing the speed-dependent wetted geometry, the turning diameter deviations were reduced from up to 7 times the sea trials data (fixed attitude model) to about 2 times the sea trial data measurements. Simultaneously reducing the heel over-prediction by 2.5–5 times compared to the fixed-attitude model. The sea trial measurements revealed a speed-dependent sign change in the heel angle; an outward heel at displacement speeds (800rpm, $Fr_L \approx 0.3$) which transitioned to an inward heel at semi-planing speeds (2050rpm, $Fr_L \approx 0.9$). The empirical formulations of Lewandowski's method assume a planing vessel; the over-prediction of inward heel at lower speeds indicates that the empirical planing model cannot be applied without any alterations to low-speed manoeuvres.

Combining the answers to the sub-questions above, the main research question can be answered. A computationally efficient 4+2DOF manoeuvring model for a high-speed craft is constructed by combining empirical hard-chine force equations with a speed-dependent running attitude look-up table within the MMG framework. The sea trial data were used in three ways: to derive the resistance curve of the pilot vessel, to construct its running attitude table, and as a full-scale reference band for validation. Because the hull forces follow from empirical formulations rather than from captive tests or CFD, the model only requires the hull geometry, the running attitude table, a resistance curve and the propeller and rudder data. Comparing the simulation model estimations across both the GPPH and pilot vessel highlights physical boundaries to the empirical planing formulae. For the GPPH (operating in the fully planing regime, $Fr_L = 1.85$), the 4+2DOF model generated results close to the CFD reference band for the turning diameter and drift angles. For the pilot vessel (operating between $Fr_L = 0.3 - 0.9$), the deviations from the sea trial reference band were more pronounced.

These deviations are mainly attributed to the physical regime for which the empirical formulae were established. Lewandowski's formulae are established for fully planing hulls, meaning they operate outside their physical domain when applied to the low-speed manoeuvres of the pilot vessel. This hypothesis is supported by the sea trial measurements, which exhibit a speed-dependent heel sign change (from outward at lowest speed to inward at highest speed) that the empirical model over-predicts as inward roll for each speed regime. Additionally, the sea trial data contained environmental influences (i.e. current and wind), and limited running attitude data with a gap between $5-9\,\mathrm{m\,s^{-1}}$. Nevertheless, implementing the running attitude for the pilot vessel did improve the turning diameter and heel over-prediction visibly. This shows that while the addition of running attitude is an essential expansion of the conventional manoeuvring models, capturing the full operational profile of a semi-planing vessel requires a combination of displacement force models with running attitude data covering the whole operating regime. Therefore, constructing a fully robust manoeuvring model across all operational speeds requires pairing dynamic running attitude tables with low-speed displacement force contributions.

This thesis showed that the existing manoeuvring methods are not suited to high-speed (semi-)planing craft. The standard models, developed for large displacement ships, rest on assumptions that do not hold in the planing regime: a fixed wetted geometry, speed-independent coefficients and negligible heave, roll and pitch. The adaptations proposed in the literature address these shortcomings only partly. Their coefficients rely on captive tests or CFD for every speed, their running attitude is taken from straight-ahead runs and thus ignores the effect of heel, and they are rarely validated against full-scale measurements. At steering angles of 20° and above, the CFD-based models spin out, while high-fidelity CFD of the same hull shows a steady turn, which points to a limitation of the models rather than of the vessel. Moreover, the published methods proved difficult to reproduce: input data were often incomplete or inconsistent, the empirical formulations contained an incorrect speed scaling and sign, and the standard MMG convention neglects the propeller torque reaction, which is significant for small high-speed craft. Finally, no quantitative manoeuvring criteria exist for high-speed craft comparable to those of IMO Resolution MSC.137(76) for large ships, so that there is no clear target against which high-speed manoeuvring models can be assessed. Manoeuvring prediction for high-speed craft therefore requires not only new models, but also reproducible reference data and dedicated performance criteria.

To advance the numerical prediction and physical understanding of high-speed craft manoeuvring, this thesis developed and verified computationally efficient 3DOF, 4DOF and 4+2DOF models within the MMG framework, capable of handling twin-propeller twin-rudder and gear-case configurations. By integrating corrected empirical formulations with speed-dependent running attitude look-up tables, the model reaches steady turns at steering angles where the reference CFD simulations spin out. The analysis revealed that roll coupling (4DOF) and running attitude (+2DOF) have opposing effects on the turning diameter, showing that both mechanisms must be included and that the drift and heel angles must be evaluated alongside the turning diameter. Furthermore, the propeller torque reaction, neglected in the standard MMG convention, was found to be a significant contribution to the roll balance of small high-speed craft, and a single-term coefficient sweep was established as a diagnostic tool for identifying missing non-linear terms. The comparison with CFD reference data and full-scale sea trials showed clear improvements over the fixed-attitude model, while identifying the lower speed limit of the empirical planing formulations. Requiring only basic hull data, the model is currently suited for early-stage design evaluations and steady-turn trend comparisons; its low-speed behaviour and dynamic response must be improved before it can support real-time onboard vessel control.

6.1. Recommendations

Based on the conclusions and limitations presented in this report, several recommendations are proposed below.

- To increase the operational regime coverage of the running attitude, the tables should be expanded to include multi-dimensional tables mapping wetted geometry changes across combinations of Froude number, trim angle and heel angle. Especially the hump-speed region should be described in detail. Incorporating the heel-dependent running attitude data will allow the wetted geometry to update dynamically in all states, providing a better physical representation.
- To perform the sensitivity sweep for a multi-coefficient fit, dedicated towing tank or virtual captive-CFD tests should be performed, with various fixed heel and drift angles to de-couple the velocity, drift and heel angles. These independent test matrices can isolate individual higher-order non-linear derivatives.
- To capture the full operational regime of a (semi-)planing vessel, a combined model should be created including the low-speed displacement manoeuvres and high-speed (semi-)planing manoeuvres. Developing a function which can transition based on Froude number between a conventional MMG model at lower speeds and the empirical planing model at higher speeds will ensure a better validity of the model across the full operational regime.
- The current model assumes calm water. To represent real operating conditions, external contributions from wind, current and waves should be added. The modular structure of the MMG framework allows these forces to be included as separate components. This would also allow the sea trial comparison to account for the wind and current present during the trials, rather than correcting for current only. For high-speed craft, waves are particularly relevant, since they alter the running attitude and wetted geometry, and can trigger instabilities such as broaching.
- In the current model, the torque is left out of the propeller force equations. However, the substitution of the torque reaction moment showed that it reduced heel over-prediction over all steering angles. The inclusion of the torque reaction provides a physically based improvement of the roll moment and should be included in the MMG framework for small high-speed (single-propeller) vessels.
- A larger question remaining is why the results between two CFD simulations or trial runs with the same conditions can lead to different results (as can be seen in the reference band for both the GPPH and the pilot vessel). Quantifying this uncertainty, through repeated trials in calm conditions with measured current and wind, and through a comparison of CFD set-ups, would make the reference bands a more reliable validation target. A valuable contribution would be to perform a sensitivity sweep of all parameters in the manoeuvring model to find the impact each one has on the total outcome of the manoeuvre.

Declaration of use of AI

For this report Generative AI (Claude and Microsoft Copilot) has been used to:

- Improve the grammar, style, layout, and/or spelling of the text
- Rephrase text passages and suggest structure, based on the author's own input
- During programming to resolve syntax errors and to assist in debugging
- As a sparring partner to brainstorm new ideas

No argument, result, interpretation or reference was produced by a generative AI tool. In all cases the work has been reviewed and corrected, and the author remains fully responsible for the content of the report

References

[1] Carolyn Q. Judge. *USNA Course Notes EN455: Seakeeping and Maneuvering*. en. Course Notes. 2019. URL: https://www.usna.edu/NAOE/academics/en455.php (visited on 03/16/2026).

[2] DTIC. "FIRST SYMPOSIUM ON SHIP MANEUVERABILITY Report". en. In: *Defence Documentation Center for Scientific and Technical Information* (1960). URL: https://apps.dtic.mil/sti/tr/pdf/AD0442036.pdf.

[3] M A Abkowitz. *Lectures on Ship Hydrodynamics - Steering and Manoeuvrability*. en. Vol. Report No. Hy-5. Lyngby, Denmark: Hydro- og Aerodynamisk Laboratorium, 1964.

[4] IMO. *Standards for Ship Manoeuvrability*. Dec. 2002. URL: https://wwwcdn.imo.org/localresources/en/KnowledgeCentre/IndexofIMOResolutions/MSCResolutions/MSC.137(76).pdf.

[5] Edward M Lewandowski. *The Dynamics of Marine Craft: Maneuvering and Seakeeping*. en. Vol. 22. Advanced Series on Ocean Engineering. WORLD SCIENTIFIC, July 2004. ISBN: 978-981-02-4755-3 978-981-256-267-8. DOI: 10.1142/4815. URL: http://www.worldscientific.com/worldscibooks/10.1142/4815 (visited on 09/21/2026).

[6] ITTC. *ITTC 75-04-02-01*. Sept. 2024. URL: https://www.ittc.info/media/11976/75-04-02-01.pdf (visited on 03/18/2026).

[7] J M J Journée and W W Massie. *Offshore Hydromechanics*. en. Second. Delft University of Technology, June 2008.

[8] Odd M. Faltinsen. *Hydrodynamics of High-Speed Marine Vehicles*. Cambridge: Cambridge University Press, 2005. ISBN: 978-0-521-84568-7. DOI: 10.1017/CBO9780511546068. URL: https://www.cambridge.org/core/books/hydrodynamics-of-highspeed-marine-vehicles/EFAC95328551E361A7DD04464F296C41 (visited on 03/12/2026).

[9] Jaap Gelling. *MT44095 04 2024-2025 - Dynamic Lift Monohulls*. Lecture slides PowerPoint. 2024. URL: https://brightspace.tudelft.nl/d2l/le/content/682190/viewContent/4016841/View.

[10] GreenOak. *Pilot boat turn behind stern of Vessel Cargo container Ship in the ocean sea concept logistic transportation team support partner working*. [Image]. Shutterstock, 2173845799. 2022. URL: https://www.shutterstock.com/sv/image-photo/pilot-boat-turn-behind-stern-vessel-2173845799 (visited on 05/28/2026).

[11] R. B. Chapman. "Free-Surface Effects for Yawed Surface-Piercing Plates". en. In: *Journal of Ship Research* 20.03 (Sept. 1976), pp. 125–136. ISSN: 0022-4502, 1542-0604. DOI: 10.5957/jsr.1976.20.3.125. URL: https://onepetro.org/JSR/article/20/03/125/175383/Free-Surface-Effects-for-Yawed-Surface-Piercing (visited on 04/30/2026).

[12] Jeffrey Bowles. "Turning Characteristics and Capabilities of High-Speed Monohulls". en. In: *SNAME Chesapeake Power Boat Symposium*. Annapolis, Maryland: SNAME, June 2012, D021S002R003. DOI: 10.5957/CPBS-2012-013. URL: https://onepetro.org/snamecpbs/proceedings/CPBS12/CPBS12/D021S002R003/540377 (visited on 03/12/2026).

[13] Chenliang Zhang et al. "Experimental and numerical investigations of advancing speed effects on hydrodynamic derivatives in MMG model, part I: Xvv,Yv,Nv". en. In: *Ocean Engineering* 179 (May 2019), pp. 67–75. ISSN: 00298018. DOI: 10.1016/j.oceaneng.2019.03.019. URL: https://linkinghub.elsevier.com/retrieve/pii/S0029801819301143 (visited on 03/10/2026).

[14] Edward V Lewis. *Principles of Naval Architecture (Second Revision)*. en. Vol. III - Motions in Waves and Controllability. Jersey City, NJ: Society of Naval Architects and Marine Engineers (SNAME), 1989. ISBN: 0-939773-02-3. URL: https://app.knovel.com/hotlink/toc/id:kpPNASRV01/principles-naval-architecture-3/principles-naval-architecture-3.

[15] Thor I Fossen. *Handbook of Marine Craft Hydrodynamics and Motion Control*. en. John Wiley & Sons, Ltd, 2011. ISBN: 978-1-119-99149-6.

[16] S. Hajizadeh, M.S. Seif, and H. H.Mehdigholi. “EVALUATION OF PLANING CRAFT MANEUVERABILITY USING MATHEMATICAL MODELING.” In: *Brodogradnja* 67.(1) (2016). ISSN: 0007-215X. URL: https://hrcak.srce.hr/file/228038 (visited on 03/16/2026).

[17] Sasan Tavakoli and Abbas Dashtimanesh. “A six-DOF theoretical model for steady turning maneuver of a planing hull”. en. In: *Ocean Engineering* 189 (Oct. 2019), p. 106328. ISSN: 00298018. DOI: 10.1016/j.oceaneng.2019.106328. URL: https://linkinghub.elsevier.com/retrieve/pii/S0029801819304949 (visited on 04/09/2026).

[18] Hironori Yasukawa, Noritaka Hirata, and Yoshiyuki Nakayama. “High-Speed Ship Maneuverability”. en. In: *Journal of Ship Research* 60.4 (Dec. 2016), pp. 239–258. ISSN: 00224502, 15420604. DOI: tudelft.idm.oclc.org/10.5957/jsr.2016.60.4.239. URL: https://onepetro-org.tudelft.idm.oclc.org/JSR/article/60/04/239/175220/High-Speed-Ship-Maneuverability (visited on 03/25/2026).

[19] Zhaoyuan Wang et al. “Physical analysis methods for planing hull turning circles”. en. In: *Ocean Engineering* 321 (Mar. 2025), p. 120348. ISSN: 00298018. DOI: 10.1016/j.oceaneng.2025.120348. URL: https://linkinghub.elsevier.com/retrieve/pii/S0029801825000630 (visited on 03/26/2026).

[20] John Bate. *Performance Analysis and Prediction of High Speed Planing Craft*. en. Dec. 1994. DOI: 10.24382/4827. URL: https://pearl.plymouth.ac.uk/bms-theses/405 (visited on 03/23/2026).

[21] Sasan Tavakoli et al. “A review on the hydrodynamics of planing hulls”. en. In: *Ocean Engineering* 303 (July 2024), p. 117046. ISSN: 00298018. DOI: 10.1016/j.oceaneng.2024.117046. URL: https://linkinghub.elsevier.com/retrieve/pii/S0029801824003834 (visited on 04/09/2026).

[22] H. Yasukawa and Y. Yoshimura. “Introduction of MMG standard method for ship maneuvering predictions”. en. In: *Journal of Marine Science and Technology* 20.1 (Mar. 2015), pp. 37–52. ISSN: 0948-4280, 1437-8213. DOI: 10.1007/s00773-014-0293-y. URL: https://link.springer.com/10.1007/s00773-014-0293-y (visited on 03/04/2026).

[23] J.P. Hooft and U. Nienhuis. “The prediction of the ship’s maneuverability in the design stage”. In: *SNAME Transactions*. Vol. 102. 1994, pp. 419–445.

[24] Zhaoyuan Wang et al. “Computational Study of Dynamic Instability for High-Speed Planing Hull Maneuvers”. en. In: *International Conference on Fast Sea Technology (FAST)* (Oct. 2025).

[25] M. Fujino. *Maneuverability in restricted waters: state of the art*. Tech. rep. 184. 1976. URL: https://deepblue.lib.umich.edu/items/1bb384ee-ff9f-4fa7-b615-3328e5eb48e8.

[26] J.A. Keuning and J. Gerritsma. “Resistance tests of a series of planing hull forms with 25 degrees deadrise angle1”. en. In: *International Shipbuilding Progress* 29.337 (Sept. 1982), pp. 222–249. ISSN: 15662829, 0020868X. DOI: 10.3233/ISP-1982-2933701. URL: https://journals.sagepub.com/doi/full/10.3233/ISP-1982-2933701 (visited on 05/11/2026).

[27] Toru Katayama, Takashige Hinami, and Yoshiho Ikeda. “Longitudinal motion of a super high-speed planing craft in regular head waves”. en. In: *Proc. Fourth Osaka Colloquium on Seakeeping Performance of Ships* (2000), pp. 214–220.

[28] K.S.M. Davidson. “On the turning and steering of ships”. In: *SNAME Transactions* 52 (1944).

[29] Donald L. Blount and Louis T. Codega. “Dynamic Stability of Planing Boats”. en. In: *Marine Technology and SNAME News* 29.01 (Jan. 1992), pp. 4–12. ISSN: 0025-3316, 1542-0566. DOI: 10.5957/mt1.1992.29.1.4. URL: https://onepetro.org/MTSN/article/29/01/4/175945/Dynamic-Stability-of-Planing-Boats (visited on 05/28/2026).

[30] Sungtek Park et al. “6DoF CFD Analysis for High-Speed Small Craft in Free Running Conditions”. en. In: *Ships and Offshore Structures* 20.9 (2024), pp. 1331–1351. ISSN: 1744-5302, 1754-212X. DOI: 10.1080/17445302.2024.2393478. URL: https://www.tandfonline.com/doi/full/10.1080/17445302.2024.2393478 (visited on 03/30/2026).

[31] F. Stern et al. *Free Running 6DOF CFD for High-Speed Small Craft*. Jan. 2023. DOI: 10.23967/marine.2023.107.

[32] Toru Katayama and Shun Ohashi. *A Study on Spinout Phenomena of Planing Craft in High Speed Turning with Radio Control Small Model*. 14th International Ship Stability Workshop (ISSW). Kuala Lumpur, Malaysia, Sept. 2014.

[33] Yifan Xue et al. “System identification of ship dynamics nonlinear model with free-running tests based on two step semi- conjugate Bayesian regression”. en. In: (2020).

[34] Weilin Luo and Xinyu Li. “Measures to diminish the parameter drift in the modeling of ship manoeuvring using system identification”. en. In: *Applied Ocean Research* 67 (Sept. 2017), pp. 9–20. ISSN: 01411187. DOI: 10.1016/j.apor.2017.06.008. URL: https://linkinghub.elsevier.com/retrieve/pii/S0141118716303881 (visited on 05/19/2026).

[35] Yi Liu et al. “Predictions of ship maneuverability based on virtual captive model tests”. en. In: *Engineering Applications of Computational Fluid Mechanics* 12.1 (Jan. 2018), pp. 334–353. ISSN: 1994-2060, 1997-003X. DOI: 10.1080/19942060.2018.1439773. URL: https://www.tandfonline.com/doi/full/10.1080/19942060.2018.1439773 (visited on 04/23/2026).

[36] E. Lotovskyi, L. Moreira, and A.P. Teixeira. “Assessment of ship manoeuvring models for the development of a collision risk evaluation framework”. en. In: *Ocean Engineering* 342 (Dec. 2025), p. 123111. ISSN: 00298018. DOI: 10.1016/j.oceaneng.2025.123111. URL: https://linkinghub.elsevier.com/retrieve/pii/S0029801825027945 (visited on 03/10/2026).

[37] Hai-peng Guo and Zao-jian Zou. “System-based investigation on 4-DOF ship maneuvering with hydrodynamic derivatives determined by RANS simulation of captive model tests”. en. In: *Applied Ocean Research* 68 (Oct. 2017), pp. 11–25. ISSN: 01411187. DOI: 10.1016/j.apor.2017.08.006. URL: https://linkinghub.elsevier.com/retrieve/pii/S0141118717304637 (visited on 05/21/2026).

[38] K. Nomoto et al. “On the steering qualities of ships”. In: *International Shipbuilding Progress* 4.35 (1957), pp. 354–370. DOI: 10.3233/isp-1957-43504.

[39] Haitong Xu et al. “Real-Time Parameter Estimation of a Nonlinear Vessel Steering Model Using a Support Vector Machine”. en. In: *Journal of Offshore Mechanics and Arctic Engineering* 141.6 (Dec. 2019), p. 061606. ISSN: 0892-7219, 1528-896X. DOI: 10.1115/1.4043806. URL: https://asmedigitalcollection.asme.org/offshoremechanics/article/doi/10.1115/1.4043806/726726/RealTime-Parameter-Estimation-of-a-Nonlinear (visited on 03/11/2026).

[40] Serge Sutulo and C. Guedes Soares. “Nomoto-type manoeuvring mathematical models and their applicability to simulation tasks”. en. In: *Ocean Engineering* 304 (July 2024), p. 117639. ISSN: 00298018. DOI: 10.1016/j.oceaneng.2024.117639. URL: https://linkinghub.elsevier.com/retrieve/pii/S0029801824009764 (visited on 03/10/2026).

[41] Omer Faruk Sukas, Omer Kemal Kinaci, and Sakir Bal. “Theoretical background and application of MANSIM for ship maneuvering simulations”. en. In: *Ocean Engineering* 192 (Nov. 2019), p. 106239. ISSN: 00298018. DOI: 10.1016/j.oceaneng.2019.106239. URL: https://linkinghub.elsevier.com/retrieve/pii/S0029801819304184 (visited on 04/08/2026).

[42] Youjun Yang and Ould El Moctar. “A mathematical model for ships maneuvering in deep and shallow waters”. en. In: *Ocean Engineering* 295 (Mar. 2024), p. 116927. ISSN: 00298018. DOI: 10.1016/j.oceaneng.2024.116927. URL: https://linkinghub.elsevier.com/retrieve/pii/S0029801824002646 (visited on 07/10/2026).

[43] Hironori Yasukawa et al. “MMG Prediction of High-Speed Planing Hull Turning Circles”. en. In: *International Conference on Fast Sea Technology (FAST)* (Oct. 2025).

[44] H. Yasukawa, R. Sakuno, and Y. Yoshimura. “Practical maneuvering simulation method of ships considering the roll-coupling effect”. en. In: *Journal of Marine Science and Technology* 24.4 (Dec. 2019), pp. 1280–1296. ISSN: 0948-4280, 1437-8213. DOI: 10.1007/s00773-019-00625-4. URL: http://link.springer.com/10.1007/s00773-019-00625-4 (visited on 03/25/2026).

[45] Yo Fukui et al. “4-DOF Mathematical Model for Manoeuvring Simulation including Roll Motion”. en. In: *Journal of the Japan Society of Naval Architects and Ocean Engineers* 24.0 (2016), pp. 167–179. ISSN: 1880-3717, 1881-1760. DOI: 10.2534/jjasnaoe.24.167. URL: https://www.jstage.jst.go.jp/article/jjasnaoe/24/0/24_167/_article/-char/ja/ (visited on 04/09/2026).

[46] R. Okuda, H. Yasukawa, and A. Matsuda. “Validation of maneuvering simulations for a KCS at different forward speeds using the 4-DOF MMG method”. en. In: *Ocean Engineering* 284 (Sept. 2023), p. 115174. ISSN: 00298018. DOI: 10.1016/j.oceaneng.2023.115174. URL: https://linkinghub.elsevier.com/retrieve/pii/S0029801823015585 (visited on 04/09/2026).

[47] Toru Katayama and Yoshiho Ikeda. “Characteristics of Hydrodynamic Forces Acting on Rapidly Accelerated Planing Craft from Rest”. en. In: *Proceedings of the Fourth International Conference on Hydrodynamics* 1 (2000).

[48] Sasan Tavakoli, Parviz Ghadimi, and Abbas Dashtimanesh. “A nonlinear mathematical model for coupled heave, pitch, and roll motions of a high-speed planing hull”. en. In: *Journal of Engineering Mathematics* 104.1 (June 2017), pp. 157–194. ISSN: 0022-0833, 1573-2703. DOI: 10.1007/s10665-016-9878-2. URL: http://link.springer.com/10.1007/s10665-016-9878-2 (visited on 04/09/2026).

[49] Kazem Sadati and Hamid Zeraatgar. “Simulation of turning maneuver using the 4+2DOF method in planing and semi-planing modes”. en. In: *Ocean Engineering* 287 (Nov. 2023), p. 115763. ISSN: 00298018. DOI: 10.1016/j.oceaneng.2023.115763. URL: https://linkinghub.elsevier.com/retrieve/pii/S0029801823021479 (visited on 03/30/2026).

[50] Chuanai Wang et al. “Numerical simulation study on ship manoeuvrability in mountainous rivers: Comprehensively considering effects of nonuniform flow, shallow water, narrow banks, winds and waves”. en. In: *Ocean Engineering* 306 (Aug. 2024), p. 118109. ISSN: 00298018. DOI: 10.1016/j.oceaneng.2024.118109. URL: https://linkinghub.elsevier.com/retrieve/pii/S0029801824014471 (visited on 03/12/2026).

[51] Matteo Diez et al. “Multi-Fidelity MMG-Model for Digital Design of High-Speed Small Craft”. en. In: *SNAME Chesapeake Power Boat Symposium*. Norfolk, Virginia, USA: SNAME, Oct. 2024, D011S002R003. DOI: 10.5957/CPBS-2024-008. URL: https://onepetro.org/snamecpbs/proceedings/CPBS24/CPBS24/D011S002R003/570539 (visited on 03/10/2026).

[52] H. Yasukawa, T. Ishikawa, and Y. Yoshimura. “Investigation on the rudder force of a ship in large drifting conditions with the MMG model”. en. In: *Journal of Marine Science and Technology* 26.4 (Dec. 2021), pp. 1078–1095. ISSN: 0948-4280, 1437-8213. DOI: 10.1007/s00773-020-00789-4. URL: https://link.springer.com/10.1007/s00773-020-00789-4 (visited on 04/09/2026).

[53] S. Inoue, M. Hirano, and K. Kijima. “Hydrodynamic derivatives on ship manoeuvring”. en. In: *International Shipbuilding Progress* 28.321 (May 1981), pp. 112–125. ISSN: 15662829, 0020868X. DOI: 10.3233/ISP-1981-2832103. URL: https://journals.sagepub.com/doi/full/10.3233/ISP-1981-2832103 (visited on 05/13/2026).

[54] Yasuo Yoshimura. “Mathematical Model for Manoeuvring Ship Motion (MMG Model)”. en. In: *Workshop on Mathematical Models for Operations involving Ship-Ship Interaction* (2005).

[55] Mina Tadros et al. “Ship Manoeuvring Research 2010–2025: From Hydrodynamics and Control to Digital Twins, AI and MASS”. en. In: *Journal of Marine Science and Engineering* 13.12 (Dec. 2025), p. 2322. ISSN: 2077-1312. DOI: 10.3390/jmse13122322. URL: https://www.mdpi.com/2077-1312/13/12/2322 (visited on 03/10/2026).

[56] Motoki Araki et al. “Estimating maneuvering coefficients using system identification methods with experimental, system-based, and CFD free-running trial data”. en. In: *Ocean Engineering* 51 (Sept. 2012), pp. 63–84. ISSN: 00298018. DOI: 10.1016/j.oceaneng.2012.05.001. URL: https://linkinghub.elsevier.com/retrieve/pii/S002980181200162X (visited on 05/21/2026).

[57] Yoshiho Ikeda, Toru Katayama, and Hideaki Okumura. “CHARACTERISTICS OF HYDRODYNAMIC DERIVATIVES IN MANEUVERING EQUATIONS FOR SUPER HIGH-SPEED PLANING HULLS”. en. In: (2000).

[58] Toru Katayama et al. “DEVELOPMENT OF MANEUVERING SIMULATION METHOD FOR HIGH SPEED CRAFT USING HYDRODYNAMIC FORCES OBTAINED FROM MODEL TESTS”. en. In: (2009).

[59] Zi-Hao Wang and Zao-Jian Zou. “Quantifying Multicollinearity in Ship Manoeuvring Modeling by Variance Inflation Factor”. en. In: *Volume 7A: Ocean Engineering*. Madrid, Spain: American Society of Mechanical Engineers, June 2018, V07AT06A001. ISBN: 978-0-7918-5126-5. DOI: 10.1115/OMAE2018-77121. URL: https://asmedigitalcollection.asme.org/OMAE/proceedings/OMAE2018/51265/Madrid,%20Spain/277714 (visited on 05/19/2026).

[60] Hyeon Kyu Yoon and Key Pyo Rhee. “Identification of hydrodynamic coefficients in ship maneuvering equations of motion by Estimation-Before-Modeling technique”. en. In: *Ocean Engineering* 30.18 (Dec. 2003), pp. 2379–2404. ISSN: 00298018. DOI: 10.1016/S0029-8018(03)00106-9. URL: https://linkinghub.elsevier.com/retrieve/pii/S0029801803001069 (visited on 05/19/2026).

[61] Yasuo Yoshimura and Yumiko Masumoto. “Hydrodynamic Force Database with Medium High Speed Merchant Ships Including Fishing Vessels and Investigation into a Maneuvering Prediction Method (translated by Y. Yoshimura)”. en. In: *Journal of JASNAOE* 14 (Dec. 2011). URL: https://www.researchgate.net/publication/347907046_HYDRODYNAMIC_DATABASE_AND_MANOEUVRING_PREDICTION_METHOD_WITH_MEDIUM_HIGH-SPEED_MERCHANT_SHIPS_AND_FISHING_VESSELS#fullTextFileContent.

[62] F. Stern et al. “Experience from SIMMAN 2008—The First Workshop on Verification and Validation of Ship Maneuvering Simulation Methods”. en. In: *Journal of Ship Research* 55.02 (June 2011), pp. 135–147. ISSN: 0022-4502, 1542-0604. DOI: 10.5957/jsr.2011.55.2.135. URL: https://onepetro.org/JSR/article/55/02/135/173675/Experience-from-SIMMAN-2008-The-First-Workshop-on (visited on 04/19/2026).

[63] Kun Dai and Yunbo Li. “Manoeuvring Prediction of KVLCC2 with Hydrodynamic Derivatives Generated by a Virtual Captive Model Test”. en. In: *Polish Maritime Research* 26.4 (Dec. 2019), pp. 16–26. ISSN: 2083-7429. DOI: 10.2478/pomr-2019-0062. URL: https://reference-global.com/article/10.2478/pomr-2019-0062 (visited on 06/08/2026).

[64] Yuxuan Duan et al. “Maneuvering prediction of a twin-propeller twin-rudder high-speed craft based on integrated CFD and empirical methods”. en. In: *Paper presented at the The 34th International Ocean and Polar Engineering Conference*. Rhodes, Greece: International Society of Offshore and Polar Engineers (ISOPE), June 2024.

[65] Zhang Zhu et al. “Study on numerical PMM test and its application to KCS hull”. en. In: *Applied Ocean Research* 127 (Oct. 2022), p. 103327. ISSN: 01411187. DOI: 10.1016/j.apor.2022.103327. URL: https://linkinghub.elsevier.com/retrieve/pii/S0141118722002590 (visited on 05/13/2026).

[66] Farhad Safari, Mansour Rafeeyan, and Mohammad Danesh. “Estimation of hydrodynamic coefficients and simplification of the depth model of an AUV using CFD and sensitivity analysis”. en. In: *Ocean Engineering* 263 (Nov. 2022), p. 112369. ISSN: 00298018. DOI: 10.1016/j.oceaneng.2022.112369. URL: https://linkinghub.elsevier.com/retrieve/pii/S0029801822016614 (visited on 04/14/2026).

[67] Sajad Hajizadeh, Mohammad seif, and Hamid Mehdigholi. “Determination of ship maneuvering hydrodynamic coefficients using system identification technique based on free-running model test”. In: *Scientia Iranica* 23 (Oct. 2016), pp. 2154–2165. DOI: 10.24200/sci.2016.3945.

[68] Elías Revestido Herrero and Francisco J. Velasco González. “Two-step identification of non-linear manoeuvring models of marine vessels”. en. In: *Ocean Engineering* 53 (Oct. 2012), pp. 72–82. ISSN: 00298018. DOI: 10.1016/j.oceaneng.2012.07.010. URL: https://linkinghub.elsevier.com/retrieve/pii/S0029801812002429 (visited on 03/12/2026).

[69] Jialun Liu et al. “An integrated empirical manoeuvring model for inland vessels”. en. In: *Ocean Engineering* 137 (June 2017), pp. 287–308. ISSN: 00298018. DOI: 10.1016/j.oceaneng.2017.04.008. URL: https://linkinghub.elsevier.com/retrieve/pii/S002980181730183X (visited on 06/10/2026).

[70] R. P. Gokarn. *A Study of Ship Manoeuvrability*. en. Singapore: Springer Nature Singapore, 2024. ISBN: 978-981-97-0624-2 978-981-97-0625-9. DOI: 10.1007/978-981-97-0625-9. URL: https://link.springer.com/10.1007/978-981-97-0625-9 (visited on 03/18/2026).

[71] Yasuo Yoshimura et al. “Empirical formulas of hydrodynamic parameters for predicting ship maneuvering based on the MMG-model”. en. In: *Ocean Engineering* 337 (Oct. 2025), p. 121831. ISSN: 00298018. DOI: 10.1016/j.oceaneng.2025.121831. URL: https://linkinghub.elsevier.com/retrieve/pii/S0029801825015379 (visited on 05/13/2026).

[72] Matteo Bonci et al. “The heel-induced sway force and yaw moment of a high-speed craft in following regular waves”. en. In: *Journal of Marine Science and Technology* 25.1 (Mar. 2020), pp. 312–325. ISSN: 0948-4280, 1437-8213. DOI: 10.1007/s00773-019-00637-0. URL: http://link.springer.com/10.1007/s00773-019-00637-0 (visited on 04/09/2026).

[73] Evan Lee, Charles R Weil, and Anne Fullerton. *Experimental Results for the Calm Water Resistance of the Generic Prismatic Planing Hull (GPPH)*. en. Tech. rep. NSWCCD-80-TR-2017/015. Naval Surface Warfare Center Carderock Division, 2017.

[74] Evan J. Lee et al. “Benchmark Testing of Generic Prismatic Planing Hull (GPPH) for Validation of CFD Tools”. en. In: *SNAME 30th American Towing Tank Conference*. West Bethesda, Maryland, USA: SNAME, Oct. 2017, D011S002R009. DOI: 10.5957/ATTC-2017-0023. URL: https://onepetro.org/snameattc/proceedings/ATTC17/ATTC17/D011S002R009/475755 (visited on 04/09/2026).

[75] Sungtek Park. “Free running 6 degree of freedom CFD for high-speed small craft”. en. In: (2022). Medium: application/pdf. DOI: 10.25820/ETD.006789. URL: https://iro.uiowa.edu/esploro/outputs/doctoral/9984362557602771 (visited on 10/24/2026).

[76] *12416 Damen Crew tender 12M*. URL: https://mdhbv.nl/object/crew-tender-12m/.

[77] Anil Kumar Dash et al. “Roll-induced bifurcation in ship maneuvering under model uncertainty”. en. In: *Journal of Marine Science and Technology* 21.4 (Dec. 2016), pp. 689–708. ISSN: 0948-4280, 1437-8213. DOI: 10.1007/s00773-016-0382-1. URL: http://link.springer.com/10.1007/s00773-016-0382-1 (visited on 08/31/2026).

[78] Yeon-Gyu Kim et al. “Prediction of the maneuverability of a large container ship with twin propellers and twin rudders”. en. In: *Journal of Marine Science and Technology* 12.3 (Sept. 2007), pp. 130–138. ISSN: 0948-4280, 1437-8213. DOI: 10.1007/s00773-007-0246-9. URL: http://link.springer.com/10.1007/s00773-007-0246-9 (visited on 08/31/2026).

[79] Sahbi Khanfir et al. “Manoeuvring characteristics of twin-rudder systems: rudder-hull interaction effect on the manoeuvrability of twin-rudder ships”. en. In: *Journal of Marine Science and Technology* 16.4 (Dec. 2011), pp. 472–490. ISSN: 0948-4280, 1437-8213. DOI: 10.1007/s00773-011-0140-3. URL: http://link.springer.com/10.1007/s00773-011-0140-3 (visited on 08/31/2026).

[80] R. Okuda et al. “Maneuvering simulations of twin-propeller and twin-rudder ship in shallow water using equivalent single rudder model”. en. In: *Journal of Marine Science and Technology* 27.2 (June 2022), pp. 948–970. ISSN: 0948-4280, 1437-8213. DOI: 10.1007/s00773-022-00881-x. URL: https://link.springer.com/10.1007/s00773-022-00881-x (visited on 09/10/2026).

A. Simulations input tables

A.1. 3DOF MMG model

Table A.1: Input data 3DOF displacement simulations; KVLCC2 data from [22], KCS data from [46]. The numbers marked with a star* have a different origin and are elaborated further in the Section 3.1 and Section 3.2.

		KVLCC2		KCS	
Scale	$1:\lambda$	1:45.7	1:1	1:65.833	1:1
Geometry	L_{pp} [m]	7.0	320.0	3.494	230
	B [m]	1.27	58.0	0.489	32.2
	d [m]	0.46	20.8	0.164	10.8
	∇ [m^3]	3.27	312 600	0.182	52 043
	C_b [-]	0.81		0.651	
	x_G [m]	0.25	11.2	-0.051	-3.39
	m'_x [-]	0.022		0.006	
	m'_y [-]	0.223		0.152	
	J'_z [-]	0.011		0.009	
Surge	R'_0* [-]	0.0176*	0.0199*	0.0194*	0.0174*
	X'_{vv} [-]	-0.040		-0.087	
	X'_{vr} [-]	0.002		-0.093	
	X'_{rr} [-]	0.011		-0.023	
	X'_{vvvv} [-]	0.771		0.809	
Sway	Y'_v [-]	-0.315		-0.243	
	Y'_r [-]	0.083		0.055	
	Y'_{vvv} [-]	-1.607		-1.675	
	Y'_{vvr} [-]	0.379		-0.083	
	Y'_{vrr} [-]	-0.391		-0.447	
	Y'_{rrr} [-]	0.008		0.020	
Yaw	N'_v [-]	-0.137		-0.105	
	N'_r [-]	-0.049		-0.036	
	N'_{vvv} [-]	-0.030		-0.288	
	N'_{vvr} [-]	-0.294		-0.579	
	N'_{vrr} [-]	0.055		-0.003	
	N'_{rrr} [-]	-0.013		-0.042	

		KVLCC2		KCS	
Scale	$1:\lambda$	1:45.7	1:1	1:65.833	1:1
Propeller	D_P [m]	0.216	9.86	0.12	7.9
	x_P [m]	-3.34*	-152.73*	-1.67*	-109.90*
	w_{P0} [-]	0.40	0.35	0.316	
	t_P [-]	0.220		0.086	
	k_0 [-]	0.2931		0.355	
	k_1 [-]	-0.2753		-0.281	
	k_2 [-]	-0.1385	-0.1359	-0.166	
	C_1 [-]	2.0		–	–
	$C_2(\beta > 0)$ [-]	1.6		–	–
	$C_2(\beta < 0)$ [-]	1.1		–	–
Rudder	H_R [m]	0.345	15.8	0.15*	9.9*
	A_R [m^2]	0.0539	112.5	0.0126	54.43
	x_R [m]	-3.5	-160	-1.747	-115
	f_α [-]	2.747		2.720*	2.725*
	ε [-]	1.09		0.76	
	κ [-]	0.50		1.03	
	t_R [-]	0.387		0.234	
	a_H [-]	0.312		0.311	
	x'_H [-]	-0.464		-0.586	
	l_R [-]	-0.710		-0.848	
	$\gamma_R(\beta_R > 0)$ [-]	0.640		0.574	
	$\gamma_R(\beta_R < 0)$ [-]	0.395		0.347	
Simulation	$U_{initial}$ [kn]	2.293*	15.5	1.786	14.5
	n_p [rev/s]	11.57*	1.711*	11.4	1.405*
	$Duration$ [s]	200	1500	200	1500
	$Rudder\ rate$ [°/s]	11.90*	1.76	19	2.32

A.2. Additional input data 4DOF MMG model

Table A.2: Additional input data 4DOF displacement simulations; KCS data from [46]. The numbers marked with a star* have a different origin and are elaborated further inSection 3.2.

		KCS	
Scale	$1:\lambda$	1:65.833	1:1
Geometry	k'_{xx} [-]	0.44	0.44
	J'_{xx} [-]	- *	- *
	GM [m]	0.038	2.5
	KM [m]	0.214	14.1
	z_H [m]	0.056	3.704
	α_z [m]	0.056*	3.704*
Surge	$X'_{v\phi}$	0.01	0.01
	$X'_{r\phi}$	0.009	0.009
	$X'_{\phi\phi}$	-0.002	-0.002
Sway	Y'_{ϕ}	0.001	0.001
	$Y'_{vv\phi}$ [-]	0.161	0.161
	$Y'_{v\phi\phi}$	-0.243	-0.243
	$Y'_{rr\phi}$	0.0	0.0
	$Y'_{r\phi\phi}$	-0.13	-0.13
Yaw	N'_{ϕ} [-]	-0.009	-0.009
	$N'_{vv\phi}$ [-]	-0.327	-0.327
	$N'_{v\phi\phi}$ [-]	-0.232	-0.232
	$N'_{rr\phi}$ [-]	0.0	0.0
	$N'_{r\phi\phi}$ [-]	0.041	0.041
Roll	a [-]	0.031	0.031
	b $[1/^\circ]$	0.002	0.002
Propeller	z_P	0.102*	6.7*
Rudder	z_R [m]	0.089*	5.85*

A.3. Twin-propeller twin-rudder model

Table A.3: Input data twin-propeller twin-rudder displacement simulations; model data from [80]. The numbers marked with a star* have a different origin and are elaborated further in Section 3.3.2.

TPTR 4DOF model			
Scale	$1:\lambda$	1:33.33	1:1
Geometry	L_{pp} [m]	3.0	100
	B [m]	0.54	18
	d [m]	0.1455	4.85
	∇ [m^3]	0.1295	4797
	C_b [-]	0.549	
	x_G [m]	-0.071	-2.36
	m'_x [-]	0.007	
	m'_y [-]	0.134	
	J'_z [-]	0.008	
	k'_{xx} [-]	0.458	
	$\overline{\mathrm{GM}}_T$ [m]	0.045	1.5
	KM [m]	0.286	9.51
	ρ [kg/m^3]	1000	1025
Propeller	D_P [m]	0.1	3.33
	x'_P [-]	0.05	
	z'_P [-]	0.588	
	$y'_{P,\mathrm{SB}}$ [-]	0.167	
	$y'_{P,\mathrm{BB}}$ [-]	-0.167	
	w_{P0} [-]	0.33	
	t_P [-]	0.105	
	k_0 [-]	0.355	0.4
	k_1 [-]	-0.281	-0.307
	k_2 [-]	-0.166	-0.115
Rudder	H_R [m]	0.1082	3.6
	A_R [m^2]	0.00849	9.4
	x_R [m]	-1.5	-50
	z_R [m]	0.0914	3.05
	$y'_{R,\mathrm{SB}}$ [-]	0.167	
	$y'_{R,\mathrm{BB}}$ [-]	-0.167	
	f_α [-]	2.33	
	ε [-]	0.79	
	κ [-]	0.72	
	t_R [-]	0.043	
	a_H [-]	0.229	
	x'_H [-]	-0.508	
	l'_R [-]	-0.8	
	$\gamma_R(\beta_R > 0)$ [-]	0.385	
	$\gamma_R(\beta_R < 0)$ [-]	0.385	
Simulation	$U_{initial}$ [kn]	1.385	–
	n_p [rev/s]	9.9	–
	$Duration$ [s]	100	–
	$Rudder\ rate$ [°/s]	13.3	2.32

TPTR 4DOF model			
Scale	$1:\lambda$	1:33.33	1:1
Surge	R'_0 [-]	0.0194	0.0254
	X'_{vv} [-]	-0.082	
	X'_{vr} [-]	-0.037	
	X'_{rr} [-]	-0.004	
	X'_{vvvv} [-]	0.632	
Sway	Y'_v [-]	-0.412	
	Y'_r [-]	0.042	
	Y'_{vvv} [-]	-1.712	
	Y'_{vvr} [-]	-0.801	
	Y'_{vrr} [-]	-0.632	
	Y'_{rrr} [-]	-0.027	
Yaw	N'_v [-]	-0.128	
	N'_r [-]	-0.066	
	N'_{vvv} [-]	-0.378	
	N'_{vvr} [-]	-0.641	
	N'_{vrr} [-]	-0.145	
	N'_{rrr} [-]	-0.035	
Roll	J'_{xx} [-]	0	
	α_z [m]	$0.344\,d$	
	z_H [m]	$0.344\,d$	
	a [-]	0.05	0.15
	b [-]	0.002	0.2
Roll coupling	$X'_{v\phi}$ [-]	0.03	
	$X'_{r\phi}$ [-]	0.014	
	$X'_{\phi\phi}$ [-]	-0.017	
	Y'_ϕ [-]	0.014	
	$Y'_{vv\phi}$ [-]	0.123	
	$Y'_{v\phi\phi}$ [-]	-0.174	
	$Y'_{rr\phi}$ [-]	0.0	
	$Y'_{r\phi\phi}$ [-]	-0.139	
	N'_ϕ [-]	-0.012	
	$N'_{vv\phi}$ [-]	-0.303	
	$N'_{v\phi\phi}$ [-]	-0.082	
	$N'_{rr\phi}$ [-]	0.0	
	$N'_{r\phi\phi}$ [-]	0.112	

A.4. Empirical coefficients model

Definitions of the parameters in the empirical formulae [5].

B_{ac}	Average wetted chine beam
β	Deadrise angle midship
$k(\beta)$	Hull added mass function (note: β in deg)
L_K	Wetted length keel
L_C	Wetted length chine
T	Transom draft (note: $T' = T/B$)
C_V	Speed coefficient
F_ϕ	Roll-induced change in dynamic normal force (one side) (note: τ in rad)
L	Length overall
τ	Dynamic trim (positive bow up)
KG	Vertical height of centre of gravity from keel (note: $KG' = KG/B$)
λ	Mean wetted length over beam ratio
h_1	Transfer of axes lever arm
$K_{D\phi}$	Dynamic roll moment rate
f_{sw}	Side wetting correction factor
KB	Estimated vertical centre of static lift
Δ	"Static" lift, i.e. buoyancy force
LCG	Longitudinal centre of gravity measured from transom
LCP	Longitudinal centre of pressure measured from transom
h_2	Lever arm for dynamic hull force (needed for $K_{D\phi}$)
L_{C2}	Chine length subject to side wetting (note: own definition, needed for f_{sw})

Some coefficients require preliminary calculations, these are done as follows [5]:

$$
\begin{aligned}
\lambda &= (L_K + L_C)/2B \\
C_V &= U/\sqrt{gB} \\
k(\beta) &= 0.06641 + 0.00716\beta + 0.0003861\beta^2 \\
h_1 &= (KG - 0.3927B\tan\beta)(KG - 0.306B) \\
\Delta &= 0.25\,\rho g\lambda^2 \sin 2\tau\, B^3 \\
KB &= B\tan\beta\,[0.5 + L_C/L_K]/6 \\
h_2 &= 0.8\pi B/(8\cos\beta) - KG\sin\beta \\
F_\phi &= -\frac{1}{4\cos^2\beta}\left\{\left[(1-\sin\beta)\,\frac{\pi\lambda}{1+\lambda} + \frac{1.33}{\pi}\right]\tau + \frac{1-\sin\beta}{\cos\beta}\,\frac{1}{2(1+\lambda)^2}\right\}\cdot\frac{1}{2}\rho U^2 B^2 \\
K_{D\phi} &= 2h_2 F_\phi \\
L_{C2} &= L_C - 3U^2\sin\tau/g \\
f_{sw} &= \begin{cases} 1, & U^2 > gB\,(\lambda - 0.16\tan\beta/\tan\tau)/3\sin\tau \\ 1 + 0.603L_{C2}/\lambda B, & U^2 < gB\,(\lambda - 0.16\tan\beta/\tan\tau)/3\sin\tau \end{cases} \\
LCP &= \lambda B\left[0.75 - 1\Big/\left(5.21\frac{C_V^2}{\lambda^2} + 2.39\right)\right]
\end{aligned}
$$

A.5. General Prismatic Planing Hull (GPPH) model

Table A.4: Input data GPPH simulations; model data from [19, 30, 43].

GPPH model		
Scale	$1:\lambda$	1:5.30
Geometry	L_{pp} [m]	2.414
	B_{ac} [m]	0.627
	d_0 [m]	0.1476
	$trim_0$ [°]	0.127
	$displ_0$ [m^3]	0.102488
	$L_K, 0$ [m]	1.664
	$L_C, 0$ [m]	0.762
	m'_x [-]	0.075 $displ_0$
	k'_{xx} [-]	0.12L_{PP}
	k'_{zz} [-]	0.32L_{PP}
	$\overline{\mathrm{GM}}_T$ [m]	0.344
	KM [m]	0.482
	KG [m]	0.138
	ρ [kg/m^3]	1000
	$\beta_{midship}$ [°]	17.2
	LCG [m]	0.844
	$T_{transom,static}$ [m]	0.148
	$x_{transom}$ [m]	-0.5L_{PP}
	$L_{towpoint}$ [m]	0.8597
Propulsion	x'_P [-]	-0.4L_{PP}
	z'_P [-]	0.078 L_{PP}
	y'_P [-]	0.261
	w_{P0} [-]	0.05
	D_P [m]	0.133
Steering	x_{GC}	-0.406 L_{PP}
	z_{GC}	0.085 L_{PP}
	φ_R [°]	0
Simulation	$U_{initial}$ [kn]	17.5
	n_p [rev/s]	55.8
	$Rudder\ rate$ [°/s]	46.2

Table A.5: Running attitude GPPH model as function of speed. The Absolute Pitch is the static trim added to the measured trim and is the value used for the running attitude. Data is from [73].

U [kn]	Fn_∇ [-]	Heave [m]	Trim [°]	Abs. pitch [°]	L_K [m]	L_C [m]
10.8	2.60	0.0745	5.8054	5.9324	1.6510	1.0922
13.0	3.13	0.0817	4.8832	5.0102	1.6256	0.9779
14.8	3.56	0.0849	4.2191	4.3461	1.6383	0.8890
17.5	4.21	0.0906	3.4218	3.5488	1.6637	0.7620
19.5	4.69	0.0927	2.9597	3.0867	1.6891	0.6731
21.6	5.19	0.0947	2.5376	2.6646	1.7082	0.5588
23.8	5.72	0.0960	2.1666	2.2936	1.7272	0.4445

B. Final simulation model

Listing 1: Propulsion force models; the gear-case (GC) is used for the GPPH and the twin-propeller model (SB and BB) for the pilot vessel.

```
def propeller_force_GC(self, u: float, v: float, U: float, nps: float,
                   beta: float, r: float, r_dash: float, delta: float,
                   p: float = 0.0,  p_dash: float = 0.0, phi: float = 0.0):
    """
    Returns:
        X_P  : surge propeller thrust [N]
        J    : advance ratio [-]
        K_T  : thrust coefficient [-]
        w_P  : effective wake fraction [-]

    Non-dimensional
        F_N = 0.5 * rho * Lpp * d * U_0²
    """
    d = self.d
    g = self.g

    x_P_dash = g.x_P_dash
    x_P = x_P_dash * g.Lpp        # dimensional lever arm [m]
    z_P_dash = g.z_P_dash
    z_P = z_P_dash * g.Lpp        # dimensional lever arm [m]
    y_P = g.y_P_dash * g.Lpp        # dimensional lever arm [m]

    # Inflow angle at propeller disc (drift angle corrected for propeller offset)
    beta_P = beta - x_P_dash * r_dash + z_P_dash * p_dash  # [-]

    # Wake fraction: Gaussian falloff with inflow angle
    brackets = np.exp(-4 * beta_P**2) #Yasukawa et al., 2015
    w_P = d.w_P0 * brackets
    w_P = float(np.clip(w_P, 0.0, 0.99))       # physical bound

    n = abs(nps)
    if n < 1e-6:
        # Stopped propeller - no thrust
        return 0.0, 0.0, 0.0, 0.0, 0.0, 0.0, w_P

    V_A = (u - y_P*r)*(1.0 - w_P)
    J = V_A / (n * g.D_p)                      # [-]

    # --- velocities to BODY FRAME ---
    trim_rad = np.radians(self._attitude_current(U)[0])   # RUNNING ATTITUDE
    #BF --- geometries derived from Wang et al. (2025) Physical analysis ...
    x_P_b = - 0.4 * g.Lpp #due to sign convention, x_GC is negative aft of COG
    z_P_b = 0.078 * g.Lpp

    u_b, v_b, _ = self.horizontal_to_body(u, v, phi, trim_rad, 0.0)  # hull drift at G; v = sway at G
    U_b    = np.sqrt(u_b**2 + v_b**2)
    beta_b = np.arctan2(-v_b, u_b)

    if self.kt_curve_GC is not None:
        J_P = U / (n * g.D_p)                  # [-]
        Fr  = U / np.sqrt(G_GRAV * g.Lpp)      # [-]
        K_T = self.kt_curve_GC(J_P, Fr)
    else:
        J_P = U_b / (n * g.D_p)                    # [-]
```

```
        # Open-water thrust coefficient (quadratic polynomial)
        if self.kt_curve is not None:
            K_T = self.kt_curve(J_P)
        else:
            K_T = d.k_0 + d.k_1 * J_P + d.k_2 * J_P**2

    # Thrust, accounting for thrust deduction fraction t_P
    sign_nps = 1.0 if nps >= 0 else -1.0
    T = g.rho * K_T * n**2 * g.D_p**4 * sign_nps

    # --- lateral and vertical forces acting on the GC
    pitch = trim_rad
    tilt = 0

    q = 0.5 * g.rho * U_b**2
    scaling = g.Lpp / 6.4516
    numerator_deg_to_rad = 180/np.pi
    in2_to_m2 = 0.00064516

    Y_P_dash = -q * (delta - beta_b) * 0.6 *scaling**2 *numerator_deg_to_rad #in2/rad
    Z_P_dash = -q * (tilt + pitch) * 1.4 *scaling**2 *numerator_deg_to_rad #in2/rad

    Fy_P = Y_P_dash * in2_to_m2 #N
    Fz_P = Z_P_dash * in2_to_m2 #N

    X_P_b = T * np.cos(delta) + Fy_P * np.sin(beta_b) - Fz_P * np.sin(pitch)
    Y_P_b = -T * np.sin(delta) + Fy_P * np.cos(beta_b) + Fz_P * np.cos(pitch) * np.sin(phi)
    Z_P_b = Fz_P * np.cos(pitch) * np.cos(phi) #N
    K_P_b = -Y_P_b * z_P_b
    M_P_b = X_P_b * z_P_b - Z_P_b * x_P_b
    N_P_b = Y_P_b * x_P_b

    # --- rotate to HORIZONTAL FRAME ---
    X_P, Y_P, Z_P = self.body_to_horizontal(X_P_b, Y_P_b, Z_P_b, phi, pitch)
    K_P_g, M_P_g, N_P_g = self.body_to_horizontal(K_P_b, M_P_b, N_P_b, phi, pitch)

    #HF --- transfer to midship reference  ---
    x_G = self.x_G
    y_G, z_G = self._cg_vertical_offset(phi)

    K_P = K_P_g + y_G * Z_P - z_G * Y_P
    M_P = M_P_g + z_G * X_P - x_G * Z_P
    N_P = N_P_g + x_G * Y_P - y_G * X_P

    return X_P, Y_P, K_P, N_P, J_P, K_T, w_P     # J_P = the J used for K_T

def propeller_force_SB(self, u: float, U: float, nps: float,
                       beta: float, r_dash: float,
                       p_dash: float = 0.0):
    """Thrust from the open-water KT polynomial.

    Args:
        u      : surge velocity [m/s]
        nps    : propeller revolutions per second [rev/s], positive = ahead
        beta   : drift angle at CG [rad]  (computed in dynamics())
        r_dash : non-dim yaw rate r*Lpp/U [-]
        p_dash : non-dim roll rate p*Lpp/U [-]

    Returns:
        X_P  : surge propeller thrust [N]
        J    : advance ratio [-]
        K_T  : thrust coefficient [-]
        w_P  : effective wake fraction [-]

    Non-dimensional
        F_N = 0.5 * rho * Lpp * d * U_0²
    """
    d = self.d
    g = self.g

    x_P_SB_dash = g.x_P_dash
    z_P_SB_dash = g.z_P_dash
    y_P_SB = g.y_P_dash * g.B_ac        # dimensional lever arm [m]
```

```
    r = r_dash * U / g.Lpp              # recover dimensional yaw rate [rad/s]

    # Inflow angle at propeller disc (drift angle corrected for propeller offset)
    beta_P_SB = beta - x_P_SB_dash * r_dash + z_P_SB_dash * p_dash  # [-]

    # Wake fraction: Gaussian falloff with inflow angle
    beta_P = beta_P_SB
    brackets = np.exp(-4 * beta_P**2) #Yasukawa et al., 2015
    w_P = d.w_P0 * brackets
    w_P_SB = float(np.clip(w_P, 0.0, 0.99))       # physical bound


    n = abs(nps)
    if n < 1e-6:
        # Stopped propeller - no thrust
        return 0.0, 0.0, 0.0, w_P_SB

    # Advance ratio  J = V_A / (n * D_p)
    V_A_SB = (u - y_P_SB*r)*(1.0 - w_P_SB)
    J_SB = V_A_SB / (n * g.D_p)                     # [-]

    # Open-water thrust coefficient (quadratic polynomial)
    if self.kt_curve is not None:
        K_T_SB = self.kt_curve(J_SB)
    else:
        K_T_SB = d.k_0 + d.k_1 * J_SB + d.k_2 * J_SB**2

    # Thrust, accounting for thrust deduction fraction t_P
    sign_nps = 1.0 if nps >= 0 else -1.0
    T = g.rho * K_T_SB * n**2 * g.D_p**4 * sign_nps
    X_P_SB = (1.0 - d.t_P) * T

    N_P_SB = -X_P_SB * y_P_SB

    return X_P_SB, N_P_SB, J_SB, K_T_SB, w_P_SB

def propeller_force_BB(self, u: float, U: float, nps: float,
                       beta: float, r_dash: float,
                       p_dash: float = 0.0):
        """Thrust from the open-water KT polynomial.

        Args:
            u      : surge velocity [m/s]
            nps    : propeller revolutions per second [rev/s], positive = ahead
            beta   : drift angle at CG [rad]  (computed in dynamics())
            r_dash : non-dim yaw rate r*Lpp/U [-]
            p_dash : non-dim roll rate p*Lpp/U [-]

        Returns:
            X_P  : surge propeller thrust [N]
            J    : advance ratio [-]
            K_T  : thrust coefficient [-]
            w_P  : effective wake fraction [-]

        Non-dimensional
            F_N = 0.5 * rho * Lpp * d * U_0²
        """
        d = self.d
        g = self.g

        x_P_BB_dash = g.x_P_dash
        y_P_BB_dash = -g.y_P_dash
        z_P_BB_dash = g.z_P_dash

        y_P_BB = y_P_BB_dash * g.B_ac        # dimensional lever arm [m]
        r = r_dash * U / g.Lpp              # recover dimensional yaw rate [rad/s]


        # Inflow angle at propeller disc (drift angle corrected for propeller offset)
        beta_P_BB = beta - x_P_BB_dash * r_dash + z_P_BB_dash * p_dash  # [-]

        # Wake fraction: Gaussian falloff with inflow angle
        beta_P = beta_P_BB
```

```
        brackets = np.exp(-4 * beta_P**2) #Yasukawa et al., 2015
        w_P = d.w_P0 * brackets
        w_P_BB = float(np.clip(w_P, 0.0, 0.99))       # physical bound

        n = abs(nps)
        if n < 1e-6:
            # Stopped propeller - no thrust
            return 0.0, 0.0, 0.0, w_P_BB

        # Advance ratio  J = V_A / (n * D_p)
        V_A_BB = (u - y_P_BB*r)*(1.0 - w_P_BB)
        J_BB = V_A_BB / (n * g.D_p)                       # [-]

        # Open-water thrust coefficient (quadratic polynomial)
        if self.kt_curve is not None:
            K_T_BB = self.kt_curve(J_BB)
        else:
            K_T_BB = d.k_0 + d.k_1 * J_BB + d.k_2 * J_BB**2

        # Thrust, accounting for thrust deduction fraction t_P
        sign_nps = 1.0 if nps >= 0 else -1.0
        T = g.rho * K_T_BB * n**2 * g.D_p**4 * sign_nps
        X_P_BB = (1.0 - d.t_P) * T

        N_P_BB = -X_P_BB * y_P_BB

        return X_P_BB, N_P_BB, J_BB, K_T_BB, w_P_BB
```

Listing 2: Steering force models; the gear-case (GC) is used for the GPPH and the twin-rudder (SB and BB) model for the pilot vessel.

```
    def _rudder_forces_GC(self, u: float, v: float, U: float, r: float, p: float, delta: float, phi:
    ↪  float):
        """
        Computes the forces on the gearcase.

        Returns:
            X_GC, Y_GC, N_GC, K_GC
        """
        d = self.d
        g = self.g

        # --- attitude ---
        trim_rad = np.radians(self._attitude_current(U)[0])   # RUNNING ATTITUDE
        pitch = trim_rad

        # --- velocities to BODY FRAME ---
        #BF --- geometries derived from Wang et al. (2025) Physical analysis ...
        x_GC = -0.406 * g.Lpp   #due to sign convention, x_GC is negative aft of COG
        z_GC = 0.085 * g.Lpp
        tilt_GC = 0

        u_b, v_b, _ = self.horizontal_to_body(u, v, phi, trim_rad, 0.0)  # hull drift at G; v = sway
        ↪  at G
        U_b    = np.sqrt(u_b**2 + v_b**2)
        beta_b = np.arctan2(-v_b, u_b)

        q = 0.5 * g.rho * U_b**2
        scaling = g.Lpp / 6.4516
        numerator_deg_to_rad = 180/np.pi

        X_GC_dash = -q * 3.5 *scaling**2 #in^2
        Y_GC_dash = - q * (delta - beta_b) * 6.8 *scaling**2 *numerator_deg_to_rad #in^2/rad
        Z_GC_dash = -q * (tilt_GC + pitch) * 1 *scaling**2 *numerator_deg_to_rad #in^2/rad

        in2_to_m2 = 0.00064516

        #BF --- gear case forces ---
        Fx_GC =  X_GC_dash *in2_to_m2  # [N]
        Fy_GC =  Y_GC_dash *in2_to_m2   # [N]
        Fz_GC =  Z_GC_dash *in2_to_m2  # [N]

```

```
        X_GC_b = Fx_GC * np.cos(beta_b) + Fy_GC * np.sin(beta_b) - Fz_GC * np.sin(pitch)  # [N]
        Y_GC_b = -Fx_GC * np.sin(beta_b) + Fy_GC * np.cos(beta_b) + Fz_GC * np.cos(pitch) *
        ↪  np.sin(phi)  # [N]
        Z_GC_b = Fz_GC * np.cos(pitch) * np.cos(phi)  # [N]

        K_GC_b = -Y_GC_b * z_GC                          # [Nm]
        M_GC_b = z_GC * X_GC_b - x_GC * Z_GC_b           # [Nm]
        N_GC_b = Y_GC_b * x_GC                           # [Nm]

        # --- rotate to HORIZONTAL FRAME ---
        X_GC, Y_GC, Z_GC = self.body_to_horizontal(X_GC_b, Y_GC_b, Z_GC_b, phi, pitch)
        K_GC_g, M_GC_g, N_GC_g = self.body_to_horizontal(K_GC_b, M_GC_b, N_GC_b, phi, pitch)

        #HF --- transfer to midship reference  ---
        x_G = self.x_G
        y_G, z_G = self._cg_vertical_offset(phi)

        K_GC = K_GC_g + y_G * Z_GC - z_G * Y_GC
        M_GC = M_GC_g + z_G * X_GC - x_G * Z_GC
        N_GC = N_GC_g + x_G * Y_GC - y_G * X_GC

        return X_GC, Y_GC, N_GC, K_GC




    def _rudder_forces_core(self, side: int, u: float, U: float,
                            beta: float, r_dash: float, delta: float, nps: float,
                            J: float, K_T: float, w_P: float,
                            p_dash: float = 0.0, phi: float = 0.0):
        """Forces of one rudder (side = +1 SB, -1 BB), single lift/drag model.

        All motion effects (v, r, p, phi) enter through the local angle of
        attack alpha_R, so no separate static rudder derivatives are needed.

        Sources: Lewandowski (2004) Ch.3 Eqs. 3.29, 3.56, 3.62, 3.108;
                 Ch.6 Table 6.2 (h3); slipstream form Yasukawa & Yoshimura (2015).

        Returns:
            X_R, U_R, Y_R, N_R, K_R, L_R, D_R, v_R, F_N
        """
        d = self.d
        g = self.g

        # --- Geometry ---
        x_R = g.x_R                                  # < 0, aft of midship [m]
        y_R = side * abs(g.y_R)                      # SB +, BB - [m]
        y_P = side * abs(g.y_P_dash) * g.B_ac        # propeller lateral position [m]
        att_trim_deg, att_L_K, _, att_T_transom = self._attitude_current(U)   # RUNNING ATTITUDE
        z_R = self._z_R(att_T_transom)               # > 0, rudder centre below the roll-equation
        ↪  origin [m]; RUNNING ATTITUDE
        trim_rad = np.radians(att_trim_deg)          # RUNNING ATTITUDE

        A_R = g.c_R * g.H_R                          # rudder area [m²]
        if g.rudder_gap:
            AR = g.H_R**2 / A_R                      # gap between rudder and hull
        else:
            AR = 2.0 * g.H_R**2 / A_R                # no gap
        LCS = 1.8 * np.pi / (1.0 + 2.8 / AR)         # lift curve slope, [1/rad]

        # --- Dimensional motion ---
        r = r_dash * U / g.Lpp                       # yaw rate [rad/s]
        p = p_dash * U / g.Lpp                       # roll rate [rad/s]
        v = -U * np.sin(beta)                        # sway velocity at midship [m/s]

        # --- Axial velocity at the rudder (Yasukawa slipstream) ---
        # Rewritten without division by J (also valid at J = 0):
        n = abs(nps)
        eta = min(g.D_p / g.H_R, 1.0)                # rudder fully in slipstream if D_p > H_R
        u_P = (u - y_P * r) * (1.0 - w_P)            # inner propeller sees less inflow in a turn
        ↪  [m/s]
        epsilon = (1.0 - d.w_R) / (1.0 - w_P)        # slipstream efficiency factor
```

```
109         kappa = d.kappa
110         K_T_pos = max(K_T, 0.0)                     # K_T from propeller_force (J uses (u - y_P*r)*(1
            ↪  - w_P))
111         u_jet = np.sqrt(u_P**2 + 8.0 / np.pi * K_T_pos * n**2 * g.D_p**2)
112         core = u_P * (1.0 - kappa) + kappa * u_jet
113         u_R = epsilon * np.sqrt(eta * core**2 + (1.0 - eta) * u_P**2)   # [m/s]
114         u_R = max(u_R, 1e-6)
115
116         # --- Inflow angle and angle of attack ---
117         d_now = self.draft_curve(U)
118         C_B = g.displ / (att_L_K * g.B_ac * d_now)   # block coefficient with RUNNING ATTITUDE
119         gamma_R = min(1.0 / (1.0 + C_B), 1.0)        # flow-straightening coefficient
120
121         # Rudder cant of this rudder: SB +phi_R, BB -phi_R (mirrored pair, tip outward positive).
122         phi_R_s = side * g.phi_R # zero for pilot vessel and gear-case
123
124         # Vertical lever of the blade normal force about the roll axis (Table 6.2 h3).
125         # Lewandowski's h3 = y*sin(phi_F) + (z*cos(trim) - x*sin(trim))*cos(phi_F) uses body
126         # coordinates (origin CG); z_R here is measured vertically from the running waterline
127         # at the transom, so the trim rotation is already in z_R and is not applied again.
128         h3 = y_R * np.sin(phi_R_s) + z_R * np.cos(phi_R_s) #* np.cos(trim_rad) - x_R *
            ↪  np.sin(trim_rad)   # [m]
129
130         # Total tilt of the blade (heel + cant)
131         tau = phi - phi_R_s
132
133         # Lateral velocity normal to the (heeled, canted) blade
134         v_R_loc = (v + x_R * r) * np.cos(tau) - h3 * p   # [m/s], y to SB
135
136         # Trim + heel: geometric angle of the trimmed, heeled blade in the axial flow
137         alpha_trim = np.sin(trim_rad) * np.sin(tau)   # [rad]
138
139         # Oblique horizontal inflow angle (drift, yaw, roll), straightened by gamma_R
140         beta_R_lat = -gamma_R * np.arctan2(v_R_loc, u_R)  # [rad]
141         # Effective inflow angle [rad]
142         beta_R_str = beta_R_lat - alpha_trim
143         alpha_R = delta - beta_R_str                      # angle of attack [rad]
144
145         # --- Lift and induced drag ---
146         q_R = 0.5 * g.rho * u_R**2 * A_R             # dynamic pressure x area [N]
147         liftcoeff_L = LCS * alpha_R
148         C_L = liftcoeff_L / (1.0 + np.abs(liftcoeff_L / g.CL_max)**g.CL_sharpness)**(1.0 /
            ↪  g.CL_sharpness)
149         L_R = q_R * C_L                              # lift, sign follows alpha_R [N]
150         D_R = q_R * C_L**2 / (np.pi * AR)            # induced drag, Eq. 3.108, always >= 0 [N]
151
152         # --- Forces in the plane of the heeled blade (body xy-plane) ---
153         Y_lift = -L_R
154         X_R = -D_R * np.cos(beta_R_lat) + Y_lift * np.sin(beta_R_lat)   # body x = boat x: no cos(phi)
155         Y_N = Y_lift * np.cos(beta_R_lat) + D_R * np.sin(beta_R_lat)    # force normal to the blade
            ↪  (body y) [N]
156
157         if g.rudder_use_aH:
158             a_H = d.a_H
159             x_H = d.x_H_ * g.Lpp
160         else:
161             a_H, x_H = 0.0, 0.0
162         Y_aH = a_H * Y_N                             # rudder-induced hull side force [N]
163
164         # --- To boat axes (xy-plane horizontal, Lewandowski p. 363) ---
165         K_R = -h3 * (Y_N + Y_aH)                     # exact roll moment of the blade-normal force
            ↪  about x, independent of phi
166         Y_R = (Y_N + Y_aH) * np.cos(tau)             # horizontal component [N]
167         y_boat = y_R * np.cos(phi) - z_R * np.sin(phi)   # lateral rudder position in boat axes [m]
168         N_R = (x_R * Y_N + x_H * Y_aH) * np.cos(tau) - y_boat * X_R   # N = x*F_y - y*F_x
169
170         F_N = L_R * np.cos(alpha_R) + D_R * np.sin(alpha_R)   # rudder normal force [N]
171         U_R = np.sqrt(u_R**2 + (u_R * np.tan(beta_R_str))**2)      # total inflow speed at the rudder
            ↪  [m/s]
172         v_R = u_R * np.tan(beta_R_str)                              # lateral inflow, MMG sign [m/s]
173
174         return X_R, U_R, Y_R, N_R, K_R, L_R, D_R, v_R, F_N
```

```
175
176
177     def rudder_forces_lewandowski_SB(self, u: float, U: float,
178                         beta: float, r_dash: float,
179                         delta: float, nps: float,
180                         J_SB: float, K_T_SB: float, w_P_SB: float,
181                         p_dash: float = 0.0, phi: float = 0.0):
182         """Starboard rudder, see _rudder_forces_core().
183
184         Returns:
185             X_R, U_R, Y_R, N_R, K_R, L_R, D_R, v_R, F_N
186         """
187         return self._rudder_forces_core(+1, u, U, beta, r_dash, delta, nps,
188                                         J_SB, K_T_SB, w_P_SB, p_dash, phi)
189
190
191     def rudder_forces_lewandowski_BB(self, u: float, U: float,
192                         beta: float, r_dash: float,
193                         delta: float, nps: float,
194                         J_BB: float, K_T_BB: float, w_P_BB: float,
195                         p_dash: float = 0.0, phi: float = 0.0):
196         """Port rudder (mirrored: y_R and y_P negative), see _rudder_forces_core().
197
198         Returns:
199             X_R, U_R, Y_R, N_R, K_R, L_R, D_R, v_R, F_N
200         """
201         return self._rudder_forces_core(-1, u, U, beta, r_dash, delta, nps,
202                                         J_BB, K_T_BB, w_P_BB, p_dash, phi)
```

Listing 3: Empirical hull force model, this is the same for both the GPPH and pilot vessel.

```
1  def hull_surge_force(self, u: float, v: float, r: float, U: float, d_now: float) -> float:
2      """Surge hull force X_H [N]:
3          X_H = -R(u)
4       R(u) from ResistanceCurve on surge speed u.
5      """
6      return self.resistance_curve(u)
7
8
9  def _planing_preliminaries(self, U: float) -> dict:
10     """Lewandowski Table 6.2 preliminary quantities"""
11     g_ = self.g
12     beta_rad = np.radians(g_.deadrise_deg)
13     trim_deg, L_K, L_C, T_transom = self._attitude(U)          # RUNNING ATTITUDE
14     self._attitude_now = (trim_deg, L_K, L_C, T_transom)       # RUNNING ATTITUDE
15     B_ac = g_.B_ac
16     trim_rad = np.radians(trim_deg)                            # RUNNING ATTITUDE
17     KG = g_.KG
18     rho = g_.rho
19
20     Lambda = (L_K / B_ac) - (np.tan(beta_rad) / (2 * np.pi * np.tan(trim_rad)))
21
22     Cv = U / np.sqrt(G_GRAV * B_ac)
23     k_beta = 0.06641 + 0.00716*g_.deadrise_deg + 0.0003861*g_.deadrise_deg**2
24     h1 = (KG - 0.3927*B_ac*np.tan(beta_rad)) * (KG - 0.306*B_ac)
25     Delta = 0.25*rho*G_GRAV*Lambda**2*np.sin(2*trim_rad)*B_ac**3
26     KB = B_ac*np.tan(beta_rad)*(1/6)*(0.5 + L_C/L_K)
27
28     F_phi = -1/(4*np.cos(beta_rad)**2) * (
29         ((1-np.sin(beta_rad)) * (np.pi*Lambda)/(1+Lambda) + 1.33/np.pi) * trim_rad
30         + (((1-np.sin(beta_rad))/np.cos(beta_rad)) * 1/(2*(1+Lambda)**2))
31     ) * 0.5 * rho * U**2 * B_ac**2
32
33     h2 = 0.8*np.pi*B_ac/(8*np.cos(beta_rad)) - KG*np.sin(beta_rad)
34     K_Dphi = 2*h2*F_phi
35
36     U_sw = G_GRAV*B_ac*(Lambda - 0.16*np.tan(beta_rad)/np.tan(trim_rad)) / (3*np.sin(trim_rad))
37     L_C2 = L_C - 3*U**2*np.sin(trim_rad)/G_GRAV
38     f_sw = 1.0 if U**2 > U_sw else 1.0 + 0.603*L_C2/(Lambda*B_ac)
39
40     LCP = Lambda*B_ac*(0.75 - 1/(5.21*(Cv**2)/(Lambda**2) + 2.39))
41
```

```
    block = np.pi/4 * (1-np.sin(beta_rad)) * np.cos(trim_rad) * (Lambda)/(1+Lambda) + 1.33/4 * Lambda * np.cos(trim_rad) * np.sin(2*trim_rad) * np.cos(beta_rad)
    brackets =  np.sin(2*trim_rad)/(2*np.cos(beta_rad)) * (block)
    L_D = 0.5*rho* U**2 * B_ac**2 * (brackets)

    return dict(Lambda=Lambda, Cv=Cv, k_beta=k_beta, h1=h1, Delta=Delta, KB=KB,
                F_phi=F_phi, K_Dphi=K_Dphi, f_sw=f_sw, LCP=LCP, h2=h2, L_D=L_D,
                trim_deg=trim_deg, L_K=L_K, L_C=L_C, T_transom=T_transom)

def _planing_derivatives(self, U: float, prelim: dict, phi:float) -> dict:
    """Lewandowski Table 6.3 hull derivatives with proposed corrections"""
    g_ = self.g
    beta_rad = np.radians(g_.deadrise_deg)
    L_K, L_C, B_ac, Loa = prelim["L_K"], prelim["L_C"], g_.B_ac, g_.Loa         # RUNNING ATTITUDE
    trim_deg, KG, LCG, rho = prelim["trim_deg"], g_.KG, g_.LCG, g_.rho          # RUNNING ATTITUDE
    Lambda, Cv, k_beta, h1 = prelim["Lambda"], prelim["Cv"], prelim["k_beta"], prelim["h1"]
    F_phi, K_Dphi, f_sw, KB, Delta, LCP, L_D = (prelim["F_phi"], prelim["K_Dphi"], prelim["f_sw"],
                                                prelim["KB"], prelim["Delta"], prelim["LCP"],
                                                prelim["L_D"])
    T_dash = prelim["T_transom"] / B_ac                                          # RUNNING ATTITUDE
    tanb = np.tan(beta_rad)

        ## Hull derivatives (Lewandowski Table 6.3) ##
    # --- Acceleration (added mass/inertia) derivatives ---
    Y_vdot_H = -B_ac**2 *rho*tanb* k_beta *(L_K + 2*L_C) / 12.0
    K_vdot_H = 0.0
    N_vdot_H = -B_ac**2 *rho*tanb*k_beta*(L_K**2 + 2*L_K*L_C + 3*L_C**2) / 48.0
    Y_rdot_H = N_vdot_H
    K_rdot_H = 0.0
    N_rdot_H = -B_ac**2 *rho*tanb*k_beta*(L_K**3 + 2*L_K**2 *L_C + 3*L_C**2 *L_K + 4*L_C**3) / 120.0
    Y_pdot_H = 0.0
    K_pdot_H = -0.010237*rho*B_ac**5 *Lambda*(1 - np.sin(beta_rad)) + h1*Y_vdot_H
    N_pdot_H = 0.0

    # --- Shift hull added mass from Lewandowski's reference point to the EoM origin (midship, waterline) ---
    # The longitudinal integrals above are measured from the transom (L_K, L_C horizontal),
    # the roll terms are about the CG -> Lewandowski reference point (x_ref, z_ref) w.r.t.
    # midship/waterline. General parallel-axis shift, derived from
    # v_ref = v_O + x_ref*r - z_ref*p, K_O = K_ref - z_ref*Y, N_O = N_ref + x_ref*Y.
    # All nine terms are kept, also those that are zero now.
    x_ref = self.x_transom                      # horizontal transom position (-0.5*Lpp while transom = AP)
    _, z_ref = self._cg_vertical_offset(phi)    # same z_G as dynamics()
    (Y_vdot_H, Y_pdot_H, Y_rdot_H,
     K_vdot_H, K_pdot_H, K_rdot_H,
     N_vdot_H, N_pdot_H, N_rdot_H) = (
        Y_vdot_H,
        Y_pdot_H - z_ref*Y_vdot_H,
        Y_rdot_H + x_ref*Y_vdot_H,
        K_vdot_H - z_ref*Y_vdot_H,
        K_pdot_H - z_ref*(K_vdot_H + Y_pdot_H) + z_ref**2*Y_vdot_H,
        K_rdot_H + x_ref*K_vdot_H - z_ref*Y_rdot_H - x_ref*z_ref*Y_vdot_H,
        N_vdot_H + x_ref*Y_vdot_H,
        N_pdot_H - z_ref*N_vdot_H + x_ref*Y_pdot_H - x_ref*z_ref*Y_vdot_H,
        N_rdot_H + x_ref*(N_vdot_H + Y_rdot_H) + x_ref**2*Y_vdot_H,
    )
    # --- Velocity/rate derivatives
    Y_v_H = -0.5*rho*U*B_ac**2 * (0.6494 * g_.deadrise_deg**0.6 * T_dash**2)
    K_v_H = Y_v_H * (-KG + 1.5145*B_ac/(g_.deadrise_deg**0.342))
    N_v_H = Y_v_H * (-LCG + (12.384*B_ac*T_dash**0.45) / (trim_deg + 5.28))

    Y_r_H = 0.5*rho*U*B_ac**2 *Loa * (55.439* g_.deadrise_deg**0.6 *T_dash**3) * (0.02754 - (0.5949*T_dash)/(trim_deg + 5.28))
    K_r_H = 0.0
    N_r_H = -0.5*rho*U*B_ac**3 *Loa * (73.918* g_.deadrise_deg**0.6 *T_dash**3) * (0.00638 + 6.714*T_dash**2/(trim_deg + 5.28)**2)

    Y_p_H = 0.0
    K_p_H = -(1-np.sin(beta_rad))*(0.029*Cv + 0.02*Lambda)*rho*G_GRAV* B_ac**4 *np.sqrt(B_ac/G_GRAV) + h1*Y_v_H
    N_p_H = 0.0
```

```
107
108     Y_phi_H = 2*F_phi*np.sin(beta_rad) + L_D
109     K_phi_H = K_Dphi + 0.624*f_sw*(-rho*G_GRAV* B_ac**3 *(L_K + 3*L_C)/48 + (KG - KB)*Delta)
110     N_phi_H = Y_phi_H * (LCP - LCG)
111
112         ## Rudder added mass/inertia (Lewandowski Table 6.4) ##
113     z_R_now = self._z_R(prelim["T_transom"])                                    # RUNNING ATTITUDE
114     x_R_SB, y_R_SB, z_R_SB = g_.x_R, g_.y_R, z_R_now
115     x_R_BB, y_R_BB, z_R_BB = g_.x_R, -g_.y_R, z_R_now
116     trim_rad = np.radians(prelim["trim_deg"])                                   # RUNNING ATTITUDE
117     A = g_.c_R * g_.H_R
118     AR = g_.H_R**2 / A if g_.rudder_gap else 2 * g_.H_R**2 / A   # same switch as _rudder_forces_core
119
120     phi_R_SB = g_.phi_R                 # cant of the SB rudder, tip outward positive [rad]
121     phi_R_BB = -g_.phi_R                # BB rudder mirrored
122     m_rudder = rho * np.pi * AR * A * g_.c_R / (4*np.sqrt(1+AR**2))
123     # h3: perpendicular distance from the horizontal roll axis to the line of action of the
124     # blade normal force (same h3 as in _rudder_forces_core). z_R is measured vertically from
125     # the running waterline at the transom, so the trim rotation is not applied again.
126     h3_SB= y_R_SB * np.sin(phi_R_SB) + z_R_SB * np.cos(phi_R_SB)  #reference point is midship
127     h3_BB= y_R_BB * np.sin(phi_R_BB) + z_R_BB * np.cos(phi_R_BB)  #reference point is midship
128
129     # --- Acceleration (added mass/inertia) derivatives ---
130     tau_SB = phi - phi_R_SB
131     tau_BB = phi - phi_R_BB
132         #starboard rudder
133     Y_vdot_R_SB = -m_rudder * (np.cos(tau_SB))**2
134     K_vdot_R_SB = m_rudder * h3_SB * (np.cos(tau_SB))
135     N_vdot_R_SB = -m_rudder * x_R_SB * (np.cos(tau_SB))**2
136     Y_rdot_R_SB = N_vdot_R_SB
137     K_rdot_R_SB = m_rudder * h3_SB * x_R_SB * (np.cos(tau_SB))
138     N_rdot_R_SB = Y_rdot_R_SB * x_R_SB
139     Y_pdot_R_SB = m_rudder * h3_SB * np.cos(tau_SB)
140     K_pdot_R_SB = -m_rudder * h3_SB**2
141     N_pdot_R_SB = Y_pdot_R_SB * x_R_SB
142
143         #port rudder
144     Y_vdot_R_BB = -m_rudder * (np.cos(tau_BB))**2
145     K_vdot_R_BB = m_rudder * h3_BB * (np.cos(tau_BB))
146     N_vdot_R_BB = -m_rudder * x_R_BB * (np.cos(tau_BB))**2
147     Y_rdot_R_BB = N_vdot_R_BB
148     K_rdot_R_BB = m_rudder * h3_BB * x_R_BB * (np.cos(tau_BB))
149     N_rdot_R_BB = Y_rdot_R_BB * x_R_BB
150     Y_pdot_R_BB = m_rudder * h3_BB * np.cos(tau_BB)
151     K_pdot_R_BB = -m_rudder * h3_BB**2
152     N_pdot_R_BB = Y_pdot_R_BB * x_R_BB
153
154         #total of both rudders
155     Y_vdot_R = Y_vdot_R_SB + Y_vdot_R_BB
156     K_vdot_R = K_vdot_R_SB + K_vdot_R_BB
157     N_vdot_R = N_vdot_R_SB + N_vdot_R_BB
158     Y_rdot_R = Y_rdot_R_SB + Y_rdot_R_BB
159     K_rdot_R = K_rdot_R_SB + K_rdot_R_BB
160     N_rdot_R = N_rdot_R_SB + N_rdot_R_BB
161     Y_pdot_R = Y_pdot_R_SB + Y_pdot_R_BB
162     K_pdot_R = K_pdot_R_SB + K_pdot_R_BB
163     N_pdot_R = N_pdot_R_SB + N_pdot_R_BB
164
165         ## total hull + rudder derivatives (Lewandowski Table 6.2/6.3 + 6.4) ##
166     # Research vessel: twin rudders, so the rudder added mass (*_R above) is included.
167     # For the GPPH gearcase model (no rudders) use the hull terms only: Y_vdot = Y_vdot_H, etc.
168     Y_vdot = Y_vdot_H + Y_vdot_R
169     K_vdot = K_vdot_H + K_vdot_R
170     N_vdot = N_vdot_H + N_vdot_R
171     Y_rdot = Y_rdot_H + Y_rdot_R
172     K_rdot = K_rdot_H + K_rdot_R
173     N_rdot = N_rdot_H + N_rdot_R
174     Y_pdot = Y_pdot_H + Y_pdot_R
175     K_pdot = K_pdot_H + K_pdot_R
176     N_pdot = N_pdot_H + N_pdot_R
177     Y_v = Y_v_H
178     K_v = K_v_H
179     N_v = N_v_H
```

```
    Y_r = Y_r_H
    K_r = K_r_H
    N_r = N_r_H
    Y_p = Y_p_H
    K_p = K_p_H
    N_p = N_p_H
    Y_phi = Y_phi_H
    K_phi = K_phi_H
    N_phi = N_phi_H

    return dict(Y_vdot=Y_vdot, K_vdot=K_vdot, N_vdot=N_vdot, Y_rdot=Y_rdot, K_rdot=K_rdot,
    ↪  N_rdot=N_rdot,
                Y_pdot=Y_pdot, K_pdot=K_pdot, N_pdot=N_pdot,
                Y_v=Y_v, K_v=K_v, N_v=N_v, Y_r=Y_r, K_r=K_r, N_r=N_r,
                Y_p=Y_p, K_p=K_p, N_p=N_p, Y_phi=Y_phi, K_phi=K_phi, N_phi=N_phi)


def hull_forces(self, v: float, p: float, r: float, phi: float, d: dict,
                x_G: float, z_G: float) -> tuple:
    """Y_H, K_H, N_H about the CG (Lewandowski's own origin), then moment-transferred to midship via
    the x_G/z_G offset (see _planing_derivatives() for the derivation)."""
    Y_H = d["Y_v"]*v + d["Y_r"]*r + d["Y_p"]*p + d["Y_phi"]*phi
    K_H = d["K_v"]*v + d["K_r"]*r + d["K_p"]*p + d["K_phi"]*phi - Y_H*z_G
    N_H = d["N_v"]*v + d["N_r"]*r + d["N_p"]*p + d["N_phi"]*phi + Y_H*x_G
    return Y_H, K_H, N_H
```

Listing 4: Equations of motion, for the steering and propulsion blocks the right equations had to be selected by hand for either the GPPH (gear-case) or the pilot vessel (twin-propeller, twin-rudder).

```
def dynamics(self, u: float, v: float, r: float, phi: float, p: float,
             delta: float, nps: float):

    g_ = self.g
    U = np.sqrt(u**2 + v**2)   # CG-referenced, per Lewandowski's own Eq. 6.1 origin
    if U < 1e-4:
        return 0.0, 0.0, 0.0, 0.0

    prelim = self._planing_preliminaries(U)
    d = self._planing_derivatives(U, prelim, phi)

    # --- CG offset from the midship/roll-axis origin, GM/KM/d convention ---
    d_now = self.draft_curve(U)

    y_G, z_G = self._cg_vertical_offset(phi)
    x_G = self.x_G

    m, I_xx, I_zG, m_x = self.m, self.I_xx, self.I_zG, g_.m_x

    # --- Rudder/propeller ---
    v_m = v - x_G*r + z_G*p
    U_rp = np.sqrt(u**2 + v_m**2)
    r_dash = r * g_.Lpp / U_rp if U_rp > 1e-4 else 0.0
    p_dash = p * g_.Lpp / U_rp if U_rp > 1e-4 else 0.0
    beta = np.arctan2(-v_m, u)

    # --- Lewandowski hull forces, about the CG, then moment-transferred to midship ---
    Y_H, K_H, N_H = self.hull_forces(v, p, r, phi, d, x_G, z_G)
    X_H = self.hull_surge_force(u, v, r, U, d_now) # surge resistance from identified curve

    #propeller forces
        #if Lewandowski is used with twin propellers:
    X_P_SB, N_P_SB, J_SB, K_T_SB, w_P_SB = self.propeller_force_SB(u, U, nps, beta, r_dash,
    ↪  p_dash=p_dash)
    X_P_BB, N_P_BB, J_BB, K_T_BB, w_P_BB = self.propeller_force_BB(u, U, nps, beta, r_dash,
    ↪  p_dash=p_dash)
    X_P = X_P_SB + X_P_BB
    N_P = N_P_SB + N_P_BB
    Y_P, K_P = 0.0, 0.0  # no sway/roll from the propellers in the twin-propeller Lewandowski model

        #if GC model is used:
    X_P, Y_P, K_P, N_P, _, _, _ = self.propeller_force_GC(u, v, U, nps,beta, r, r_dash, delta, p=p,
    ↪  p_dash=p_dash, phi=phi)
```

```
41
42      #rudder forces
43          #If lewandowski rudder model is used:
44      X_R_BB, U_R_BB, Y_R_BB, N_R_BB, K_R_BB, L_R_BB, D_R_BB, v_R_BB, F_N_BB =
        ↪  self.rudder_forces_lewandowski_BB(u, U_rp, beta, r_dash, delta, nps, J_BB, K_T_BB, w_P_BB,
        ↪  p_dash=p_dash, phi=phi)
45      X_R_SB, U_R_SB, Y_R_SB, N_R_SB, K_R_SB, L_R_SB, D_R_SB, v_R_SB, F_N_SB =
        ↪  self.rudder_forces_lewandowski_SB(u, U_rp, beta, r_dash, delta, nps, J_SB, K_T_SB, w_P_SB,
        ↪  p_dash=p_dash, phi=phi)
46
47      X_R_total = X_R_BB + X_R_SB  # total rudder surge moment (both rudders)
48      Y_R_total = Y_R_BB + Y_R_SB  # total rudder sway moment (both rudders)
49      K_R_total = K_R_BB + K_R_SB   # total rudder roll moment (both rudders)       #defined negative
50      N_R_total = N_R_BB + N_R_SB   # total rudder yaw moment (both rudders)
51
52          #if gearcase rudder model is used:
53      X_GC, Y_GC, N_GC, K_GC = self._rudder_forces_GC(u, v, U, r, p, delta, phi=phi)
54
55      X_R_total = X_GC
56      Y_R_total = Y_GC
57      K_R_total = K_GC
58      N_R_total = N_GC
59
60      z_R = g_.z_R
61
62      #total forces and moments           (Y_P and K_P only in gearcase model)
63      X = X_H + X_R_total + X_P
64      Y = Y_H + Y_R_total + Y_P
65      K = K_H + K_R_total + K_P
66      N = N_H + N_R_total + N_P
67
68      u_dot = (
69          (X)
70          + (m - d["Y_vdot"]) * v_m * r       # Coriolis (sway inertia acts on surge)
71          - d["Y_rdot"] * r**2                # added-mass Coriolis, -a2*r with a2 = -(Y_vdot*v +
            ↪  Y_pdot*p + Y_rdot*r)
72          - d["Y_pdot"] * p * r               # idem, roll part
73          + m * x_G * r**2                    # centripetal from CG offset
74          - m * z_G * r * p                   # roll-yaw-rate coupling into surge
75      ) / (m_x + m)
76
77      # Full mass matrix about midship/waterline: rigid body + all nine added-mass
78      # derivatives (hull shifted to midship in _planing_derivatives, rudder already midship).
79      sway_added_mass         = m - d["Y_vdot"]
80      sway_roll_coupling      = -m*z_G - d["Y_pdot"]
81      sway_yaw_coupling       = m*x_G - d["Y_rdot"]
82      roll_sway_coupling      = -m*z_G - d["K_vdot"]                  # K_vdot shifted to the waterline
83      roll_added_mass_inertia = I_xx + m*z_G**2 - d["K_pdot"]
84      roll_yaw_coupling       = -m*x_G*z_G - d["K_rdot"]
85      yaw_sway_coupling       = m*x_G - d["N_vdot"]
86      yaw_roll_coupling       = -m*x_G*z_G - d["N_pdot"]
87      yaw_added_mass_inertia  = I_zG + m*x_G**2 - d["N_rdot"]
88
89      M3 = np.array([
90          [sway_added_mass,    sway_roll_coupling,      sway_yaw_coupling],
91          [roll_sway_coupling, roll_added_mass_inertia, roll_yaw_coupling],
92          [yaw_sway_coupling,  yaw_roll_coupling,       yaw_added_mass_inertia],
93      ])
94
95      b_v = Y - m*u*r
96      b_p = K + m*z_G*u*r
97      b_r = N - m*x_G*u*r
98
99      # Solve gives v_m_dot (midship-referenced), matching this mass matrix's
100     # structure - converted back to CG-referenced v_dot
101     v_m_dot, p_dot, r_dot = np.linalg.solve(M3, np.array([b_v, b_p, b_r]))
102     v_dot = self._vG_dot(v_m_dot, r_dot, p_dot, p, phi)
103
104     return u_dot, v_dot, r_dot, p_dot
```